



MINISTÉRIO DA CIÊNCIA, TECNOLOGIA E INOVAÇÃO
INSTITUTO NACIONAL DE PESQUISAS ESPACIAIS

sid.inpe.br/mtc-m21b/2015/02.27.16.38-TDI

**LOCATION OF LARGE SCALE RECONNECTION AT
EARTH'S DAYSIDE MAGNETOPAUSE AS PROBED BY
ANALYTICAL X LINE MODELS AND IN SITU
OBSERVATIONS**

Vitor Moura Cardoso e Silva Souza

Doctorate Thesis of the Graduate
Course in Space Geophysics, su-
pervised by Drs. Daiki Koga, and
Odim Mendes Junior, approved in
February 24, 2015.

URL of the original document:

<<http://urlib.net/8JMKD3MGP3W34P/3J3GFGP>>

INPE
São José dos Campos
2015

PUBLISHED BY:

Instituto Nacional de Pesquisas Espaciais - INPE

Gabinete do Diretor (GB)

Serviço de Informação e Documentação (SID)

Caixa Postal 515 - CEP 12.245-970

São José dos Campos - SP - Brasil

Tel.:(012) 3208-6923/6921

Fax: (012) 3208-6919

E-mail: pubtc@sid.inpe.br

**COMMISSION OF BOARD OF PUBLISHING AND PRESERVATION
OF INPE INTELLECTUAL PRODUCTION (DE/DIR-544):****Chairperson:**

Marciana Leite Ribeiro - Serviço de Informação e Documentação (SID)

Members:

Dr. Gerald Jean Francis Banon - Coordenação Observação da Terra (OBT)

Dr. Amauri Silva Montes - Coordenação Engenharia e Tecnologia Espaciais (ETE)

Dr. André de Castro Milone - Coordenação Ciências Espaciais e Atmosféricas
(CEA)

Dr. Joaquim José Barroso de Castro - Centro de Tecnologias Espaciais (CTE)

Dr. Manoel Alonso Gan - Centro de Previsão de Tempo e Estudos Climáticos
(CPT)

Dr^a Maria do Carmo de Andrade Nono - Conselho de Pós-Graduação

Dr. Plínio Carlos Alvalá - Centro de Ciência do Sistema Terrestre (CST)

DIGITAL LIBRARY:

Dr. Gerald Jean Francis Banon - Coordenação de Observação da Terra (OBT)

Clayton Martins Pereira - Serviço de Informação e Documentação (SID)

DOCUMENT REVIEW:

Simone Angélica Del Ducca Barbedo - Serviço de Informação e Documentação
(SID)

Yolanda Ribeiro da Silva Souza - Serviço de Informação e Documentação (SID)

ELECTRONIC EDITING:

Marcelo de Castro Pazos - Serviço de Informação e Documentação (SID)

André Luis Dias Fernandes - Serviço de Informação e Documentação (SID)



MINISTÉRIO DA CIÊNCIA, TECNOLOGIA E INOVAÇÃO
INSTITUTO NACIONAL DE PESQUISAS ESPACIAIS

sid.inpe.br/mtc-m21b/2015/02.27.16.38-TDI

**LOCATION OF LARGE SCALE RECONNECTION AT
EARTH'S DAYSIDE MAGNETOPAUSE AS PROBED BY
ANALYTICAL X LINE MODELS AND IN SITU
OBSERVATIONS**

Vitor Moura Cardoso e Silva Souza

Doctorate Thesis of the Graduate
Course in Space Geophysics, su-
pervised by Drs. Daiki Koga, and
Odim Mendes Junior, approved in
February 24, 2015.

URL of the original document:

<<http://urlib.net/8JMKD3MGP3W34P/3J3GFGP>>

INPE
São José dos Campos
2015

Cataloging in Publication Data

Souza, Vitor Moura Cardoso e Silva.

So89l Location of large scale reconnection at Earth's dayside magnetopause as probed by analytical X line models and in situ observations / Vitor Moura Cardoso e Silva Souza. – São José dos Campos : INPE, 2015.

xxv + 187 p. ; (sid.inpe.br/mtc-m21b/2015/02.27.16.38-TDI)

Thesis (Doctorate in Space Geophysics) – Instituto Nacional de Pesquisas Espaciais, São José dos Campos, 2015.

Guiding : Drs. Daiki Koga, and Odim Mendes Junior.

1. Magnetic reconnection. 2. Dayside magnetopause. 3. Earth's magnetosphere. 4. Turning function. I.Title.

CDU 533:537.8

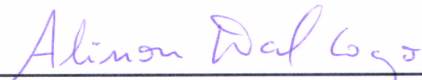


Esta obra foi licenciada sob uma Licença [Creative Commons Atribuição-NãoComercial 3.0 Não Adaptada](https://creativecommons.org/licenses/by-nc/3.0/).

This work is licensed under a [Creative Commons Attribution-NonCommercial 3.0 Unported License](https://creativecommons.org/licenses/by-nc/3.0/).

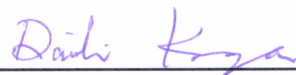
Aprovado (a) pela Banca Examinadora
em cumprimento ao requisito exigido para
obtenção do Título de **Doutor(a)** em
**Geofísica Espacial/Ciências do Ambiente
Solar-Terrestre**

Dr. Alisson Dal Lago



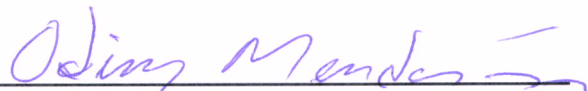
Presidente / INPE / São José dos Campos - SP

Dr. Daiki Koga



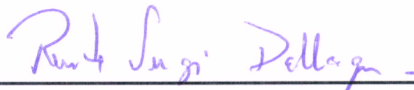
Orientador(a) / INPE / São José dos Campos - SP

Dr. Odim Mendes Junior



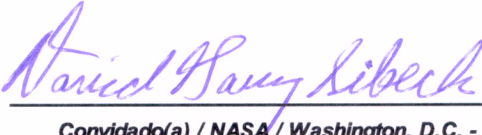
Orientador(a) / INPE / SJC Campos - SP

Dr. Renato Sérgio Dallaqua




Membro da Banca / INPE / São José dos Campos - SP

Dr. David Gary Sibeck



Convidado(a) / NASA / Washington, D.C. - USA

Dra. Flávia Reis Cardoso



Convidado(a) / EEL - USP / Lorena - SP

Este trabalho foi aprovado por:

() maioria simples

() unanimidade

Aluno (a): **Vítor Moura Cardoso e Silva Souza**

São José dos Campos, 24 de Fevereiro de 2015

“Assim como existem o trigo, os frutos e as árvores, cada pensamento, credo e religião é uma manifestação de Deus e, portanto, digna do nosso sincero e maior respeito”.

CHICO XAVIER

A meu "meteoro," meu amado irmão Levi (in memoriam).

ACKNOWLEDGEMENTS

Em toda minha vida tive a bênção de contar com pessoas maravilhosas com as quais aprendi, e continuo a aprender, inestimáveis lições de amor, alegria e obstinação. Durante os cinco anos de doutorado, não foi diferente. Estas pessoas, e muitas outras que conheci durante esta jornada, me apoiaram fervorosamente, doando um pouco de si para que eu chegasse onde estou hoje. Portanto, a estas pessoas, meus familiares e amigos, quero agradecer, de todo o coração, por todos os momentos que passamos juntos, ou distantes fisicamente, mas sempre, a todos os instantes, contando com suas doces preces a chegarem ao meu coração, acalmando-me em tempos turbulentos, ou trazendo-me alegria e paz. Em especial, agradeço a minha mãe, Margarida, meu pai, Genilson, aos meus amados irmãos Ciro e Levi (*in memoriam*) e a minha avó pelo coração Alayde, que não hesitaram, em nenhum momento sequer, em me apoiar e a me infundir coragem. Que o nosso bondoso Deus Pai continue a encher suas vidas de bênçãos.

Agradeço a minha pequena-grande Fernanda que tive a imensa honra de conhecer durante os primeiros passos desta jornada. Seu jeito meigo e encantador continua a cativar, cada vez mais, o meu coração, trazendo-me alegria e tranquilidade. Que Deus te abençoe, minha amada!

Gratidão eterna aos amados amigos Íris Lantyer e Terra, e Íris Lívia e Marcelo, cujo apoio basilar tocou fundo em meu coração e permitiu-me prosseguir, intimorato, no caminho escolhido do aperfeiçoamento intelectual.

Sou imensamente grato pela companhia e amizade dos queridos conterrâneos Mariana e Pedro. Muito obrigado por tolerar-me durante todo este período. Deus os abençoe!

O meu preito de gratidão, com muito carinho, aos orientadores Drs. Walter Gonzalez, Daiki Koga e Odim Mendes Júnior, que através de seus sábios conselhos pude seguir com segurança os árduos caminhos do doutoramento.

Sou grato, em especial, ao mentor e amigo Dr. David G. Sibeck que acolheu, não somente a mim, mas a muitos outros visitantes brasileiros no laboratório de pesquisa em que atua nos EUA com o mesmo entusiasmo e alegria. Seus conselhos e exemplos foram fundamentais para a minha formação profissional. Muito obrigado! Agradeço, também, por ter gentilmente se predisposto a vir até o Brasil para participar da minha banca de tese, certamente melhorando sobremaneira a minha parca con-

tribuição à comunidade científica (I'd like to give special thanks to my mentor and friend Dr. David G. Sibeck who warmly welcomed not only me, but many other brazilian visitors at the laboratory he works at USA. Your wise advices and your good example in both life and science were indispensable on my vocational training. Many thanks! I would also like to thank Dr. Sibeck who kindly agreed to participate as an external member in my Ph.D's evaluation committee, surely contributing to improve my rather small contribution to the scientific community).

Agradeço ao amigo e colaborador Dr. Brian M. Walsh, cuja ajuda foi inestimável na minha preparação como pesquisador (I would like to thank my friend and collaborator Dr. Brian M. Walsh, whose invaluable advices were fundamental on my education as a researcher).

Um agradecimento especial ao meu amigo Paul Butterworth que me acolheu por um ano em sua casa com muito carinho e solicitude. Muita paz pra você! (A special thanks to my great friend Paul Butterworth who hosted me for a whole year in his place. A thoughtful and attentive guy. Peace to you, my friend!)

A todos os pesquisadores e colegas com quem tive o privilégio de conversar e aprender, sou e serei muito grato.

Agradeço aos Drs. Vassilis Angelopoulos, Philippe Escoubet, e Andrew Fazakerley que forneceram dados das missões THEMIS, CLUSTER e DOUBLE STAR TC-1, respectivamente.

Sou muito grato ao INPE que me forneceu toda a infraestrutura necessária para que eu pudesse levar meu trabalho adiante.

Finalmente, agradeço às agências CAPES e CNPq pelo apoio financeiro.

ABSTRACT

The magnetic reconnection process is believed to occur throughout the Universe whenever distinct magnetized plasma regimes come together and interact. It has also been shown to be the dominant process for the solar wind-magnetosphere interaction. In this work the large scale aspect of the magnetic field reconnection process is investigated: where does reconnection occur along the Earth's dayside magnetopause and what are the key parameters governing its location? We perform an intercomparison of three analytical models, which predict the reconnection X-line location and orientation, namely [Trattner et al. \(2007\)](#), [Gonzalez and Mozer \(1974\)](#), and [Swisdak and Drake \(2007\)](#) against two sets of reconnection events which are identified mostly by the *in situ* detection of accelerated plasma flows. In the first set, we show four fortuitous, quasi-simultaneous dayside magnetopause crossing events where two widely separated spacecraft detect reconnection signatures, and the possible X-line location can be inferred from the observations. The X-line models are then used and their predictions are compared with the expected X-line location obtained from observation. The results suggest that an extended (> 5 Earth radii in length), component-type reconnection X-line may in fact be a likely scenario at Earth's dayside magnetopause, connecting and structuring the reconnection characteristics on far apart observation points. In the second set of reconnection events, we have analyzed the X-line model's performance in predicting the observed reconnection outflow direction, i.e., its north-south and/or east-west senses, in a total of 116 single magnetopause crossing events where reconnection-generated plasma flows were clearly present. We found that the [Swisdak and Drake \(2007\)](#)'s X-line model had a slightly better performance in predicting both accelerated plasma flow components: north-south (72% of the cases) and east-west (54% of the cases), as compared to the [Trattner et al. \(2007\)](#) model (66% north-south, 37% east-west), and [Gonzalez and Mozer \(1974\)](#) model (60% north-south, 42% east-west). The [Swisdak and Drake \(2007\)](#) model takes into account the realistic asymmetrical magnetic fields and plasma density conditions across the magnetopause boundary layer, thus the result suggests that in addition to external boundary conditions such as the interplanetary magnetic field orientation and solar wind dynamic pressure value, the local plasma and magnetic field conditions play an important role in determining the large scale X-line orientation at Earth's dayside magnetopause, in particular the local plasma β , as it has been shown elsewhere ([PHAN et al., 2013](#)).

ANÁLISE DA LOCALIZAÇÃO DA RECONEXÃO MAGNÉTICA EM LARGA ESCALA NA MAGNETOPAUSA DIURNA TERRESTRE POR MEIO DE MODELOS ANALÍTICOS DE LINHA X E OBSERVAÇÕES *IN SITU*

RESUMO

Acredita-se que o processo de reconexão magnética seja capaz de ocorrer por todo o Universo toda vez que plasmas magnetizados distintos interajam. Tem-se também mostrado que a reconexão magnética é o processo dominante na interação vento solar-magnetosfera terrestre. Neste trabalho, o aspecto de larga escala do processo de reconexão magnética é investigado. Em particular, busca-se identificar em qual(is) região(ões) ao longo da magnetopausa diurna terrestre a reconexão magnética ocorre, e ainda quais os parâmetros-chave que ditam o modo como a linha X deve localizar-se. Utilizando dois conjuntos de eventos de reconexão magnética, os quais são identificados principalmente pela detecção de fluxos de plasma acelerados, faz-se uma comparação entre três modelos analíticos: [Trattner et al. \(2007\)](#), [Gonzalez and Mozer \(1974\)](#), and [Swisdak and Drake \(2007\)](#), que predizem a localização e orientação da linha X de reconexão. No primeiro conjunto de eventos, mostram-se quatro eventos fortuitos de cruzamentos quasi-simultâneos da magnetopausa diurna terrestre nos quais dois satélites amplamente espaçados detectam assinaturas de reconexão, e como a localização da provável linha X pode ser inferida através das observações. Os modelos de linha X são então utilizados e suas respectivas previsões comparadas com a localização esperada da linha X. Os resultados sugerem que uma extensa (> 5 raios terrestres em comprimento) linha X de reconexão por componente pode de fato constituir um cenário provável na magnetopausa diurna terrestre. Tal linha conectaria e estruturaria as assinaturas de reconexão detectadas em pontos substancialmente distantes. No segundo conjunto de eventos de reconexão, analisou-se a performance dos modelos de linha X em prever a direção, isto é, sentidos norte-sul e/ou leste-oeste, dos plasmas acelerados em 116 eventos de cruzamentos simples (somente um satélite) pela magnetopausa diurna terrestre para os quais os fluxos de plasma provenientes do processo de reconexão estivessem claramente presentes. Encontrou-se que o modelo de linha X de [Swisdak and Drake \(2007\)](#) obteve uma performance ligeiramente melhor na previsão de ambas as componentes dos plasmas acelerados: norte-sul (72% dos casos) e leste-oeste (54% dos casos), quando comparado com o modelo de [Trattner et al. \(2007\)](#) (66% norte-sul, 37% leste-oeste), e o modelo de [Gonzalez and Mozer \(1974\)](#) (60% norte-sul, 42% leste-oeste). O modelo de [Swisdak and Drake \(2007\)](#) leva em consideração condições realísticas de assimetrias nos campos magnéticos e densidades do plasma através da magnetopausa, portanto o resultado acima sugere que além de condições de contorno externas, tais como a orientação do campo magnético interplanetário e o valor da pressão dinâmica do vento solar, as condições locais de campo magnético e plasma, em particular o parâmetro β , possuem papel fundamental na determinação da orientação da linha X de larga escala na magnetopausa diurna terrestre, como tem sido mostrado na literatura ([PHAN et al., 2013](#)).

LIST OF FIGURES

| | <u>Page</u> |
|--|-------------|
| 2.1 Not to scale artistic view of the solar wind-magnetosphere interaction. | 5 |
| 2.2 Meridional view of the Earth’s magnetosphere and adjacent regions. | 8 |
| 3.1 Sketch of two approaching plasma regimes with antiparallel magnetic fields. | 14 |
| 3.2 Sweet–Parker’s reconnection geometry. | 16 |
| 3.3 Petschek’s reconnection geometry. | 18 |
| 3.4 Sketch of the subsolar dayside magnetopause reconnection geometry for antiparallel magnetic fields. | 22 |
| 4.1 Antiparallel reconnection sites, following Crooker (1979)’s criterion. | 26 |
| 4.2 Shue et al. (1998)’s magnetopause stand-off distance. | 29 |
| 4.3 View from the Sun of the draping of the magnetosheath magnetic field from the Cooling et al. (2001) model around the paraboloidal magnetopause. | 30 |
| 4.4 View from the Sun of the Alexeev et al. (2003)’s magnetospheric magnetic field model just inside the paraboloidal magnetopause boundary | 31 |
| 4.5 3-D perspectives of the plot shown in panel b) of Figure 4.1. | 33 |
| 4.6 Saddle point determination on shear angle plots | 35 |
| 4.7 Trattner et al. (2007)’s maximum shear X-line for a southward-duskward IMF orientation. | 36 |
| 4.8 (Top) View from the Sun onto the yz_{GSM} plane of the Chapman-Ferraro current density magnitude, $ \mathbf{J}_{CF} $ in units of mA/m, over the paraboloidal magnetopause surface. (Bottom) 3-D perspective of the top panel plot with $ \mathbf{J}_{CF} $ being the third dimension. | 40 |
| 4.9 2-D and 3-D schematic views of the reconnection plane formed by oppositely directed magnetic fields of the magnetosheath and magnetosphere. | 41 |
| 4.10 Local current sheet coordinate system used in the Swisdak and Drake (2007) model. | 43 |
| 4.11 Plot of α_{SD} versus the shear angle θ for the case $B_2/B_1 = 0.5$ and $\rho_2/\rho_1 = 10$ | 45 |
| 4.12 Section of the simulation grid adopted in all (36) BATS-R-US runs used in this thesis work. | 47 |
| 4.13 (Top) Plot of current density magnitude, $ \mathbf{J} $ in units of $\mu\text{A}/\text{m}^2$, on the noon-midnight meridian plane modeled by the BATS-R-US code. (Bottom) $ \mathbf{J} $ profile along the red line shown on the top panel. | 50 |

| | | |
|------|--|-----|
| 4.14 | Current density magnitude, $ \mathbf{J} $ in units of $\mu\text{A}/\text{m}^2$, modeled by the BATS-R-US code and normal vectors evaluation. | 53 |
| 4.15 | Magnetosheath (magnetosphere) locations just outside (inside) the BATS-R-US magnetopause current layer. | 54 |
| 4.16 | Plot of the reconnection outflow speed, V_{out} , versus the angle α_{SD} that orients the reconnection X-line relative to the reconnecting magnetic fields. | 55 |
| 4.17 | View from the Sun of the reconnection outflow speed values V_{out} in units of km/s, over the BATS-R-US dayside magnetopause. | 57 |
| 5.1 | Configuration of the GSM and local boundary normal coordinates (LMN) systems. The Earth is represented at the center. | 62 |
| 6.1 | Cluster 4's and Double Star TC1's magnetic field components represented in GSM coordinates (top panels), MVA coordinates (middle panels) and in boundary normal coordinates obtained via the Shue et al. (1998) magnetopause model (bottom panels). | 69 |
| 6.2 | Cluster 4 magnetopause crossing on 2007-03-05. | 71 |
| 6.3 | Double Star TC1 magnetopause crossing on 2007-03-05. | 73 |
| 6.4 | Themis A magnetopause crossing on 2007-06-14. | 76 |
| 6.5 | Double Star TC1 magnetopause crossing on 2007-06-14. | 77 |
| 6.6 | Cluster 3 magnetopause crossing on 2009-05-22. | 79 |
| 6.7 | Themis B magnetopause crossing on 2009-05-22. | 81 |
| 6.8 | Themis A magnetopause crossing on 2009-07-07. | 83 |
| 6.9 | Themis C magnetopause crossing on 2009-07-07. | 85 |
| 6.10 | Trattner et al. (2007)'s Maximum Shear Angle Model test against quasi-simultaneous magnetic reconnection plasma jet observations. | 89 |
| 6.11 | Gonzalez and Mozer (1974)'s X-line model test against quasi-simultaneous magnetic reconnection plasma jet observations. | 92 |
| 6.12 | Swisdak and Drake (2007)'s X-line model test against quasi-simultaneous magnetic reconnection plasma jet observations. | 95 |
| 7.1 | Time-shifting histogram for a total of 109 events for which the method was applicable. | 102 |
| 7.2 | (Left) Cross-correlation analysis of the magnetic field clock angle from ACE and THEMIS D spacecraft for the 2009-09-28 reconnection event. (Right) 1 hour and 10 minutes interval in which THEMIS D spacecraft spent in the magnetosheath region on 2009-09-28. | 104 |
| 7.3 | Lagged ACE's magnetic field data by means of cross-correlation analysis. | 107 |
| 7.4 | Histograms of IMF components and the Earth's dipole tilt angle. | 108 |
| 7.5 | THEMIS E outbound magnetopause crossing event on 2008-10-22. | 110 |

| | | |
|------|---|-----|
| 7.6 | Plot of ion energy flux versus ion energy for the THEMIS E magnetopause crossing event on 2008-10-22. | 111 |
| 7.7 | Histogram plots of the quality measure, ΔV_A^* , of the agreement between observed and predicted flow acceleration, and the angular displacement, θ_{op} , of the observed jet direction from the field-aligned direction. | 114 |
| 7.8 | X-line models test against <i>in situ</i> observations of reconnection plasma jets. | 122 |
| 7.9 | X-line models test against <i>in situ</i> observations of reconnection plasma jets. | 125 |
| 7.10 | X-line models test against <i>in situ</i> observations of reconnection plasma jets. | 128 |
| 7.11 | X-line models test against <i>in situ</i> observations of reconnection plasma jets. | 131 |
| 7.12 | X-line models test against <i>in situ</i> observations of reconnection plasma jets. | 135 |
| 7.13 | X-line models test against <i>in situ</i> observations of reconnection plasma jets. | 137 |
| 7.14 | Plot of the magnetic shear angle θ_{shear} versus $\Delta\beta$ values for all 90 THEMIS reconnection events analyzed in this study. | 153 |
| A.1 | Scale-space representation of a synthetic image by convolution with a separable discrete kernel. | 174 |
| A.2 | Sub-pixel ridge detection method as presented in Lindeberg (1993). | 177 |
| B.1 | X line models test against <i>in situ</i> observations of reconnection plasma jets. | 180 |
| B.2 | X line models test against <i>in situ</i> observations of reconnection plasma jets. | 181 |
| B.3 | X line models test against <i>in situ</i> observations of reconnection plasma jets. | 182 |
| B.4 | X line models test against <i>in situ</i> observations of reconnection plasma jets. | 183 |
| B.5 | X line models test against <i>in situ</i> observations of reconnection plasma jets. | 184 |
| B.6 | X line models test against <i>in situ</i> observations of reconnection plasma jets. | 185 |
| B.7 | X line models test against <i>in situ</i> observations of reconnection plasma jets. | 186 |
| B.8 | X line models test against <i>in situ</i> observations of reconnection plasma jets. | 187 |

LIST OF TABLES

| | <u>Page</u> |
|---|-------------|
| 6.1 Quasi-simultaneous magnetopause crossing events. | 87 |
| 6.2 Number of times the given X-line model correctly predicted the north-south (N-S) and/or east-west (E-W) senses of the observed plasma jet directions. | 97 |
| 7.1 Number of single magnetopause crossing events during reconnection periods distributed according to IMF orientation and three Earth's dipole tilt inclination intervals. | 117 |
| 7.2 (Continuation of Table 7.1). | 118 |
| 7.3 Number of times the Trattner et al. (2007)'s X-line model correctly predicted the north-south (N-S) and/or east-west (E-W) senses of the observed plasma jet directions. $\psi \geq 0$ | 147 |
| 7.4 Number of times the Trattner et al. (2007)'s X-line model correctly predicted the north-south (N-S) and/or east-west (E-W) senses of the observed plasma jet directions. $\psi < 0$ | 148 |
| 7.5 Number of times the Gonzalez and Mozer (1974)'s X-line model correctly predicted the north-south (N-S) and/or east-west (E-W) senses of the observed plasma jet directions. $\psi \geq 0$ | 149 |
| 7.6 Number of times the Gonzalez and Mozer (1974)'s X-line model correctly predicted the north-south (N-S) and/or east-west (E-W) senses of the observed plasma jet directions. $\psi < 0$ | 150 |
| 7.7 Number of times the Swisdak and Drake (2007)'s X-line model correctly predicted the north-south (N-S) and/or east-west (E-W) senses of the observed plasma jet directions. $\psi \geq 0$ | 151 |
| 7.8 Number of times the Swisdak and Drake (2007)'s X-line model correctly predicted the north-south (N-S) and/or east-west (E-W) senses of the observed plasma jet directions. $\psi < 0$ | 152 |

LIST OF SYMBOLS

| | | |
|---------------|---|---|
| \mathbf{B} | – | Magnetic induction vector |
| c | – | Speed of light |
| \mathbf{E} | – | Plasma electric field in the laboratory frame |
| f | – | Two-dimensional image |
| H | – | Hessian matrix |
| L | – | Half length of the reconnection layer |
| ℓ | – | Scale length for appreciable variations in the plasma |
| \mathcal{L} | – | Scale-space representation of an image f |
| \mathbb{R} | – | Set of real numbers |
| R_m | – | Magnetic Reynolds number |
| T | – | Discrete analogue of a gaussian kernel |
| s | – | Scale parameter |
| \mathbf{V} | – | Plasma bulk velocity |
| V_{in} | – | Inflow plasma speed into the reconnection layer |
| V_{out} | – | Outflow plasma speed from the reconnection layer |
| \mathbb{Z} | – | Set of integer numbers |
| δ | – | Half width the reconnection layer |
| μ_o | – | Magnetic permeability of free space |
| σ_o | – | Plasma conductivity |
| ∇ | – | Nabla operator |

CONTENTS

| | <u>Page</u> |
|--|-------------|
| 1 INTRODUCTION | 1 |
| 2 NEAR-EARTH ENVIRONMENT | 5 |
| 3 ON THE MAGNETIC RECONNECTION PROCESS | 11 |
| 3.1 The Frozen-In law | 11 |
| 3.2 Qualitative Description of Reconnection | 13 |
| 3.3 Steady-State Magnetic Reconnection Models | 15 |
| 3.3.1 Sweet–Parker model | 15 |
| 3.3.2 Petschek’s model for fast reconnection | 17 |
| 3.4 Reconnection at Earth’s dayside magnetopause | 18 |
| 3.5 Walén test | 20 |
| 4 ANALYTICAL X-LINE MODELS | 25 |
| 4.1 Maximum Shear Angle Model: Trattner et al. (2007) | 25 |
| 4.1.1 Model description | 25 |
| 4.1.2 Model implementation | 27 |
| 4.1.2.1 The magnetosheath magnetic field model | 27 |
| 4.1.2.2 Magnetospheric magnetic field model | 29 |
| 4.1.2.3 Determining the X-line location: Antiparallel branches | 32 |
| 4.1.2.4 Determining the X-line location: Subsolar branch | 33 |
| 4.2 Maximum Current Density Model: Gonzalez and Mozer (1974) | 36 |
| 4.2.1 Model description | 36 |
| 4.2.2 Model implementation | 38 |
| 4.3 Maximum Reconnection Outflow Speed Model: Swisdak and Drake (2007) | 39 |
| 4.3.1 Model description | 39 |
| 4.3.2 Model implementation | 46 |
| 4.3.2.1 The BATS-R-US model | 46 |
| 4.3.2.2 Defining the BATS-R-US dayside magnetopause location | 49 |
| 4.3.2.3 Normal vector to the local magnetopause | 51 |
| 4.3.2.4 Obtaining the maximum reconnection outflow speed V_{out} | 54 |
| 4.3.2.5 Determining the X-line location over the dayside magnetopause | 56 |

| | | |
|----------|--|-----------|
| 5 | INSTRUMENTATION AND COORDINATE SYSTEM | 59 |
| 5.1 | THEMIS mission | 59 |
| 5.2 | CLUSTER mission | 60 |
| 5.3 | DOUBLE STAR TC-1 mission | 61 |
| 5.4 | Coordinate systems | 61 |
| 6 | X LINE MODEL COMPARISONS: PART I | 65 |
| 6.1 | Quasi-simultaneous magnetopause crossing events | 65 |
| 6.1.1 | Spacecraft observations | 67 |
| 6.1.1.1 | 2007-03-05 crossing | 68 |
| 6.1.1.2 | 2007-06-14 crossing | 74 |
| 6.1.1.3 | 2009-05-22 crossing | 78 |
| 6.1.1.4 | 2009-07-07 crossing | 82 |
| 6.1.1.5 | Summary of the quasi-simultaneous magnetopause crossing observations | 86 |
| 6.1.2 | X-line models test against <i>in situ</i> quasi-simultaneous magnetic reconnection plasma jet observations | 86 |
| 6.1.2.1 | Maximum Shear Angle Model test (TRATTNER et al., 2007) | 88 |
| 6.1.2.2 | Maximum Chapman-Ferraro Current Density test (GONZALEZ; MOZER, 1974) | 91 |
| 6.1.2.3 | Maximum Reconnection Outflow Speed test (SWISDAK; DRAKE, 2007) | 94 |
| 6.1.2.4 | Summary of X-line models test against quasi-simultaneous magnetic reconnection plasma jet observations | 97 |
| 7 | X LINE MODEL COMPARISONS: PART II | 99 |
| 7.1 | Statistical analysis of single spacecraft magnetopause crossings | 99 |
| 7.1.1 | Obtaining solar wind's magnetic field and plasma parameters | 100 |
| 7.1.1.1 | Time-shifting OMNI's data | 100 |
| 7.1.1.2 | 5 minutes average from OMNI data | 102 |
| 7.1.1.3 | Cross-correlation with ACE's magnetic field data | 103 |
| 7.1.1.4 | ACE's hourly-averaged magnetic field data | 106 |
| 7.1.2 | Interplanetary magnetic field conditions for the statistical survey | 106 |
| 7.1.3 | Single spacecraft observations of magnetic reconnection events | 109 |
| 7.1.3.1 | Reconnection signatures | 109 |
| 7.1.3.2 | Large scale picture | 114 |
| 7.1.4 | Dataset separation | 115 |
| 7.1.5 | Input conditions for generating the model X-lines | 116 |

| | | |
|----------|--|------------|
| 7.1.6 | X-line models test against <i>in situ</i> magnetic reconnection plasma jet observations | 120 |
| 7.1.6.1 | Summary of X-line models test against <i>in situ</i> magnetic reconnection plasma jet observations | 139 |
| 8 | CONCLUSIONS | 155 |
| | REFERENCES | 159 |
| | APPENDIX A - Ridge Detection Method | 173 |
| A.1 | Scale-Space Representation | 173 |
| A.2 | Ridge Definition at a Fixed Scale | 175 |
| A.3 | Determining the ridge-like points in an 2-D image | 176 |
| | APPENDIX B - X-line model test against <i>in situ</i> reconnection jet observations - Part II | 179 |

1 INTRODUCTION

The Universe is most likely everywhere filled with plasmas. Whenever different regimes of magnetized plasmas come together they may interact in such a way that their magnetic field configurations become interconnected, and therefore a “doorway” is created between them enabling the exchange of mass and momentum. Achieving a new magnetic topological configuration, however, results in an explosive release of stored magnetic energy into plasma kinetic energy and heat. All of these processes are possible to occur via a single physical mechanism: magnetic field reconnection (VASYLIUNAS, 1975).

Magnetic reconnection has been shown to occur in a multitude of environments with distinct plasma properties, such as the Earth’s magnetosphere (PASCHMANN et al., 2013), Saturn’s and other solar system’s planetary magnetospheres (FUSELIER et al., 2014, and references therein), the solar corona (SU et al., 2013), current sheets in the solar wind (GOSLING et al., 2005), and also in fusion devices at laboratory plasmas (ZWEIBEL; YAMADA, 2009).

Reconnection is an inherently multi-scale process. One can focus, for instance, on kinetic aspects related with the most fundamental levels of the reconnection phenomena; or, for MHD scale, carry out a study on how the reconnection loci (or X-line) are structured over, say, the whole dayside magnetopause of a planet. In this thesis work we are concerned with the second of these topics, i.e., the large scale aspect of magnetic field reconnection at Earth’s dayside magnetopause as probed by both *in situ* spaceborne observations of accelerated plasma flows and analytical models which predict the location and orientation of the reconnection X-line.

In an attempt to predict the orientation of the assumed large scale reconnection X-line at Earth’s dayside magnetopause, Sonnerup (1974) and Gonzalez and Mozer (1974) proposed that at the subsolar magnetopause the X-line would have an orientation relative to the ecliptic, i.e., a tilt, depending upon the ratio of the east-west (B_y) over the north-south (B_z) interplanetary magnetic field (IMF) components. The higher B_y/B_z ratios are, the higher the tilt would be. Such a line of thought would give rise to the so-called component-type reconnection scenario whereby the interacting magnetic fields would not have to be strictly antiparallel. On the other hand, Crooker (1979) and subsequently Luhmann et al. (1984) advocated that reconnection should be more efficient and therefore occurs preferentially wherever the magnetic fields are nearly antiparallel ($\sim 180^\circ$), which in turn generated the antiparallel-type reconnection scenario. In terms of predictions of the reconnection

X-line location, the two scenarios provide strikingly different results when there is a non-zero IMF B_y component, which in the antiparallel (component) case reconnection would cease (be active) in the subsolar region and the most likely reconnection X-line locations would be shifted to high latitudes for the antiparallel case, but the component reconnection cannot occur at such latitude (see e.g., [Sibeck and Lin \(2011\)](#)).

Observational evidence has accumulated showing the feasibility for occurrence of both reconnection types at Earth's dayside magnetopause. By investigating remotely sensed precipitating and mirroring ions [Trattner et al. \(2007\)](#) have suggested that both types of reconnection would occur simultaneously. Surveys of magnetopause crossing events have shown that for different IMF orientations, and shear angles¹ substantially less than 180° the directions of accelerated plasma flows, which are the most readily discernible dayside magnetopause reconnection signatures, are consistent with tilted, subsolar, component-type reconnection X-lines ([PU et al., 2005](#); [TRENCHI et al., 2008](#)).

Where reconnection would occur over the Earth's dayside magnetopause, and which model is appropriate for, i.e., component or antiparallel, have been an active research topic over the years. The empirical [Trattner et al. \(2007\)](#)'s model predicts that the reconnection X-line will be located in places where the magnetic shear angle is maximized. The model has been successfully tested against a limited amount of *in situ* spacecraft observations of reconnection signatures ([FUSELIER et al., 2014](#)). While the maximum shear angle model incorporates both reconnection scenarios for X-line estimation, other models have been developed following only the component-type reconnection. Among them is the earliest and standard X-line model of [Gonzalez and Mozer \(1974\)](#) which claims that the X-line should follow the Chapman-Ferraro current streamline passing through the subsolar point. This model has also been successfully tested against observations ([TRENCHI et al., 2008](#)). Another component-type X-line reconnection model is the one developed by [Swisdak and Drake \(2007\)](#) where it incorporates realistic effects of asymmetric magnetic fields and plasma densities across the dayside magnetopause on the X-line orientation. As far as we know the [Swisdak and Drake \(2007\)](#) model has been successfully tested only in Hall-MHD simulations ([SCHREIER et al., 2010](#)). Other class of purely numerical X-line models, i.e., those obtained entirely from global MHD simulations, have also been

¹In the magnetospheric physics context, particularly at the dayside magnetopause, the shear angle is defined as the angle formed by the magnetosheath and magnetospheric magnetic field vectors adjacent to the magnetopause. For an exactly 180° shear angle the fields are antiparallel, whereas for an exactly 0° shear angle they are parallel to each other.

proposed (KOMAR et al., 2013), but they have not been tested against observations so far.

Each model briefly described above uses a parameter, or a small set of parameters, to explain the possibly complex behavior of the large scale reconnection X-line location over the Earth's dayside magnetopause. Thus there is still no consensus in the literature on what are the key parameters that govern the dayside magnetopause X-line location. Our goal in this thesis work is to give one more step towards answering this question. We therefore perform an intercomparison of three analytical X-line models, namely Trattner et al. (2007), Gonzalez and Mozer (1974), and Swisdak and Drake (2007), against two sets of reconnection events. In the first set, we have collected four fortuitous, quasi-simultaneous magnetopause crossing events where two widely separated spacecraft detected reconnection signatures (mostly accelerated flows), and the possible X-line location could be inferred from the observations. The X-line models were then used and their predictions were compared with the expected X-line location obtained from observation. The results suggest that an extended (> 5 Earth radii in length), component-type reconnection X-line may in fact be a likely scenario at Earth's dayside magnetopause, connecting and structuring the reconnection characteristics on far apart observation points. In the second set of reconnection events, we have analyzed the X-line models performance in predicting the observed reconnection outflow direction in a total of 116 single magnetopause crossing events where reconnection-generated plasma flows were clearly present. On both sets of reconnection events, we have found that the three X-line models had roughly the same performance but the Swisdak and Drake (2007) model performs slightly better than the other two. This result indicates that in addition to external boundary conditions such as the interplanetary magnetic field orientation, and solar wind dynamic pressure value, the local plasma and magnetic field conditions play an important role in determining the large scale X-line orientation at Earth's dayside magnetopause, in particular the local plasma β , as it has been shown elsewhere (PHAN et al., 2013).

This thesis work is structured in the following way: in Chapter 2, a brief description of the near-Earth environment is presented. Next, in Chapter 3, both qualitative and quantitative descriptions of the magnetic field reconnection phenomena are discussed. The analytical X-line models used in this thesis work are described in Chapter 4. In Chapter 5 the instrumentation and the coordinate systems used to present the observational data are shown. The results are divided into two parts. The first one, Chapter 6, shows the X-line model comparison by using a set of four

fortuitous, quasi-simultaneous magnetopause crossing events, whereas in the second part of the results, i.e., in Chapter 7, a statistical analysis for the agreement between observed reconnection plasma jet directions and the respective X-line model predictions is presented. Lastly, Chapter 8 brings the conclusions and future works.

2 NEAR-EARTH ENVIRONMENT

The interaction of the super-Alfvénic and magnetized solar wind plasma with the dipole-like magnetic field from Earth generates a region surrounding our planet where the geomagnetic field dominates the dynamics of charged particles. Such a region is known as the magnetosphere. On the dayside region the Earth’s dipole-like field is compressed toward Earth due to solar wind’s dynamic pressure, while at the nightside the magnetic field lines are stretched out antisunward for more than 200 R_E ($R_E =$ Earth radius ~ 6374 km) forming the *magnetotail*, as artistically shown in Figure 2.1.

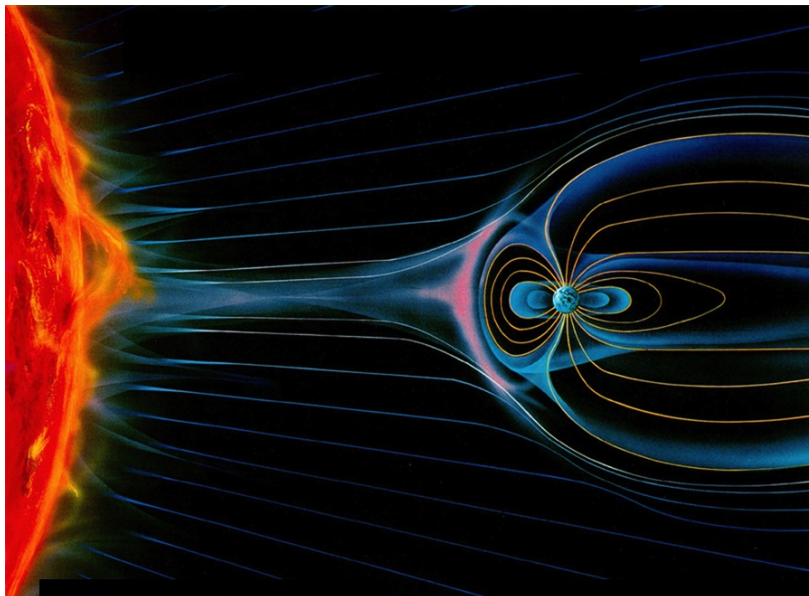


Figure 2.1 - Not to scale artistic view of the solar wind-magnetosphere interaction.
SOURCE: Adapted from NOAA (2014)

As the solar wind travels towards Earth with a typical speed of $V_{sw} = 400$ km/s, i.e., about eight times the typical solar wind’s Alfvén speed $V_A^{sw} \approx 21B_{sw} [\text{nT}]/\sqrt{n_{sw} [\text{cm}^{-3}]} [\text{km/s}] \approx 50 \text{ km/s}^1$, a collisionless shock front (*bow shock*) is developed in order to divert the solar wind flow from the magnetospheric obstacle. When the flow crosses the bow shock it is slowed down, compressed and heated. The solar wind’s magnetic field is also compressed upon crossing the bow shock and has its magnitude increased usually by a factor of 4 (FARRIS; RUSSELL, 1994). The

¹Where typical solar wind magnetic field magnitude $B_{sw} = 5$ nT and density $n_{sw} = 5 \text{ cm}^{-3}$ were used.

region composed by the shocked solar wind is known as the *magnetosheath*, where typical densities and ion temperatures are about 20 cm^{-3} and 200 eV^2 , respectively.

The shocked solar wind flow deviates from the magnetospheric obstacle when it encounters the Earth's magnetopause current layer, which according to ideal MHD theory it can be typically regarded as an impenetrable barrier separating the dense and relatively cold plasma in the magnetosheath from the tenuous ($\sim 0.3 \text{ cm}^{-3}$) and hot ($\sim 10 \text{ keV}$) plasma in the near-magnetopause magnetosphere (SIBECK et al., 1999, p. 209). As a first-order approximation, the magnetopause distance from the Earth's center can be estimated via pressure balance arguments. We then consider that the dayside magnetopause should be located where the dominant (which is usually the thermal) pressure term in the magnetosheath region just outside the magnetopause is balanced by the dominant (which is the magnetic) pressure term in the magnetosphere region just inside the magnetopause boundary. Thus, one can have

$$\rho_{sw} V_{sw}^2 \cos^2 \xi = \frac{B_{sp}^2}{2\mu_o}, \quad (2.1)$$

where we have considered that all solar wind dynamic pressure, $P_{dyn} = \rho_{sw}(V_{sw} \cos \xi)^2$, is converted into thermal pressure in the magnetosheath. In equation 2.1, $\rho_{sw} = n_{sw} m_{ion}$ is the ion solar wind's mass density, μ_o the magnetic permeability of free space, B_{sp} the magnetospheric magnetic field confined within the magnetopause boundary, and ξ is the angle the solar wind flow makes with the local magnetopause normal direction. Thus for the pressure balance equilibrium on the dayside magnetopause region only the normal flow incidence is taken into account in this approximation. For the subsolar magnetopause, $\xi = 0^\circ$. Considering the magnetospheric field as a dipole, we can arrive to an estimative of the Earth's magnetopause stand-off distance R_{mp} as being (in units of R_E) (BAUMJOHANN; TREUMANN, 1996, p. 189)

$$R_{mp} = \left(\frac{\kappa B_E^2}{2\mu_o \rho_{sw} V_{sw}^2} \right)^{1/6}, \quad (2.2)$$

where B_E is the dipole magnetic field magnitude at Earth's surface, and $\kappa > 1$ is a factor included to account for the magnetospheric magnetic field enhancement due

²1 eV = 11600 K (BAUMJOHANN; TREUMANN, 1996, p. 5)

to the presence of the magnetopause current layer which in turn carries a magnetic field of its own that reinforces the magnetospheric magnetic field just inside the magnetopause boundary and weakens the magnetosheath magnetic field just outside the boundary. If we assume $\kappa = 2$ (BAUMJOHANN; TREUMANN, 1996, p. 189), $B_E = 3.1 \times 10^4$ nT, and the typical solar wind density and speed conditions, i.e., $n_{sw} = 5$ cm⁻³ and $V_{sw} = 400$ km/s, one will find $R_{mp} = 9.9 R_E$, which is in line with typical observed values (see, e.g., Sibeck et al. (1991)). Notice that R_{mp} varies only with one to the sixth power of the values involved, thus it is not very sensitive to small variations in the solar wind dynamic pressure.

On the magnetopause flanks, however, where the normal magnetosheath flow is nearly zero, i.e, $\xi \approx 90^\circ$, some other term must replace the solar wind dynamic pressure. Such a term is the solar wind thermal pressure as given by $P_{sw} = \gamma n_{sw} k_B T_{sw}$, where $\gamma = 5/3$, k_B and T_{sw} are the specific heats ratio, the Boltzmann's constant and the solar wind temperature. For typical solar wind conditions ($T_{sw} \sim 1.3 \times 10^5$ K), one finds $P_{sw} \approx 1.5 \times 10^{-2}$ nPa, while $P_{dyn} \approx 1.5$ nPa, i.e., P_{dyn} is about 100 times bigger than P_{sw} which is why the solar wind thermal pressure is neglected in first-order pressure balance considerations at the dayside (subsolar) region where the normal flow incidence is the highest. Nevertheless, at the magnetopause flanks the thermal (and possibly magnetic) pressure (P_{sw}) usually is the most significant term to balance with the magnetospheric magnetic field. Thus, replacing P_{sw} by P_{dyn} in equation 2.1, and using the same parameter values mentioned above one can find that the magnetopause stand-off distance on the flanks, R_{mpf} (at $x_{GSM} = 0^3$), is found to be approximately $1.8 R_{mp}$, which is somewhat above some observations of R_{mpf} (SIBECK et al., 1991, $\sim 1.3 R_{mp}$). According to Baumjohann and Treumann (1996, p.190) that means that even on the flanks some non-negligible normal flow is present, thereby increasing the local pressure at these locations, and therefore decreasing R_{mpf} . Figure 2.2 illustrates the regions discussed so far and also show other magnetospheric regions whose characteristics are briefly described below.

- Polar Cusp:
 - a region of weak magnetic field due to the dipole geomagnetic field geometry, and it is believed to be a place for direct magnetosheath plasma entry (SIBECK et al., 1999, p. 278).
- Tail Lobe:

³See Section 5.4 for description of the coordinate systems used in this thesis work.

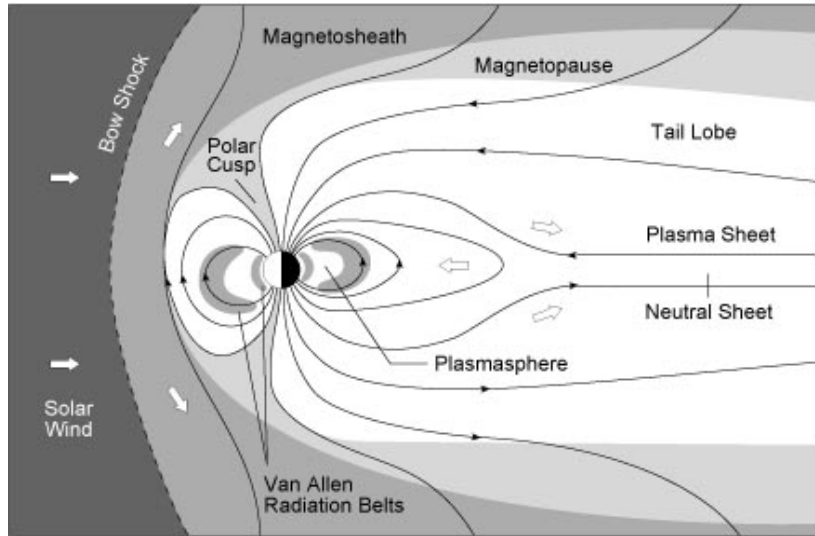


Figure 2.2 - Meridional view of the Earth's magnetosphere and adjacent regions. The Sun is to the left. The thick white arrows denote the incoming solar wind flow, while arrowed black lines represent magnetic field lines.
SOURCE: TUFTS (2014)

– the outer part of the magnetotail on the nightside magnetosphere and stretched Earth's magnetic field lines are connected to higher latitude regions. The field lines forming the tail lobe have been dragged antisunward by the solar wind flow and have a typical magnitude of about 30 nT (BAUMJOHANN; TREUMANN, 1996). On the northern hemisphere the field lines point predominantly sunward, whereas in the southern hemisphere they point predominantly antisunward. According to Faraday's law, between the northern and southern tail lobes a *neutral current sheet* must exist, and in Figure 2.2 such a current system points out of the plane of the page. Electron densities in this region are particularly low ($< 0.05 \text{ cm}^{-3}$).

- Plasma Sheet:

- region located around the tail midplane where most of the magnetotail plasma is concentrated. It has a thickness of about $10 R_E$, and the average electron density and magnetic field are about 0.5 cm^{-3} , and 10 nT, respectively (BAUMJOHANN; TREUMANN, 1996).

- Plasmasphere:

- region of dense ($> 10^3 \text{ cm}^{-3}$) and cold ($\sim 1 \text{ eV}$) particles which

originate from the ionosphere. The plasmasphere co-rotates with the Earth.

- Radiation Belts:
 - they consist of an energetic population of both electrons and ions which are trapped on dipolar field lines between about 2 and 6 R_E (BAUMJOHANN; TREUMANN, 1996, p. 7).

3 ON THE MAGNETIC RECONNECTION PROCESS

3.1 The Frozen-In law

Before discussing about what magnetic reconnection really is, it is instructive, and important as well, to mention and analyze the so-called “frozen-in” law.

The “frozen-in” law states that in a *perfectly* conducting magnetized plasma, there is no electric field in the plasma reference frame which otherwise would give rise to infinitely large electric currents. In this sense, plasma and magnetic field are “attached” to each other, or alternatively it is said that plasma is “frozen” to the magnetic field lines. Therefore, any plasma parcel’s movement *across*, i.e., perpendicular to the magnetic field is forbidden.

According to one of the simplest forms of the Ohm’s law, we have:

$$\mathbf{E} + \mathbf{V} \times \mathbf{B} = \frac{1}{\sigma_o} \mathbf{J}, \quad (3.1)$$

where $\mathbf{E} + \mathbf{V} \times \mathbf{B}$ is the electric field in the fixed reference frame and \mathbf{J} and σ_o are the plasma current density and conductivity, respectively. For perfectly conducting plasmas ($\sigma_o \rightarrow \infty$), the right-hand side of Equation 3.1 vanishes, and therefore the “frozen-in” condition is reached:

$$\mathbf{E} + \mathbf{V} \times \mathbf{B} = 0, \quad (3.2)$$

i.e., plasma movement across magnetic field lines is associated with an electric field (in the laboratory frame of reference), or alternatively the plasma moves perpendicular to both electric and magnetic fields with a *drift* velocity \mathbf{V}_E given by:

$$\mathbf{V}_E = \frac{\mathbf{E} \times \mathbf{B}}{B^2}. \quad (3.3)$$

If Equation 3.1 is solved for \mathbf{E} and the result is placed in the Faraday’s law, and after some algebra, we will get an important equation which expresses the dynamical evolution of the plasma’s magnetic field, and also with this same equation one can visualize the “frozen-in” law (Bittencourt, 2004):

$$\frac{\partial \mathbf{B}}{\partial t} = \nabla \times (\mathbf{V} \times \mathbf{B}) + \frac{1}{\mu_o \sigma_o} \nabla^2 \mathbf{B}. \quad (3.4)$$

In the infinite conductivity limit, the second term on the right hand side of Equation 3.4 vanishes, which means that in such a regime the magnetic field does not diffuse across the plasma, thus the convection term ($\nabla \times (\mathbf{V} \times \mathbf{B})$) dominates the dynamics and it can be shown¹ that plasma and magnetic field, \mathbf{B} , must move together². Since plasma cannot diffuse across magnetic field lines (and vice-versa), a corollary of the “frozen-in” law is that a plasma parcel tied to a specific magnetic field line will remain attached to the same field line at all times, meaning that in principle different magnetized plasma parcels cannot spontaneously *mix*.

It must be emphasized, however, that there is not always such infinite conductivity in real plasmas. There is some finite resistivity ($1/\sigma_o > 0$) in a laboratory plasma and the ionosphere, but for cosmic plasmas the “frozen-in” condition as stated in Equation 3.2 is generally fulfilled with an excellent accuracy; in other words $\mathbf{E} + \mathbf{V} \times \mathbf{B} \simeq 0$. In order to check such statement, one needs to perform a simple scaling analysis on the right-hand side of Equation 3.4 and analyze the result in the context of the plasma domain under study. If we consider that ℓ is a characteristic scale length for appreciable variations in the plasma, i.e., $\nabla \sim 1/\ell$, and after taking the ratio of the convection to the diffusion terms in Equation 3.4, we will obtain (Bittencourt, 2004):

$$\frac{VB/\ell}{B/\sigma_o\mu_o\ell^2} = R_m = \mu_o\sigma_oV\ell, \quad (3.5)$$

where R_m is known as the magnetic Reynolds number which simply tells us in which regime the plasma is: convection ($R_m \gg 1$, or “frozen-in”) or diffusion ($R_m \lesssim 1$) dominated. If we take the solar wind plasma as an example, $\ell \sim 10^9$ m, $\sigma_o \sim 1$ mho, and $V \sim 400$ km/s yields $R_m \sim 10^7$, where it is seen that the “frozen-in” condition is easily fulfilled for interplanetary plasmas. Note that the magnetic Reynolds number is proportional to the scale length ℓ which is always big ($\gg 1$ meter) for astrophysical plasmas, so it is expected $R_m \gg 1$ for such domains.

On the other hand, it is in some regions, within which the diffusion term in Equa-

¹For a rigorous proof of the “frozen-in” theorem the reader is referred to e.g., Stern (1966).

²Again, it is noted that the plasma collective motion relative to the local magnetic field direction is allowed, within the “frozen-in” law framework, only in the perpendicular direction. Plasma particles are free to move in the parallel (to the magnetic field) direction.

tion 3.4 is comparable to ($R_m \lesssim 1$) or even surpass the convection term, where the “frozen-in” condition breaks down, and such places are ideal for magnetic reconnection to occur. These ideal places are usually found within thin current sheets where through some dissipative processes (e.g., electron-ion collisions) the magnetic field is allowed to diffuse across the plasma, change its magnetic topology, and thus enabling distinct plasma parcels to mix. In the next sections, both qualitative and quantitative descriptions of reconnection are presented.

3.2 Qualitative Description of Reconnection

Originally envisioned by Giovanelli (1946) to explain the sudden acceleration of charged particles in solar flares, magnetic reconnection is one of the main physical mechanisms thought to occur throughout the Universe, e.g., in planetary magnetospheres where it is responsible for geomagnetic storms (GONZALEZ et al., 1994); in solar and stellar atmospheres where it causes flares (SU et al., 2013); in coronae of accretion disks in active galactic nuclei where it has the potential to efficiently accelerate electrons up to Lorentz factors of about 2000 (SCHOPPER et al., 1998), and also powering sawtooth oscillations in laboratory plasmas (see e.g. Zweibel and Yamada (2009)).

Magnetic reconnection is able to occur whenever distinct highly conductive magnetized plasma regimes interact with each other along thin current sheets. In this sense, it can be understood, in a simple fashion, as a topological rearrangement of the interacting magnetic field lines with a consequent rapid conversion of the available magnetic energy into plasma kinetic and thermal energies.

Despite the enormous efforts that have been spent to understand the characteristics of reconnection in its most fundamental levels (see e.g., Vasyliunas (1975), Sonnerup et al. (1981), Mozer et al. (2002), Swisdak et al. (2003), Phan et al. (2007), Cassak and Shay (2007), Daughton et al. (2011), Walsh et al. (2014)), the exact physics on how the magnetic topology is changed and also some microphysical aspects of the process still remain unknown. The upcoming NASA’s Magnetospheric Multi-Scale (MMS) mission which is being specifically designed to assess the microphysics of reconnection is expected to shed light (or even to definitely answer some open questions) on the subject.

Under typical circumstances, as those found in the solar wind or in the Earth’s magnetosphere, highly conductive plasmas can not spontaneously mix, as mentioned in Section 3.1. At the dayside magnetopause, for instance, the plasma coming from

the magnetosheath region can not penetrate the magnetopause boundary and the plasma is deviated along the magnetosphere, meaning that the magnetopause is regarded as a “closed” boundary. The plasma can enter the magnetosphere, however, through diffusive processes, and most importantly through magnetic reconnection.

Reconnection establishes a magnetic “linkage” between the incoming plasma regimes which were not allowed to interact with each other. Alternatively, we can say that a magnetic field component normal to the current sheet boundary separating the incoming plasmas appears as a result of the magnetic reconnection process. The existence of such a normal magnetic field component means that the boundary that separates the two interacting plasmas is now “opened”, and as a consequence mass and momentum can be transferred from one plasma regime to another, i.e., a coupling between them is introduced. Figure 3.1 shows a sketch of how such process occurs in 2D plasmas with antiparallel magnetic fields: the two distinct plasma regimes approach each other ($t < 0$), and in some localized region – the diffusion region – the magnetic field lines are allowed to change their topology and interconnect ($t = 0$), then, the newly reconnected (and bent) field lines ($t > 0$) tend to relax to its state of minimum energy, i.e., get straightened, while plasma is being ejected and accelerated (vertical white arrows) perpendicular to the inflow direction (horizontal white arrows).

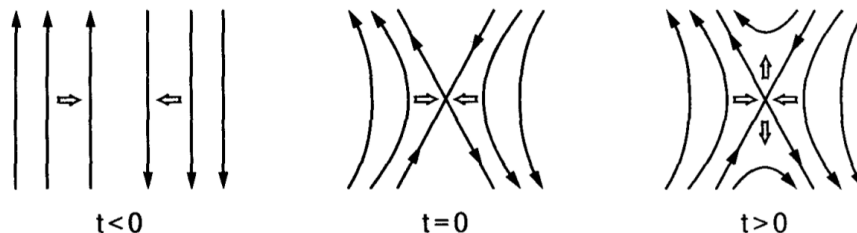


Figure 3.1 - Sketch of two approaching plasma regimes with antiparallel magnetic fields. At $t < 0$ there is no reconnection. The onset occurs at $t = 0$, and the process continues for later times ($t > 0$). The horizontal white arrows depict the (normal) direction of the incoming plasma flow, while the vertical ones show the outflow direction.

SOURCE: After Baumjohann and Treumann (1996)

Since the field lines at both center and rightmost part of Figure 3.1 approach each other forming an “X”, the point of field line crossing is known as an X-type neutral point and at this location the magnetic field vanishes³. If we imagine that the same

³As noted by Vasyliunas (1975), the in-plane magnetic field components vanish at the neutral

process is occurring both in- and out-of-the-plane of the page in Figure 3.1, the neutral point becomes a neutral line, or simply an X-line, and its length is one of the spatial scales involved in the reconnection process. The X-line concept and its main characteristics play a key role in this work and will be discussed in more detail later on.

The reconnection process is inherently three dimensional, but the 2D picture is still useful since it allows a more mathematically tractable way of analyzing its main features analytically. In the next section, a more quantitative description of 2D steady-state reconnection is presented.

3.3 Steady-State Magnetic Reconnection Models

In order to exemplify some of the first and more standard theoretical developments on the magnetic reconnection theory we briefly describe the Sweet–Parker and Petschek models.

3.3.1 Sweet–Parker model

Among the hydromagnetic descriptions of magnetic reconnection the independent works of P. A. Sweet (SWEET, 1958) and E. N. Parker (PARKER, 1957) were the pioneers. The so-called Sweet–Parker model describes the time-independent magnetic reconnection of non-relativistic approaching plasmas with antiparallel magnetic fields due to the effect of a finite resistivity η which in turn is considered to be due to collisions between electrons and ions. Such resistivity is important only in a thin current layer of half width δ and half length L which separates the incoming plasmas, and whereby the magnetic field reverses direction (cf. Figure 3.2). Everywhere else the plasma is “frozen” to the magnetic field as explained in Section 3.1, and therefore incoming plasmas far from the central current layer approach it with a drift velocity given by Equation 3.3.

Figure 3.2 depicts the Sweet–Parker reconnection geometry. The incoming plasmas with same mass density ρ , and magnetic field vectors (of same magnitude B) lying in the $\pm x$ direction move toward each other with the same inflow speed V_{in} in the $\pm y$ direction. As a consequence of Ampère’s law (i.e., $\mathbf{J} = \frac{1}{\mu_0} \nabla \times \mathbf{B}$) an out-of-plane-directed current sheet develops in the region where the plasmas meet as illustrated by the orange rectangular box in Figure 3.2. Within this region the magnetic field lines have their topologies changed by collisional (resistive) effects and the newly

point by definition, but an out-of-plane magnetic (guide) field component generally exists.

reconnected field lines, and plasma as well, leave the central (diffusion) region with an outflow speed $V_{out} = V_A = B/\sqrt{\mu_o\rho}$, which is the Alfvén speed, in both $+$ and $-x$ directions. The plasma outflow is accelerated to Alfvénic speeds through the action of the magnetic tension ($\frac{1}{\mu_o}(\mathbf{B} \cdot \nabla)\mathbf{B}$) of the sharply bent reconnected field lines which tend to relax, thus releasing stored magnetic energy to the particles of the plasma in the form of kinetic and thermal energies.

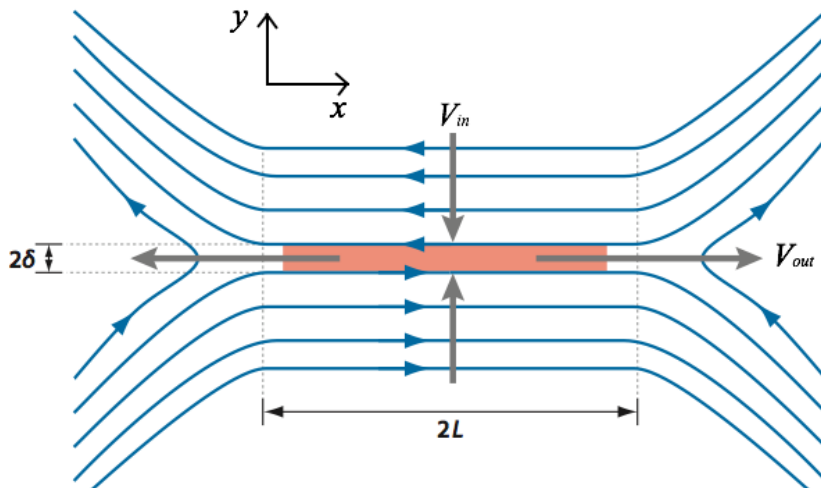


Figure 3.2 - Sweet–Parker’s reconnection geometry. Plasmas with oppositely directed magnetic fields (solid blue lines) approach the current sheet (orange box) from above and below. The accelerated plasma outflow which results from reconnection exits the current sheet sideways (horizontal gray arrows). The whole process is in steady-state.

SOURCE: Adapted from [Zweibel and Yamada \(2009\)](#)

To evaluate how fast, or alternatively how efficient the Sweet-Parker (collisional) mechanism is, one can use the ratio between the inflow and the outflow speeds, i.e., V_{in}/V_{out} , so an estimative can be achieved on how much magnetic flux is being reconnected via this process. What remains to be determined is the inflow speed which can be obtained by equating the out-of-plane convection electric field (in the laboratory frame of reference) of the ideal Ohm’s law (equation 3.2) which is present everywhere outside the reconnection layer, $E \sim V_{in}B$, and the resistive electric field inside the reconnection layer given by $E \sim \eta J \sim \frac{\eta B}{\mu_o\delta}$, then yielding $V_{in} \sim \frac{\eta}{\mu_o\delta}$. The reason why the electric fields inside and outside the reconnection layer are the same comes from the fact that in a steady-state ($\partial/\partial t \equiv 0$), assumption under which the Sweet-Parker model was developed, the Faraday’s law ($\nabla \times \mathbf{E} = -\partial\mathbf{B}/\partial t$) states that in such conditions the tangential electric field must be spatially continuous,

i.e., everywhere it must be the same. Therefore, we can achieve the Sweet-Parker reconnection rate as being given by:

$$\frac{V_{in}}{V_{out}} \sim \sqrt{\frac{\eta}{\mu_o L V_A}}, \quad (3.6)$$

where the mass conservation law ($V_{in}L \sim V_{out}\delta$) has been used to achieve equation 3.6. Notice that the Sweet-Parker reconnection rate is inversely proportional to $L^{1/2}$ which in turn is usually very large for space plasmas, and also η is small for space plasmas since they are not collision dominated. That means that the reconnection rate is small and the characteristic time for the process to occur is too long to explain reconnection-based processes such as solar flares and solar wind's mass and momentum transfer to the Earth's magnetosphere.

3.3.2 Petschek's model for fast reconnection

The Petschek model also uses resistive hydromagnetic theory to address the magnetic reconnection phenomenon. It enables reconnection to occur at a higher pace as compared to the Sweet-Parker model. As mentioned in the previous section, the Sweet-Parker model produces reconnection rates too low to explain reconnection-triggered phenomena (e.g., solar flares) which occur on characteristic times far below those predicted by theory. One of the reasons the Sweet-Parker model gives such lower reconnection rates is the macroscopic size of the reconnection layer. While the width δ is defined by the collisional plasma resistivity η , the length L is of the order of the system size, which is quite big for space plasmas. Thus, in [Petschek \(1964\)](#)'s model the reconnection layer size is reduced in such a way that the reconnection rate can be increased and then achieve values consistent with expectations for fast reconnection, i.e, $V_{in}/V_{out} \sim 0.1$. In the [Petschek \(1964\)](#) model the whole plasma does not necessarily need to pass through the reconnection layer, which is why its size is proposed to be reduced. Instead, it would be redirected and accelerated up to Alfvénic speeds by standing shock waves, as illustrated by the four thick solid lines in [Figure 3.3](#) which connect to the edges of the central (rectangular) reconnection layer of length $2L^*$. Alfvénic

Notice that if we replace L in equation 3.6 by a shorter length L^* , the reconnection rate will increase by a factor of $\sqrt{L/L^*}$ ([KULSRUD, 2001](#)). In Petschek's theory, L^* seems to be a free parameter, thus he chooses L^* as short as possible in order to maximize the reconnection rate which is found to be $V_{in} \sim V_A(\pi/8 \ln S)$, where

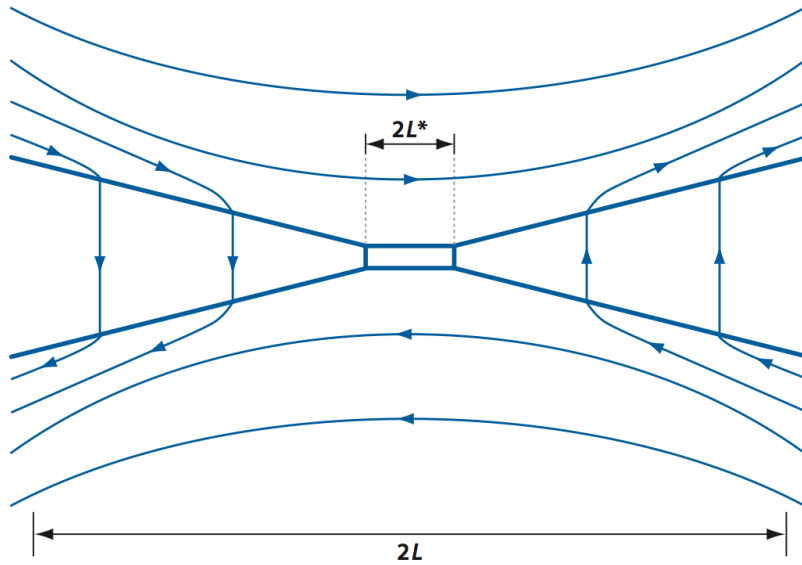


Figure 3.3 - Petschek's reconnection geometry. Plasmas with oppositely directed magnetic fields (solid arrowed lines) approach the small sized current sheet from above and below. Some fraction of the plasma pass through the reconnection layer while the remaining part is redirected by standing shock waves (thick solid lines). The whole process is in steady-state.

SOURCE: After Zweibel and Yamada (2009)

$S = \mu_o L V_A / \eta$ is the Lundquist⁴ number which is the ratio of the global Ohmic diffusion time, $\tau_{diff} = \mu_o L^2 / \eta$, to the global Alfvén time, $\tau_A = L / V_A$. The Petschek reconnection rate value is generally a few percent of the Alfvén speed, fast enough to account for most astrophysical phenomena (ZWEIBEL; YAMADA, 2009).

3.4 Reconnection at Earth's dayside magnetopause

The Earth's magnetosphere, which is filled with the geomagnetic field and the plasma from the ionosphere and solar wind, is a natural and accessible laboratory for space plasma physics studies. At the magnetopause, i.e., the boundary which in a first-order approximation separates the sub-Alfvénic, relatively cold (~ 0.2 KeV), and dense ($\sim 10 \text{ cm}^{-3}$) plasma of the magnetosheath, from the tenuous ($\sim 0.2 \text{ cm}^{-3}$) and hot (~ 10 KeV) plasma from the Earth's magnetosphere, a series of plasma processes takes place such as magnetic reconnection, Kelvin-Helmholtz instability, and diffusion. Most of them enables the exchange of mass, momentum and energy between magnetosheath and magnetospheric plasmas, but according to Sibeck et al.

⁴Notice that we can rewrite equation 3.6 in terms of the Lundquist number S , obtaining $V_{in}/V_{out} \sim S^{-1/2}$.

(1999, p. 277) only reconnection has been shown to be the “dominant mode for the dynamic solar wind-magnetosphere interaction”.

After the efforts of Dungey (1961) for bringing the magnetic Walén field reconnection concept to magnetospheric physics, researchers have found, since that time, a large body of indirect evidence in favor of an open, or reconnecting magnetosphere. Among the most important topics, as pointed out by Sonnerup et al. (1995, p. 167), they had “the observed dependence of geomagnetic activity on the interplanetary magnetic field (IMF) direction, the observed inward motion of the magnetopause following southward turning of the IMF, the observed direct access of energetic solar protons to the polar cap regions, and the ion dispersion effects observed in the cusp regions.”

The first direct, *in situ* evidence that reconnection was indeed occurring at the Earth’s dayside magnetopause was reported by Paschmann et al. (1979). By looking at magnetic field and plasma data collected during dayside magnetopause crossings by the *International Sun-Earth-Explorer Mission* (ISEE) spacecraft, Paschmann et al. (1979) were able to distinguish both a non-zero average magnetic field component normal to the local magnetopause, as a requirement for an open magnetosphere, and accelerated plasma flows along the dayside magnetopause whose characteristics were consistent with theoretical expectations of magnetic reconnection. Specifically, the magnitude of the observed tangential (to the magnetopause) plasma flow was around 74% of the predicted Alfvénic plasma flow which in turn would be caused by the so-called magnetic slingshot effect whereby sharply bent, newly reconnected magnetic field lines would accelerate the local plasma as they relax toward a state of minimum energy (see Figure 3.1).

Ever since, an ever-growing number of papers have been shown direct evidence of dayside magnetopause reconnection mostly through the detection of accelerated plasma flows, also known as plasma jets, at the subsolar magnetopause (SONNERUP et al., 1981; PHAN et al., 2000; PHAN et al., 2004; PU et al., 2005; TRENCHI et al., 2008; WALSH et al., 2014), at the low-latitude flank magnetopause (GOSLING et al., 1986; PHAN et al., 2006), and also at the high latitude magnetopause on locations poleward of the cusps (KESSEL et al., 1996; PHAN et al., 2003).

When looking for reconnection events at Earth’s dayside magnetopause in spacecraft data, the plasma jets are the most readily discernible fluid⁵ signatures of reconnect-

⁵There is also reconnection signatures which pertain to a kinetic level, i.e., those which are not described by MHD, such as ion reflection and transmission at the magnetopause, and time of flight effects associated with magnetopause layers. The reader is referred to Fuselier (1995) for

tion. In order to categorize a given jet as being a result of tangential magnetic stresses acting on the local plasma and accelerating it up to Alfvénic speeds, we use the so-called Walén test, which is going to be discussed in the next section.

3.5 Walén test

The Walén relation establishes a way of testing whether the change in velocity undergone by the plasma constituents when crossing a discontinuity separating different magnetized plasma regimes is due to the effect of tangential (to the discontinuity) magnetic stresses (HUDSON, 1970). The Earth’s dayside magnetopause, for instance, can be considered as such a structure separating the relatively cold (~ 0.2 KeV) and dense ($\sim 10 \text{ cm}^{-3}$) magnetosheath plasma from the hot (~ 10 KeV) and tenuous ($\sim 0.2 \text{ cm}^{-3}$) plasma from the magnetosphere. The derivation of the Walén relation consists in considering the discontinuity as a locally one-dimensional, time-stationary and infinitesimally thin⁶ ideal MHD layer known as rotational discontinuity. Thus, by confirming via the Walén relation that the accelerated plasma flows (jets) occurring at the Earth’s dayside magnetopause are a (likely) result from local magnetic stresses, we are considering that, locally, the magnetopause is considered as a rotational discontinuity which is “open” to the magnetosheath flow to enter the magnetosphere, and therefore exchange mass and momentum. According to Sonnerup et al. (1995, p. 170), a successful Walén relation means that “magnetic field reconnection was occurring or had been occurring in the immediate past to a sufficient extent to have dynamic consequences over some finite portion of the magnetopause surface”.

For a rotational discontinuity there is a constant (in both space and time), and finite mass flow across it, i.e., the normal component of the flow V_n is non-zero. More importantly, in a rotational discontinuity there is also a non-zero normal magnetic field component B_n which interconnects the magnetized plasmas on both sides of the discontinuity. Furthermore, its value is related with the normal plasma flow V_n by (PASCHMANN et al., 1986)

$$V_n = \pm(1 - \alpha)^{1/2} \frac{B_n}{\sqrt{\mu_0 \rho}}, \quad (3.7)$$

more details on kinetic signatures of reconnection at the Earth’s magnetopause.

⁶ According to Baumjohann and Treumann (1996), magnetohydrodynamic discontinuities are thin with respect to the scale lengths of the fluid parameters, but thick with respect to Debye length and ion gyroradius.

where μ_o , ρ and $\alpha = (P_{\parallel} - P_{\perp})\mu_o/B^2$ are the magnetic permeability of free space, the plasma mass density, and P_{\parallel} and P_{\perp} are, respectively, the thermal pressures parallel and perpendicular to the magnetic field vector \mathbf{B} whose magnitude is represented by B .

We are interested in how the tangential flow components are going to change as a result of magnetic stress. By invoking the conservation of tangential momentum across the discontinuity, and also recalling that we are assuming a one-dimensional, time-stationary discontinuity across which the tangential electric field ($\mathbf{E}_{\text{tangential}} = -(\mathbf{V} \times \mathbf{B})_{\text{tangential}}$) is continuous, we can find (PASCHMANN et al., 1986, equation (7))

$$\Delta \mathbf{V}_{\text{predicted}} = \mathbf{V}_2 - \mathbf{V}_1 = \pm \left(\frac{1 - \alpha_1}{\mu_o \rho_1} \right)^{1/2} \left[\mathbf{B}_2 \left(\frac{1 - \alpha_2}{1 - \alpha_1} \right) - \mathbf{B}_1 \right], \quad (3.8)$$

where we have considered that $\mathbf{V} = \mathbf{V}_{\text{normal}} + \mathbf{V}_{\text{tangential}}$, thus equation 3.7 has been incorporated in equation 3.8. Subscripts 1 and 2 denote both sides of the discontinuity. At the dayside magnetopause, the subscripts 1 and 2 will correspond, in this work, to the magnetosheath (inflow) region and the outflow jet region, respectively. Equation 3.7 shows that when crossing a rotational discontinuity the plasma velocity will change in response to spatial variations on the magnetic fields and plasma densities and pressures. The choice of sign in the equations above depends on the relative signs of V_n and B_n . If we consider $V_n < 0$, i.e., the magnetosheath plasma moving towards the dayside magnetopause, then the upper (lower) sign corresponds to $B_n < 0$ ($B_n > 0$). In terms of the reconnection geometry, the negative (positive) B_n case corresponds to the case where the spacecraft crossed the dayside magnetopause above (below) the reconnection line, as shown in Figure 3.4.

In this work we compare the predicted plasma flow change (rightmost part of equation 3.8) with the observed plasma flow. On the magnetosheath side of the magnetopause, the magnetic fields, densities and thermal pressures, i.e., \mathbf{B}_1 , ρ_1 and α_1 , respectively, are obtained as one-minute averages, and the criteria for choosing the magnetosheath side interval are given below.

- I) Ion density values usually higher than or equal to 10 cm^{-3} ;
- II) presence of positively charged particles with energies within the energy range 200 – 350 eV as shown by the ion omni-directional energy flux spectra (when

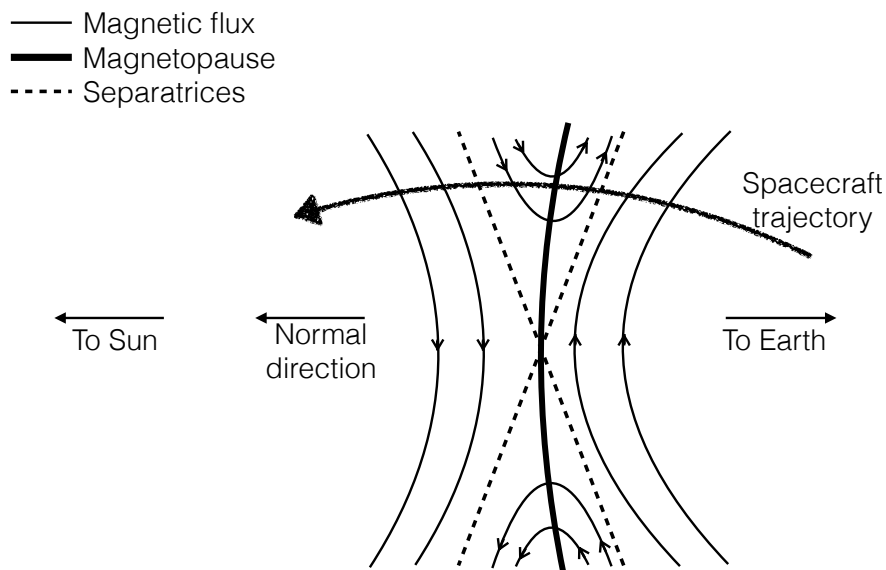


Figure 3.4 - Sketch of the subsolar dayside magnetopause (thick line) reconnection geometry for antiparallel magnetic fields (solid arrowed lines). The incoming magnetic fields reconnect at the X point where the two separatrices (dashed lines) meet. The reconnected magnetic fields move away from the central region. When crossing the magnetopause above (below) the X-line, which extends into and out of the plane at the X point, a spacecraft will detect a reconnected magnetic field line which has a negative (positive) normal component.

available);

- III) one-minute interval as close (in time) as possible from the magnetopause satisfying all the requirements above, and taken right after the magnetic field has completed its rotation through the magnetopause boundary.

The observed jet velocity is obtained in the following way. We look for the instant t_{max} when the maximum plasma velocity magnitude, \mathbf{V}_{max} , is observed. Such an instant usually occurs when the spacecraft is on the earthward side of the dayside magnetopause boundary. Then, a one-minute average plasma velocity vector from the magnetosheath side of the magnetopause is taken using the same magnetosheath interval mentioned above. This averaged velocity vector is considered to be the background magnetosheath flow, $\mathbf{V}_{background}$. The observed jet velocity is considered to be given by $\Delta\mathbf{V}_{observed} = \mathbf{V}_{max} - \mathbf{V}_{background}$. When subtracting the background velocity from the maximum observed velocity we are assuming that the remaining term is due to the magnetic reconnection process. The remainder terms used to compose the predicted jet velocity $\Delta\mathbf{V}_{predicted}$, i.e., \mathbf{B}_2 and α_2 , are taken at the

instant t_{max} where the maximum plasma flow is observed.

Once we have both $\Delta\mathbf{V}_{observed}$ and $\Delta\mathbf{V}_{predicted}$ we derive the parameter ΔV_A^* , which is used as a quality measure of the agreement between observed and predicted flow acceleration:

$$\Delta V_A^* = \frac{\Delta\mathbf{V}_{observed} \cdot \Delta\mathbf{V}_{predicted}}{|\Delta\mathbf{V}_{predicted}|^2} = r_{op} \cos(\theta_{op}). \quad (3.9)$$

$\Delta V_A^* = 1$ means perfect agreement with theory, while lower ΔV_A^* values a poorer agreement. The r_{op} and θ_{op} parameters refer to the observed to predicted flow ratio, $r_{op} = |\Delta\mathbf{V}_{observed}|/|\Delta\mathbf{V}_{predicted}|$, and the angular displacement of the observed jet direction from the predicted (magnetic field-aligned) direction, $\theta_{op} = \cos^{-1}[\Delta\mathbf{V}_{observed} \cdot \Delta\mathbf{V}_{predicted}/|\Delta\mathbf{V}_{observed}||\Delta\mathbf{V}_{predicted}|]$.

We follow the same criteria adopted in [Phan et al. \(2013\)](#), i.e., for $\Delta V_A^* > 0.5$ we deem the magnetopause crossing event as a reconnection event. If $\Delta V_A^* < 0.5$, further confirmation is required, and they will be discussed, when needed, in Section 7.1.3.1.

4 ANALYTICAL X-LINE MODELS

Here, the analytical models which predict both X-line orientation and location along the Earth’s dayside magnetopause are presented.

4.1 Maximum Shear Angle Model: [Trattner et al. \(2007\)](#)

4.1.1 Model description

Following the known fact that magnetic reconnection has a higher chance to occur when the reconnecting magnetic fields are precisely oppositely directed, [Trattner et al. \(2007\)](#) have proposed a theory whereby the location over the dayside magnetopause where reconnection should occur, i.e., the X-line location, should be such that the local (shear) angle θ_{shear} between the reconnecting magnetic fields of the magnetosphere and magnetosheath regions is maximized. This idea has its foundations on the work of [Crooker \(1979\)](#) which was extended and tested for a variety of IMF orientations using more realistic models of both magnetospheric and magnetosheath magnetic fields ([LUHMANN et al., 1984](#)).

[Crooker \(1979\)](#) proposed potential sites for magnetic reconnection to take place establishing that such regions would occur over the dayside magnetopause where the local shear angle is nearly or exactly 180° . Figure 4.1 shows, for different IMF orientations, the shear angles $\theta_{shear} = \cos^{-1}[\mathbf{B}_{sh} \cdot \mathbf{B}_{sp}/(|\mathbf{B}_{sh}||\mathbf{B}_{sp}|)]$ over the surface of a paraboloidal magnetopause which is seen from the Sun and projected onto the yz_{GSM} plane. The magnetopause surface is discretized in regularly spaced intervals of $0.2 R_E$ in both y_{GSM} and z_{GSM} directions. At each point over the magnetopause surface, both magnetosheath (sh) and magnetosphere (sp) magnetic fields (\mathbf{B}) are calculated over and just inside the magnetopause boundary, respectively, using different analytical models which are going to be discussed in this chapter, and then the local θ_{shear} value is determined. As shown in the color bars, θ_{shear} goes from zero degree, i.e., exactly parallel magnetic fields, up to 180 degrees, meaning antiparallel magnetic fields. According to [Crooker \(1979\)](#)’s criterion, the most likely regions where magnetic reconnection should take place are located within the 170° contour (thick black line) shown in all panels of Figure 4.1. The location of such antiparallel regions are highly dependent on the IMF orientation which is indicated on the center part of each panel. In [Crooker \(1979\)](#)’s antiparallel reconnection model, only for a due southward IMF orientation (panel a) is the subsolar region a likely region for magnetic reconnection to occur. For a positive IMF B_y component, as illustrated, the northern (southern) narrow antiparallel region emerges from the cusp and ex-

tend to the dusk (dawn) flank of the dayside magnetopause when there is also the presence of a negative and zero IMF B_z component (panels b and c). For a positive IMF B_z component, the antiparallel regions are located poleward of the cusps (panel d). For a negative IMF B_y component, the symmetry is reversed.

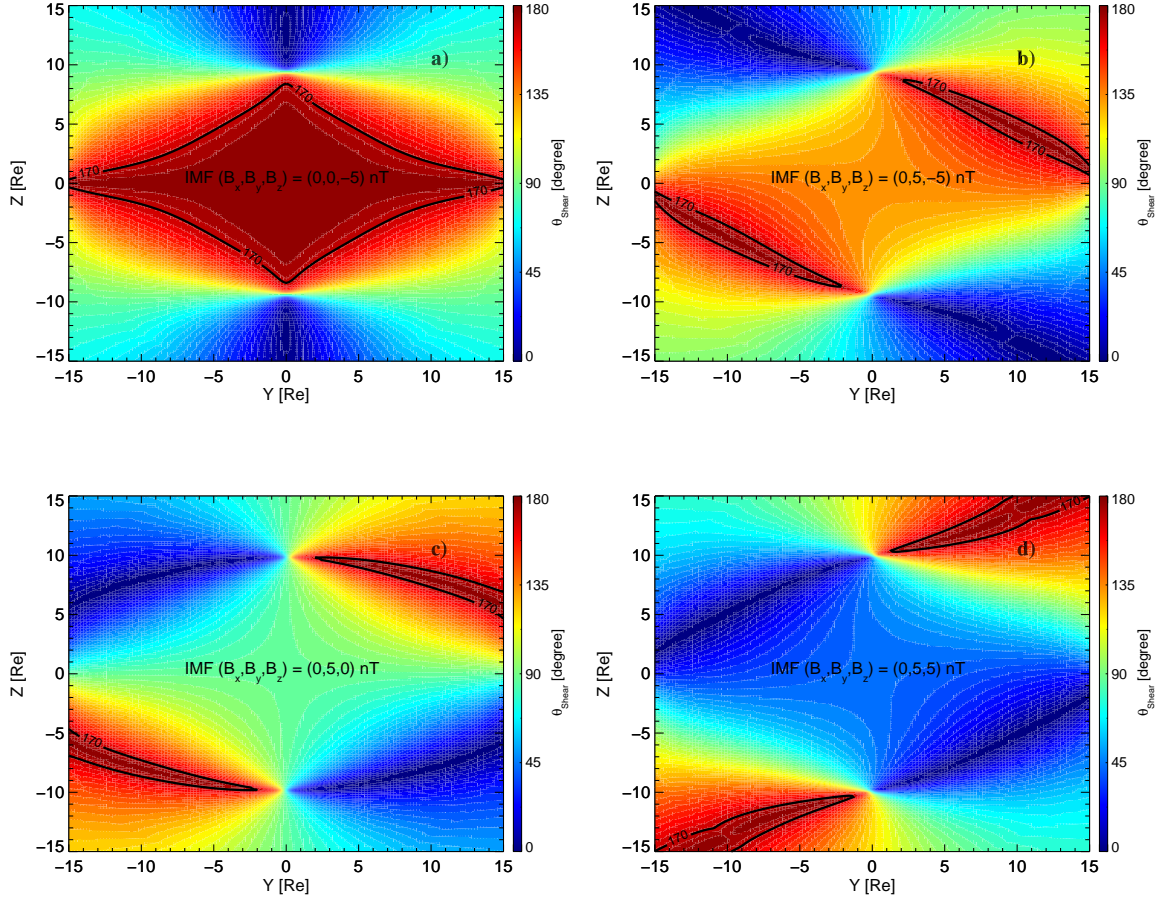


Figure 4.1 - Antiparallel reconnection sites (regions within the 170° thick, black contour lines), following Crooker (1979)'s criterion, for different IMF conditions shown in the center of each panel. The (shear) angle, $\theta_{shear} = \cos^{-1}[\mathbf{B}_{sh} \cdot \mathbf{B}_{sp}/(|\mathbf{B}_{sh}||\mathbf{B}_{sp}|)]$ between the magnetic fields from the magnetosheath (sh) and magnetosphere (sp) regions, is evaluated at each point belonging to the surface of a paraboloidal magnetopause model which is being visualized from the Sun and projected onto the yz_{GSM} plane. θ_{shear} ranges from 0° (exactly parallel magnetic fields) up to 180° (antiparallel magnetic fields).

The Trattner et al. (2007)'s X-line model is an improvement over Crooker (1979)'s antiparallel reconnection model. The difference is that the subsolar magnetopause is regarded as a likely region for reconnection to occur when the IMF B_y component is

non-zero. This is equivalent to say that in the [Trattner et al. \(2007\)](#) model the X-line is composed of two branches: one of them being located over the antiparallel regions, as shown in [Figure 4.1](#), and the other being located over the subsolar magnetopause region, as it will be shown later on.

In the next subsections the underlying analytical models which are used to generate the plots shown in [Figure 4.1](#), and therefore [Trattner et al. \(2007\)](#)'s X-line model, are discussed as well as the methods we have used to find both X-line branches.

4.1.2 Model implementation

Here, the building blocks required to construct the [Trattner et al. \(2007\)](#)'s X-line model are described.

4.1.2.1 The magnetosheath magnetic field model

The magnetosheath magnetic field model employed here is the same one used in the flux tube motion model of [Cooling et al. \(2001\)](#). The [Cooling et al. \(2001\)](#) magnetosheath magnetic field model is a simplification of the more general [Kobel and Flückiger \(1994\)](#) model, which in turn derives the magnetosheath magnetic field based on the assumption that within the magnetosheath region the magnetic field is current-free, i.e., $\nabla \times (\mathbf{B}_{sh}/\mu_o) = \mathbf{J}_{sh} = 0$, (except for the Earth's bow shock and magnetopause boundaries). The [Kobel and Flückiger \(1994\)](#) model requires only three inputs: the stand-off distances of the bow shock, R_{bs} [R_E], and of magnetopause, R_{mp} [R_E], and the three IMF components, B_x^{IMF} , B_y^{IMF} and B_z^{IMF} [nT]. Both bow shock and magnetopause boundaries are defined as paraboloids of revolution about the x_{GSM} axis with focus midway between the Earth and the subsolar point. Each point over the magnetopause surface (x_{mp}, y_{mp}, z_{mp}) [R_E] obeys the following equation

$$x_{mp} = R_{mp} - \frac{(y_{mp}^2 + z_{mp}^2)}{2R_{mp}}. \quad (4.1)$$

The [Cooling et al. \(2001\)](#) model then adapts the [Kobel and Flückiger \(1994\)](#) model in such a way that it gives the magnetosheath magnetic field components, B_x^{sh} , B_y^{sh} and B_z^{sh} [nT] at a given location $(x, y, z)_{GSM}$ immediately outside the magnetopause boundary as:

$$B_x^{sh} = -A \left[-B_x^{IMF} \left(1 - \frac{R_{mp}}{2l} \right) + B_y^{IMF} \left(\frac{y}{l} \right) + B_z^{IMF} \left(\frac{z}{l} \right) \right], \quad (4.2)$$

$$B_y^{sh} = A \left[-B_x^{IMF} \left(\frac{y}{2l} \right) + B_y^{IMF} \left(2 - \frac{y^2}{lR_{mp}} \right) - B_z^{IMF} \left(\frac{yz}{lR_{mp}} \right) \right], \quad (4.3)$$

$$B_z^{sh} = A \left[-B_x^{IMF} \left(\frac{z}{2l} \right) - B_y^{IMF} \left(\frac{yz}{lR_{mp}} \right) + B_z^{IMF} \left(2 - \frac{z^2}{lR_{mp}} \right) \right], \quad (4.4)$$

where

$$A = \frac{2R_{bs} - R_{mp}}{2(R_{bs} - R_{mp})}, \quad (4.5)$$

being A typically equals to two. The distance from the focus to the magnetopause surface is given by the parameter l as

$$l = \frac{3R_{mp}}{2} - x \quad [R_E]. \quad (4.6)$$

As pointed out by [Cooling et al. \(2001\)](#) equations 4.2 through 4.6 are valid only on the paraboloid surface defined by l . Notice that in order to determine l in equation 4.6, the magnetopause stand-off distance, R_{mp} , must be known in advance. We then use the semi-empirical expression for R_{mp} derived by [Shue et al. \(1998\)](#) which takes into account the influence of both the north-south IMF component, B_z [nT], and the solar wind dynamic pressure, P_{dyn} [nPa]:

$$R_{mp} = \{10.22 + 1.29 \tanh[0.184(B_z + 8.14)]\} P_{dyn}^{-1/6.6} \quad [R_E]. \quad (4.7)$$

Equation 4.7 correctly describes the earthward movement of the subsolar magnetopause, i.e., smaller values of R_{mp} , when B_z becomes increasingly negative, and when the solar wind dynamic pressure increases as shown in Figure 4.2.

The [Cooling et al. \(2001\)](#) magnetosheath magnetic field model allows for draping in three-dimensions, as does the original [Kobel and Flückiger \(1994\)](#) model. Figure 4.3 shows a view from the Sun of the magnetosheath magnetic field draping, as derived from the [Cooling et al. \(2001\)](#) model, over the paraboloidal magnetopause surface defined by equation 4.1. The IMF orientations shown are the same as those in Figure 4.1.

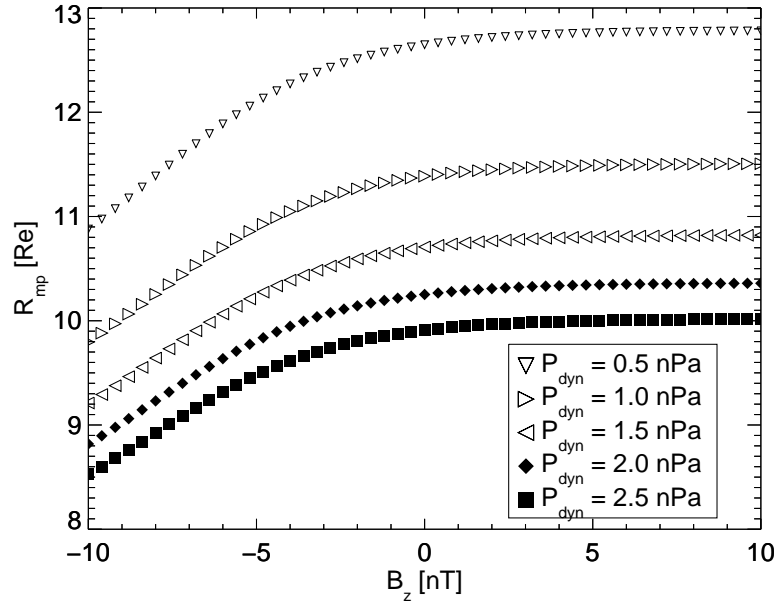


Figure 4.2 - Plot of the Shue et al. (1998)'s magnetopause stand-off distance, R_{mp} , versus the north-south IMF B_z component for various values of the solar wind dynamic pressure P_{dyn} .

4.1.2.2 Magnetospheric magnetic field model

The geomagnetic field model used here is that of Alexeev et al. (2003, and references therein) which confines the magnetospheric magnetic field within a paraboloid. Such magnetic field is considered to be given by the sum of magnetic fields of the geomagnetic dipole, the ring current, the geotail current system, the Chapman-Ferraro currents, and some parts of the IMF parallel and perpendicular (to the magnetopause) components penetrating into the magnetosphere.

As input to the magnetospheric paraboloid model¹, one needs to provide:

- 1) the date: year, month, day and Universal Time in order to properly determine the geomagnetic dipole tilt angle,
- 2) the solar wind density [cm^{-3}] and speed [km/s], and the IMF B_z [nT] component,
- 3) both *Disturbance Storm Time* (D_{st} [nT]) and *Amplitude Lower* (AL [nT])

¹The FORTRAN subroutine which calculates the magnetospheric magnetic field in the paraboloid model can be found in the following website: <http://smdc.sinp.msu.ru/models/parab.for>.

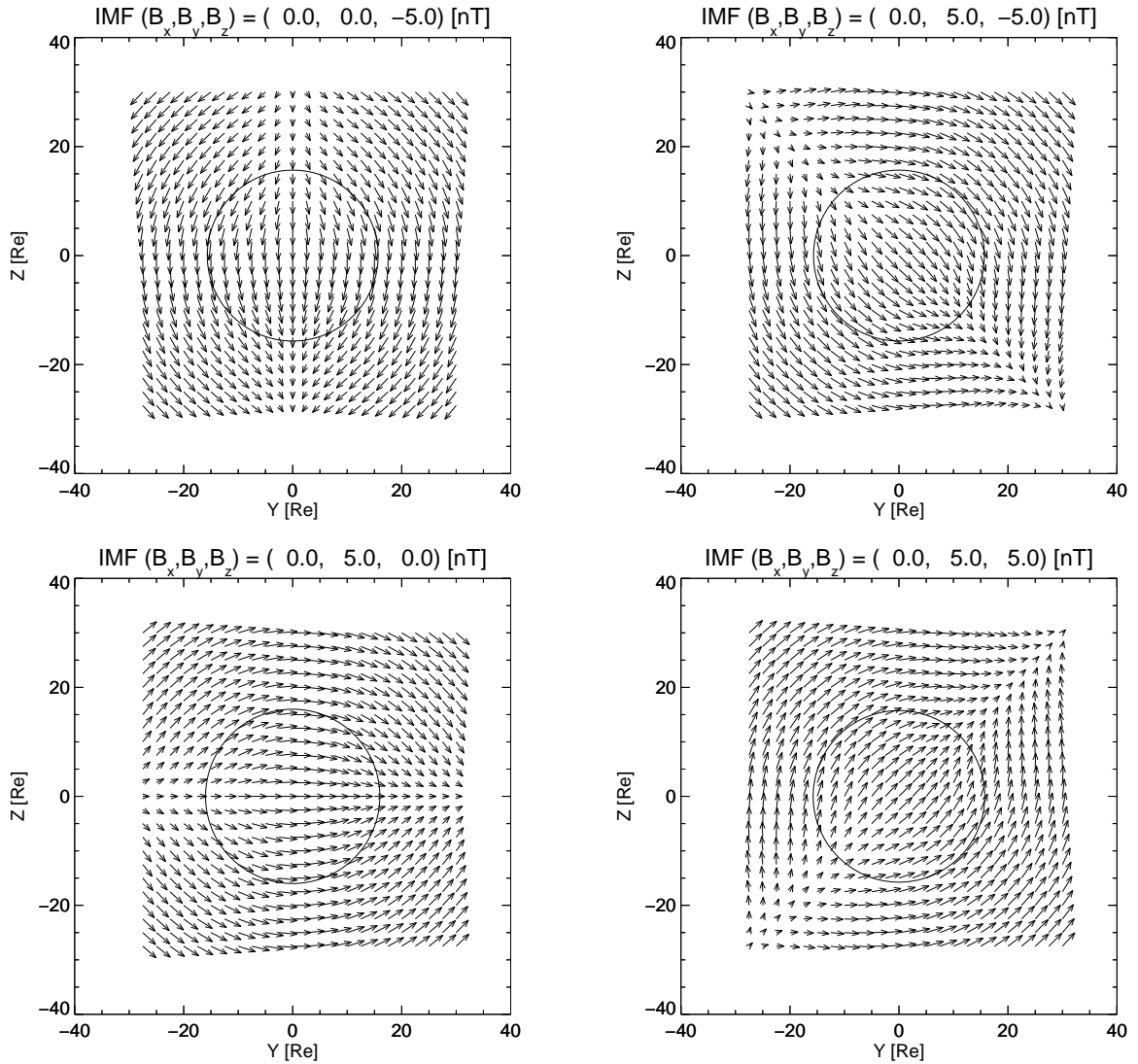


Figure 4.3 - View from the Sun of the draping of the magnetosheath magnetic field from the [Cooling et al. \(2001\)](#) model around the paraboloidal magnetopause. The IMF orientation for each case is shown on the top of each panel. For negative IMF B_y values the symmetry is reversed. The black circle represents the terminator ($x_{GSM} = 0 R_E$).

index values, which describe the disturbance levels recorded by ground magnetometers on the low latitude and auroral zones, respectively,

- 4) and finally, the $(x, y, z)_{GSM}$ location where the magnetospheric magnetic field vector should be evaluated.

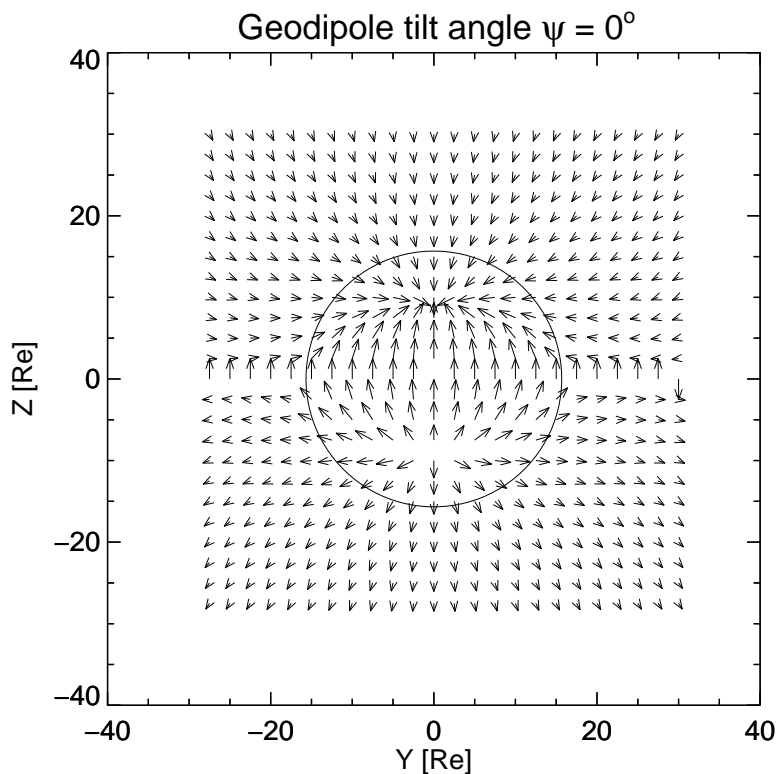


Figure 4.4 - View from the Sun of the [Alexeev et al. \(2003\)](#)'s magnetospheric magnetic field model just inside the paraboloidal magnetopause boundary for the case when there is no geodipole tilt angle, i.e., $\psi = 0^\circ$. The model input parameters used to generate this plot were: $n = 5 \text{ [cm}^{-3}\text{]}$, $V_{sw} = 400 \text{ [km/s]}$, $\psi = 0^\circ$, and a purely southward IMF, with $B_z = -5 \text{ [nT]}$. The black circle represents the terminator ($x_{GSM} = 0 R_E$).

In Figure 4.4 it is plotted a view from the Sun of the [Alexeev et al. \(2003\)](#)'s magnetospheric magnetic field configuration just inside the magnetopause boundary defined by equation 4.1 for the case when the geomagnetic dipole tilt inclination ψ is 0° . Notice that the cusps, regions of convergence and divergence of magnetic field vectors on the northern and southern hemispheres, respectively, are located around $z_{GSM} \sim \pm 10 R_E$. As ψ assumes higher positive (negative) ψ values, the northern cusp moves equatorward (tailward), while the southern cusp moves tailward (equa-

torward) as expected.

Once we have the magnetosheath (\mathbf{B}_{sh}) and magnetosphere (\mathbf{B}_{sp}) magnetic field vectors on both sides of the magnetopause boundary, we can determine the shear angle value θ_{shear}

$$\theta_{shear} = \cos^{-1}[\mathbf{B}_{sh} \cdot \mathbf{B}_{sp}/(|\mathbf{B}_{sh}||\mathbf{B}_{sp}|)], \quad (4.8)$$

over the whole magnetopause surface, and the shear angle maps are shown in Figure 4.1. In particular, the magnetosheath magnetic field, \mathbf{B}_{sh} , is determined precisely over a point at the magnetopause surface, namely $(x_{mp}, y_{mp}, z_{mp}) [R_E]$, as given by equation 4.1, while the magnetospheric magnetic field, \mathbf{B}_{sp} , is evaluated at the point $0.99(x_{mp}, y_{mp}, z_{mp}) [R_E]$ which is just inside the magnetopause boundary ($0.01 R_E$ in radial distance).

4.1.2.3 Determining the X-line location: Antiparallel branches

In previous subsections we have seen the analytical magnetic field models used here in order to derive the shear angle values over the whole magnetopause surface. Now, in this subsection, we determine the location over the magnetopause of the two antiparallel branches of the [Trattner et al. \(2007\)](#)'s X-line model, i.e., the regions over the whole magnetopause surface for which the shear angle values are the highest (near 180°). In order to do that, we use a ridge-detection algorithm developed by [Lindeberg \(1998, and references therein\)](#) which is described in details in [Appendix A](#).

Firstly, we show that the regions where we want to apply the [Lindeberg \(1998\)](#) technique are indeed ridge-like regions. Consider, as an example, panel b) in Figure 4.1. Now, imagine that we can see the same plot from 3-D perspectives where the third dimension would correspond to the shear angle (θ_{shear}) values. Such a plot is presented in Figure 4.5 which shows, on the left panel, a colored 3-D surface of shear angle values, with the red (blue) colored regions having the highest (lowest) shear angle values. The right panel of Figure 4.5 shows the same 3-D surface of the left panel, but rotated just to emphasize the peaks and valleys of the analyzed surface.

The reddish regions, with highest ($> 160^\circ$) shear angle values, are the ridge-like regions where we are going to apply the [Lindeberg \(1998\)](#) technique, which in turn establish local maxima criteria for locating these ridge points within the image being analyzed (cf. [Appendix A](#) for details). With the exception of the purely southward IMF case with no Earth's dipole tilt (panel a in Figure 4.1), we notice that, in general, there will be two ridge-like (peaked) regions even for other IMF orientations

and non-zero dipole tilt angles. Thus, two antiparallel branches will constitute a part of the [Trattner et al. \(2007\)](#)'s X-line model.

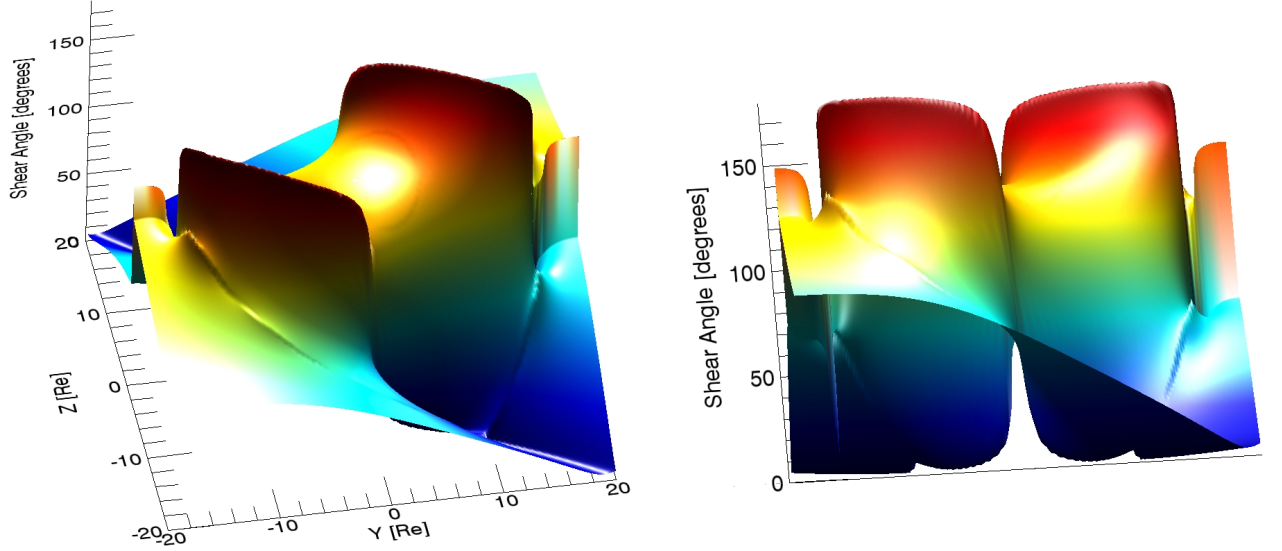


Figure 4.5 - 3-D perspectives of the plot shown in panel b) of Figure 4.1. The ridge-like regions correspond to the reddish regions with highest ($> 160^\circ$) shear angle values. The maximum shear angle value is 180° .

Once both antiparallel branches of the [Trattner et al. \(2007\)](#)'s X-line are determined, it is shown, in the next subsection, the way the subsolar X-line branch is derived.

4.1.2.4 Determining the X-line location: Subsolar branch

Here, we want to know where the subsolar portion of the [Trattner et al. \(2007\)](#)'s X-line will be located. When we refer to the subsolar portion of the X-line, we are restricting the analyzed area of the dayside magnetopause to regions in between the two antiparallel regions including, of course, the subsolar point ($y_{GSM} = z_{GSM} = 0 R_E$), and where the shear angle values obtained by the analytical models described above are usually larger than 90° , i.e., $\theta_{shear} > 90^\circ$ (see the central part of panels b and c of Figure 4.1 for reference).

The [Lindeberg \(1998\)](#) method used in the previous subsection is not able to determine the full extent of the X-line in the subsolar branch due to the saddle-like shape of the subsolar portion of the 3-D shear angle surface (see left panel in Figure 4.5). In such regions the maxima criteria may not be satisfied (cf. [Appendix A](#)). Thus,

we have adopted another method which is described below.

The first step in our implementation for finding the X-line's subsolar branch location is to determine the saddle point's $(y, z)_{GSM}$ location on the image being analyzed. As an example, we will use the same image shown at panel b) of Figure 4.1, which shows the shear angle configuration over the model magnetopause surface for a southward($B_z < 0$)-duskward($B_y > 0$) IMF orientation. The difference between the aforementioned figure and Figure 4.6 is that in the latter another four isocontours (black thick lines) of shear angle have been inserted, namely 133° , 134° , 135° , 136° . The purpose of showing such isocontours is to delineate the saddle-like shape of the shear angle plots, which is present whenever the IMF B_y component is non-zero. Notice that we have highlighted a point in the center of the plot (black filled circle) which is the saddle point. Such a point was determined by increasing the number of shear angle isocontours up to 2500. By doing that, the isocontours' locations tend to meet up at a point in the subsolar region, the saddle point, without ever intersecting each other. Through this simple method the saddle point location has an uncertainty of $0.2 R_E$, which corresponds to the cell size used for discretizing the magnetopause surface for the current analyzed X-line model.

The saddle point coincides with the subsolar point when there is neither Earth's dipole tilt inclination nor IMF B_x component. These two variables have an effect to displace the maximum shear X-line location from the subsolar point (TRATTNER et al., 2007).

Once the saddle point is determined, an iterative process for determining the $(y, z)_{GSM}$ locations of the X-line's subsolar branch is performed as follows.

- I) Consider the $(y, z)_{GSM}$ saddle point location as corresponding to an $(i = i_s, j = j_s) \in \mathbb{Z}^+$ element of the discretized magnetopause surface.
- II) Calculate the shear angle (θ_{shear}) values which lie in the immediate vicinity of the (i_s, j_s) pair, i.e., at the eight neighbouring locations: $(i - 1, j - 1)$, $(i - 1, j)$, $(i - 1, j + 1)$, $(i, j - 1)$, $(i, j + 1)$, $(i + 1, j - 1)$, $(i + 1, j)$, $(i + 1, j + 1)$.
- III) Locate the (i, j) pair among the eight pairs defined in Step II, for which the shear angle value is a maximum, and store its corresponding $(y, z)_{GSM}$ location.
- IV) Update the initial (i_s, j_s) pair with that found in Step III, e.g., $(i_s, j_s) = (i + 1, j + 1)$.

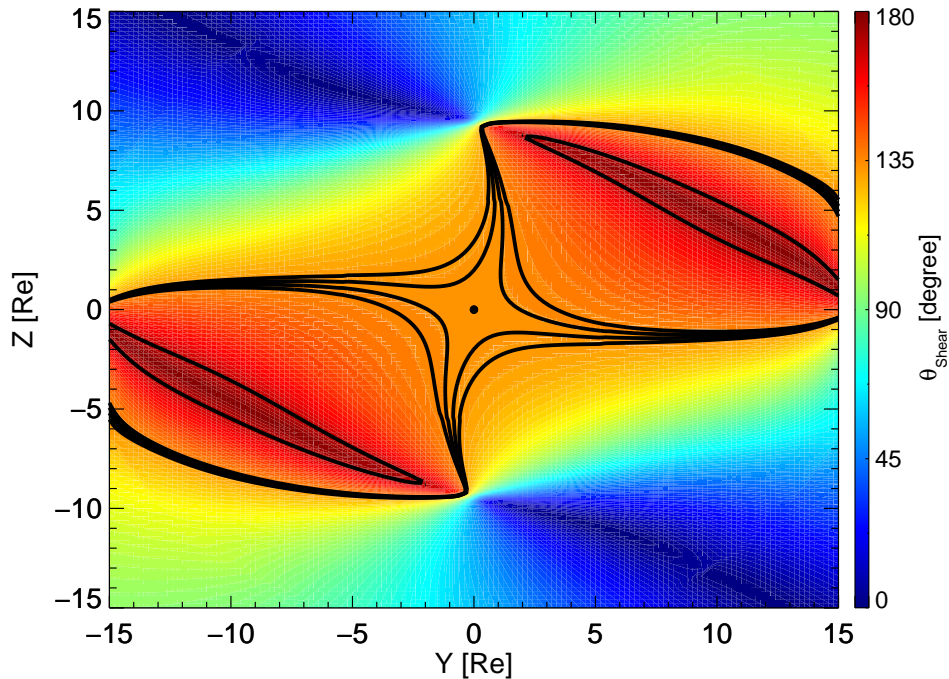


Figure 4.6 - Saddle point (black filled circle) determination on shear angle plots (see text for details). The plot shown is the same as that in panel b) of Figure 4.1, with the difference that another four shear angle isocontours (black thick lines) have been inserted, namely 133° , 134° , 135° , 136° .

V) Repeat Steps II through IV until the condition $\theta_{shear}^{(i_s, j_s)} \geq 170^\circ$ is satisfied.

With the iterative process described above only one part of the X-line's subsolar branch is determined, i.e., the part that emerges from the saddle point and goes toward either antiparallel branches of the maximum shear X-line. In order to determine the remaining part of the subsolar X-line, another (i_s, j_s) pair near the saddle point location must be taken so that the iterative process described above can be applied once again. Such a point is chosen in the following way: consider that the first part of the X-line's subsolar branch is determined using the method described above and, for example, it emerges from the saddle point and goes up to the northern antiparallel region². The necessary (i_s, j_s) pair for determining the remaining part of the X-line's subsolar branch will be the point closest to the saddle point but taken in the direction opposite to that formed by the first part of the X-line's subsolar branch. Then, the iterative process start out from the new (i_s, j_s) pair and generates the remaining part of the X-line's subsolar branch. The final result for the

²For all cases analyzed here, such a path will be a straight line in the y_{GSM} plane, and it will have a tilt relative to the y_{GSM} axis depending on the relative magnitude of the IMF components B_y and B_z .

Trattner et al. (2007)’s X-line in the southward-duskward IMF case illustrated in Figure 4.6 is shown in Figure 4.7. The subsolar branch of the maximum shear X-line crosses the subsolar point, and it is tilted relative to the y_{GSM} axis. This behavior is consistent with a component-type reconnection X-line (GONZALEZ; MOZER, 1974; SONNERUP, 1974).

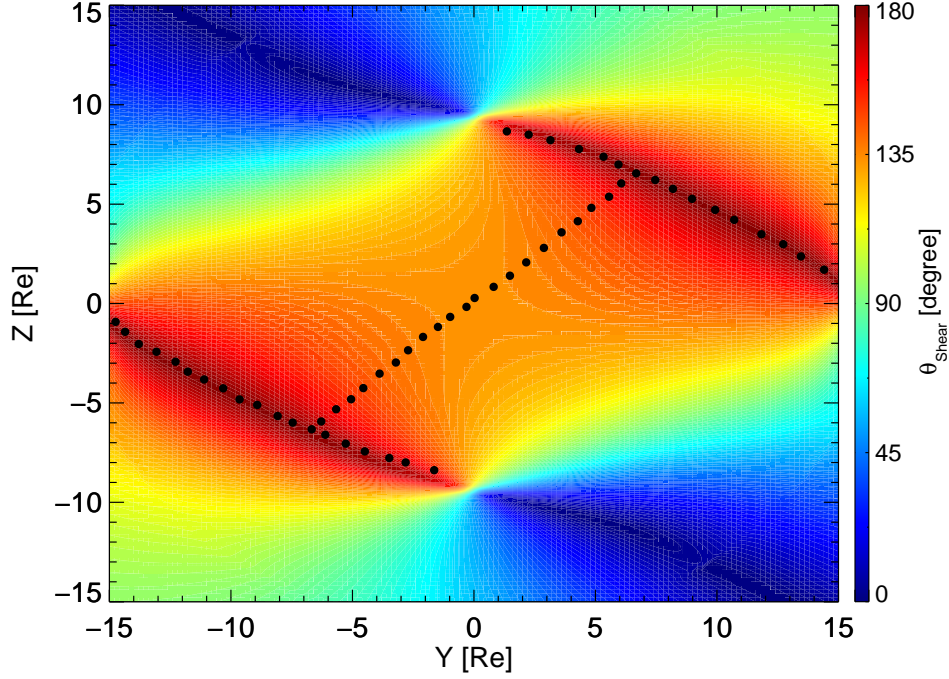


Figure 4.7 - Trattner et al. (2007)’s maximum shear X-line (filled black circles) for a southward ($B_z = -5$ nT)-duskward ($B_y = 5$ nT) IMF orientation. The antiparallel branches, i.e., dark red regions where the local shear angle θ_{shear} surpasses 170° , are determined via the Lindeberg (1998)’s technique (cf. Appendix A), while the subsolar branch, the part of the X-line approximately 45° tilted relative to the y_{GSM} axis, is obtained by an iterative process described in Section 4.1.2.4 (see text for details).

4.2 Maximum Current Density Model: Gonzalez and Mozer (1974)

4.2.1 Model description

Originally, Gonzalez and Mozer (1974) proposed that the dayside reconnection X-line would be best represented by a subsolar streamline of the Chapman-Ferraro current density, \mathbf{J}_{CF} , of the magnetopause as given by

$$\mathbf{J}_{CF} = \frac{1}{\mu_0} \nabla \times (\mathbf{B}_{sh} - \mathbf{B}_{sp}), \quad (4.9)$$

where \mathbf{B}_{sh} and \mathbf{B}_{sp} are the magnetosheath and magnetospheric magnetic fields, respectively, adjacent to the magnetopause boundary. The subsolar Chapman-Ferraro current streamline would behave like a tilted line relative to the y_{GSM} axis for IMF orientations in which the B_y component was non-zero. This method is akin to the subsolar branch of the maximum shear X-line presented in the previous section (see Figure 4.7), while for purely southward IMF such a streamline would be located over the equator extending throughout the dayside magnetopause region. (GONZALEZ; MOZER, 1974; SONNERUP, 1974).

A drawback of this approach is an unclear choice of a starting point from which the current density streamline is going to be integrated. In other words, one must choose *which* streamline will best represent the reconnection X-line. A natural choice of the starting point is the current density streamline that pass through the subsolar point where it is believed the magnetosheath plasma will first contact the magnetopause. Such a hypothesis has been used by Sibeck and Lin (2011) in their study of reconnection-associated flux tube motion along the dayside magnetopause. Requiring, however, the X-line to necessarily cross the subsolar point seems a restrictive choice, since reconnection may happen at the stagnation rather than the subsolar point where the magnetosheath flow would spend more time, then giving more chances for reconnection conditions to be satisfied. Thus, the subsolar point choice for starting the Chapman-Ferraro's streamline integration is not unique, and other choices may be equally valid.

Based on the aforementioned argumentation, we need to improve the Gonzalez and Mozer (1974)'s idea on how the X-line should be represented. One of the possibilities is that, instead of an X-line parallel to a given current density streamline, the X-line should be located wherever the Chapman-Ferraro current density magnitude, $|\mathbf{J}_{CF}|$, is a maximum. There have been works (see e.g. Semenov and Pudovkin (1985) and Alexeev et al. (1998)) which advocate the idea that dayside magnetopause reconnection would be initiated in places where the current density magnitude would surpass a certain threshold and, as a result, current-driven instabilities would provide the anomalous resistivity required for the reconnection process to proceed in a higher rate. With this choice we get rid of the requirement of the X-line necessarily crossing the subsolar point. Although we have adopted a slightly different criterion to establish the X-line location, the Chapman-Ferraro current density is still being used to accomplish this task, therefore we will continue to refer to this X-line model as pertaining to Gonzalez and Mozer (1974).

4.2.2 Model implementation

The magnetosheath and magnetospheric magnetic field models required for determining the Chapman-Ferraro current, as defined by equation 4.9, are the same used in the implementation of the maximum shear X-line (see Sections 4.1.2.1 and 4.1.2.2 for details). The model magnetopause surface is therefore the same one used in the previous section, and it is defined by equation 4.1.

In order to properly determine the Chapman-Ferraro current density, \mathbf{J}_{CF} , it is needed to project \mathbf{J}_{CF} over the paraboloidal surface in such a way that at every point (x_{mp}, y_{mp}, z_{mp}) belonging to the modeled magnetopause surface the current density is perpendicular to the local normal vector, $\hat{\mathbf{n}}$, i.e., $\mathbf{J}_{CF} \cdot \hat{\mathbf{n}} = 0$. The normal vector at each (x_{mp}, y_{mp}, z_{mp}) point can be calculated in the following way: since we have an analytical expression for the magnetopause surface, as given by equation 4.1, we can consider the x_{mp} coordinate as a function of the independent variables y_{mp} and z_{mp} , i.e., $x_{mp} = x_{mp}(y_{mp}, z_{mp})$. Therefore, we can use standard techniques³ to derive the normal vector $\hat{\mathbf{n}}$ of a generic 3-D surface which is a function of two independent variables yielding:

$$n_x = R_{mp} / \sqrt{R_{mp}^2 + y_{mp}^2 + z_{mp}^2}, \quad (4.10)$$

$$n_y = y_{mp} / \sqrt{R_{mp}^2 + y_{mp}^2 + z_{mp}^2}, \quad (4.11)$$

$$n_z = z_{mp} / \sqrt{R_{mp}^2 + y_{mp}^2 + z_{mp}^2}. \quad (4.12)$$

Projecting \mathbf{J}_{CF} onto the paraboloidal magnetopause surface yields:

$$J_x = 10^3 \mu_o^{-1} [n_y(B_z^{sh} - B_z^{sp}) - n_z(B_y^{sh} - B_y^{sp})], \quad [\text{mA/m}] \quad (4.13)$$

$$J_y = 10^3 \mu_o^{-1} [n_z(B_x^{sh} - B_x^{sp}) - n_x(B_z^{sh} - B_z^{sp})], \quad [\text{mA/m}] \quad (4.14)$$

$$J_z = 10^3 \mu_o^{-1} [n_x(B_y^{sh} - B_y^{sp}) - n_y(B_x^{sh} - B_x^{sp})], \quad [\text{mA/m}] \quad (4.15)$$

where the 10^3 factor was used only to express the current density value in units of miliAmpère per meter. The current density magnitude plots that will be shown latter on are expressed in this unity.

Once the current density vector is known everywhere over the paraboloidal magne-

³See <http://mathworld.wolfram.com/NormalVector.html> and references therein.

topause surface, we can calculate its magnitude at each point and make a plot like the one shown on the top panel of Figure 4.8, for which the IMF orientation is IMF $B_z = -5$ nT and IMF $B_y = 5$ nT, with no dipole tilt inclination and no IMF B_x . The bottom panel of Figure 4.8 shows a 3-D surface of \mathbf{J}_{CF} as the third dimension, akin to that shown in Figure 4.5. The bottom panel of Figure 4.8 is shown just to emphasize the ridge-like shape of the central portion of the \mathbf{J}_{CF} surface where the highest current density magnitude values are concentrated. Such a shape is ideal to apply the Lindeberg (1998)'s technique, which is used here to determine Gonzalez and Mozer (1974)'s X-line. The result of Lindeberg (1998)'s technique applied to this case is shown on the top panel of Figure 4.8 as black filled circles which constitute the X-line.

4.3 Maximum Reconnection Outflow Speed Model: Swisdak and Drake (2007)

4.3.1 Model description

In this model, the X-line should point in the direction where the reconnection outflow speed, V_{out} , which is a function of the local magnetic fields and plasma densities, must be maximized. Since the X-line orientation and location in this model depend on magnetic field and plasma parameters on both sides of the current sheet (magnetopause), it is equivalent to take into account the effect of possible asymmetries in the aforementioned parameters, i.e., in general magnetic field and plasma densities on both sides of the magnetopause current sheet will be different.

In order to better visualize how the X-line in the Swisdak and Drake (2007) model can be oriented, let us consider both 2-D and 3-D schematic views of the reconnection plane on panels a) and b), respectively, of Figure 4.9 for a small section of the subsolar magnetopause where we can approximate it as a plane parallel to the YZ plane. The coordinate system would be the GSM and its axes are shown on the top part of each panel.

On panel a) of Figure 4.9, the weaker magnetosheath magnetic field, \mathbf{B}_2 , considered to have a purely southward orientation (vertical dashed arrows), and the stronger geomagnetic field, \mathbf{B}_1 , with a purely northward orientation (vertical solid black arrows), convect toward the dayside magnetopause (black dotted lines), and form the reconnection plane (green rectangle). These fields will actually meet in a small region (the diffusion region) within the reconnection plane, and there their topology change will take place at the X point, represented by the green circle in the center

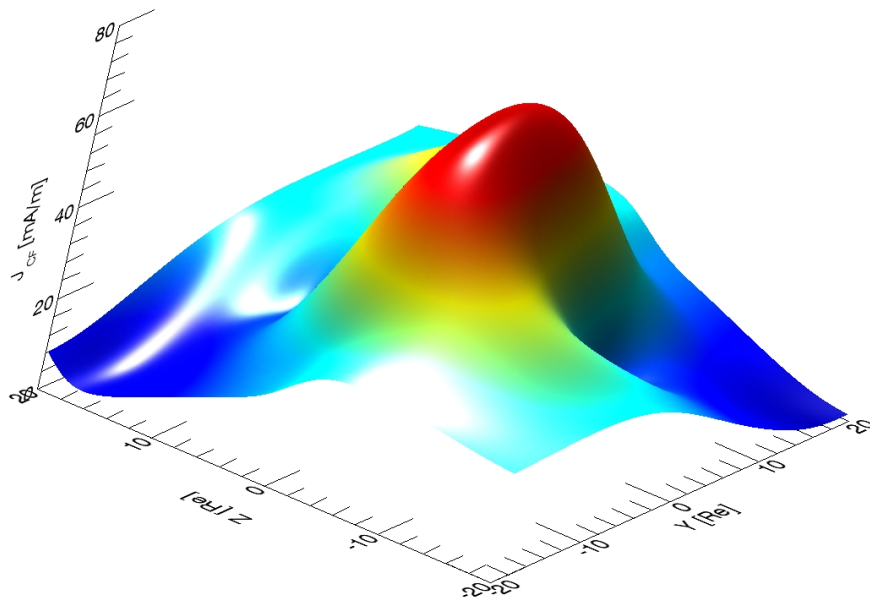
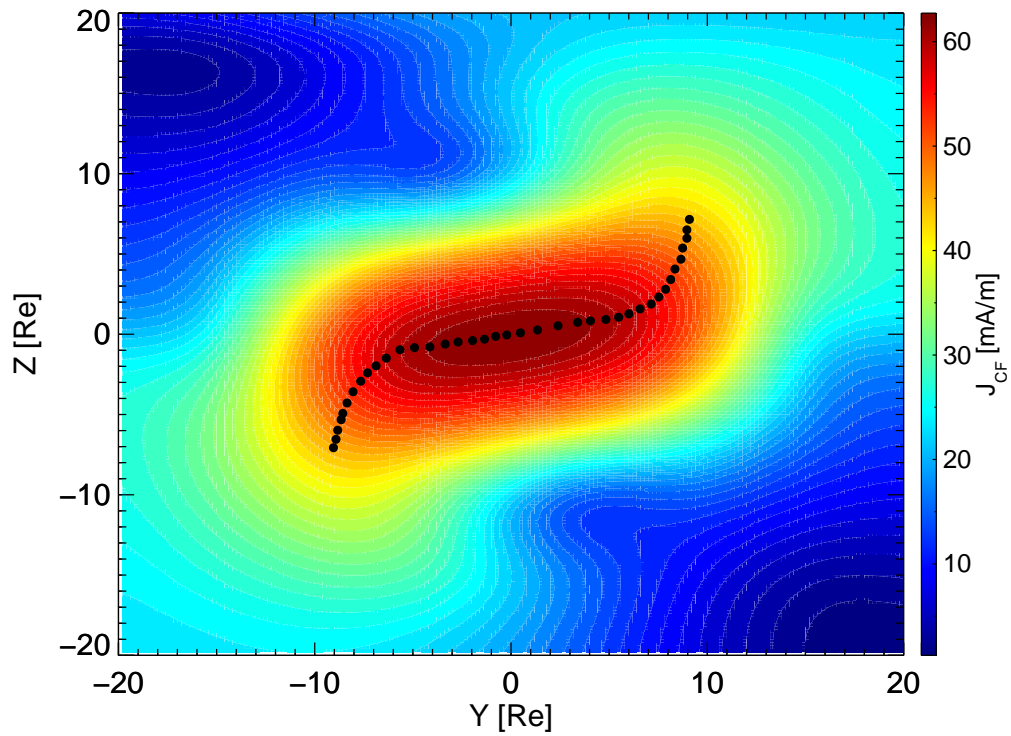


Figure 4.8 - **(Top)** View from the Sun onto the yz_{GSM} plane of the Chapman-Ferraro current density magnitude, $|\mathbf{J}_{CF}|$ [mA/m], over the paraboloidal magnetopause surface. The filled black circles represent the X-line taken at the points where $|\mathbf{J}_{CF}|$ is a local maximum according to Lindeberg (1998)'s technique (see Appendix A for details). **(Bottom)** 3-D perspective of the top panel plot with $|\mathbf{J}_{CF}|$ being the third dimension, which emphasize the ridge-like shape of the central portion of the $|\mathbf{J}_{CF}|$ surface where the highest current density values are concentrated.

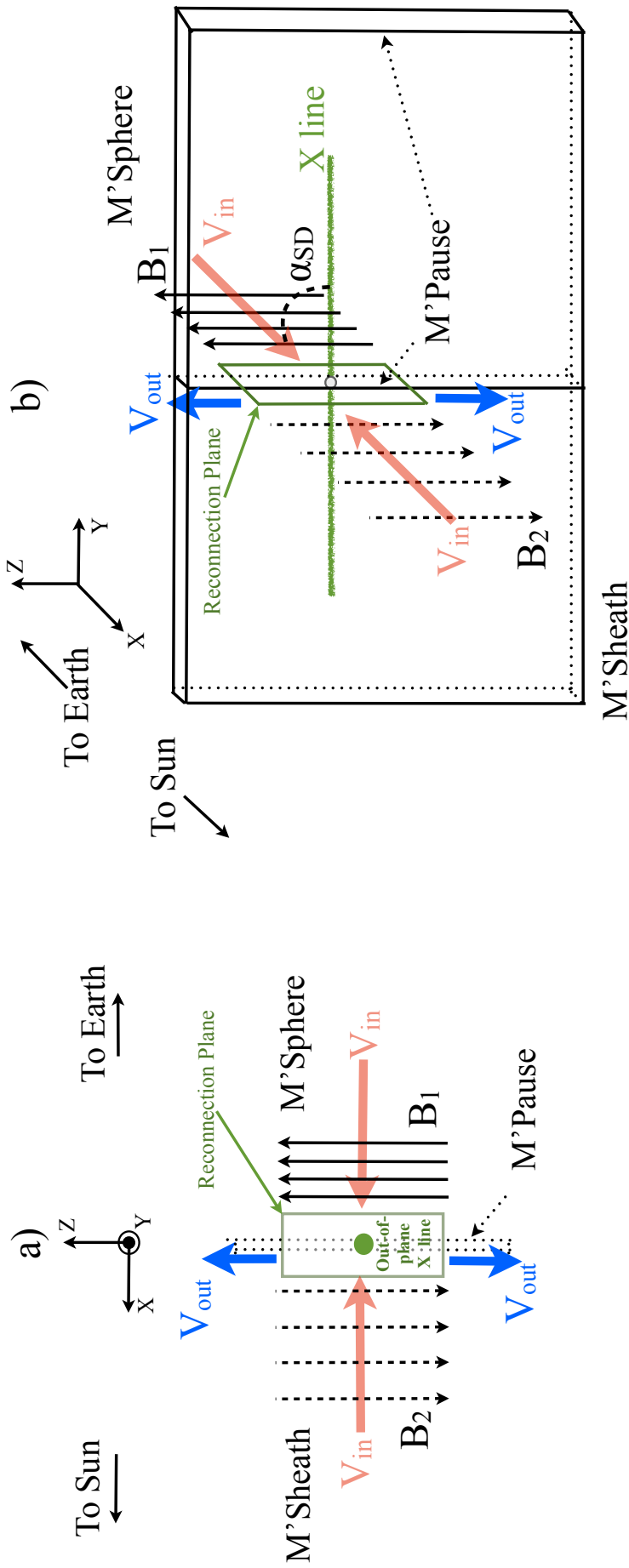


Figure 4.9 - 2-D (panel a) and 3-D (panel b) schematic views of the reconnection plane formed by oppositely directed magnetic fields of the magnetosheath (B_2 , vertical dashed arrows) and magnetosphere (B_1 , vertical solid black arrows). The magnetized magnetosheath and magnetosphere plasmas with mass densities ρ_2 and ρ_1 , respectively, approach the dayside magnetopause with an inflow speed V_{in} (thick light red arrows) along the $\pm X$ directions, while the reconnection outflow speed, V_{out} (thick blue arrows), exits the reconnection region in the $\pm Z$ directions. GSM coordinates are used. In 2-D (panel a) the X-line (green horizontal line in panel b) is seen as a dot (green circle) within the reconnection plane.

of the reconnection plane. Although drawn in the center of the reconnection plane, it is noticed, however, that for such an asymmetrical reconnecting magnetic field configuration, the X point location should be displaced towards the region of weaker magnetic field (cf., Cassak and Shay (2007)), i.e., the magnetosheath region. As a result of the reconnection process, plasma exits the reconnection region with a V_{out} speed (thick blue arrows) in both $+$ and $-Z$ directions. Again, panel a) shows how the reconnection process would occur in 2-D for a given Y position. If we consider that for other Y positions the same process is occurring as well, the X point in panel a) becomes an X-line (green horizontal line) in panel b) of Figure 4.9, which shows a 3-D perspective of all features presented in panel a).

Turning back to the Swisdak and Drake (2007) model, they argue that the X-line will have an orientation, i.e., an angle α_{SD} between \mathbf{B}_1 and the X-line that V_{out} should be a maximum. For the configuration shown in panel b) of Figure 4.9, i.e., for a shear angle of 180° , $\alpha_{SD} = 90^\circ$ would maximize the outflow speed, V_{out} . In this case, the X-line would be located over the Y axis as shown on panel b). Notice that α_{SD} is concerned to a localized extent of the X-line where the relevant plasma parameters, \mathbf{B}_1 , \mathbf{B}_2 , ρ_1 and ρ_2 are assumed to be spatially constant. Thus, at another section of the dayside magnetopause, the local plasma and magnetic field parameter values would be different than those shown in panels a) and b) of Figure 4.9, resulting in a different X-line orientation, i.e., α_{SD} would no longer necessarily be 90° .

From the discussion above, it is essential to determine the functional dependence of the outflow speed on the local plasma and magnetic field parameters, and also on the α_{SD} angle. In order to derive V_{out} , Swisdak and Drake (2007) make use of the time-stationary magnetohydrodynamical (MHD) theory. The goal is to find the angle α_{SD} , as shown in Figure 4.10, that maximizes the reconnection outflow speed, V_{out} , given the magnetic fields (\mathbf{B}_1 and \mathbf{B}_2) and densities (ρ_1 and ρ_2) on both sides of the magnetopause.

Before discussing how V_{out} is derived, it is important to define the coordinate system used in the model, which is shown in Figure 4.10. The XZ plane corresponds to the local current sheet (magnetopause) plane, and the Y direction is perpendicular to it. The correspondence between Swisdak and Drake (2007) coordinates and those of the GSM system at the magnetopause is $(X, Y, Z) \rightarrow (Z, X, Y)_{GSM}$. Notice that in Figure 4.10, the magnetic fields \mathbf{B}_1 and \mathbf{B}_2 meet up at the ZX (YZ_{GSM}) plane at an arbitrary shear angle $\theta = \cos^{-1}[(\mathbf{B}_1 \cdot \mathbf{B}_2)/(|\mathbf{B}_1||\mathbf{B}_2|)]$. The reconnection X-line is considered to lie in the Z direction. The α_{SD} angle is taken as the X-line orientation

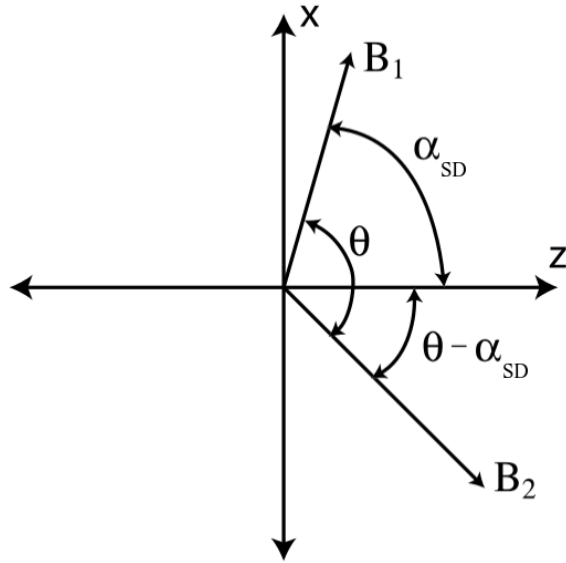


Figure 4.10 - Local current sheet coordinate system used in the [Swisdak and Drake \(2007\)](#) model. The Y (out-of-plane) direction corresponds to the local normal direction. Plasmas with distinct magnetic fields (\mathbf{B}_1 and \mathbf{B}_2) and mass densities (ρ_1 and ρ_2) meet up at the plane shown at an arbitrary shear angle $\theta = \cos^{-1}[(\mathbf{B}_1 \cdot \mathbf{B}_2)/(|\mathbf{B}_1||\mathbf{B}_2|)]$. The X-line is considered to lie in the Z direction and it is oriented relative to the fields \mathbf{B}_1 and \mathbf{B}_2 according to the angles α_{SD} and $\theta - \alpha_{SD}$, respectively. α_{SD} lies between 0 and θ , i.e., $0 \leq \alpha_{SD} \leq \theta$.

SOURCE: Adapted from [Swisdak and Drake \(2007\)](#).

relative to the magnetospheric magnetic field, \mathbf{B}_1 , and the X-line orientation relative to the magnetosheath magnetic field, \mathbf{B}_2 , is given by $\theta - \alpha_{SD}$. Given the magnetic fields and plasma mass densities, the only unknown is the angle α_{SD} , which is going to be determined as $\partial V_{out}/\partial \alpha_{SD} = 0$. Furthermore, α_{SD} is considered to lie between 0 and θ , i.e., $0 \leq \alpha_{SD} \leq \theta$.

Now, it is briefly described how the reconnection outflow speed, V_{out} , is determined. For more details, we refer to the [Swisdak and Drake \(2007\)](#) paper.

As mentioned above, in the [Swisdak and Drake \(2007\)](#) model V_{out} is derived on the basis of steady-state, 2-D ideal MHD theory. The considered assumptions are the following: *i*) plasmas with distinct mass densities (ρ_1 and ρ_2), and magnetic field strengths (B_1 and B_2) and directions, approach a 2-D reconnection layer (YX plane) with distinct inflow speeds (v_1 and v_2); *ii*) within the reconnection layer the plasmas mix in some proportion; *iii*) V_{out} is a result of magnetic tension forces of reconnected magnetic field lines acting on the plasma and accelerating it up to a V_{out} value at the

edge of the reconnection layer; *iv*) mass is conserved across the reconnection layer; *v*) at the X-line location, the in-(YX)-plane magnetic field and plasma velocity vanish; *vi*) within the reconnection layer the magnetic tension ($(B_y \partial B_x / \partial y)$) and advection ($(v_x \partial v_x / \partial x)$) terms are the dominant ones in the X component (outflow direction) of the momentum equation.

With such considerations the reconnection outflow speed, V_{out} , can be expressed in terms of the angles shown in Figure 4.10, and also as a function of the magnetic field and plasma parameters on both sides of the current sheet, as (SWISDAK; DRAKE, 2007):

$$V_{out} = \sqrt{\frac{B_1 \sin \alpha_{SD} + B_2 \sin(\theta - \alpha_{SD})}{\mu_o \left(\frac{\rho_1}{B_1 \sin \alpha_{SD}} + \frac{\rho_2}{B_2 \sin(\theta - \alpha_{SD})} \right)}} \quad [\text{km/s}]. \quad (4.16)$$

When the magnetic field and plasma conditions are symmetric, i.e., when $\theta = 180^\circ$, $\alpha_{SD} = 90^\circ$, $B_1 = B_2 = B$ and $\rho_1 = \rho_2 = \rho$, equation 4.16 reduces to the known Alfvén speed, $B/\sqrt{\mu_o \rho}$. When either density is infinite or either field vanishes the outflow speed goes to zero, as expected.

Once the functional form of V_{out} is determined, the extrema condition $\partial V_{out} / \partial \alpha_{SD} = 0$ is applied to equation 4.16, and α_{SD} can be found as the root of the following non-linear equation:

$$0 = \left(\frac{\rho_2}{\rho_1} \right) \sin^2(\alpha_{SD}) \left[\sin(\theta - 2\alpha_{SD}) - \left(\frac{B_2}{B_1} \right) \sin(2\theta - 2\alpha_{SD}) \right] + \left(\frac{B_2}{B_1} \right) \sin^2(\theta - \alpha_{SD}) \left[\sin(2\alpha_{SD}) + \left(\frac{B_2}{B_1} \right) \sin(\theta - 2\alpha_{SD}) \right], \quad (4.17)$$

which is subject to the constraint $0 \leq \alpha_{SD} \leq \theta$. In order to have an idea on what the exact solution of equation 4.17 looks like as a function of the shear angle θ , a B_2/B_1 ratio of 0.5 and $\rho_2/\rho_1 = 10$ were chosen. The magnetosheath to magnetosphere magnetic field strength ratio B_2/B_1 adjacent to the dayside magnetopause is usually less than one for nominal solar wind conditions, while the magnetosheath plasma density is typically ten times higher than that in the magnetosphere for these same conditions. With such values applied in equation 4.17, it is possible to see in Figure 4.11 that the exact solution of equation 4.17 is somewhat close to the solution where α_{SD} bisects the shear angle θ , i.e., $\alpha_{SD} = \theta/2$. As the ρ_2/ρ_1 ratio approaches one,

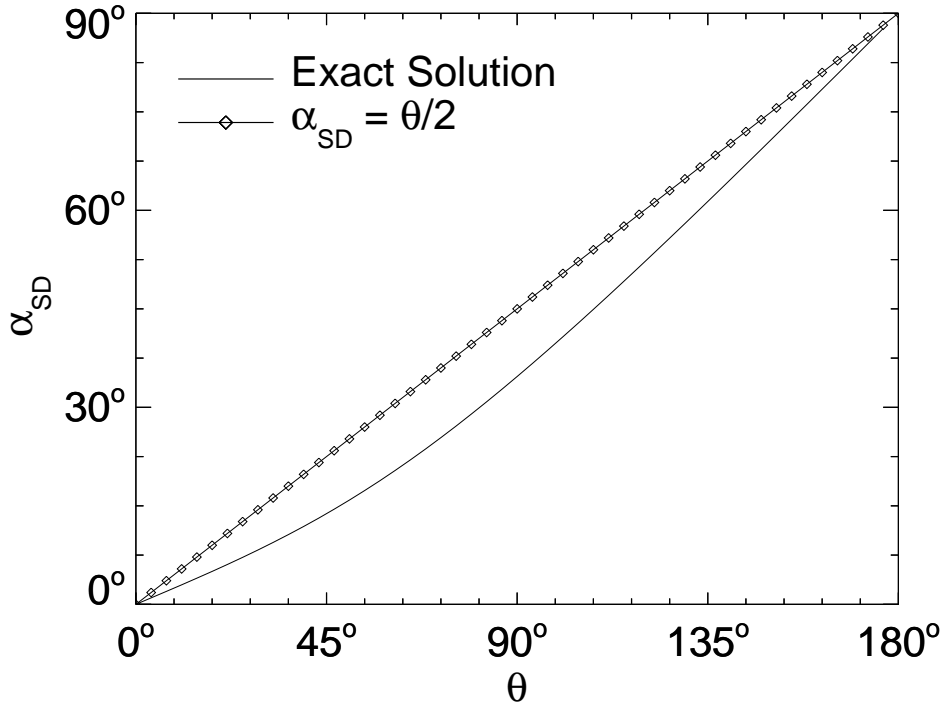


Figure 4.11 - Plot of α_{SD} versus the shear angle θ for the case $B_2/B_1 = 0.5$ and $\rho_2/\rho_1 = 10$ (exact solution). The solution where α_{SD} bisects the shear angle is shown for reference.

the two curves in Figure 4.11 lay practically on top of each other.

Figure 4.11 also shows that reconnection will occur ($\alpha_{SD} \neq 0$) in the model whenever the reconnecting magnetic fields are not exactly parallel, i.e., whenever θ is not strictly zero.

Another characteristic of equation 4.17 is that for $\theta = \pi$, the value of α_{SD} that maximizes V_{out} is $\alpha_{SD} = \theta/2 = \pi/2$, regardless of both ρ_2/ρ_1 and B_2/B_1 values. That is the case shown in panel b) of Figure 4.9, but again such α_{SD} value is only locally valid. In the case of Figure 4.9, only a small section of the dayside magnetopause is shown, which in turn allows considering it locally as a plane. Furthermore, as mentioned above, it was assumed that magnetic fields and plasma parameters on both sides of the magnetopause were spatially constant, which would result in the same α_{SD} along the whole (yet small) analyzed magnetopause section.

4.3.2 Model implementation

The Swisdak and Drake (2007)'s X-line location along the dayside magnetopause will be identified as a set of points where the reconnection outflow speed, V_{out} , as given by equation 4.16, is a local maximum. It is noted that finding maximum V_{out} requires information of not only the local magnetic field strengths and directions on both sides of the magnetopause, which could be accomplished with analytical models available in the literature, but also the plasma mass densities on both sides. Thus, a self-consistent numerical model is required to demonstrate the Swisdak and Drake (2007)'s X-line model.

4.3.2.1 The BATS-R-US model

The global 3-D MHD Solar Wind Modeling Framework (SWMF)/BATS-R-US (Block-Adaptive-Tree-Solar wind-Roe-Upwind-Scheme) code (TÓTH et al., 2005, and references therein) developed at the University of Michigan was chosen to provide the plasma parameters needed in the V_{out} computation. The BATS-R-US code has been extensively and successfully used by the scientific community in studies of solar wind-magnetosphere-ionosphere interaction (KOMAR et al., 2013). Currently the BATS-R-US code allows us the use of a large set of MHD models, e.g., resistive, Hall, multi-species, among others. Since we are interested in the large scale solar wind-magnetosphere interaction the single-fluid ideal MHD equations used here already provide reliable results. The set of MHD equations is solved on a three-dimensional adaptive cartesian grid in which the cell size increases away from the Earth. For all 36 BATS-R-US simulation runs presented in this thesis work, the smallest cell size encompassing the dayside magnetopause region was $0.25 R_E$ ($1/4 R_E$) within a simulation box of dimensions: $-15 \leq X \leq 15 R_E$, $-15 \leq Y \leq 15 R_E$ and $-15 \leq Z \leq 15 R_E$. Figure 4.12 shows an example of a section of the simulation grid adopted in all BATS-R-US runs used in this study. The box surrounding the Earth (at $X = Z = 0 R_E$) with the aforementioned dimensions has an $1/4 R_E$ grid resolution. Inside such a box there is a region of $5.25 R_E$ radius surrounding the Earth (at $X = Z = 0 R_E$) where the grid resolution is $1/8 R_E$, but this grid resolution is used at the inner boundary of the model from where ionospheric models start to be solved. Away from that box, the cell size increases in factors of two. The largest cell size shown is $4 R_E$ ($Z \leq -32$ and $Z \geq 32 R_E$).

Four out of 36 BATS-R-US runs used here and presented latter on in this thesis in Section 6.1, were obtained by running the BATS-R-US code on the Geomagnetism Research Group (GEOMA's) cluster, here at the National Institute for Space Re-

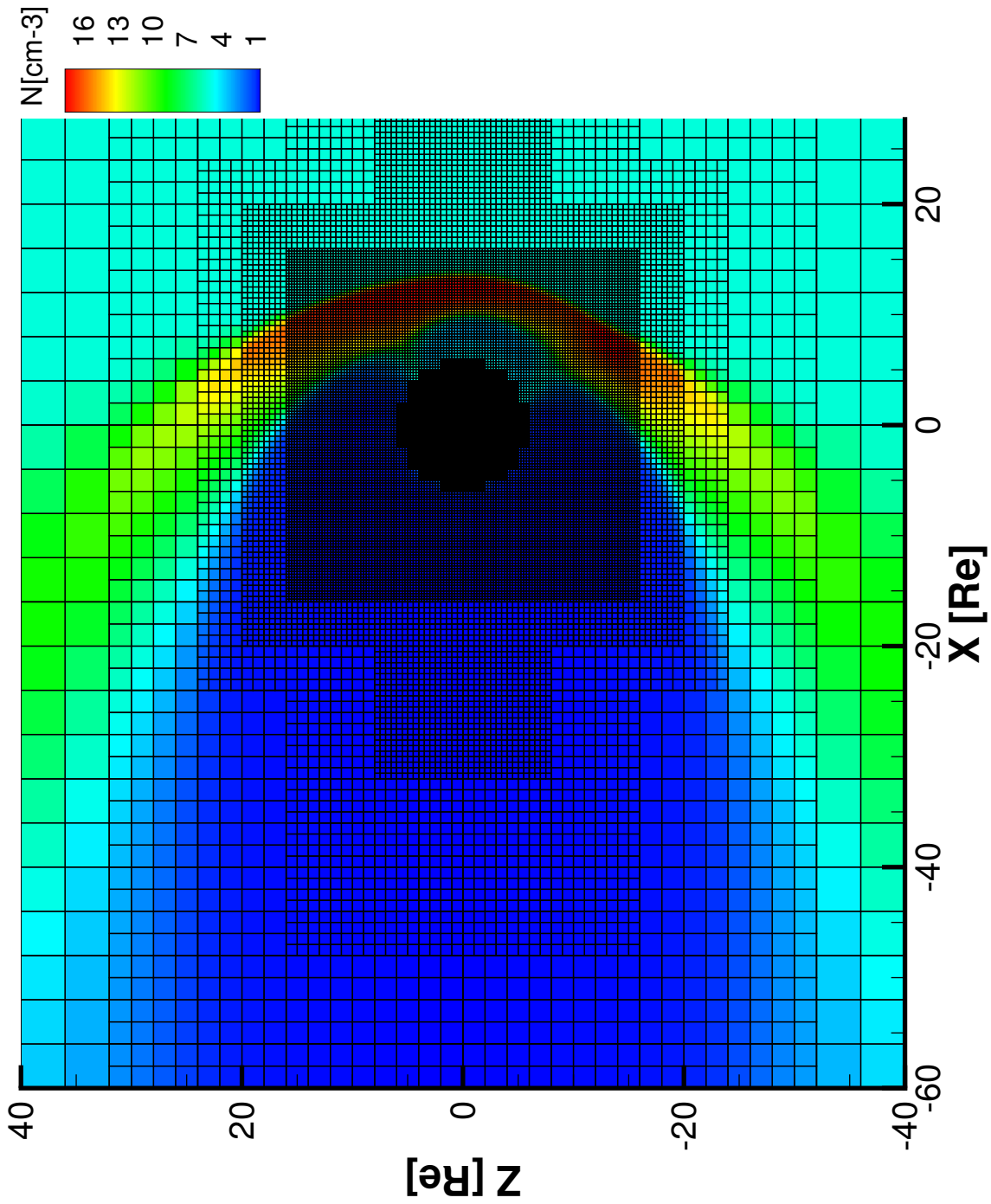


Figure 4.12 - Section of the simulation grid adopted in all (36) BATS-R-US runs used in this thesis work. The plane shown is the noon-midnight meridian ($Y=0$). The box surrounding the Earth (at $X = Z = 0 R_E$) has dimensions of $-15 \leq X \leq 15 R_E$, $-15 \leq Y \leq 15 R_E$ and $-15 \leq Z \leq 15 R_E$, with a cell resolution of $1/4 = 0.25 R_E$. Away from that box, the cell size increases in factors of two. The largest cell size shown is $4 R_E$ ($Z \leq -32$ and $Z \geq 32, R_E$). The $5.25 R_E$ radius black circle surrounding the Earth corresponds to the inner boundary of the model from where ionospheric models start to be solved. The colored contour plot corresponds to the modeled ion plasma density on the $Y = 0$ plane shown.

search (INPE). In particular, the simulation result shown in Figure 4.12 was generated here at INPE. A recent Ph.D thesis work has been done using such infrastructure, and more details regarding technical information of the GEOMA’s cluster and also on solar wind-magnetosphere global interaction using the BATS-R-US code can be found in Jauer (2014).

The majority (32) of all 36 BATS-R-US runs used here were obtained by using the resources of the Community Coordinated Modeling Center (CCMC)⁴ located at NASA/Goddard Space Flight Center, Maryland, USA. The CCMC hosts a number of space science numerical models concerned with physical phenomena initiating at the solar atmosphere (solar models), traveling through the interplanetary media (heliosphere models), and interacting with both the magnetosphere (magnetosphere models) and the ionosphere-thermosphere system (ionosphere-thermosphere models). The user can request, via the world wide web, up to 8 runs per day of any model available. The model outputs can be visualized online at CCMC’s website: <http://ccmc.gsfc.nasa.gov/index.php>, or the user can also download them in a standardized (Common Data Format⁵, CDF) format.

In order to generate the BATS-R-US output file, the same boundary conditions are provided at each integration step. The code is run until a steady-state is achieved, which is typically reached with 3000 integration steps (TÓTH et al., 2011). Then, the last output file is taken for further analysis. The parameters given as input to our simulations, and in fact used for any BATS-R-US run, were: the IMF components, B_x , B_y , and B_z [nT], the solar wind flow velocity, V_x , V_y , and V_z [km/s], the solar wind density, n [cm⁻³], and finally the ion plasma temperature, T [K].

In order to properly handle with the downloaded BATS-R-US output files, an interpolator library belonging to a software suite developed by the CCMC staff was used: the Kameleon Software⁶. Kameleon is a software suite which allows “heterogeneous model outputs to be stored uniformly in a common science data format”. To date, Kameleon supports 5 models, including BATS-R-US. The Kameleon Interpolator library contains a series of both FORTRAN 77 and C source codes which, among other functionalities, can take as input one or more of the model output variables⁷,

⁴<http://ccmc.gsfc.nasa.gov/index.php>

⁵<http://cdf.gsfc.nasa.gov/>

⁶<http://ccmc.gsfc.nasa.gov/downloads/kameleon.php>

⁷BATS-R-US output variables are: current density vector components J_x , J_y , and J_z [$\mu\text{A}/\text{m}^2$], magnetic field vector components B_x , B_y , and B_z [nT], velocity field vector components V_x , V_y , and V_z [km/s], thermal pressure P [nPa], the ion number density n [cm⁻³], and finally the magnetohydrodynamical energy $E_{mhd} = P/(\gamma - 1) + \rho V^2/2 + B^2/2\mu_o$ [Joules], where γ , ρ and μ_o are the

and the $(x, y, z) R_E$ position where the model output variable should be evaluated. As output, the user gets the value of the model output variable, e.g., all magnetic field components B_x , B_y , and B_z , evaluated at the (x, y, z) input location provided by the user. With such a tool, the user can obtain the value of a given model output variable at any point within the simulation domain.

After introducing the tool we have used to obtain the magnetic fields and plasma parameters everywhere within the simulation box, the next step to obtain the reconnection outflow speed over the dayside magnetopause is to determine the modeled magnetopause location, which is discussed in the next subsection.

4.3.2.2 Defining the BATS-R-US dayside magnetopause location

The modeled dayside magnetopause is identified here as the loci where the current density magnitude, $|\mathbf{J}|$, is a maximum. Since the magnetopause is defined as a current sheet, the maximum current density magnitude criterion adopted here seems a natural way of determining its location.

In order to find such maxima current density values, radial profiles of $|\mathbf{J}|$ are computed, and the location of the first maximum along each one of these radial profiles is considered as the magnetopause location. Thus, spherical coordinates (r_s, θ_s, ϕ_s) are used. The “dayside” sector, which is considered to lie in the region defined by $0 \leq \theta_s \leq 180^\circ$ and $-90 \leq \phi_s \leq 90^\circ$, is discretized, on both θ_s and ϕ_s directions, in 100 bins of 1.8° width each, i.e., $\Delta\theta_s = \Delta\phi_s = 180^\circ/100 = 1.8^\circ$.

The relation between the spherical and cartesian GSM coordinates are the following:

$$x_{GSM} = r_s \sin(\theta_s) \cos(\phi_s), \quad (4.18)$$

$$y_{GSM} = r_s \sin(\theta_s) \sin(\phi_s), \quad (4.19)$$

$$z_{GSM} = r_s \cos(\theta_s). \quad (4.20)$$

Through the definitions shown in equations 4.18–4.20, the azimuthal ϕ_s angle is zero degrees at the Earth-Sun line (x_{GSM} axis), and equal to $\pm 90^\circ$ at the dusk and dawn terminators, respectively. Likewise, the polar θ_s angle is zero degrees and 180° at the $\pm z_{GSM}$ axes, respectively, and 90° at the equator plane.

By fixing both θ_s and ϕ_s , we allow r_s to vary from $8 R_E$ up to $25 R_E$ in equally

adiabatic specific heats ratio (considered to be equal to 5/3), the plasma mass density ($= m_{ion}n$) and the magnetic permeability of the free space.

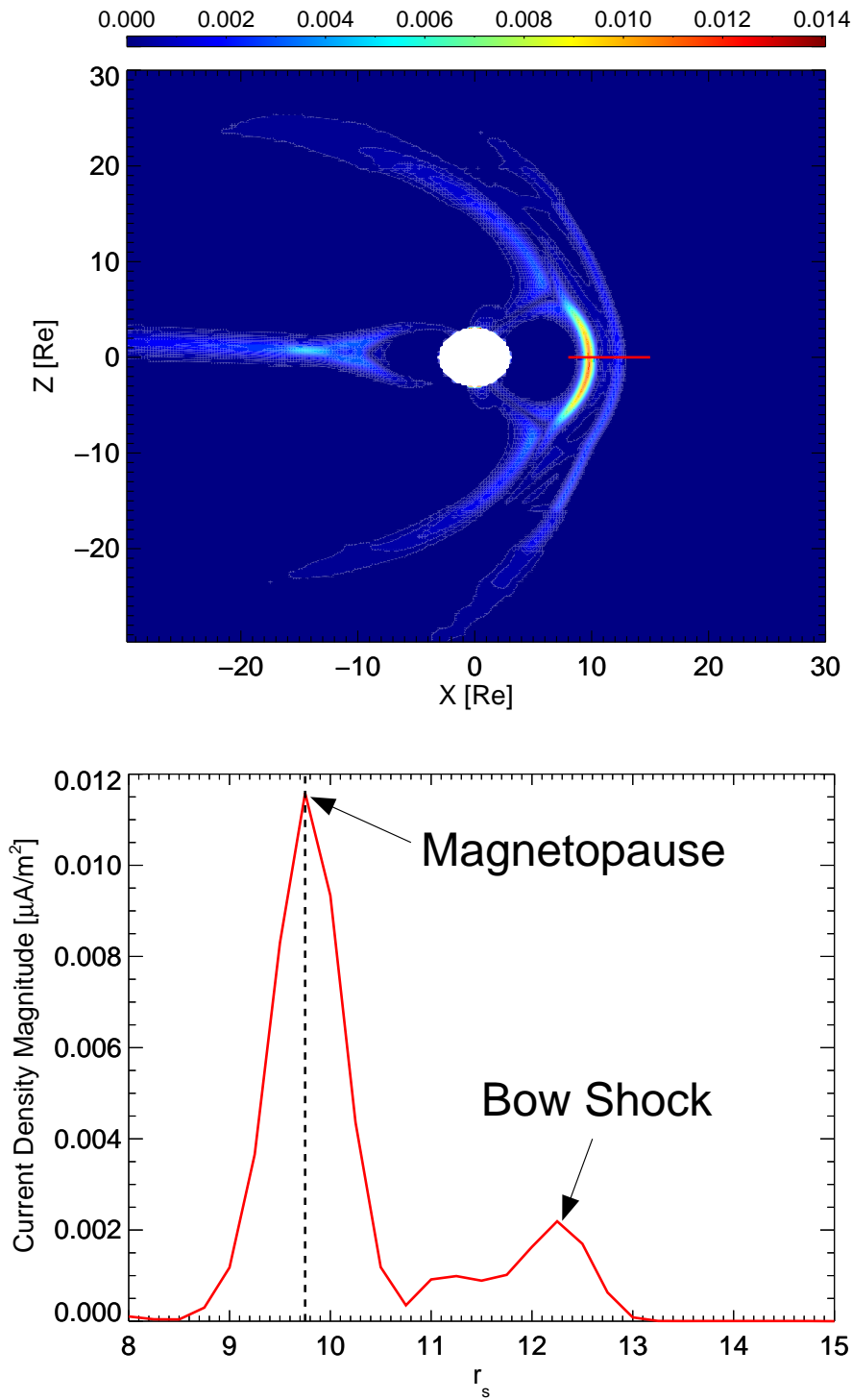


Figure 4.13 - **(Top)** Plot of current density magnitude, $|\mathbf{J}|$ [$\mu\text{A}/\text{m}^2$], on the noon-midnight meridian ($Y = 0$) plane modeled by the BATS-R-US code. The white circle in the center of the figure represents the inner boundary of the model from where ionospheric models start to be solved. **(Bottom)** $|\mathbf{J}|$ profile along the red line shown on the top panel. The first current density maximum ($r_s = 9.75 R_E, \theta_s = 90^\circ, \phi_s = 0^\circ$) is identified as the magnetopause current sheet, while the second one as the bow shock.

spaced steps of $1/4 R_E$ in order to obtain a given radial profile of the current density magnitude, $|\mathbf{J}|$. An example is shown in the bottom panel of Figure 4.13. Such a profile was taken along the Earth-Sun line, i.e., $\theta_s = 90^\circ$ and $\phi_s = 0^\circ$, as shown by the thick red line in the top panel of Figure 4.13, which in turn shows the modeled current density magnitude, $|\mathbf{J}|$ [$\mu\text{A}/\text{m}^2$], on the noon-midnight meridian ($Y = 0$). The first peak, which occurs at $r_s = 9.75 R_E$, is identified as the magnetopause location, according to the definition adopted here. The second peak $r_s \sim 12.3 R_E$ corresponds to the bow shock location. Moreover, such structures are readily discernible in the top panel of Figure 4.13, with the magnetopause being earthward of the bow shock, as it should be. Once the maximum current density magnitude at the magnetopause is identified, equations 4.18–4.20 are used to determine the $(x, y, z)_{GSM}$ location of the magnetopause. For the example at hand, the spherical coordinates $r_s = 9.75 R_E$, $\theta_s = 90^\circ$ and $\phi_s = 0^\circ$ would result in $(x, y, z) = (9.75, 0, 0) R_E$. The same process can be repeated for whatever values of the pair (θ_s, ϕ_s) pertaining to the intervals defined above, i.e., $0 \leq \theta_s \leq 180^\circ$ and $-90 \leq \phi_s \leq 90^\circ$.

After determining the local magnetopause location, one needs to obtain the magnetic fields, \mathbf{B}_1 and \mathbf{B}_2 , and the plasma mass densities, ρ_1 and ρ_2 , on both sides of the magnetopause. Thus one more step can be given on determining the local reconnection outflow speed V_{out} . In order to do that, the local magnetopause normal vector is found, and along that normal direction the magnetic field and plasma parameters are taken at a one Earth radius ($1 R_E$) distance from the local magnetopause position. The way the normal vector is found is discussed in the next subsection.

4.3.2.3 Normal vector to the local magnetopause

For simplicity, we have considered that the local magnetopause normal direction, $\hat{\mathbf{n}}$, could be approximated by the local radial direction, $\hat{\mathbf{r}}_s$, as given by:

$$\hat{\mathbf{n}} \equiv \hat{\mathbf{r}}_s = (x_{mp}, y_{mp}, z_{mp}) / \sqrt{x_{mp}^2 + y_{mp}^2 + z_{mp}^2}, \quad (4.21)$$

where $(x_{mp}, y_{mp}, z_{mp}) [R_E]$ is a point in GSM coordinates pertaining to the magnetopause surface, as defined in the previous section. Besides the easiness in deriving the radial unitary vector, $\hat{\mathbf{r}}_s$ has been shown to be well-behaved near the cusp regions, i.e., its direction in those regions was near the expected outward normal direction. With the aim of checking the consistency of our choice for the normal vector direction, in Figure 4.14 the unitary radial vector directions, $\hat{\mathbf{r}}_s$ (white arrows),

are compared with two estimates for the local normal vector (red arrows) along the BATS-R-US magnetopause: 1) $\hat{\mathbf{n}}_{\mathbf{J} \times \mathbf{B}_{sh}} = (\mathbf{J} \times \mathbf{B}_{sh})/|\mathbf{J} \times \mathbf{B}_{sh}|$ (top row of Figure 4.14), and 2) $\hat{\mathbf{n}}_{\mathbf{J} \times \mathbf{B}_{sp}} = (\mathbf{J} \times \mathbf{B}_{sp})/|\mathbf{J} \times \mathbf{B}_{sp}|$ (bottom row of Figure 4.14), where the subscripts *sh* and *sp* refer to the magnetosheath and magnetosphere regions, respectively, adjacent to the magnetopause. The \mathbf{J} (magnetopause current density) vector is evaluated at $(x_{mp}, y_{mp}, z_{mp}) [R_E]$. The normal vector estimates and unitary radial vector directions are compared over the noon-midnight meridian ($y_{GSM} = 0$) plane (left column of Figure 4.14), and at the equator ($z_{GSM} = 0$) plane (right column of Figure 4.14). Both normal vector estimates (red arrows) satisfy the condition $\hat{\mathbf{n}} \cdot \hat{\mathbf{X}} > 0$ where $\hat{\mathbf{X}}$ is the x_{GSM} unitary vector. In other words, all of them have an imposed sunward component in order to point outward.

Looking at the left column of Figure 4.14, in particular the vicinity of the northern cusp ($Z \sim 7 R_E$), the normal vector estimate $\hat{\mathbf{n}}_{\mathbf{J} \times \mathbf{B}_{sp}}$ (bottom panel) do not show the expected normal vector direction at this location, which should have a northward ($+Z$) component. On the other hand, the $\hat{\mathbf{n}}_{\mathbf{J} \times \mathbf{B}_{sh}}$ estimate (top panel) seems to perform better in this region than the other, but the transition from poleward to equatorward of the cusp is not well-ordered as shown for the $\hat{\mathbf{r}}_s$ (white arrows) estimate. In the region between both northern and southern cusps, the unitary radial direction agrees reasonably well (within 30°) with both normal vector estimates $\hat{\mathbf{n}}_{\mathbf{J} \times \mathbf{B}_{sh}}$ and $\hat{\mathbf{n}}_{\mathbf{J} \times \mathbf{B}_{sp}}$, including the equator plane (right column in Figure 4.14), as well as other azimuthal planes (not shown) both above and below the equator plane.

Overall, using the radial vector as an approximation for the actual magnetopause normal vector seems a reasonable choice for the purposes sought here: determine the locations just inside and outside the dayside magnetopause where the plasma and magnetic field parameters are going to be evaluated. The $(x_i, y_i, z_i)_{GSM}$ location just inside ($i = sp$) and outside ($i = sh$) the dayside magnetopause is determined in the following way:

$$x_i = x_{mp} \pm D_{mp}(\hat{\mathbf{r}}_s \cdot \hat{\mathbf{X}}), \quad (4.22)$$

$$y_i = y_{mp} \pm D_{mp}(\hat{\mathbf{r}}_s \cdot \hat{\mathbf{Y}}), \quad (4.23)$$

$$z_i = z_{mp} \pm D_{mp}(\hat{\mathbf{r}}_s \cdot \hat{\mathbf{Z}}), \quad (4.24)$$

where the ‘+’ and ‘−’ signs in equations 4.22–4.24 are used for determining the (x_i, y_i, z_i) location just outside (magnetosheath, $i = sh$), and inside (magnetosphere, $i = sp$) the magnetopause, respectively. Notice that equations 4.22–4.24 depend

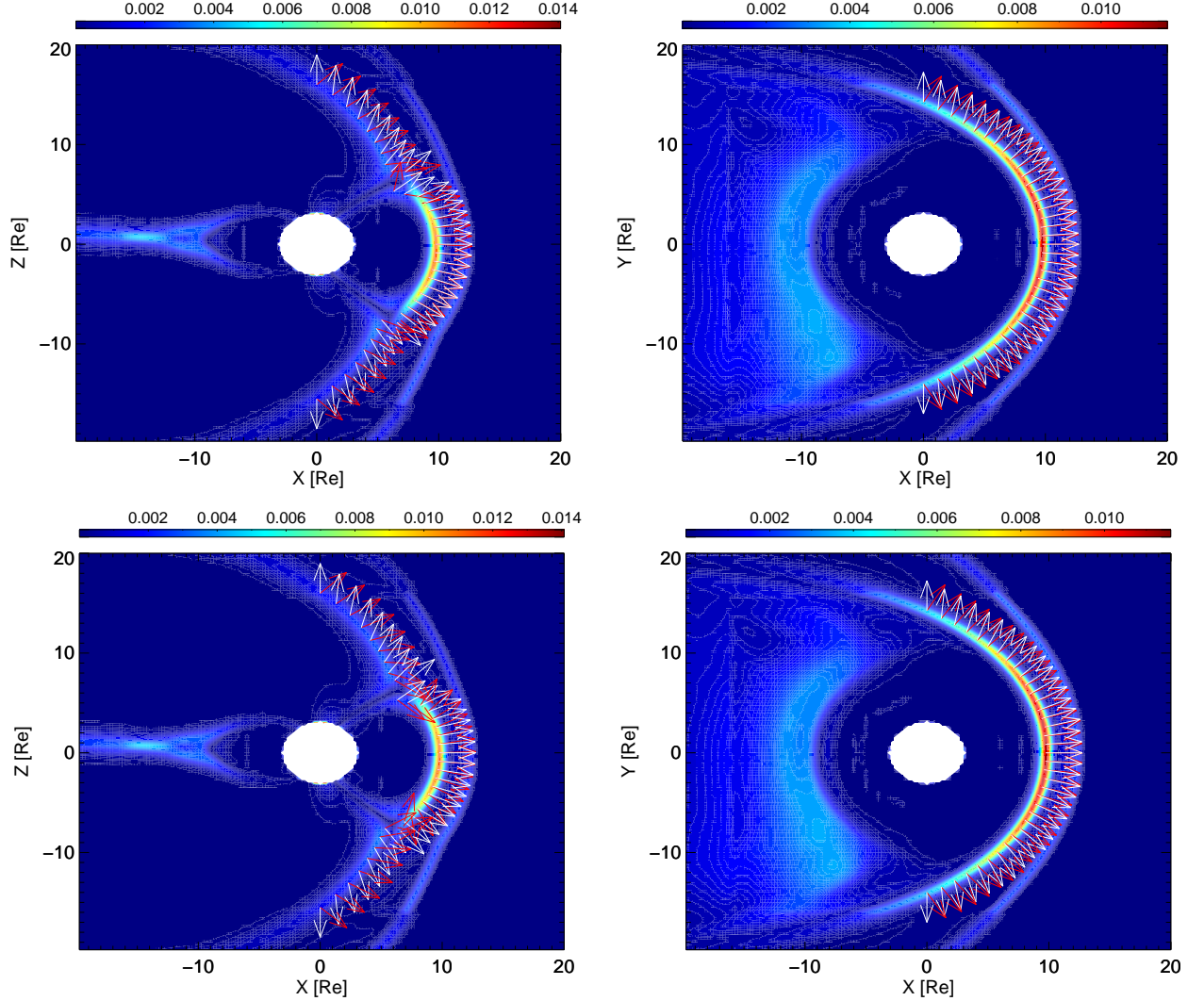


Figure 4.14 - Current density magnitude, $|\mathbf{J}|$ [$\mu\text{A}/\text{m}^2$], modeled by the BATS-R-US code and visualized on the $y_{GSM} = 0$ plane (left column) and the $z_{GSM} = 0$ plane (right column). The white arrows show the directions of the unitary radial vector $\hat{\mathbf{r}}_s$ at the local magnetopause, while the red arrows represent the direction of both normal vector estimates $\hat{\mathbf{n}}_{\mathbf{J} \times \mathbf{B}_{sh}} = (\mathbf{J} \times \mathbf{B}_{sh})/|\mathbf{J} \times \mathbf{B}_{sh}|$ (top row panels), and $\hat{\mathbf{n}}_{\mathbf{J} \times \mathbf{B}_{sp}} = (\mathbf{J} \times \mathbf{B}_{sp})/|\mathbf{J} \times \mathbf{B}_{sp}|$ (bottom row panels), where the subscripts sh and sp stand for the magnetosheath and magnetospheric regions, respectively. The \mathbf{J} (magnetopause current density) vector is evaluated at (x_{mp}, y_{mp}, z_{mp}) [R_E] according to equation 4.21 (see text for details).

on the parameter D_{mp} [R_E], which will correspond to the distance from the local magnetopause, along the normal ($\hat{\mathbf{r}}_s$) direction, to the point (x_i, y_i, z_i) . In order to ensure that (x_i, y_i, z_i) will be taken at the proper regions, i.e., $(x_{sh(sp)}, y_{sh(sp)}, z_{sh(sp)})$ sunward (earthward) of and adjacent to the magnetopause, D_{mp} was set to $1 R_E$.

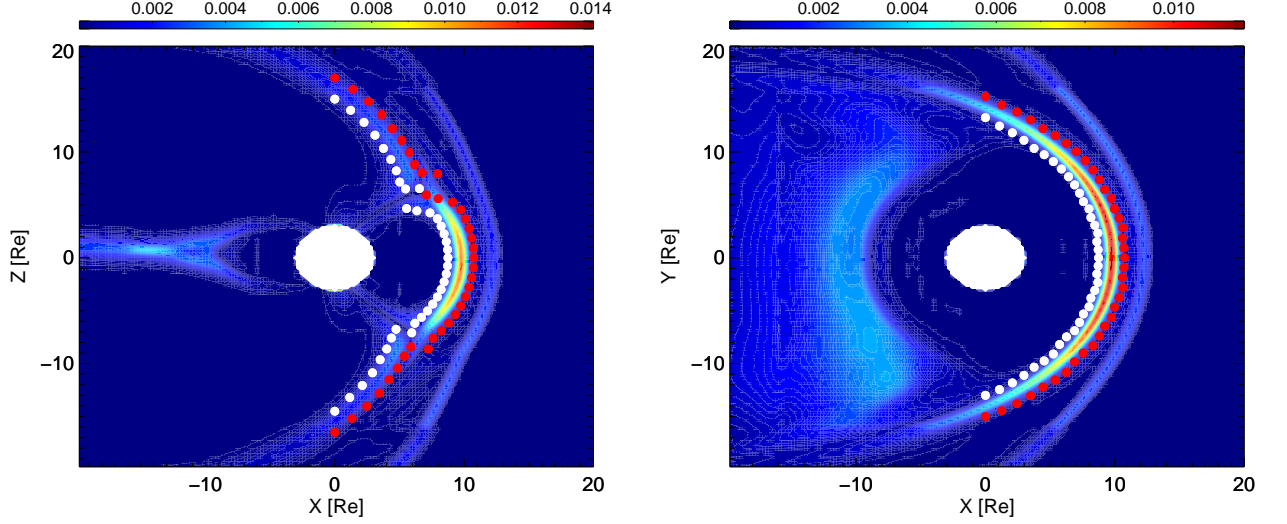


Figure 4.15 - Current density magnitude, $|\mathbf{J}|$ [$\mu\text{A}/\text{m}^2$], modeled by the BATS-R-US code and visualized on the $y_{GSM} = 0$ (left panel) and $z_{GSM} = 0$ (right panel) planes. The filled white (red) circles correspond to locations at $1 R_E$ radial distance earthward (sunward) of the local dayside magnetopause. These locations were calculated via equations 4.22–4.24 (see text for details).

The filled red (white) circles in Figure 4.15 show the $(x_{sh(sp)}, y_{sh(sp)}, z_{sh(sp)})$ [R_E] points on the $y_{GSM} = 0$ plane (left panel) and $z_{GSM} = 0$ plane (right panel) for the same BATS-R-US run presented in Figures 4.13 and 4.14. Such points were determined from equations 4.22–4.24 with $D_{mp} = 1 R_E$. As it can be seen, using $\hat{\mathbf{r}}_s$ as the local magnetopause normal vector and $D_{mp} = 1 R_E$, the locations where both plasma and magnetic field parameters are going to be taken are well defined: the magnetosheath (magnetospheric) magnetic field \mathbf{B}_2 (\mathbf{B}_1) and mass density ρ_2 (ρ_1) being taken at the red (white) circles location.

4.3.2.4 Obtaining the maximum reconnection outflow speed V_{out}

Once we know how to determine the magnetic field and plasma parameters just inside and outside the modeled BATS-R-US dayside magnetopause, we can proceed in finding the α_{SD} angle for which the reconnection outflow speed, V_{out} , is maximized.

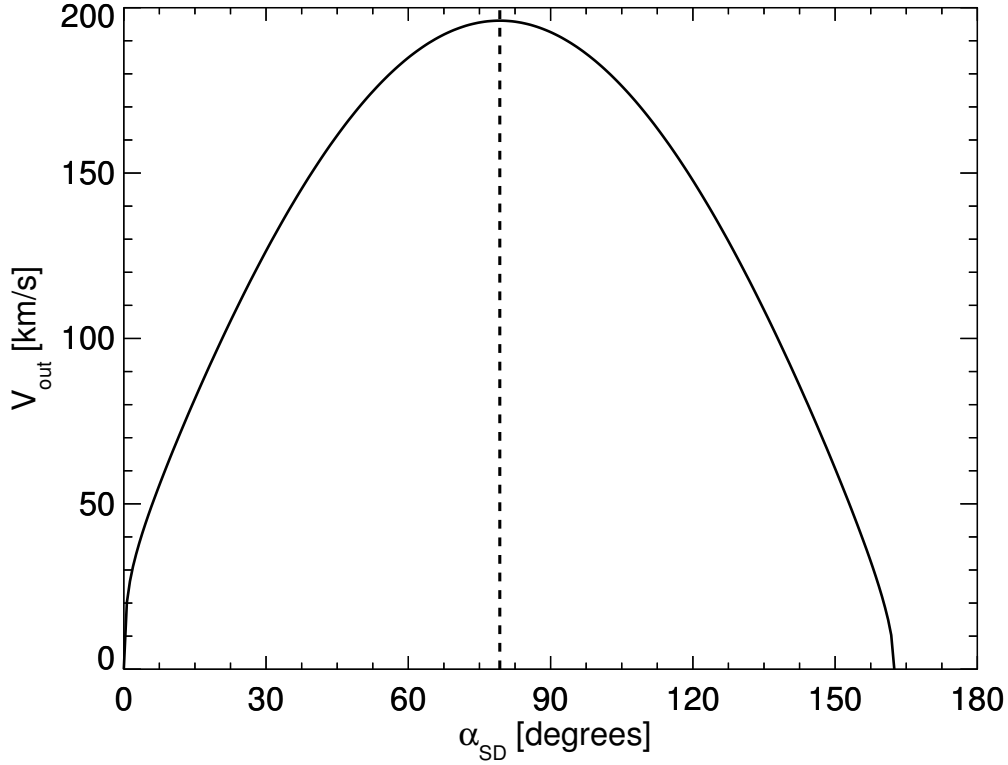


Figure 4.16 - Plot of the reconnection outflow speed, V_{out} , versus the angle α_{SD} that orients the reconnection X-line relative to the reconnecting magnetic fields. The magnetic fields and plasma parameters used as input to V_{out} are shown in the text. The maximum in V_{out} , i.e., 196.07 [km/s], occurs for $\alpha_{SD} = 79.29^\circ$.

Firstly, consider the same BATS-R-US output shown in previous sections. It was shown in Section 4.3.2.2 that the magnetopause location along the Earth-Sun line was $(x_{mp}, y_{mp}, z_{mp}) = (9.75, 0, 0)[R_E]$ GSM. Secondly, let's use this particular point, as an example, to calculate the maximum V_{out} value. Thus, the magnetosheath magnetic field \mathbf{B}_2 , and ion number density n_2 [cm^{-3}] ($\rho_2 = m_{ion}n_2$) will then be evaluated at the point $(x_{sh}, y_{sh}, z_{sh}) = (10.75, 0, 0)[R_E]$ GSM, as determined by equations 4.22–4.24. Likewise, the magnetospheric parameters will be evaluated at $(x_{sp}, y_{sp}, z_{sp}) = (8.75, 0, 0)[R_E]$ GSM. For this example, the parameter values obtained at (x_{sh}, y_{sh}, z_{sh}) and (x_{sp}, y_{sp}, z_{sp}) are: $\mathbf{B}_1 = (-2.48, 2.30, 61.34)$ [nT], $\mathbf{B}_2 = (-1.86, 6.56, -25.90)$ [nT], $n_1 = 4.79$ [cm^{-3}], and $n_2 = 24.42$ [cm^{-3}]. The shear angle $\theta = \cos^{-1}[(\mathbf{B}_1 \cdot \mathbf{B}_2)/(|\mathbf{B}_1||\mathbf{B}_2|)]$ can be calculated and it is $\theta = 162.48^\circ$. Looking at equation 4.16, notice that in order to determine V_{out} the only parameter still unknown is α_{SD} . As Swisdak and Drake (2007) suggest, α_{SD} will be such that it maximizes V_{out} , thus if we plot V_{out} as a function of α_{SD} ($0 \leq \alpha_{SD} \leq \theta$), using the magnetic field and plasma parameters derived above, the graphic shown in Figure

4.16 is obtained. Notice that $\alpha_{SD} = 79.29^\circ$ is the angle that maximizes V_{out} . In particular, the maximum reconnection outflow speed obtained in Figure 4.16 was 196.07 [km/s].

Recall that all these steps for the determination of V_{out} were applied only at the subsolar point, i.e., $\theta_s = 90^\circ$ and $\phi_s = 0^\circ$. For another (θ_s, ϕ_s) pair, the whole procedure is repeated, and it is summarized as follows:

- 1) For a given (θ_s, ϕ_s) pair, determine the respective magnetopause location triad $(x_{mp}, y_{mp}, z_{mp}) [R_E]$ using the procedure described in Section 4.3.2.2.
- 2) Obtain the local magnetopause normal as given by equation 4.21.
- 3) Derive the (x, y, z) locations just inside and outside the magnetopause according to equations 4.22–4.24.
- 4) Evaluate the relevant magnetic field (\mathbf{B}_1 and \mathbf{B}_2) and plasma parameters (ρ_1 and ρ_2) at the (x, y, z) locations provided in the previous step.
- 5) Plot V_{out} (equation 4.16) versus α_{SD} , with $0 \leq \alpha_{SD} \leq \theta$, find the maximum V_{out} ($\partial V_{out} / \partial \alpha_{SD} = 0$), and store this value.
- 6) Repeat steps 1 through 5 for all remaining (θ_s, ϕ_s) pairs.

4.3.2.5 Determining the X-line location over the dayside magnetopause

After finding all V_{out} values for the whole discretized magnetopause, which means a matrix with dimensions of 100×100 ⁸, a “ V_{out} map” is generated. Such a map is presented in Figure 4.17, which shows a view from the Sun of the V_{out} [km/s] values over the BATS-R-US dayside magnetopause for the same reconnection event that has been used in previous subsections, and that it is going to be described in details latter on in Section 6.1.

In Figure 4.17, the dayside magnetopause was projected onto the yz_{GSM} plane. The largest (> 150 km/s) V_{out} values occur over the entire azimuthal extension of the dayside magnetopause, and are confined in the polar (z_{GSM}) direction between $-7 \lesssim z_{GSM} \lesssim 7 R_E$. The extent, however, of such a region of largest V_{out} values will heavily depend on the IMF conditions, as will be shown latter on in Section 6.1

⁸The matrix dimensions are related with the chosen number of both θ_s and ϕ_s bins. It was determined here that such a number would be 100, and it would be the same for both variables.

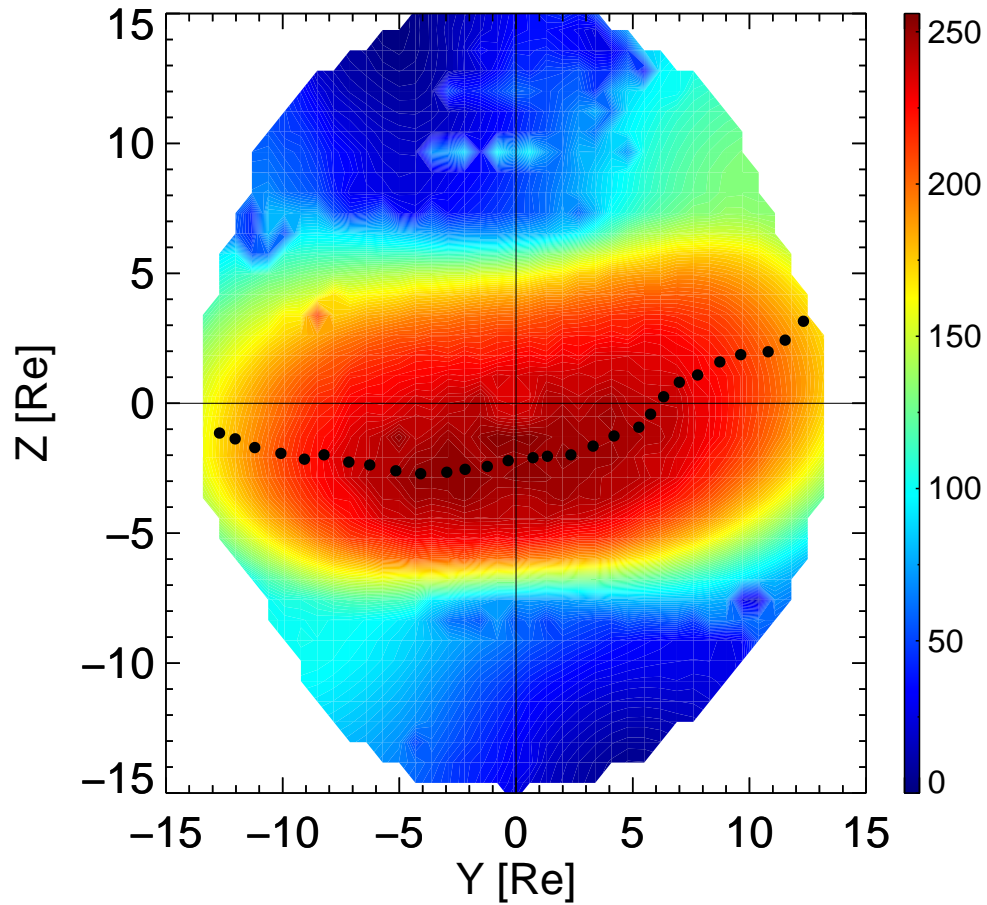


Figure 4.17 - View from the Sun of the reconnection outflow speed values V_{out} [km/s] over the BATS-R-US dayside magnetopause of one of the magnetic reconnection events used in this work. The black filled circles compose the Swisdak and Drake (2007)'s X-line and were determined by Lindeberg (1998)'s ridge-detection method (see text for details). The white region corresponds to the post-terminator ($x_{GSM} < 0 R_E$) region.

where reconnection X-line models are tested against quasi-simultaneous observations of magnetic reconnection at the dayside magnetopause.

We will consider here that the X-line should be located over the dayside magnetopause where V_{out} is a local maximum. Thus, just by looking at Figure 4.17, one would infer that the X-line should be located somewhere within the reddish region. In order to precisely determine the set of points over the dayside magnetopause surface where V_{out} is a local maximum, a method developed by Lindeberg (1998) for finding such (ridge) points in a 2-D image has been used. We can apply this method to our cases and determine the X-line location as a set of points where some parameter is a local maximum (cf. Appendix A). In the case of the present model being discussed, such a parameter will be the reconnection outflow speed V_{out} . In Figure 4.17 the Swisdak and Drake (2007)'s X-line, as determined by Lindeberg (1998)'s ridge-detection method, is shown as black filled circles. Notice that the X-line does not necessarily pass through the subsolar point ($y_{GSM} = z_{GSM} = 0 R_E$), but instead where the reconnection outflow speed is a local maximum.

5 INSTRUMENTATION AND COORDINATE SYSTEM

In this chapter we describe the spacecraft orbits and instruments used in the preparation of this thesis.

5.1 THEMIS mission

We start out with NASA's *Time History of Events and Macroscale Interactions during Substorms* (THEMIS) mission¹, which was launched on February 17, 2007. The THEMIS mission consists of five identical micro-satellites (THEMIS A, B, C, D and E) equipped with five instruments each, measuring ions and electrons from ~ 5 eV to ~ 1 MeV and electromagnetic waves from DC to > 4 KHz (ANGELOPOULOS, 2008).

The orbits are highly elliptical and near equatorial. The apogee rotates slowly around the Earth to cover the dayside, dawnside, nightside, and duskside of the magnetosphere². Right after launch, the 5 THEMIS were lined up in the same orbit. Since 2011, THEMIS B and C went to orbit the moon and became ARTEMIS (*Acceleration Reconnection Turbulence & Electrodynamics of Moon's Interaction with the Sun*³). The 3 remaining spacecraft (THEMIS A, D and E) are still orbiting the Earth.

The instruments aboard the THEMIS spacecraft used in this thesis were the *Flux Gate Magnetometer* (FGM) (AUSTER et al., 2008) which provided measures of the magnetic field vector, and the *Electro-Static Analyzer* (ESA) (MCFADDEN et al., 2008) for plasma moments.

The FGM instrument is capable of detecting variations of the magnetic field with amplitudes of 0.01 nT. The magnetometer is designed to cover measurements in different regions of the near-Earth environment: solar wind, magnetosheath, magnetotail, outer magnetosphere, and up to the region dominated by the Earth's dipole field (AUSTER et al., 2008). The FGM can provide magnetic field vector samples up to a rate of 128 samples per second. We use in this work, however, the spin-averaged (1 sample at each 3 seconds, i.e, ~ 0.33 Hz) or the 4 Hz time resolution data.

The ESA instrument was designed to measure the ion and electron distribution functions over the energy range from a few eV up to 30 keV for electrons and 25 keV

¹<http://themis.ssl.berkeley.edu/index.shtml>

²<http://themis.ssl.berkeley.edu/orbits.shtml>

³<http://artemis.ssl.berkeley.edu/>

for ions. In this thesis work we use the plasma moments provided at each spacecraft spin (3 s): ion bulk flow velocity vector [km/s], ion and electron densities [cm^{-3}], and ion and electron temperatures [eV] parallel and perpendicular to the magnetic field. We also make use of 1-spin-resolution ion omni-directional spectra which is an energy-time spectrogram plot with the ion energy range ($\sim 7 - 25000$ eV) divided logarithmically into 32 energy channels. Ion pitch angle distributions are used as well, where the polar angle range ($0^\circ - 180^\circ$) is linearly divided into 16 bins which can achieve up to a 5.625° width.

5.2 CLUSTER mission

The European Space Agency’s Cluster mission⁴ is composed of four identical satellites (Clusters 1, 2, 3 and 4) carrying eleven instruments each designed to study the Earth’s near-space environment. When crossing the dayside magnetopause the four satellites generally form a tetrahedron. The inter-spacecraft distances range from 600 km up to 20000 km (ESCOUBET et al., 2001).

The Cluster satellites were launched on 16 July and 9 August, 2000, with each launch carrying two Cluster spacecraft. Their orbits are elliptical and polar with an initial perigee of $4 R_E$ ($R_E = \text{Earth radius}$) and an apogee of $19.6 R_E$. The orbital period is 57 hours (FEAR, 2006).

Among the eleven instruments aboard each Cluster spacecraft, we used the following set: *Flux Gate Magnetometer* (FGM)(BALOGH et al., 2001), both analyzers of the *Cluster Ion Spectrometry* (CIS)(RÉME et al., 2001) I) CIS-CODIF (*Composition and Distribution Function analyzer*), and II) CIS-HIA (*Hot Ion Analyzer*); and finally the *Plasma Electron and Current Experiment* (PEACE) (JOHNSTONE et al., 1997).

We have used data from Clusters 3 and 4 only, since CIS data was unavailable in Cluster 2 and every so often Cluster 1’s CIS data was not available. The magnetic field data provided by the FGM instrument and used in this work has spin-resolution, i.e., ~ 0.25 Hz. The ion plasma moments (density [cm^{-3}], temperature [eV] parallel and perpendicular to the magnetic field, and bulk flow velocity [km/s]), along with ion omni-directional energy spectra and ion pitch angle distributions provided by the CIS-HIA at Cluster 3 and CIS-CODIF at Cluster 4, are also used in spin-resolution. Electron pitch angle distributions, with 15° polar angle resolution, provided by the PEACE instrument, which in turn measures electrons from a few eV to ~ 25 keV on both satellites, are used here in spin-resolution as well.

⁴<http://sci.esa.int/cluster/>

The CIS-CODIF analyzer measures the mass per charge composition of major magnetospheric ions (H^+ , He^+ , He^{++} , O^+), providing full, three-dimensional ion distributions from thermal energies to about 40 keV. The CIS-HIA analyzer, on the other hand, does not provide mass resolution, but has both a better polar angular and azimuthal resolutions as compared to CIS-CODIF.

5.3 DOUBLE STAR TC-1 mission

Double Star is a Sino-European collaborative mission with two satellites, TC-1 and TC-2. Double Star TC-1, whose data is used in this thesis work, was launched on December 29, 2003 into an elliptical equatorial orbit, while the second one on July 25, 2004 into an elongated polar orbit.

From the eight scientific instruments provided by ESA to the Double Star mission, seven were spares from the Cluster mission, thus identical to those shown in the previous section.

In this thesis work we use spin-resolution (~ 4 s) from: magnetic field data provided by the FGM instrument (CARR *et al.*, 2005), ion plasma moments (density [cm^{-3}], temperature [eV] parallel and perpendicular to the magnetic field, and bulk flow velocity [km/s]) provided by the CIS-HIA instrument (when available), and electron omni-directional energy flux spectra and electron pitch angle distributions given by the PEACE instrument (FAZAKERLEY *et al.*, 2005).

5.4 Coordinate systems

The Geocentric Solar Magnetospheric (GSM) coordinate system is used throughout this thesis work along with the boundary normal coordinate system LMN. In the former system, the \mathbf{x}_{GSM} direction coincides with the Sun-Earth line and its positive sense is toward the Sun. The \mathbf{y}_{GSM} direction is aligned perpendicular to the Earth's magnetic dipole, and its positive sense is toward the dusk region of the magnetosphere. The $\mathbf{z}_{GSM} = \mathbf{x}_{GSM} \times \mathbf{y}_{GSM}$ direction completes the right-handed set, and it points northward.

The LMN system is used to represent vector quantities such as magnetic field and plasma velocity in local magnetopause coordinates. N is the local outward normal vector, and here it is obtained via the Shue *et al.* (1998)'s magnetopause model (described below), unless otherwise stated. The M direction is obtained through the cross product between N and the \mathbf{z}_{GSM} direction, and it points toward the dawn region of the magnetosphere. The L direction points approximately due north and

completes the orthogonal set as $L = M \times N$. Figure 5.1 shows the configuration of both the GSM and the local LMN systems at the dayside magnetopause.

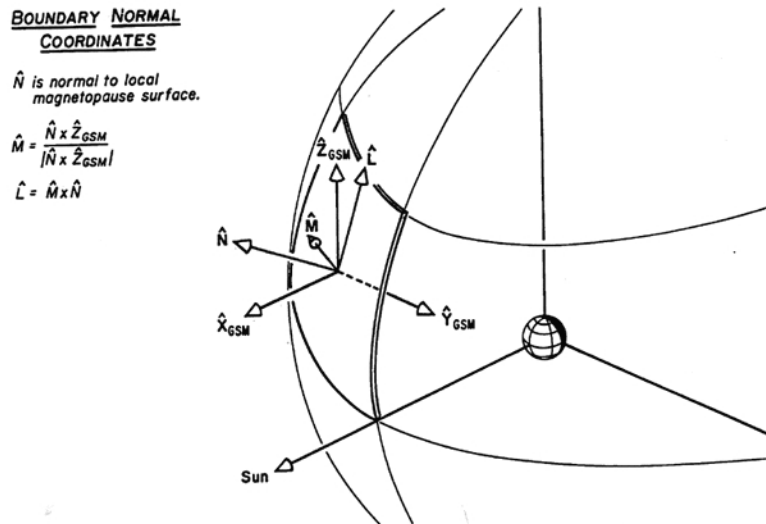


Figure 5.1 - Configuration of the GSM and local boundary normal coordinates (LMN) systems. The Earth is represented at the center.

SOURCE: After Russell and Elphic (1978).

The Shue et al. (1998) model is an empirical model which uses a large database of magnetopause crossings (> 800) to fit the size and shape of the magnetopause to an axis-symmetric paraboloid of revolution described by the following equation

$$r = R_{mp} \left(\frac{2}{1 + \cos \theta} \right)^{\alpha_{sh}} \quad (5.1)$$

where R_{mp} (equation 4.7) is the stand-off magnetopause distance from the Earth's center in units of Earth radii, and

$$\alpha_{sh} = (0.58 - 0.007B_z)[1 + 0.024 \ln(P_{dyn})], \quad (5.2)$$

is the level of tail flaring, which depends on both the IMF north-south component B_z [nT] and the solar wind dynamic pressure P_{dyn} [nPa], as does R_{mp} . In equation 5.1, r is the radial distance, from the Earth's center, of the model magnetopause

surface and θ is the angle formed by the r direction and the Sun-Earth line. In the model the x_{GSM} direction, i.e., the direction which coincides with the Sun-Earth line, corresponds to the revolution axis, and the following equations are valid

$$x_{GSM} = r \cos \theta, \quad (5.3)$$

$$\sqrt{y_{GSM}^2 + z_{GSM}^2} = r \sin \theta. \quad (5.4)$$

Since we have an analytical expression for the magnetopause surface, the outward normal vector, $\hat{\mathbf{n}}$, can be obtained everywhere along such a surface by the following expression

$$\hat{\mathbf{n}} = \frac{\nabla r}{|\nabla r|}. \quad (5.5)$$

6 X LINE MODEL COMPARISONS: PART I

In this chapter the analytical models which predict the orientation and location of the reconnection X-line at the Earth's dayside magnetopause are compared and tested against *in situ* observations of reconnection plasma jets. The main purpose is to determine among the models used here which model best agrees with observations. Two steps are then employed:

- I) analyze in the next section fortuitous quasi-simultaneous magnetopause crossings by two spacecraft with large ($> 5 R_E$) spatial separation while magnetic reconnection was active at both spacecraft locations. Such method has been used before (see e.g., Phan et al. (2006), Dunlop et al. (2011)) to estimate the X-line location relative to both spacecraft and also to argue for the extended operation of magnetic reconnection along the dayside magnetopause. Since the chances of finding such events are exceedingly small as pointed out by Phan et al. (2006) due to highly variable IMF conditions, the number of events used here (< 10) were not sufficient to perform a statistical analysis, which then brings us to the second step:
- II) use a large number (> 100) of single spacecraft magnetopause crossings during reconnection periods to determine, in a meaningful statistical sense, which of the analyzed models best fits observational data (Chapter 7).

6.1 Quasi-simultaneous magnetopause crossing events

Walén

Looking for observational evidence of extended dayside magnetopause reconnection is not an easy task. The ideal way would be to have a constellation of many spacecraft simultaneously covering the entire extension of the dayside magnetopause whose area accounts for more than 15 Earth radii squared! Unfortunately, this is not economically feasible, most likely unrealizable, and furthermore the spacecraft separation of up to 20000 km at current spacecraft constellations (e.g., CLUSTER) is still considered too local if one takes into account the large spatial scales involved. Therefore, considering the limited spacecraft spatial coverage, one of the best solutions to detect magnetic reconnection across the whole extension of Earth's dayside magnetopause is finding conjunctions whereby two or more spacecraft cross the dayside magnetopause nearly simultaneously during a period when reconnection is occurring. Such a period can be identified by the presence of reconnection-associated

plasma jets which in turn are characterized by a local acceleration of plasma particles relative to the ambient plasma, caused by the reconnection between magnetosheath and Earth's magnetic fields. These conjunctions, although rare, have been reported elsewhere (cf. Walsh et al. (2014)).

In spite of the fact that so few spacecraft cross the magnetopause quasi-simultaneously in these conjunctions, the assumption that reconnection may still be taking place in the region in between (or even beyond) the two (or more) measurements is not necessarily invalidated since there is observational evidence of continuous, quasi-steady, magnetopause reconnection (Phan et al. (2004)) under steady IMF conditions. Thus, if the analyzed conjunction occurs during a period of a relatively steady IMF, say 20 minutes, it is reasonable to state that the conditions required for reconnection to occur at both spacecraft locations may be satisfied at other regions as well, i.e., along the X-line.

An indirect way to unambiguously determine the extended operation of dayside magnetopause reconnection is to investigate the presence of ionospheric signatures of reconnection spanning many hours of magnetic local time (MLT), as reported by Pinnock et al. (2003). By using the SuperDARN radar network and a Defense Meteorological Satellite Program (DMSP) F13 satellite, PINNOCK et al. identified ionospheric evidences of subsolar dayside reconnection as *i*) enhanced ionospheric plasma convection and *ii*) an equatorward displacement of the polar cap boundary occurring over more than 7 hours of MLT. The polar cap boundary can be understood as the high-latitude ionospheric footprints of the magnetic field lines pertaining to the magnetopause. Thus, by determining the polar cap boundary location the implied X-line length can be obtained via field-line tracing. PINNOCK et al. have found that for this event which occurred during a 30 min period of a southward IMF B_Z component, the X-line length was $38 R_E$, which was in good agreement with *in situ* observational expectations reported by Phan et al. (2001) concerning the same event. It is noted that during the aforementioned period, a simultaneous conjunction of two satellites at the dawn flank magnetopause detected bi-directional reconnection jets (PHAN et al., 2000) which further confirmed the presence of dayside magnetic reconnection.

It should be noted, however, that during nearly simultaneous magnetopause crossing events it may be the case that radar data may not have their best scatter conditions. As a result, the expected ionospheric signatures in response to dayside magnetopause reconnection may not be detected. Furthermore, it may also happen that there is

insufficient radar spatial coverage at the dayside region when both spacecraft cross the magnetopause. Thus, conjunctions of both ground-based and multi spacecraft observations during periods of dayside magnetic reconnection as the one reported by PINNOCK *et al.* are not easily found.

Despite the difficulty for finding the quasi-simultaneous magnetopause crossing events, there is a crucial information which must be known in advance in order to facilitate the search for such events, i.e., the satellite orbits. If we take the THEMIS mission as an example, the satellites slowly rotate around the Earth to cover the dayside, dawnside, nightside, and duskside of the magnetosphere following near equatorial orbits. On the other hand, the dayside season of the CLUSTER mission has a different configuration: high inclination orbits which cross the magnetopause only at high latitudes near local noon (12:00 local time), and at lower latitudes along the flanks. Thus, it is of fundamental importance to know in which magnetospheric region the satellites will be in order to increase the chances for finding periods when the magnetopause is being quasi-simultaneously crossed by two or more satellites.

Next, the *in situ* plasma observations of four multi-spacecraft magnetopause crossing events are presented.

6.1.1 Spacecraft observations

The interplanetary magnetic field (IMF) and solar wind plasma conditions were probed via the OMNI¹ dataset whereby magnetic field and plasma data taken from some solar wind monitor, e.g. ACE (STONE *et al.*, 1998) and WIND (LEPPING *et al.*, 1995, and references therein) spacecraft, are propagated/time-shifted to the Earth's bow shock nose model of Farris and Russell (1994)². The representative solar wind's dynamic pressure and magnetic field vectors for the quasi-simultaneous magnetopause crossing events are given as 20 minutes time averages prior to the first magnetopause crossing by one spacecraft belonging to the analyzed spacecraft pair. The reason behind this procedure is that solar wind's magnetized plasma takes some time, usually less than 20 minutes, to propagate from the bow shock nose to the dayside magnetopause, thus both the 20 minutes average IMF fields and dynamic pressure values as given by the OMNI dataset at the instant of the magnetopause crossing can be taken as correct representative values if solar wind's plasma and magnetic field variations are steady enough. We use the data whose standard devia-

¹<http://omniweb.gsfc.nasa.gov/form/dx2.html>

²More details on the time shifting process used at OMNI data can be found in the following website: http://omniweb.gsfc.nasa.gov/html/sc_merge_data1.html

tion, σ_{sd} , of the 20 minutes time series of each of the IMF components and dynamic plasma pressure does not exceed 20% of their respective absolute mean values, i.e. $\sigma_{sd}^{B_i^{IMF}} / |\overline{B_i^{IMF}}|$ and $\sigma_{sd}^{P_{dyn}} / \overline{P_{dyn}} \leq 0.20$, where $i = x, y, z$. That is the case for the four quasi-simultaneous magnetopause crossing events shown below. At the beginning of each following subsection describing the quasi-simultaneous spacecraft observations, the mean IMF magnetic field components and mean dynamic pressure values along with their respective standard deviations are presented.

6.1.1.1 2007-03-05 crossing

The representative (mean) IMF fields and dynamic pressure values and their respective standard deviations for this crossing were: $B_x^{IMF} = -4.02 \pm 0.21$, $B_y^{IMF} = 1.26 \pm 0.13$, $B_z^{IMF} = -4.48 \pm 0.22$ nT, and $P_{dyn} = 2.05 \pm 0.35$ nPa.

The *in situ* plasma observations of Cluster 4 and Double Star TC1 spacecraft encompassing their respective magnetopause crossing intervals are shown in Figures 6.2 and 6.3. First, attention is focused on Cluster 4 observations then we move to Double Star's.

In general, the boundary normal coordinates LMN were determined, in this work, via Shue et al. (1998)'s magnetopause model (see Section 5.4 for model's description). For the present event the normal magnetic field component is expected to have small deviations from zero and also be small in comparison with other components, but it did not present such characteristics for neither Cluster 4 nor Double Star TC1 magnetopause crossings as it can be seen in Figure 6.1. On the left (right) side of Figure 6.1, Cluster 4 (Double Star TC1) magnetic field data components are presented in Geocentric Solar Magnetospheric (GSM³) coordinates (top panel), and boundary normal coordinates, LMN, generated via minimum variance analysis of the magnetic field (MVA)(Sonnerup; Cahill, 1967; Sonnerup; Scheible, 1998) (middle panel) and by using the Shue et al. (1998) magnetopause model (bottom panel). The normal magnetic field component (B_N , green line) obtained by the Shue et al. (1998) magnetopause model is off the zero level for both Cluster 4 and Double Star TC1 crossings. One way of measuring the deviation from the zero level is by taking the standard deviation of B_N for the whole interval shown. This was done for the MVA and the Shue et al. (1998) cases. For the Cluster 4 interval, the standard deviations of B_N were 4.15 (MVA) and 15.42 nT (Shue et al. (1998)), respectively. For the Double Star TC1 interval these values were 4.87 (MVA) and 14.65 nT (Shue et al.

³See Section 5.4 for a description of the coordinate systems used in this work.

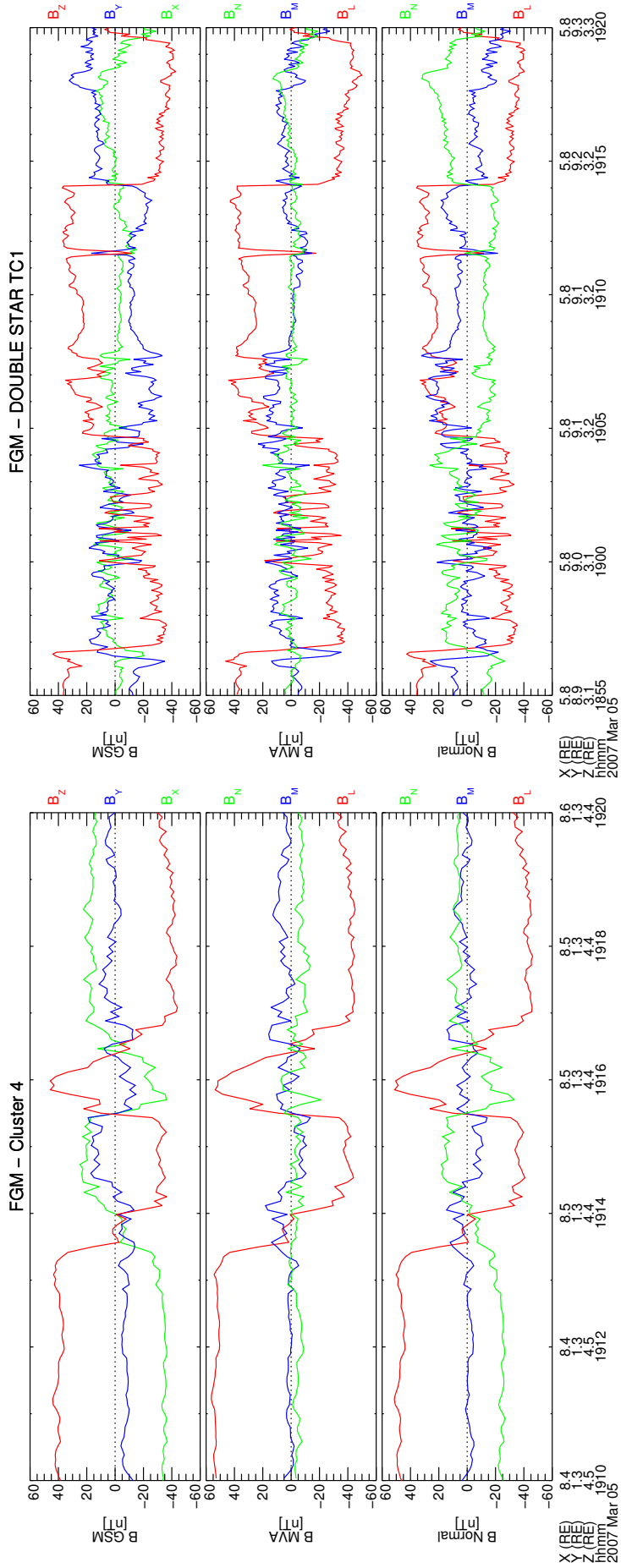


Figure 6.1 - Magnetic field components represented in Geocentric Solar Magnetospheric (GSM) coordinates (top panels), in boundary normal coordinates by using MVA (middle panels) and the Shue et al. (1998) magnetopause model (bottom panels). On the left side, Cluster 4 data is presented while Double Star data on the right side.

(1998)). Since the normal magnetic field component seems to be better represented, i.e. having a smaller standard deviation, for the MVA case, this method has been employed for this event.

The chosen time interval to apply the method was 19:12:00 to 19:15:00 UT within which Cluster 4 crosses, for the first time, the dayside magnetopause above the equator ($z_{GSM} \sim 4.4 R_E$) and slightly duskward of the noon-midnight meridian plane ($y_{GSM} \sim 1.3 R_E$). The LMN directions were found to be $L = (-0.578, -0.143, 0.803)$, $M = (-0.143, -0.952, -0.271)$ and $N = (0.803, -0.271, 0.529)$ in the GSM coordinate system, where L points approximately due north, M is directed downward and N is the local magnetopause normal pointing, in this case, predominantly in the positive x_{GSM} direction. The intermediate over minimum eigenvalues ratio which is an indicator of the “goodness” of the normal vector estimation was approximately 4.02 for this crossing. A ratio larger than two is often taken as a good normal vector determination (cf. e.g., Sonnerup and Scheible (1998)). Thus the estimation of the normal direction was proper for the present study.

Cluster 4 crossed the dayside magnetopause from the magnetosphere into the magnetosheath slightly duskward of the noon sector ($y_{GSM} \sim 1.3 R_E$) and above the equator ($z_{GSM} \sim 4.4 R_E$) around at 19:14:00 UT, as evidenced by the southward turning of the magnetic field B_L component at that time. The magnetospheric side of the magnetopause current sheet is identified in this crossing by a predominantly northward magnetic field orientation ($B_L > 0$), and hot (~ 10 keV) and tenuous ($\sim 0.3 \text{ cm}^{-3}$) plasma, while in the magnetosheath side the plasma is usually much more dense ($\sim 10 \text{ cm}^{-3}$) and cooler (~ 0.2 keV) as shown in Figure 6.2. Upon reaching the earthward side of the magnetopause ($\sim 19:12:50$ UT), local plasma acceleration is detected, an increase of around 200 km/s in the V_L component relative to flow speed (~ 100 km/s) in the magnetosheath side of the magnetopause. Given the almost purely southward ($B_L < 0$) orientation of the magnetosheath magnetic field, such a local northward acceleration is in line with the scenario where the magnetic reconnection between Earth’s and magnetosheath magnetic fields takes place somewhere southward of the spacecraft location (cf. e.g., Paschmann et al. (1979)). Furthermore, this acceleration is marginally consistent with theoretical expectations since $\theta_{op} = 24.05^\circ$ and $r_{op} = 0.60$ which gives $\Delta V_A^* = 0.55$ (see Section 3.5 for description of the Walen test), meaning that plasma is likely being accelerated by magnetic tension forces of sharply bent and newly reconnected field lines. Another observational feature that support this interpretation is that around the same time when the plasma jet is measured, hot (> 1 keV) ions which are likely coming from

FGM & CIS-CODIF - Cluster 4

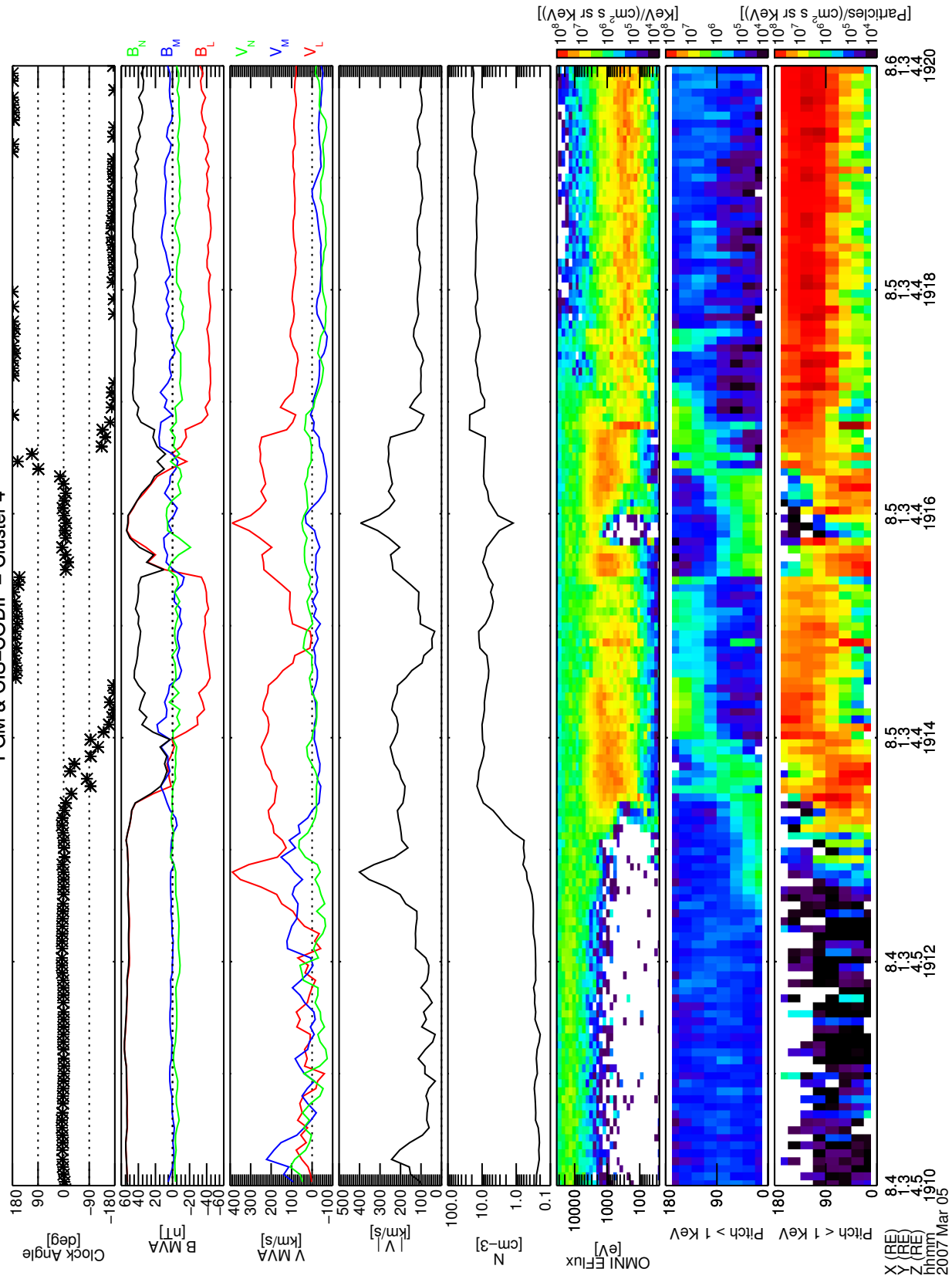


Figure 6.2 - Cluster 4 magnetopause crossing. From top to bottom: clock angle, magnetic and velocity field components in boundary normal coordinates LMN, the plasma velocity magnitude, the ion (ionized hydrogen atom) plasma density, the ion omnidirectional energy flux, and pitch angle distributions for ion energies above or equal to 1 keV and below 1 keV.

the magnetosheath side are streaming parallel to the local magnetic field orientation (from $\sim 19:12:30$ UT up to $\sim 19:13:50$ UT on the penultimate panel in Figure 6.2). The result indicates that these ions are entering the magnetosphere along magnetic field lines which were “opened”⁴ via the reconnection process. After the first magnetopause crossing at 19:14:00 UT, the energetic particles are now flowing antiparallel to the local magnetosheath’s magnetic field orientation ($B_L < 0$), in agreement with the idea of an open magnetosphere whereby (likely) magnetospheric ions (and also electrons) are able to flow towards the magnetosheath along reconnected field lines.

Right after the first magnetopause crossing, the magnetopause probably moves inwards, and hence Cluster 4 reenters into the magnetosphere at around 19:15:55 UT. Then, after 20~30 s later, Cluster 4 detects reconnection signatures similar to those found in its first crossing, namely *i*) a reconnection jet, i.e., a positive V_L enhancement, with $r_{op} = 0.60$, $\theta_{op} = 14.34^\circ$ and $\Delta V_A^* = 0.58$, *ii*) parallel streaming followed by antiparallel streaming ions as the spacecraft crosses the magnetopause and *iii*) a boundary layer with a mixture of magnetospheric-like and magnetosheath ions from ~ 0.8 up to ~ 3 keV energies. The second encounter with a reconnecting magnetopause indicates that reconnection was active and occurring somewhere southward of Cluster 4’s location at least for the five minutes since the first encounter.

Double Star TC1’s observations on the duskside magnetopause ($y_{GSM} \sim 9.1 R_E$) and above the equator ($z_{GSM} \sim 3.1 R_E$) are depicted in Figure 6.3. The first five plots have the same format of Cluster 4’s observations, i.e., clock angle, magnetic and velocity field components in the boundary normal coordinates, the ion plasma velocity magnitude and plasma density. The remaining four plots account for electron omni-directional energy flux and electron pitch angle distributions for three different energy channels, namely: 22, 175 and 429 eV. The white stripes on the spectra plots are data gaps. As before, the boundary normal coordinate system was determined by MVAB in the time interval 19:04:00–19:07:00 UT, and the LMN vectors were $L = (-0.088, -0.491, 0.867)$, $M = (0.457, -0.793, -0.402)$ and $N = (0.885, 0.361, 0.294)$ in the GSM coordinates. The intermediate to minimum eigenvalues ratio for this crossing was 3.22.

Double Star TC1’s first encounter with the dayside magnetopause occurs at around 18:56:50 UT, where B_L changes from positive to negative sign and the ion plasma density reaches typical magnetosheath values ($\gtrsim 10 \text{ cm}^{-3}$). The magnetic field rota-

⁴“Open” magnetic field lines are referred to as those field lines which has one footprint in one of the Earth’s hemispheres and the other footprint to the “solar wind”.

FGM, HIA & PEACE – DOUBLE STAR TC1

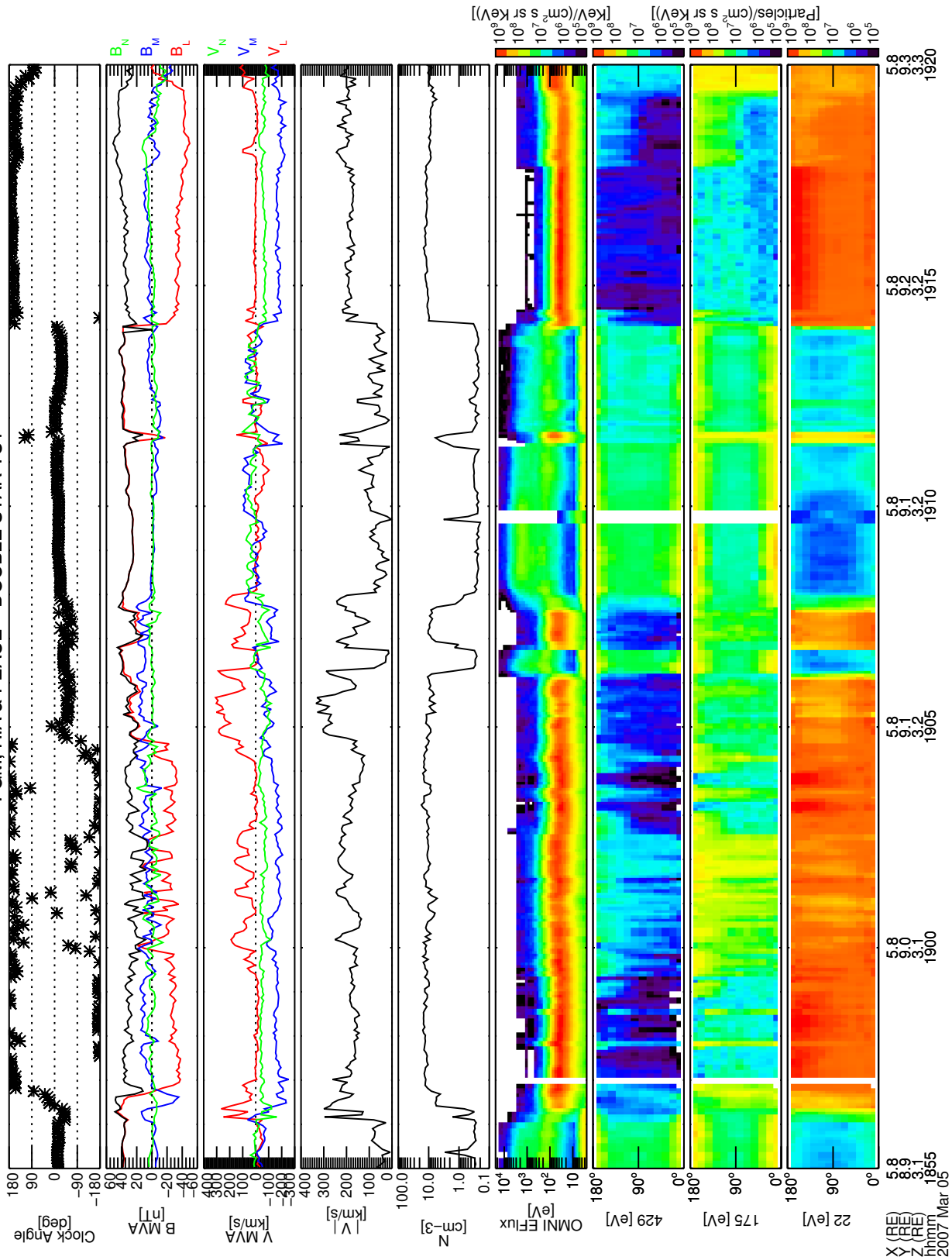


Figure 6.3 – Double Star TC1 magnetopause crossing. From top to bottom: clock angle, magnetic and velocity field components in boundary normal coordinates LMN, the plasma velocity magnitude, the plasma density, electron omni-directional energy flux, and electron pitch angle distributions for the energy channels shown on the left.

tion was nearly 180 degrees, as seen in the clock angle (top panel). Just before the magnetopause crossing, a reconnection jet, i.e., a positive (reconnection-associated) enhancement on the V_L component, is detected. The plasma velocity magnitude increases around 150 km/s relative to magnetosheath flow speed and such a plasma jet corresponds to 77% of the theoretical predicted value ($r_{op} = 0.77$). Although the jet direction was 22.4° away from the field-aligned direction, $\Delta V_A^* = 0.71$ remained above the chosen criterion to identify a reconnection-like plasma jet, which was defined as $\Delta V_A^* > 0.5$. As it travels through the magnetosheath, Double Star TC1 encounters a boundary layer from $\sim 18:59:25$ UT up to $\sim 19:02:30$ UT, as evidenced by *i*) accelerated flows (positive enhancements in the V_L component), *ii*) the presence of both antiparallel streaming magnetospheric-like (429 eV) and energized magnetosheath-like (175 eV) electrons, and *iii*) a modest elevation on electron's omni-directional energy flux as compared to adjacent magnetosheath values. At around 19:04:20 UT, another boundary layer is reached with more pronounced plasma flows having the same (northward) orientation as those found previously. The plasma jet is mainly located on magnetic field lines with magnetospheric configuration, i.e. $B_L > 0$, and densities in this region are slightly lower, i.e. ~ 10 – 20% , than in the magnetosheath proper. Also, the observed accelerated flow is 89% ($r_{op} = 0.89$) of the theoretical value predicted by the reconnection process. Such a flow is 10.24° away from the field-aligned direction, thus the implied ΔV_A^* value of 0.88 indicates a good agreement with theory, indicating that Double Star TC1 has likely crossed a rotational discontinuity at $\sim 19:04:20$ UT.

The continued presence of reconnection-accelerated plasma flows and also of either parallel or antiparallel streaming electrons throughout the ~ 8 minutes period encompassing two Double Star TC1 magnetopause crossings, as well as the persistent (mainly) northward directed component of the accelerated plasma flows, suggests that reconnection was active during this period and occurring somewhere southward of the spacecraft location, similar to what was observed in the Cluster 4 spacecraft.

6.1.1.2 2007-06-14 crossing

The representative (mean) IMF components and dynamic pressure values and their respective standard deviations for this crossing were: $B_x^{IMF} = -7.44 \pm 0.57$, $B_y^{IMF} = 5.56 \pm 0.33$, $B_z^{IMF} = -6.47 \pm 0.91$ nT, and $P_{dyn} = 1.90 \pm 0.12$ nPa.

This event has already been reported by [Dunlop et al. \(2011\)](#), and it has recently been used to provide a single test case to the [Laitinen et al. \(2007\)](#) X-line model ([HOILJOKI et al., 2014](#)). Here we summarize its main features.

Here and for the remaining magnetopause crossing events that will be presented latter on, the boundary normal coordinates LMN are determined by using the Shue et al. (1998) magnetopause model. Briefly, at each spacecraft location (x, y, z) , the normal to the magnetopause model, N, is computed, and after that the M and L vectors are derived in the following way: M, which points westward, is identified as the cross product between N and z_{GSM} directions, and finally L, which points approximately due north, completes the left-handed orthogonal system being defined as the cross product between the M and N vectors.

Themis A and Double Star TC1 observations are shown in Figures 6.4 and 6.5, respectively. Firstly, Themis A observations are discussed followed by Double Star's.

On 14 June 2007, at around 04:42:40 UT, Themis A has crossed the Earth's day-side magnetopause from the magnetosphere towards the magnetosheath region, as evidenced by the southward turning of the magnetic field B_L component, and also a factor of ~ 10 increase in ion plasma density. On the earthward side of the magnetopause a strong plasma jet of ~ 410 km/s is detected. Such a value corresponds to 68% of the predicted reconnection jet speed, and also the jet direction is only 10.84° away from the field-aligned direction, resulting in a $\Delta V_A^* = 0.67$. Thus, the flow enhancement is consistent with the magnetic reconnection picture. Moreover, between 04:42:20 and 04:42:50 UT, i.e. at the current sheet center, the ion energy flux peaks in ~ 2 keV whose value is higher than the one usually found for magnetosheath ions (~ 0.2 keV), meaning that a local mechanism is accelerating these ions to such energies. This fact is once again consistent with the reconnection theory which attributes the cause of local plasma acceleration to the action of sharply bent reconnected field lines. Furthermore, the pitch angle distribution signatures also corroborate with this scenario in a similar way as that described above with the Cluster 4 spacecraft on the 2007-03-05 magnetopause crossing event. The parallel streaming ions with magnetosheath-like energies on magnetospheric magnetic field lines ($B_L > 0$) prior the magnetopause crossing followed by antiparallel streaming ions on magnetosheath magnetic field lines ($B_L < 0$) is indicative of magnetosheath plasma entry via open field lines, and that such a plasma transfer occurs northward of the assumed reconnection X-line.

For the Double Star TC1 magnetopause crossing, there were no ion plasma data available, but the PEACE instrument provided both omni-direction electron energy flux data and electron pitch angle distributions for several energy channels, as shown in the last three bottom panels of Figure 6.5. Double Star TC1 crosses the

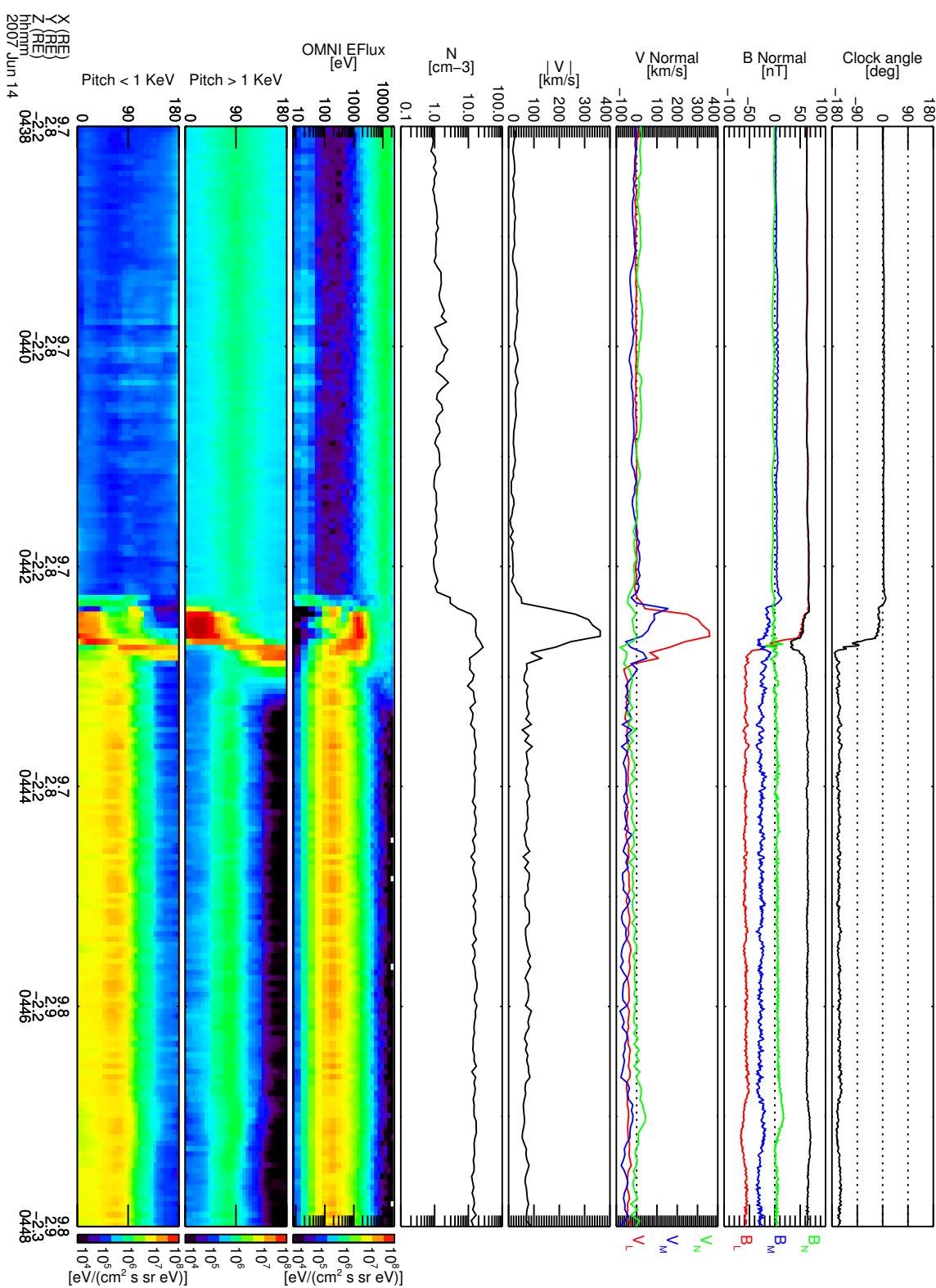


Figure 6.4 - Themis A magnetopause crossing. This event has already been reported by Dunlop et al. (2011). From top to bottom: clock angle, magnetic and velocity field components in boundary normal coordinates LMN, the plasma velocity magnitude, the ion (ionized hydrogen atom) plasma density, the ion omni-directional energy flux, and pitch angle distributions for ion energies above or equal to 1 keV and below 1 keV.

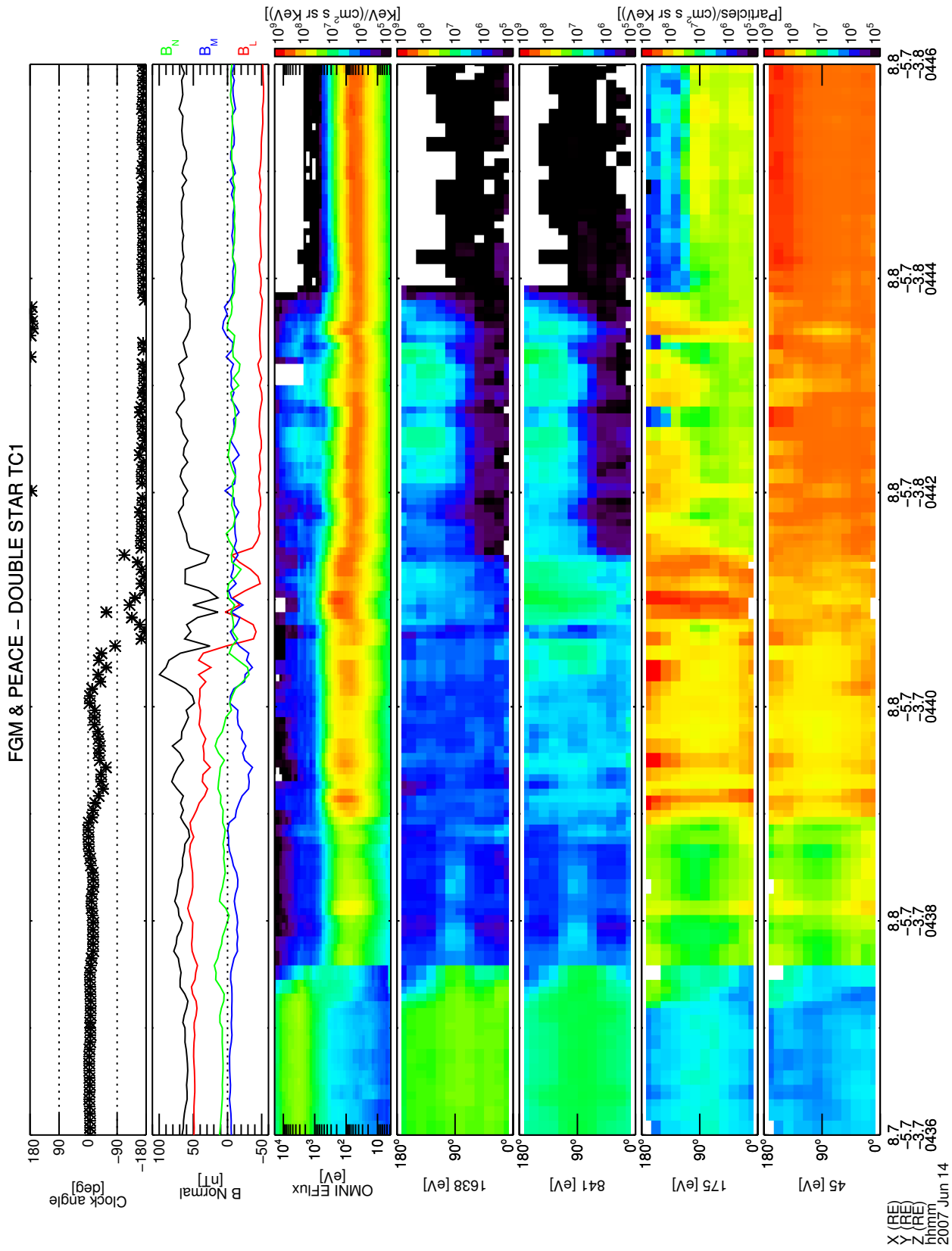


Figure 6.5 - Double Star TC1 magnetopause crossing. This event has already been reported by Dunlop et al. (2011). From top to bottom: clock angle, magnetic and velocity field components in boundary normal coordinates LMN, the plasma velocity magnitude, the ion (ionized hydrogen atom) plasma density, the ion omni-directional energy flux, and pitch angle distributions for ion energies above or equal to 1 keV and below 1 keV.

magnetopause from the magnetosphere towards the magnetosheath approximately 2 minutes before Themis A does, i.e. at around 04:41:00 UT where the B_L component changes sign. They were separated in the y_{GSM} direction by $\sim 8 R_E$. Notice that a boundary layer is encountered before the magnetopause crossing itself, as it can be seen by the sharp change in electron omni-directional energy flux at $\sim 04:37:05$ UT, and also a factor of ~ 10 decrease in magnetospheric-like electron flux (841 and 1638 eV panels) and a concomitant increase in magnetosheath-like electron flux (45 and 175 eV panels). After 04:39 UT, on the earthward side of the magnetopause, there is a clear presence of both counterstreaming and beamed populations with magnetosheath energies (45 and 175 eV panels). It suggests that magnetosheath electrons are flowing towards the magnetosphere mirroring in the ionosphere and turning back to the spacecraft detector along magnetic field lines which have been opened by reconnection (DUNLOP et al., 2011). At 04:41 UT, the magnetic field magnitude (black line on the second plot from top to bottom) decreases at the same time the electron omni-directional energy flux undergoes a small enhancement, indicating that electrons are being energized in the center of the magnetopause current sheet. After 04:42 UT, antiparallel streaming electrons with both magnetospheric-like energies (841 and 1638 eV panels) and elevated magnetosheath energy (175 eV panel) are detected, suggesting “escaping” electrons from the magnetosphere, and possibly magnetosheath reflected (in the ionosphere) electrons, with both cases being consequences of dayside magnetic reconnection which should be occurring somewhere southward of Double Star TC1 location.

6.1.1.3 2009-05-22 crossing

The representative (mean) IMF components and dynamic pressure values and their respective standard deviations for this crossing were: $B_x^{IMF} = -4.35 \pm 0.13$, $B_y^{IMF} = 1.99 \pm 0.24$, $B_z^{IMF} = -2.75 \pm 0.15$ nT, and $P_{dyn} = 1.71 \pm 0.05$ nPa.

Cluster 3 and Themis B observations are shown in Figures 6.6 and 6.7, respectively. The boundary normal coordinates, LMN, were determined by using the Shue et al. (1998) magnetopause model, as previously done for the 2007-06-14 event presented above. Cluster 3 observations are discussed first, followed by Themis B observations.

Cluster 3 was in an outbound trajectory on 22 May 2009 in the dawn sector of the magnetosphere when it has found the earthward edge of the magnetopause at around 16:22:00 UT. At $\sim 16:22:10$ UT, the maximum positive enhancement in the V_L component was detected relative to its negative values in the magnetosheath proper (from 16:26 UT onward). At $\sim 16:23:00$ UT, the B_L component changed from

FGM & CIS-HIA Cluster 3

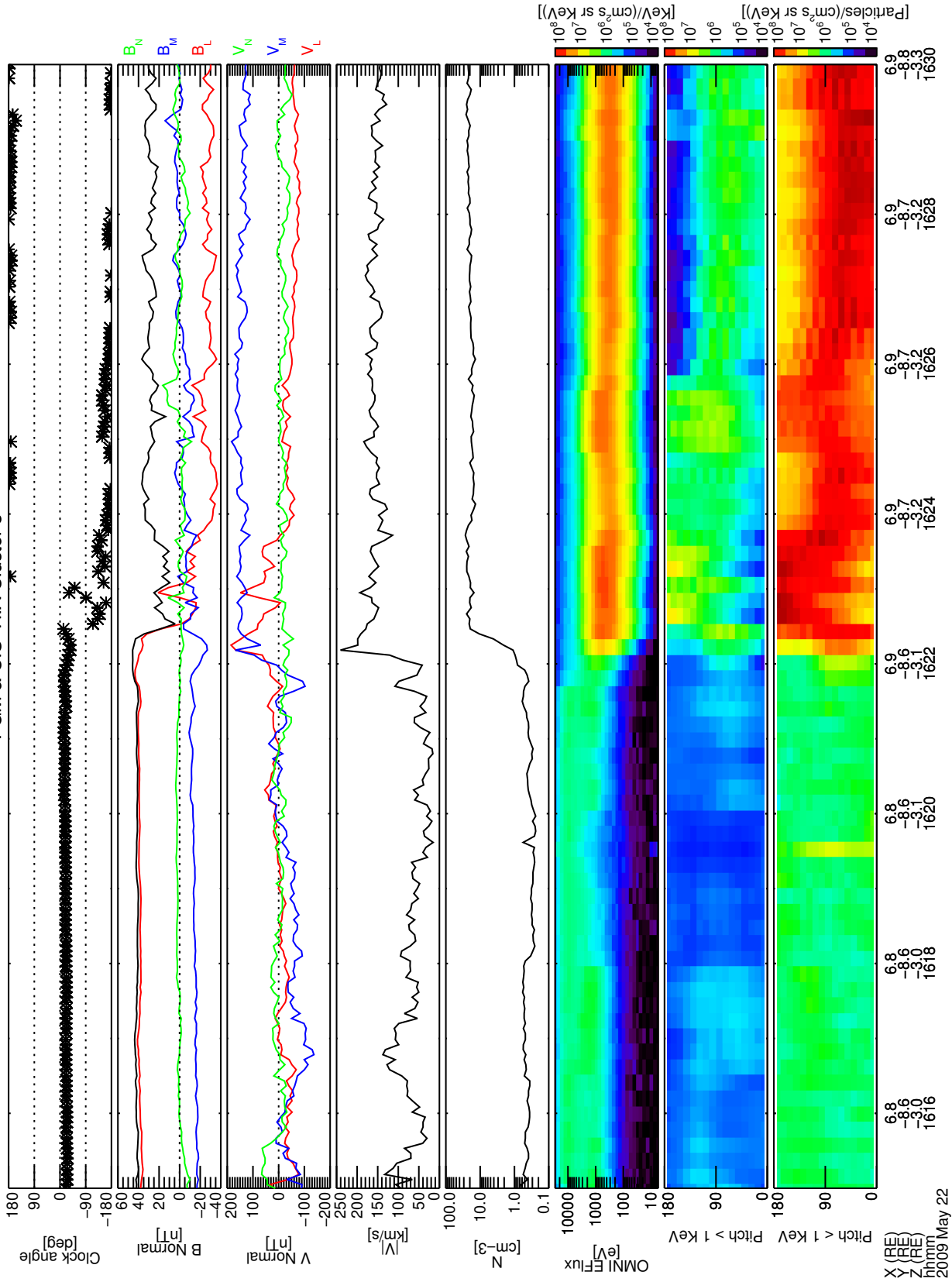


Figure 6.6 - Cluster 3 magnetopause crossing. From top to bottom: clock angle, magnetic and velocity field components in boundary normal coordinates LMN, the plasma velocity magnitude, the ion (ionized hydrogen atom) plasma density, the ion omnidirectional energy flux, and pitch angle distributions for ion energies above or equal to 1 keV and below 1 keV.

magnetospheric ($B_L > 0$) to magnetosheath ($B_L < 0$) magnetic field orientations and the magnetic field magnitude (black line in the second panel from top to bottom) reached the smallest value (~ 5 nT) for the whole interval shown. Right after that, the B_L component did a brief excursion to positive values while accelerated plasma flows, i.e. a positive enhancement in V_L , were still being measured, suggesting the presence of an acceleration mechanism acting somewhere southward of the spacecraft location. The ion omni-directional energy flux remained slightly elevated, relative to magnetosheath proper levels, during the approximately 2 minute interval following the main B_L reversal, within which there were accelerated plasma flows. Moreover, within this same 2 minute interval, both magnetosheath- and magnetospheric-like ions were antiparallel streaming along field lines with magnetosheath magnetic field lines orientation ($B_L < 0$). In terms of the reconnection scenario, the antiparallel streaming magnetosheath-like ions could be interpreted as a population which mirrored in the northern ionosphere and returned back to the spacecraft detector along reconnected field lines. The magnetospheric ions seen in magnetosheath magnetic field lines would be interpreted as escaping ions flowing along field lines “opened” by the reconnection process.

For the magnetopause crossing that occurred at $\sim 16:23:00$ UT, the observed plasma jet was ~ 207 km/s which corresponds to 54% of the theoretical prediction. The θ_{op} was 26.62° , resulting in a $\Delta V_A^* = 0.49$. Despite the relatively poor agreement with theory, this event was still deemed as a reconnection event primarily because of the presence of the reconnection signatures mentioned above, and also by the fact that to the best of our knowledge no other physical mechanism would be capable to explain the observed plasma behavior. A poor Walén agreement means that the current sheet being analyzed, which is the magnetopause in the present case, is a structure that deviates from the idealized one dimensional, time-stationary discontinuity assumed in theory (see e.g., Section 2.3.1 in Paschmann et al. (2013)). Another contributing factor for a poor agreement between theory and observation, i.e., the observed to predicted jet magnitude ratio r_{op} far from unity, is that measured plasma density possesses a minor fraction of ions heavier than protons (e.g., He^{++}). If we can measure heavier ions properly, the plasma density would be higher than present observation, then the local Alfvén speed, which is proportional to $(\text{density})^{-1/2}$, would be lower thereby increasing r_{op} (see e.g., Puhl-Quinn and Scudder (2000) and references therein). For such cases other evidences are needed, as shown above, in order to characterize an event as a reconnection event or not (see also Phan et al. (2013) for some examples).

FGM & ESA - THEMIS B

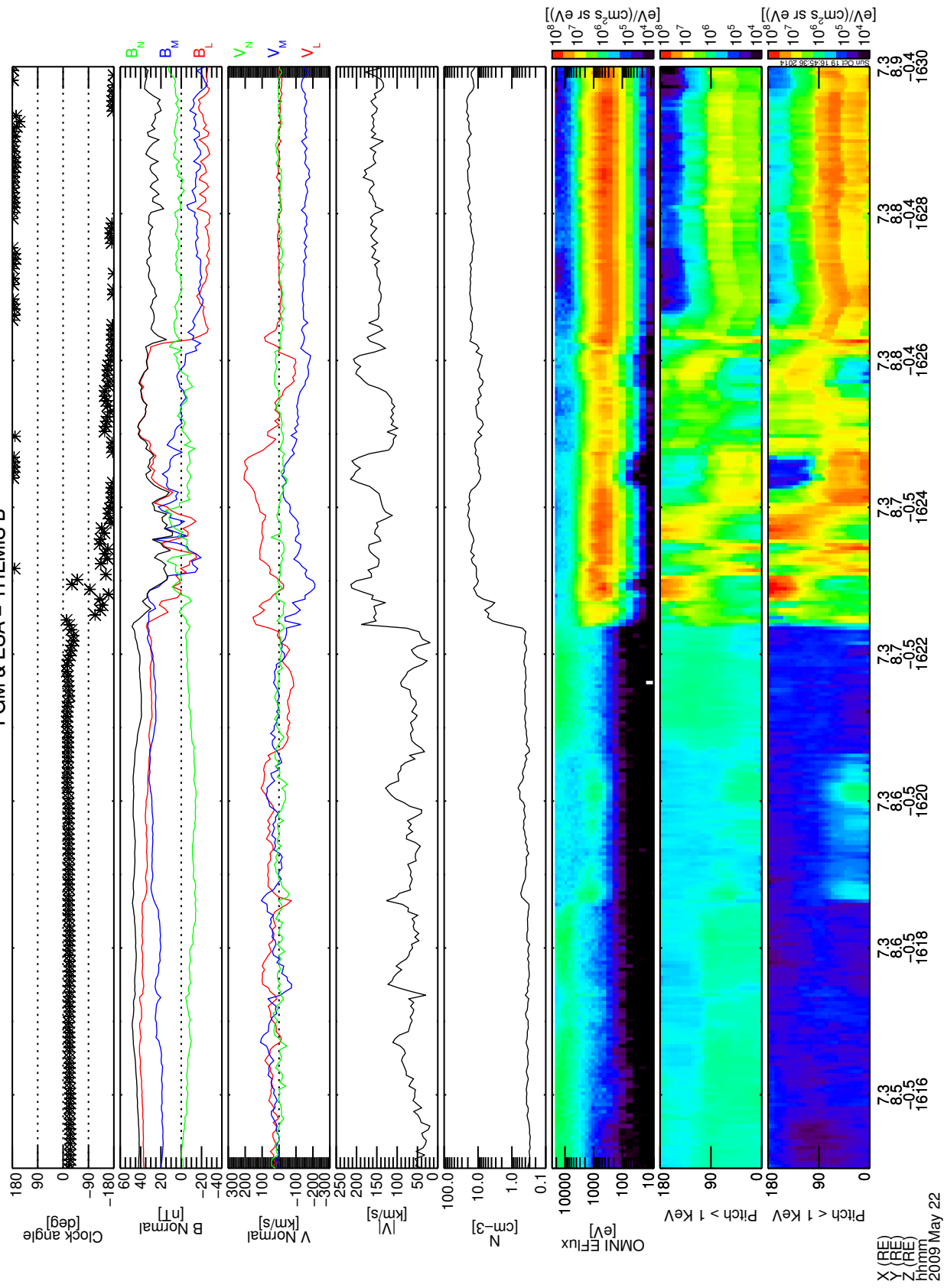


Figure 6.7 - Themis B magnetopause crossing. From top to bottom: clock angle, magnetic and velocity field components in boundary normal coordinates LMN, the plasma velocity magnitude, the ion (ionized hydrogen atom) plasma density, the ion omnidirectional energy flux, and pitch angle distributions for ion energies above or equal to 1 keV and below 1 keV.

In Figure 6.7, Themis B encounters the earthward edge of the magnetopause at $\sim 16:22:25$ UT, almost simultaneously with Cluster 3 (16:22:00 UT). Themis B has crossed the magnetopause on the dusk sector very close to and below the equator ($z_{GSM} \sim -0.5 R_E$). It was approximately $16 R_E$ away from Cluster 3 in the y_{GSM} direction. Upon crossing the earthward edge of the magnetopause, Themis B detects accelerated plasma flows, i.e. positive enhancements in both V_L and V_M velocity components. Notice that for the latter, since the background flow has a negative M (duskward) component, a positive V_M enhancement is detected as a less negative V_M value as compared to the magnetosheath flow, as seen at $\sim 16:22:30$ UT and at $\sim 16:24:25$ UT. The plasma jet, identified as the maximum plasma flow value within the magnetopause current sheet minus the magnetosheath background flow was ~ 240 km/s, corresponding to 64% of the theoretically predicted value. On the other hand, the jet direction agreement with theory was very good, i.e. $\theta_{op} = 2.76^\circ$. The implied ΔV_A^* value was also 0.64. Thus, the observed accelerated flows are consistent with the reconnection theory as well as the picture where magnetic reconnection was occurring somewhere southward and slightly duskward of the spacecraft location, being the latter statement based on the local jet direction (northward and slightly dawnward). Themis B was in the Low Latitude Boundary Layer (LLBL) at $\sim 16:26$ UT when Cluster 3 was going out from the so-called Magnetosheath Boundary Layer (MSBL) to the magnetosheath ($\sim 16:25:55$ UT).

6.1.1.4 2009-07-07 crossing

The representative (mean) IMF components and dynamic pressure values and their respective standard deviations for this crossing were: $B_x^{IMF} = -2.11 \pm 0.26$, $B_y^{IMF} = 3.79 \pm 0.25$, $B_z^{IMF} = -2.88 \pm 0.39$ nT, and $P_{dyn} = 2.22 \pm 0.11$ nPa.

For this event two Themis spacecraft, Themis A and Themis C, have crossed the dusk sector magnetopause, i.e. $y_{GSM}^{ThA} \sim 10.5 R_E$ and $y_{GSM}^{ThC} \sim 2.8 R_E$, below the equator with $z_{GSM}^{ThA} \sim -4.9 R_E$ and $z_{GSM}^{ThC} \sim -3.1 R_E$. They were heading towards the magnetosheath.

Themis A observations, which are discussed first, are shown in Figure 6.8. The time interval shown spans 50 minutes of observations, as compared with eleven minutes for Themis C. The reason of such a choice was to show the numerous encounters of a mixture of magnetosheath and magnetospheric plasma. At all these boundaries, magnetosheath-like ion densities ($\sim 10 \text{ cm}^{-3}$), energized magnetosheath ions ($\sim 0.6 \text{ keV}$), accelerated plasma flows relative to magnetosheath values, and generally antiparallel streaming ions were detected. In particular, these accelerated plasma

flows had a consistent southward ($V_L < 0$) component. Such characteristics are consistent with the idea of magnetic reconnection occurring somewhere northward of the spacecraft location for at least 35 minutes, i.e. from $\sim 14:15:00$ UT to $\sim 14:50:00$ UT. Looking closely to the $14:23:00$ UT boundary layer encounter, one notices a flux transfer event (FTE)-like bipolar (-/+) signature in the magnetic field normal component B_N (green line in second panel). The total magnetic field in the center of such structure, i.e. at the B_N reversal at around $14:22:55$ UT, is higher than in the surrounding regions, also consistent with an FTE signature (Russell; Elphic, 1978). The negative followed by positive B_N variation implies a southward flux tube motion, which would contribute to the reconnection scenario mentioned above where an active reconnection X-line would be located northward of the spacecraft location giving rise to reconnected flux tubes, i.e. FTEs, propagating southward. Themis A was in the magnetosphere at around $14:45:40$ UT when the highest plasma flow enhancement in the $-L$ (southward) direction was detected earthward of the magnetopause. The plasma jet at this time was ~ 228 km/s, corresponding to 90% of the predicted theoretical value, i.e. $r_{op} = 0.90$. The jet's angular distance from the field-aligned direction was $\theta_{op} = 13.57^\circ$, and the ΔV_A^* value was 0.87. Therefore, the good agreement with theory of both jet magnitude and angular displacement categorize this event as a magnetic reconnection event.

Themis C has crossed the magnetopause approximately 6 minutes prior to Themis A, i.e. at around $14:39:20$ UT when the magnetic field component B_L changed sign. Themis C remained in the magnetosheath about 1 minute and half before it briefly reentered the boundary layer on the earthward side of the magnetopause, as seen by the negative to positive sign change in the B_L component at $\sim 14:40:50$ UT and the positive to negative B_L sign change at $\sim 14:41:25$ UT. Prior to the first magnetopause encounter, i.e. at around $14:39:20$ UT, an enhanced plasma flow in both $-V_L$ and $-V_M$ components is detected, being the V_L enhancement more pronounced. The plasma jet at this time (~ 243 km/s) was 70% of the predicted value, while the angular distance from the field-aligned direction, $\theta_{op} = 0.48^\circ$, was remarkably good. Thus, ΔV_A^* was equal to 0.70. Therefore, the local plasma acceleration likely comes from the magnetic reconnection between Earth's and magnetosheath magnetic fields (PASCHMANN et al., 1979).

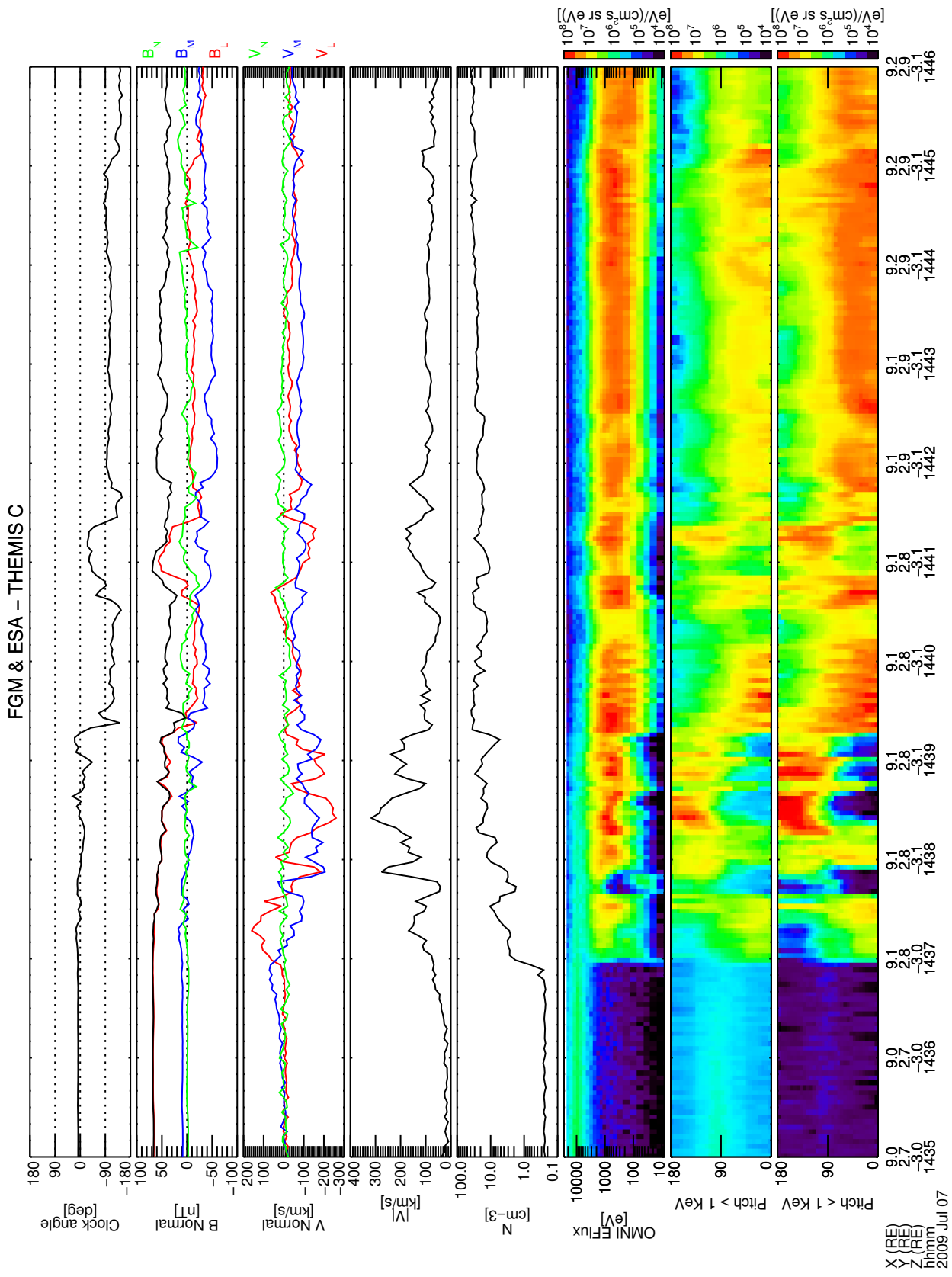


Figure 6.9 - Themis C magnetopause crossing. From top to bottom: clock angle, magnetic and velocity field components in boundary normal coordinates LMN, the plasma velocity magnitude, the ion (ionized hydrogen atom) plasma density, the ion omni-directional energy flux, and pitch angle distributions for ion energies above or equal to 1 keV and below 1 keV.

6.1.1.5 Summary of the quasi-simultaneous magnetopause crossing observations

The main characteristics, i.e., IMF conditions, Earth's dipole tilt angle and so forth, of the four fortuitous quasi-simultaneous magnetopause crossing events discussed in previous sections are shown in Table 6.1 below.

According to the so-called component reconnection models (GONZALEZ; MOZER, 1974; SONNERUP, 1974) where the IMF B_y component plays an important role on the reconnection X-line location, it is expected a tilted subsolar reconnection X-line coming from the southward-dawnward(duskward) direction and extending all the way up to the northward-duskward(dawnward) sector of the dayside magnetopause if the IMF B_y is positive (negative). Therefore, to a first order approximation where the reconnection outflows are supposed to leave the diffusion region perpendicular to the local X-line orientation, the observed reconnection plasma flow adjacent to the tilted X-line is expected to have, for IMF $B_y > 0$, an eastward (westward)-southward (northward) component if the spacecraft is below (above) the tilted X-line, and for IMF $B_y < 0$ an westward (eastward)-southward (northward) component if the spacecraft is below (above) the tilted X-line.

For three of four events the assumed reconnection X-line is expected to lie somewhere southward of both spacecraft locations, thereby being responsible for generating the observed northward reconnection plasma jets. On the other hand, for the 2009-07-07 event southward plasma jet components were observed on both Themis A and C spacecraft locations suggesting an X-line northward of them.

In the next section, reconnection X-line models are compared against the *in situ* quasi-simultaneous observations of magnetic reconnection discussed above. The plasma jets are represented in GSM coordinates since the yz GSM plane is the projection plane in which the magnetopause surface and hence the X-line models will be presented.

6.1.2 X-line models test against *in situ* quasi-simultaneous magnetic reconnection plasma jet observations

Here, the chosen X-line models, namely Maximum Shear Angle (TRATTNER *et al.*, 2007), Chapman-Ferraro current (GONZALEZ; MOZER, 1974) and Maximum Reconnection Outflow Speed (SWISDAK; DRAKE, 2007) models are tested against quasi-simultaneous observations. As discussed in Section 4.1.1, both Trattner *et al.* (2007)

Table 6.1 - Quasi-simultaneous magnetopause crossing events, and some key parameters such as: location of each spacecraft when the magnetopause was crossed; Earth's dipole tilt (ψ) inclination as obtained by the [Tsyganenko and Stern \(1996\)](#) magnetospheric magnetic field model; interplanetary conditions, i.e., IMF components and dynamic pressure P_{dyn} ; the plasma jet magnitude V_{jet} ; the observed to predicted jet magnitude ratio r_{op} ; the angular displacement of the observed jet direction from the field-aligned direction θ_{op} ; and the ΔV_A^* parameter (see Section 3.5 for details).

| S/C | Position [R_E] | | M'pause crossing time | Dipole tilt (ψ) | IMF [nT] | | P_{dyn} [nPa] | V_{jet} [km/s] | r_{op} | θ_{op} | $\Delta V_A^* = r_{op} \cos \theta_{op}$ |
|---------------------------------|--------------------|-----------|-----------------------|------------------------|-----------|-------|-----------------|------------------|----------|---------------|--|
| | X_{GSM} | Y_{GSM} | | | Z_{GSM} | B_x | | | | | |
| Cluster 4 Double Star TC1 | 8.5 | 1.3 | 4.5 | 2.7° | -4.02 | 1.26 | 2.05 | 321 | 0.60 | 24.05° | 0.55 |
| | 5.8 | 9.1 | 3.2 | | | | | | | | |
| Themis A Double Star TC1 | 9.7 | 2.8 | -2.2 | 13.1° | -7.44 | 5.56 | 1.90 | 413 | 0.68 | 10.84° | 0.67 |
| | 8.8 | -5.7 | -3.8 | | | | | | | | |
| Cluster 3 Themis B | 6.9 | -8.6 | -3.1 | 30.5° | -4.34 | 1.99 | 1.71 | 206 | 0.54 | 26.62° | 0.49 |
| | 7.3 | 8.8 | -0.4 | | | | | | | | |
| Themis A Themis C | 4.0 | 10.8 | -4.0 | 30.7° | -2.11 | 3.79 | 2.22 | 198 | 0.90 | 13.57° | 0.87 |
| | 9.1 | 2.8 | -3.1 | | | | | | | | |

and Gonzalez and Mozer (1974) model plots presented below use the paraboloidal magnetopause, as modeled by the Alexeev et al. (2003) model, projected on the yz GSM plane. In the Swisdak and Drake (2007) case, the magnetopause was modeled by using the BATS-R-US code (see Section 4.3.2 for details), and only its dayside part, i.e. $\phi = [-90^\circ, +90^\circ]$ and $\theta = [0^\circ, 180^\circ]$, is projected on the yz GSM plane⁵. The color coding in the following plots represents the intensity of the modeled parameter being visualized, i.e., the magnetic shear angle for Trattner et al. (2007), the Chapman-Ferraro current density magnitude $|\mathbf{J}_{CF}|$ [mA/m] for Gonzalez and Mozer (1974), and the reconnection outflow velocity magnitude, V_{out} , for Swisdak and Drake (2007). Next, the results are presented for each model.

6.1.2.1 Maximum Shear Angle Model test (TRATTNER et al., 2007)

The observed plasma jet directions in GSM coordinates for the quasi-simultaneous reconnection events, and the X-line generated via the Maximum Shear Angle model are shown in Figure 6.10. Panels a), b), c) and d) correspond to the quasi-simultaneous reconnection events analyzed in Section 6.1.1: 2007-03-05, 2007-06-14, 2009-05-22 and 2009-07-07, respectively. The IMF components in nanoTesla and the dipole tilt angle, ψ , used to generate the shear angle color plots are indicated on the top of each panel. The maximum shear X-line is represented by filled black circles while the spacecraft position with ‘X’ marks. The jet directions, but not their magnitudes, are represented by the black arrows which have the same length.

For panel a), the X-line location is consistent with the observed jet direction at Cluster 4 location, i.e. the ‘X’ mark closest to the noon-midnight meridian ($y_{GSM} = 0$). As mentioned at the end of Section 6.1.1, for a positive IMF B_y the reconnection outflow adjacent to and above the tilted subsolar X-line is expected to have a northward-westward component as seen by Cluster 4 spacecraft. Therefore, for Cluster 4 observations the maximum shear X-line predicted the correct north-south as well as the east-west sense of the observed reconnection jet direction. The same can not be said at Double Star TC1’s location ($y_{GSM} \sim 9 R_E$). The plasma jet has a strong $-y_{GSM}$ (westward) component and a northward ($+z_{GSM}$) component as well. On the basis of the simple assumption considered here that the reconnection outflow should be directed perpendicular to the local X-line orientation, the expected jet direction at Double Star TC1’s location would have to have both westward and southward components. The agreement of the maximum shear X-line location with

⁵See Section 4.3.2 for a detailed description on how the BATS-R-US magnetopause was determined and the underlying limitations of the chosen approach.

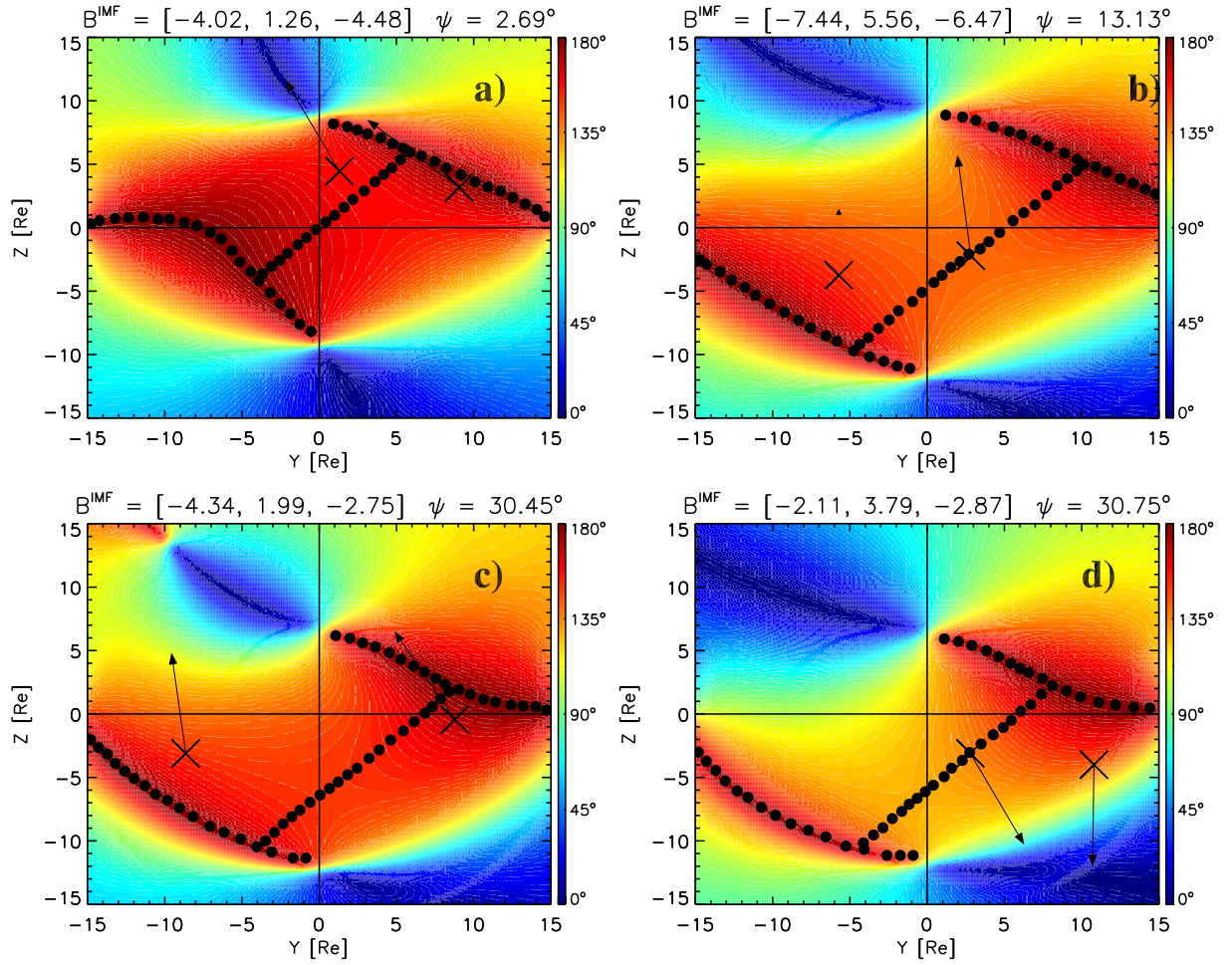


Figure 6.10 - Trattner et al. (2007)'s Maximum Shear Angle Model test against quasi-simultaneous magnetic reconnection plasma jet observations. Panels a) through d) correspond to the reconnection events described in Sections 6.1.1.1 through 6.1.1.4, respectively. The maximum shear X-line is represented by black filled circles while the observed reconnection jets by black arrows. The 'X' marks indicate the spacecraft position when the magnetopause was crossed. The color coding represents the value of the shear angle, $\theta_{shear} = \cos^{-1}[(\mathbf{B}_{MS} \cdot \mathbf{B}_{GM})/(|\mathbf{B}_{MS}||\mathbf{B}_{GM}|)]$, over the modeled paraboloidal magnetopause seen from the Sun onto the yz GSM plane. \mathbf{B}_{GM} is the inner magnetospheric magnetic field of Alexeev et al. (2003) and \mathbf{B}_{MS} is the fully draped magnetosheath magnetic field of Cooling et al. (2001). The IMF components in nanoTesla and the Earth's dipole tilt angle, ψ , are shown on the top of each panel.

the observed direction of Double Star TC1's plasma jet occurs only for the east-west sense.

Looking at panel b) in Figure 6.10, only Themis A's jet direction is shown (black

arrow at $y_{GSM} \sim 3 R_E$) since Double Star TC1 did not have ion plasma data available for that period. However, as already analyzed in Section 6.1.1, electron pitch angle distributions (see Figure 6.5) suggest that Double Star TC1 should be northward of the X-line, as it is indicated by the filled up triangle above Double Star TC1’s ‘X’ mark ($y_{GSM} \sim -6 R_E$). The maximum shear X-line location agrees with Double Star TC1’s observations with respect to the north-south sense. Without ion plasma flow data it is not possible to infer the east-west sense of the jet at Double Star TC1’s location relative to the assumed X-line. As for Themis A, the result is less clear since for the IMF and dipole tilt angle conditions determined as representative for this event the maximum shear X-line, as obtained in Section 4.1, is collocated with Themis A position. Therefore, it is not possible to state whether the maximum shear X-line prediction agrees with Themis A observation or not since Themis A position falls within the X-line location uncertainty of $\leq 0.5 R_E$ (TRATTNER et al., 2007).

At panel c), the maximum shear X-line is consistent with Cluster 3’s ($y_{GSM} \sim -9 R_E$) north-south jet direction. As for the east-west sense the jet direction has a slightly westward component while the modeled X-line would predict an eastward component of the flow. That follows from the fact that since Cluster 3’s position is closest to the antiparallel branch of the X-line, where the shear angle is near 180° , rather than to the tilted subsolar branch (where the flows above the X-line should have a westward component), it would be expected reconnection flows with a prevailing eastward component. Thus, for Cluster 3’s reconnection jet observation the maximum shear X-line location agrees only with the north-south sense of it. Concerning the Themis B ($y_{GSM} \sim 9 R_E$) reconnection jet observation the maximum shear X-line fails to predict the north-south sense of the observed jet. Based on the assumption of locally perpendicular (to the X-line) reconnection flows, the north-south prediction of the plasma jet at Themis B location would be a southward directed flow. As for the east-west sense, the prediction is not so clear even considering the simple assumption of locally perpendicular reconnection flows. Since Themis B location is near the junction between the antiparallel and tilted subsolar X-line branches, perhaps at this location the westward flow component arising from the former would cancel out the eastward flow component arising from the latter as a result from Themis B being approximately equidistant from both branches, thus there would be no net contribution to the jet direction in the east-west sense, but only north-south. In summary, it is concluded that the maximum shear X-line location fails to predict the north-south component of Themis B’s jet direction, as mentioned above, whilst the east-west sense prediction is not clear.

At panel d), the maximum shear X-line prediction for Themis C ($y_{GSM} \sim 3 R_E$) jet observation is similar to that of Themis A shown in panel b) of Figure 6.10. Likewise, Themis C location is collocated with the tilted subsolar X-line, so it is not possible to infer whether the jet direction prediction agrees with the observation or not. On the other hand, at Themis A location ($y_{GSM} \sim 10 R_E$ in panel d)) the maximum shear X-line correctly predicts the southward component flow of Themis A's jet. As for the east-west sense, the maximum shear X-line prediction is not so clear based on the premise that the reconnection outflow direction should be locally perpendicular to the X-line. Perhaps the same argument used for Themis B's jet prediction on the 2009-05-22 event shown in panel c) of Figure 6.10 can be used here, namely the eastward and westward flow components arising from the X-line's subsolar tilted and antiparallel branches, respectively, cancel each other out and the remaining flow component is directed southward.

6.1.2.2 Maximum Chapman-Ferraro Current Density test (GONZALEZ; MOZER, 1974)

Figure 6.11 shows the Gonzalez and Mozer (1974) X-line model test against quasi-simultaneous plasma jet observations in the same format presented in Figure 6.10. At this time, the color coding shows the Chapman-Ferraro current density magnitude, $|\mathbf{J}_{CF}|$ in units of mA/meter (see Section 4.2 for details on how $|\mathbf{J}_{CF}|$ was calculated). The plotted X-line points (filled black circles) represent locations on the modeled magnetopause surface where $|\mathbf{J}_{CF}|/|\mathbf{J}_{CF}^{max}| > 0.7$, where $|\mathbf{J}_{CF}^{max}|$ is the maximum current density magnitude value over the whole magnetopause surface. The reason of this threshold value is the following: any threshold value would specify an X-line length in such a way that the higher thresholds, the shorter would be this length since one would have a lesser number of points satisfying this condition. Since there was an event (2009-05-22, panel c, Figure 6.11) with a spacecraft separation in the y_{GSM} direction of more than $\sim 17 R_E$, the chosen $0.7|\mathbf{J}_{CF}^{max}|$ threshold guarantees an X-line length large enough to analyze the jet direction predictions. In the corollary of such (or any threshold) choice, we are implicitly assuming that below this value reconnection does not locally occur, although current density magnitude or current-driven plasma instabilities may be the main magnetic reconnection drivers.

For panel a) in Figure 6.11, only Cluster 4's ($y_{GSM} \sim 2 R_E$) jet direction would be correctly predicted by the present X-line model location. Apart from the noon-midnight meridian ($y_{GSM} > 0$) the X-line, which is southward of Cluster 4's location, tends to curl up towards the northward-duskward sector of the magnetosphere, which

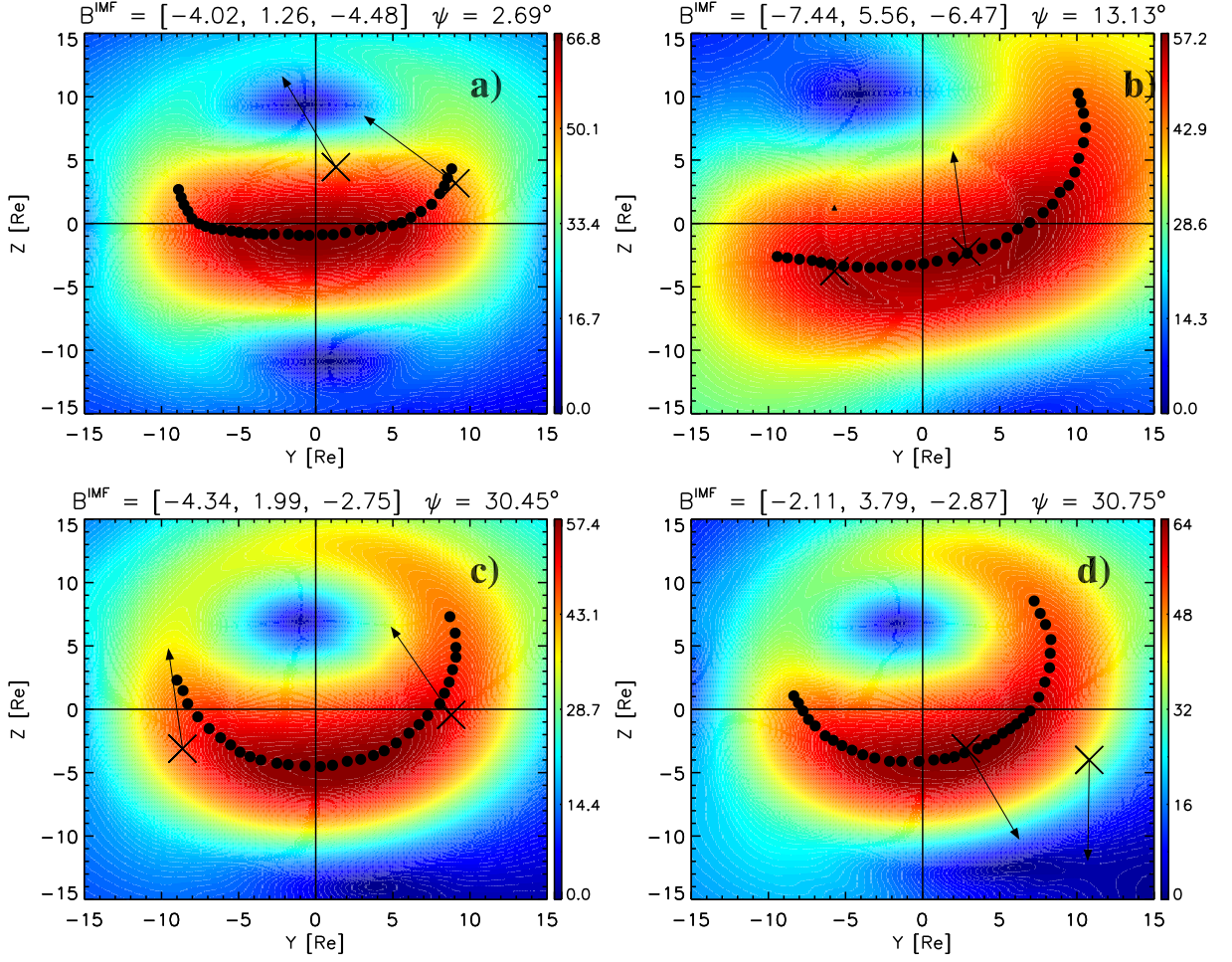


Figure 6.11 - Gonzalez and Mozer (1974)'s X-line model test against quasi-simultaneous magnetic reconnection plasma jet observations. Panels a) through d) correspond to the reconnection events described in Sections 6.1.1.1 through 6.1.1.4, respectively. The X-line (filled black circles) is defined where the Chapman-Ferraro current density magnitude, $|\mathbf{J}_{CF}|$, is greater than 70% of its maximum value, $|\mathbf{J}_{CF}^{max}|$, over the whole modeled magnetopause surface. The plasma jet directions are represented by black arrows of same length while the spacecraft positions at the magnetopause crossing by 'X' marks. The color coding shows the $|\mathbf{J}_{CF}|$ value over the magnetopause surface, in units of mA/meter, seen from the Sun onto the yz GSM plane. $\mathbf{J}_{CF} = (1/\mu_0)\nabla \times (\mathbf{B}_{MS} - \mathbf{B}_{GM})$, being \mathbf{B}_{MS} and \mathbf{B}_{GM} the magnetosheath and inner magnetospheric magnetic field models of Cooling et al. (2001) and Alexeev et al. (2003), respectively. The IMF components in nanoTesla and the Earth's dipole tilt angle, ψ , are shown on the top of each panel.

in turn would be consistent with the westward jet component observed on Cluster 4's location assuming, again, locally perpendicular (to the X-line) reconnection outflows. The northward jet component would be explained by the model X-line as well since

the X-line lies below the spacecraft position. As for Double Star TC1's ($y_{GSM} \sim 9 R_E$) jet observation, the X-line model fails to predict both the jet's north-south and east-west sense. For the current Double Star TC1 position the X-line model would predict southward and eastward flows.

Moving on to panel b), where the reconnection event reported by [Dunlop et al. \(2011\)](#) is being used, the maximum Chapman-Ferraro current density X-line predicts Double Star TC1's ($y_{GSM} \sim -6 R_E$) jet with both southward and westward components. Regarding the observed jet's north-south sense, the X-line model does not predict it correctly, since according to observations, Double Star TC1 should be located above the assumed X-line. It is noticed, however, that the distance, along the paraboloidal magnetopause surface, between Double Star TC1 and the X-line's segment closest to Double Star TC1 location is $\sim 0.56 R_E$, which is slightly above the assumed uncertainty of the X-line location ($\leq 0.5 R_E$), so the X-line's jet direction prediction is considered valid for Double Star TC1. As already mentioned above, with no ion plasma data available at the analyzed period, it was not possible to infer Double Star TC1's location relative to the assumed X-line with respect to the east-west sense. Therefore, the east-west X-line's jet direction prediction could not be tested. For Themis A's ($y_{GSM} \sim 3 R_E$) jet observation, the X-line's jet direction prediction is not clear, since Themis A position falls within the X-line location uncertainty of $\leq 0.5 R_E$.

At panel c), neither Cluster 3 ($y_{GSM} \sim -9 R_E$) nor Themis B ($y_{GSM} \sim 9 R_E$) jet's north-south sense are correctly predicted for the X-line location shown. The model would predict jets with southward components as opposed to the observed northward flow components. At Cluster 3 location the predicted east-west sense of the plasma jet should be westward. Furthermore, based on the simple assumption considered before of locally perpendicular (to the X-line) reconnection outflows, such westward component should be large. The observed Cluster 3 jet has a small westward component compared to its northward component ($V_y^{jet}/V_z^{jet} \sim 0.1$), but even so the X-line model correctly predicts the westward sense of the Cluster 3 jet. The same did not occur for Themis B. Based on Themis B location, the inferred reconnection jet direction by the model X-line should have a southward-eastward direction, which is precisely opposite to what was observed, i.e. a northward-westward jet direction.

For panel d), Themis C's ($y_{GSM} \sim 3 R_E$) jet prediction by the X-line model is uncertain, since the spacecraft position falls within the X-line location uncertainty, as it was the case for Themis A spacecraft in the previous analyzed event (2007-

06-14, panel b). Thus, no jet direction prediction is available for Themis C. As for Themis A ($y_{GSM} \sim 10 R_E$, panel d), the jet direction prediction would result in a southward-eastward directed jet assuming, as before, locally perpendicular (to the X-line) reconnection outflows. The north-south sense prediction agrees with the observed jet's north-south sense, but no eastward jet component was observed as expected. Hence, for Themis A location, the X-line model prediction of the jet direction agrees only with the observed north-south sense.

6.1.2.3 Maximum Reconnection Outflow Speed test (SWISDAK; DRAKE, 2007)

Following the same format presented in previous sections, the observed plasma jet directions in GSM coordinates for the quasi-simultaneous reconnection events, and the X-line generated via the Maximum Reconnection Outflow Speed model are shown in panels a), b), c) and d) of Figure 6.12. Akin to the procedure adopted in the Gonzalez and Mozer (1974) model, we plot the points composing the X-line for which the respective V_{out} value is greater than 70% of the maximum V_{out} value over the whole dayside magnetopause. This percentage was chosen to limit the X-line extension over the dayside magnetopause. We also believe that the higher V_{out} values, the higher is the probability for reconnection to occur, since according to Swisdak and Drake (2007) the reconnection rate, which scales proportionally to V_{out} , should also be higher.

Before discussing the results, we want to draw the reader's attention to some artifacts that appear in all panels of Figure 6.12. They are present on the dusk region ($y_{GSM} \sim 10 R_E$), both above ($z_{GSM} \sim 4 R_E$) and below ($z_{GSM} \sim -4 R_E$) the equator at panels a) and b), and only above the equator at panels c) and d). Such artifacts are believed to be related with the method used to find the modeled BATS-R-US magnetopause, described in Section 4.3.2.2. If any point (filled black circles) pertaining to the X-line happened to fall within such regions, that point was removed from the plot. These artifact regions, when present, were usually small as compared to the whole plotted region, and their presence could easily be detected, which did not jeopardize the analysis.

Looking at Figure 6.12, we first notice the X-line (filled black circles) general behavior as the IMF changes. For a major southward ($B_z < 0$ [nT]) IMF component, as it is the case at panel a), the X-line is roughly parallel to the equator presenting, at the dusk sector, a slight tilt towards the northern hemisphere, which is consistent with a component reconnection X-line type (GONZALEZ; MOZER, 1974; SONNERUP,

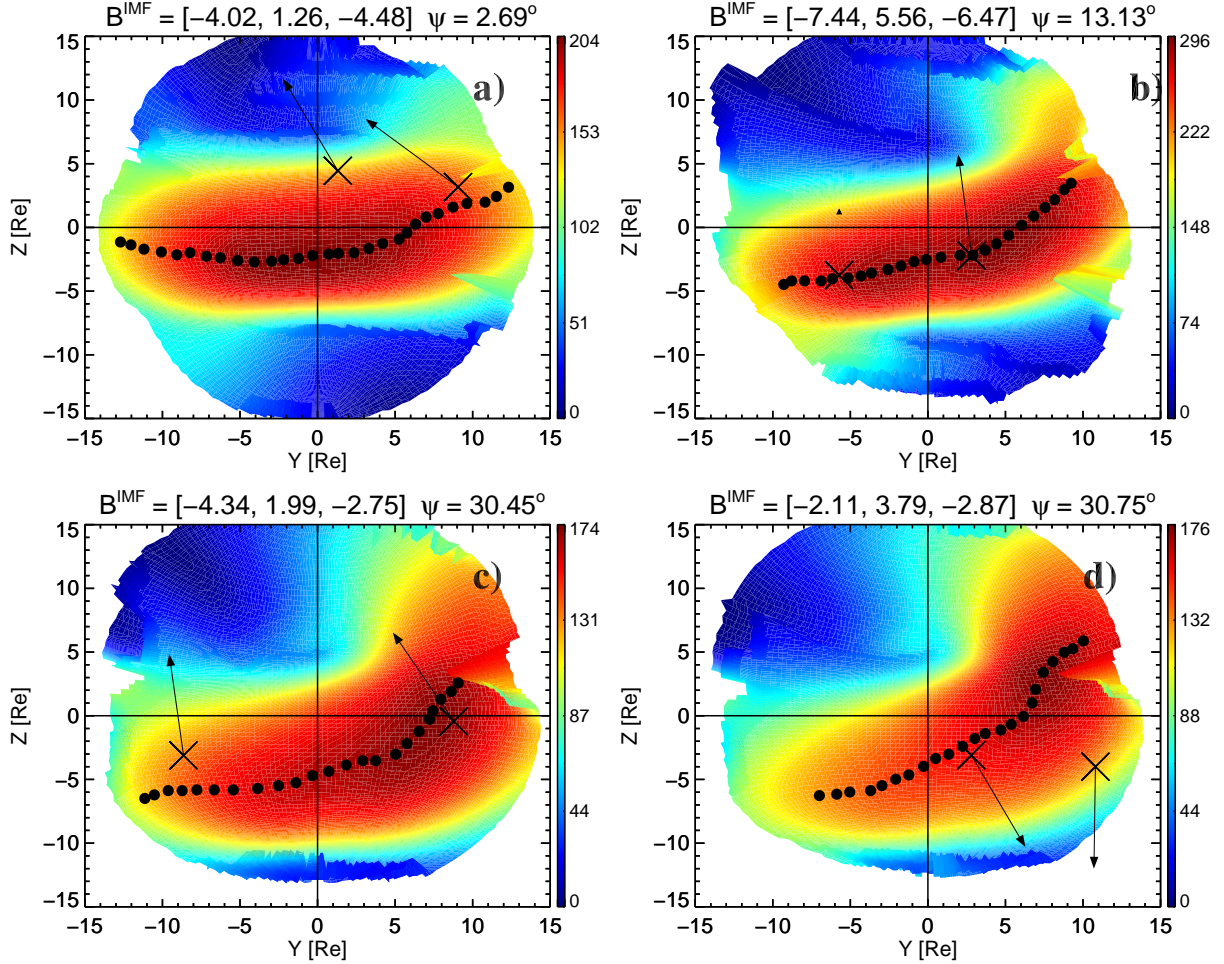


Figure 6.12 - Swisdak and Drake (2007)'s X-line model test against quasi-simultaneous magnetic reconnection plasma jet observations. Panels a) through d) correspond to the reconnection events described in Sections 6.1.1.1 through 6.1.1.4, respectively. The X-line (filled black circles) is defined where the reconnection outflow speed, V_{out} , is greater than 70% of its maximum value, V_{out}^{max} , over the whole modeled magnetopause surface. The plasma jet directions are represented by black arrows of same length while the spacecraft positions at the magnetopause crossing by 'X' marks. The color coding shows the V_{out} value over the magnetopause surface, in units of km/s, seen from the Sun onto the yz GSM plane. The blank region correspond to the post-terminator ($x_{GSM} < 0 R_E$) region. The IMF components in nanoTesla and the Earth's dipole tilt angle, ψ , are shown on the top of each panel.

1974). This is not surprise since the Swisdak and Drake (2007) model was derived based on the component reconnection premise that magnetic fields with orientations other than anti-parallel, i.e., with shear angles less than 180° , may reconnect. As the east-west IMF (B_y) component becomes comparable to the B_z component (panels b and c), the overall reconnection X-line's tilt relative to y_{GSM} axis becomes higher as compared with the X-line inclination at panel a). Lastly, when the IMF B_y surpasses the B_z component at panel d), the X-line tilt becomes even more pronounced.

We start out the results in panel a) of Figure 6.12. At both spacecraft locations, as shown by the 'X' marks, the X-line location correctly predicts both north-south and east-west sense of the observed plasma jets. Assuming once again that the reconnection flows are perpendicularly oriented relative to a local X-line segment, the pronounced westward sense of the plasma jet at Double Star TC1's location ($y_{GSM} \sim 9 R_E$) would suggest an X-line segment, at that location, with a higher tilt relative to the y_{GSM} axis.

Moving on to panel b), we can not say much about the X-line model prediction since both spacecraft locations practically coincide with that of the X-line. Perhaps one would be able to argue that at Double Star TC1's location ($y_{GSM} \sim -6 R_E$) the X-line was slightly southward of it, and therefore the X-line location would be consistent with Double Star TC1 observations, but due to their proximity to the X-line of about $0.1 R_E$ such a conclusion may not be the most acceptable. In the THEMIS A case ($y_{GSM} \sim 3 R_E$), it is even harder to reach a conclusion. The observed jet direction suggests an X-line located southward of the spacecraft. If the X-line was below THEMIS A, it would correctly predict both north-south and east-west sense of the observed jet direction. On the contrary, if it was above the X-line model it would fail to predict any sense of the observed jet direction.

At panel c), only at CLUSTER 3's location ($y_{GSM} \sim -9 R_E$) the X-line prediction agrees with the observed jet direction. Still looking at CLUSTER 3's neighbourhood, if we judge from the local X-line segment inclination relative to y_{GSM} axis, we would expect a plasma jet direction with a strong north-south component, and a small west component, as observed. Such a signature would be consistent with the reconnection plasma jet being locally perpendicular to the local X-line segment. At THEMIS B location, however, the X-line model fails to predict both north-south and east-west sense of the observed jet direction. While at THEMIS B position a northward-westward plasma jet direction is observed, a precisely opposite (southward-eastward) jet direction is predicted.

At panel d), the jet direction prediction at THEMIS C location ($y_{GSM} \sim 3 R_E$) agrees well with the observed plasma jet direction assuming, as we have done throughout this Chapter, that reconnection plasma jets are oriented perpendicularly to the adjacent X-line segment. Regarding the X-line prediction at THEMIS A's location ($y_{GSM} \sim 10 R_E$), we can only say that the due southward orientation of the observed plasma jet was correctly predicted. The almost purely southward observed jet direction suggests an X-line segment nearly parallel to the equator, and above THEMIS A's location. Thus, the current X-line location does not correctly predict the east-west sense of jet direction observed at THEMIS A's position.

6.1.2.4 Summary of X-line models test against quasi-simultaneous magnetic reconnection plasma jet observations

We count the number of times the model X-line location was such that it would correctly predict the north-south (N-S) and/or the east-west (E-W) senses of the observed jet direction at a given spacecraft location. Since there were 4 quasi-simultaneous events with two spacecraft each, the best agreement with observations for a given X-line model would result in 8 N-S and 7 E-W for all reconnection events together. Notice that 7 east-west predictions were available instead of 8 because in the 2007-06-14 event there was no how to determine the east-west sense of one of the spacecraft location relative to the X-line. For each event separately, the model's best agreement with observations would be 2 N-S and 2 E-W for the 2007-03-05 event, 2 N-S and 2 E-W for the 2009-05-22 event, 2 N-S and 2 E-W for the 2009-07-07 event, and 2 N-S and 1 N-S for the 2007-06-14 event. In Table 6.2 both N-S and E-W numbers for each X-line model are shown.

Table 6.2 - Number of times the given X-line model correctly predicted the north-south (N-S) and/or east-west (E-W) senses of the observed plasma jet directions. See text for more details.

| Quasi-simultaneous reconnection event | Trattner et al. (2007) Agreement with observations | | Gonzalez and Mozer (1974) Agreement with observations | | Swisdak and Drake (2007) Agreement with observations | |
|---------------------------------------|---|-----------|--|-----------|---|-----------|
| | N-S | E-W | N-S | E-W | N-S | E-W |
| 2007-03-05 | 1 | 2 | 2 | 1 | 2 | 2 |
| 2007-06-14 | 1 | ? | 1,? | ? | ?,? | ? |
| 2009-05-22 | 1 | 0,? | 0 | 1 | 1 | 1 |
| 2009-07-07 | 1,? | ?,? | 1,? | 0,? | 2 | 1,? |
| | Total N-S | Total E-W | Total N-S | Total E-W | Total N-S | Total E-W |
| | 4 | 2 | 4 | 2 | 5 | 4 |

The question marks in Table 6.2 represent those cases where the X-line prediction was not clear either because the spacecraft location fell within the X-line location uncertainty or the X-line geometry did not allow an unambiguous prediction. If two question marks are present for either north-south or east-west senses, it means that no prediction was possible at both spacecraft locations. If only one question mark is present, it means that at one spacecraft location there was no clear prediction, while at the other the X-line model may or may not have failed to predict the respective observed jet sense, thus we put a one (zero) near the question mark if the X-line model did (not) correctly predict the respective observed jet sense. For the 2007-06-14 event, however, one question mark means that the X-line prediction was unclear only at THEMIS A location, since there was no how to determine the east-west sense of Double Star TC1's location relative to the X-line, due to a lack of ion plasma data for the analyzed period.

If we sum the number of times that a given X-line model correctly predicted only the north-south sense of the observed jet directions, one can see that for the four quasi-simultaneous magnetopause crossing events analyzed here, the Swisdak and Drake (2007)'s X-line model in 5 out of 8 cases performed better than the other models (4 out of 8 cases each).

Turning to the analysis of the X-line model prediction of the east-west sense of the observed jet direction, we will also find that the Swisdak and Drake (2007) model performed better than the other two models, being correct for 4 out of 8 cases. Both Gonzalez and Mozer (1974) and Trattner et al. (2007) were correct in 2 out of 4 cases.

Although the Swisdak and Drake (2007) model has been shown to perform better in predicting both north-south and east-west senses of the observed jet directions in this limited set of quasi-simultaneous observations of magnetic reconnection at Earth's dayside magnetopause, we are aware that such results do not have the desired statistical significance. They do, however, provide us an idea on which X-line model may better represent the large scale feature of dayside magnetopause reconnection on a case-by-case basis.

7 X LINE MODEL COMPARISONS: PART II

7.1 Statistical analysis of single spacecraft magnetopause crossings

Since it was not found a sufficient number of quasi-simultaneous magnetic reconnection events to determine, in a meaningful statistical sense, which X-line model best fits plasma jets' data, as briefly mentioned in the beginning of the previous chapter, a total of 116 events of single spacecraft magnetopause crossings during periods of magnetic reconnection were collected in order to achieve this task.

Before obtaining the aforementioned number of reconnection events, a pre-selection of the magnetopause crossing events was made as follows. Firstly, an online tool¹ developed by the Space Physics Data Facility (SPDF) team at NASA's Goddard Space Flight Center was used in order to generate a list of hourly-averaged, user-specified solar wind data, e.g., southward IMF B_z component and dynamic pressure (P_{dyn}) values belonging to user-defined intervals of $-10 \leq B_z \leq -2$ nT and $1 \leq P_{dyn} \leq 2.5$ nPa. The tool would then look for hourly-averaged solar wind data, as provided by several solar wind monitors, which fall within the pre-defined intervals. The idea of using such a tool was to obtain a list of dates and hours for which the hourly-averaged IMF B_z , as provided by some solar wind monitors, had a southward ($B_z < 0$) component. Secondly, another online tool², also developed by the SPDF team, was used to determine a second list with the date and time when a user-defined number of spacecraft has crossed a modeled magnetopause. In the case of the present work we have chosen a time interval for collecting magnetopause crossing events going from January 2000 until June 2013, and the spacecraft chosen were DOUBLE STAR TC1 and the two satellite constellations THEMIS and CLUSTER. Using the second list we would find the modeled magnetopause crossing dates that matched those on the first list of hourly-averaged solar wind data, and whose model magnetopause crossing times were up to 3 hours after the respective hours on the first list. Such a procedure limited the number of possible magnetopause crossings to be analyzed, and also provided a clue of which dates and hours the IMF would have a non-zero southward ($B_z < 0$) component which is ideal for the dayside reconnection process to occur. After all this process, we had to check whether all remaining events on the second list were indeed corresponding to *real* magnetopause crossings, and if they were we would look for reconnection signatures which will be discussed later on in this Chapter. A total of 116 events fulfilled the criteria in order to be deemed

¹<http://omniweb.gsfc.nasa.gov/form/dx2.html>

²<http://sscweb.gsfc.nasa.gov/cgi-bin/Locator.cgi>

as reconnection events.

We would like to emphasize that a much larger number of reconnection events must have occurred during an almost 13-year period. The fact we have found only 116 events is the result of the pre-selection described above which limited the analyzed time period for which hourly-averaged IMF B_z was negative.

The dataset spans the time period from June 2002 up to March 2013. From the total number of events, 90 (78%) were given by THEMIS, 19 (16%) by CLUSTER and 7 (6%) by DOUBLE STAR TC1 spacecraft.

As mentioned in the beginning of Section 6.1.1, the OMNI dataset, which was used as the main source for probing solar wind’s plasma parameters in this study, must be either averaged over some time period depending upon the steadiness of the IMF or to be propagated/time-shifted to the spacecraft position on the magnetopause in order to compose a representative set of solar wind parameters for the event being analyzed. The latter method was pursued since steady solar wind conditions were not often found. When the OMNI data were not available, other ways of determining the solar wind conditions were used. These methods are going to be described in details in the following sections.

7.1.1 Obtaining solar wind’s magnetic field and plasma parameters

In what follows, the methods to determine the solar wind’s plasma conditions near the magnetopause are presented.

7.1.1.1 Time-shifting OMNI’s data

Although the OMNI data have been already time-shifted from a solar wind probe to the bow shock nose, we need to time-shift the data to the magnetopause.

It is worthwhile to emphasize that the time-shifting process does not alter the data values at all, but only changes their time tags so we can estimate the appropriate solar wind conditions for a given event. By using a time-shifting procedure it is assumed that the magnetosheath magnetic field is being convected along with the magnetosheath flow, and also that the plasma properties remain unchanged. For the magnetosheath region as a whole, the former statement is usually satisfied since the flow is “frozen”³ to the magnetic field, except for the center of reconnecting magnetosheath currents (e.g., Phan et al. (2011)). For the latter statement regarding

³See Section 3.1 for a description of the “frozen-in” concept.

the constancy of magnetosheath plasma parameters, we believe this can generally be the case for time-scales of few ($\lesssim 10$) minutes, as it is the case here. Exception is made, however, when magnetosheath current sheets are present as just mentioned above, which in turn will locally alter the plasma parameters.

The time-shifting method used here estimates the traveling time required for the magnetosheath plasma flow, V_{sh} , from the x GSM coordinate of the Earth's bow shock nose, x_{bsn} , to the spacecraft's x GSM coordinate, $x_{s/c}$. In order to do that, an interval is chosen under the conditions that the spacecraft enters the magnetosheath region and remains there for, at least, two minutes. Then, the corresponding time-averaged values of V_{sheath} (\bar{V}_{sh} [km/s]), x_{bsn} (\bar{x}_{bsn} [R_E]), and $x_{s/c}$ ($\bar{x}_{s/c}$ [R_E]) are computed and the time shift, t_s , is estimated as:

$$t_s = \frac{6374}{60} \frac{\bar{x}_{bsn} - \bar{x}_{s/c}}{\bar{V}_{sheath}} \quad [\text{minutes}]. \quad (7.1)$$

The time intervals the spacecraft spent in the magnetosheath region varied between 4 minutes and 1 hour following the magnetopause crossing time. The t_s values ranged between 2.18 and 12.47 minutes as it can be seen in the histogram shown in Figure 7.1. The majority (68%) of the events for which the time-shifting method was applicable (a total of 109 events) had $t_s \leq 5$ minutes. The method was usable whenever the spacecraft remained two minutes or more within the magnetosheath, and when both ion plasma flow and OMNI data were available. Since x_{bsn} values had one minute resolution, a less than two minutes period within the magnetosheath wouldn't allow t_s to be obtained through an average, which is the reason why the two minutes threshold mentioned above was chosen.

Within the OMNI dataset context, the Farris and Russell (1994) bow shock stand off distance model (R_{bsn} , equation 11 of their paper) is used to determine x_{bsn} in equation 7.1 in the following way:

$$x_{bsn} = -\frac{R_{bsn} V_x^{sw}}{|\mathbf{V}^{sw}|} \quad [R_E], \quad (7.2)$$

where \mathbf{V}^{sw} is the solar wind (sw) flow velocity corrected for the orbital motion of ~ 30 km/s of the Earth around the Sun, and V_x^{sw} represents its x GSM component. After time-shifting OMNI data, the IMF was taken at the same time tag of the spacecraft's magnetopause crossing.

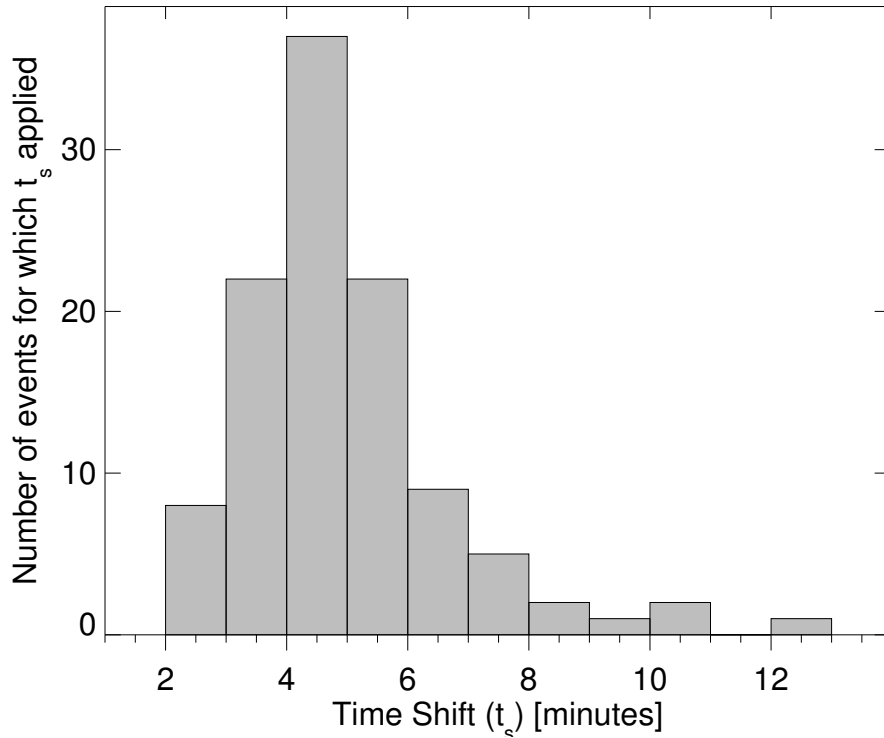


Figure 7.1 - Time-shifting histogram for a total of 109 events for which the method was applicable (see text for details). The binsize is one minute.

7.1.1.2 5 minutes average from OMNI data

Whenever the spacecraft remained for less than two minutes⁴ in the magnetosheath region, and when there was OMNI data available for a time period of, at least, 20 minutes encompassing the spacecraft magnetopause crossing time, the IMF was considered to be given as a 5 minutes average taken before the spacecraft crossed the magnetopause. Such an interval was chosen based on the results found in the previous subsection where for 68% of the events (74/109) for which the time-shifting process was applicable, the time-shifting period, t_s , was less than or equal to five minutes. For such an interval the ratio of the standard deviation of each IMF component, $\sigma_{sd}^{B_i^{IMF}}$, did not surpass 20% of their respective absolute mean values, i.e. $\sigma_{sd}^{B_i^{IMF}} / |B_i^{IMF}| \leq 0.2$, where $i = x, y, z$. Only two events met these criteria: CLUSTER 4 on 2011-06-12, and THEMIS D on 2013-02-24.

⁴Refer to Section 7.1.1.1 for the reasoning behind the two minutes threshold.

7.1.1.3 Cross-correlation with ACE's magnetic field data

Cross-correlation between the Advanced Composition Explorer's (ACE, Stone et al. (1998)) and a magnetopause crossing spacecraft's magnetic field data was used only for two events (both THEMIS D and E spacecraft) since there was no OMNI data available for the analyzed period. The purpose of the method is to find the amount of time by which ACE's magnetic field data need to be lagged/shifted in order to have the best linear correlation with THEMIS magnetic field data. Such a method can be used only when THEMIS, or whatever spacecraft used, is within the magnetosheath region. The premise is that when the IMF, as measured by ACE, crosses the Earth's bow shock the IMF clock angle, $\theta_{ACE} = \tan^{-1}(B_y^{IMF}/B_z^{IMF})$, is largely conserved, thus clock angle values in the magnetosheath, as measured by THEMIS, will be somewhat similar to those in the interplanetary medium. For an appropriate time lag applied to ACE's magnetic field data, a positive correlation is expected between the IMF and THEMIS magnetic field clock angles.

The time series of the clock angle of the magnetic field observed by THEMIS in the magnetosheath region, $\theta_{TH} = \tan^{-1}(B_y^{TH}/B_z^{TH})$, and the corresponding time series of ACE's magnetic field clock angle, $\theta_{ACE} = \tan^{-1}(B_y^{IMF}/B_z^{IMF})$, are used and a linear correlation coefficient, l_{cc} ⁵, is obtained for the analyzed time window:

$$l_{cc} = \frac{\sum_{l=1}^{\tau} (\theta_{ACE}^l - \overline{\theta_{ACE}^l}) (\theta_{TH}^l - \overline{\theta_{TH}^l})}{\sqrt{\sum_{l=1}^{\tau} (\theta_{ACE}^l - \overline{\theta_{ACE}^l})^2} \sqrt{\sum_{l=1}^{\tau} (\theta_{TH}^l - \overline{\theta_{TH}^l})^2}}. \quad (7.3)$$

In equation 7.3, τ is the number of clock angle samples within the analyzed time window (of, say, one hour), and the overbar denotes a time average over the whole time window. We used ACE's magnetic field with a time resolution of 16 seconds.

What is done in the cross-correlation method employed here is to time-shift ACE magnetic field data. To this end, we proceed in the following way: firstly, calculate the clock angle (θ_{ACE}), and then apply a 0 seconds time lag, then compute the correlation coefficient l_{cc} and store the value; secondly, for the same θ_{ACE} time series obtained in the previous step apply a 16 seconds time lag, then compute the correlation coefficient l_{cc} and store the value; thirdly, for the θ_{ACE} time series obtained in the first step apply a 32 seconds time lag, then compute the correlation coefficient l_{cc} and store the value, and so forth. The chosen time lag will be such

⁵See e.g., <http://mathworld.wolfram.com/CorrelationCoefficient.html> and references therein.

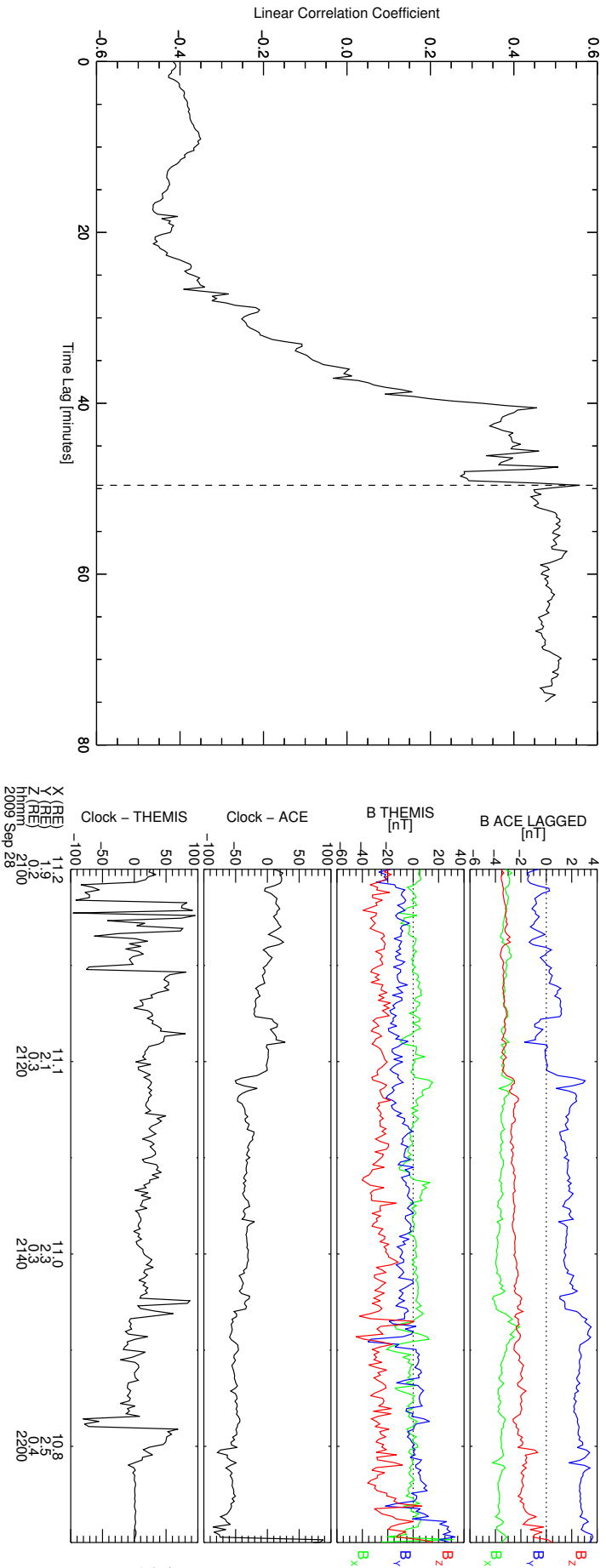


Figure 7.2 - **(Left)** Cross-correlation analysis of the magnetic field clock angle from ACE, $\theta_{ACE} = \tan^{-1}(B_y^{IMF}/B_z^{IMF})$, and THEMIS D, $\theta_{TH} = \tan^{-1}(B_y^{TH}/B_z^{TH})$, spacecraft for the 2009-09-28 reconnection event. The plot shows the linear correlation coefficient, l_{cc} , as function of ACE's magnetic field time lag in minutes. The vertical dashed line marks the time lag, 49.6 min, for which l_{cc} is a maximum. In this case $l_{cc} = 0.558$. **(Right)** 1 hour and 10 minutes interval in which THEMIS D spacecraft spent in the magnetosheath region on 2009-09-28. From top to bottom: 16 seconds resolution (time lagged) magnetic field data from ACE spacecraft in GSM coordinates, THEMIS D magnetic field data with spin-averaged ($\sim 3s$) resolution also in GSM coordinates, IMF clock angle (in degrees) from ACE (θ_{ACE}), and finally THEMIS D magnetic field clock angle (θ_{TH}) in degrees. The time lag applied to ACE's magnetic field data of 49.6 min was obtained by cross correlation analysis according to the description of the left panel.

that it maximizes l_{cc} , as presented in the left panel of Figure 7.2, which shows l_{cc} as function of the time lag applied to the 2009-09-28 reconnection event used in this study. The vertical dashed line in the left panel of Figure 7.2 indicates the time lag (49.6 min) for which l_{cc} reaches its maximum value, which is 0.558. Notice that both the time window size (1 hour and 10 minutes in this case) within which each l_{cc} value will be evaluated and the θ_{TH} time series (bottom panel on the right side of Figure 7.2) remain the same in the entire process.

The right side of Figure 7.2 shows, from top to bottom, an 1 hour and 10 minutes interval of: ACE's 16s resolution magnetic field data that has been time lagged by 49.6 min following the cross-correlation analysis; THEMIS D spin-averaged (~ 3 s) magnetic field data; ACE's (time lagged) magnetic field clock angle, θ_{ACE} , and THEMIS D magnetic field clock angle, θ_{TH} . The time interval shown concerns the period THEMIS D spent in the magnetosheath before crossing the dayside magnetopause at $\sim 22:12$ UT.

For the THEMIS E 2008-10-22 event (not shown) where the same method was applied, l_{cc} reached 0.601 by taking a 2 hours and 40 minutes interval following THEMIS E magnetopause crossing. In this case, the lag time for which l_{cc} was a maximum was 66.9 minutes. The l_{cc} value had a modest increase relative to the THEMIS D event in spite of current sheets being present in the magnetosheath region. However, if one looks at the linear correlation coefficients between ACE's and THEMIS E's magnetic field components B_z and B_y separately, the respective $l_{cc}^{B_i}$ values, as given by equation 7.4 below, taken where l_{cc} is a maximum, were $l_{cc}^{B_z} = 0.937$ and $l_{cc}^{B_y} = 0.780$. Such high correlation coefficient values of $l_{cc}^{B_z}$ and $l_{cc}^{B_y}$ are attributed to the presence of current sheets in the interplanetary medium, as measured by ACE, which have crossed the Earth's bow shock and have been detected by THEMIS E in the magnetosheath region. On the other hand, for the previously analyzed case of THEMIS D, there were no current sheets (or other structures) in the magnetosheath region that could be matched in the interplanetary medium, resulting in lower $l_{cc}^{B_z}$ and $l_{cc}^{B_y}$ values, i.e., 0.357 and 0.546, respectively.

$$l_{cc}^{B_i} = \frac{\sum_{l=1}^{\tau} (B_{i,ACE}^l - \overline{B_{i,ACE}}^l) (B_{i,TH}^l - \overline{B_{i,TH}}^l)}{\sqrt{\sum_{l=1}^{\tau} (B_{i,ACE}^l - \overline{B_{i,ACE}}^l)^2} \sqrt{\sum_{l=1}^{\tau} (B_{i,TH}^l - \overline{B_{i,TH}}^l)^2}}, \quad i = y, z. \quad (7.4)$$

After time-shifting ACE data, the IMF was taken at the same time tag of the

spacecraft’s magnetopause crossing.

7.1.1.4 ACE’s hourly-averaged magnetic field data

There were 3 events for which there was no OMNI data available within, at least, 20 minutes of the magnetopause crossing time. Thus, no 5 minutes average could be done neither the time-shifting procedure discussed in Section 7.1.1.1. Since the spacecraft, for all 3 cases, did not spend much time (< 15 minutes) within the magnetosheath region the cross correlation analysis with ACE’s magnetic field data could not ensure reliable results and therefore it was not used in such cases. Hence, another procedure had to be performed in order to obtain the representative IMF component values. The chosen method was to hourly average the 16s ACE’s magnetic field components prior to the spacecraft magnetopause crossing. Figure 7.3 shows the 16s resolution magnetic field components B_x , B_y and B_z , measured by ACE during the one hour interval preceding each of the three spacecraft magnetopause crossings: (left panel) THEMIS D on 2013-02-22 at around 12:27:26 UT, (center panel) THEMIS D on 2013-03-08 at around 22:58:21 UT, and (right panel) THEMIS E spacecraft on 2013-03-08 at around 23:19:37 UT.

A common characteristic of all three cases was that the IMF B_z component was directed southward almost the entire interval, with average values less than or equal to -2.1 nT. The average B_x component in two cases (left and center panels) was near zero (~ 0.3 nT), while in the remaining case it was mainly negative (-1.4 nT). For two events displayed on the center and right panels of Figure 7.3 the average B_y was positive, i.e., 1.7 and 0.5 nT, respectively, while for the remaining event (left panel) it was mainly negative (-3.9 nT).

7.1.2 Interplanetary magnetic field conditions for the statistical survey

After using all the methods described in the previous subsections to determine the IMF conditions, it is presented in Figure 7.4 histograms of the observed IMF components, B_x (top left), B_y (top right), and B_z [nT] (bottom left) for all 116 reconnection events used in this study. Also, a histogram of the Earth’s dipole tilt angle is shown in the bottom right panel of Figure 7.4 for all events as obtained by [Tsyganenko and Stern \(1996\)](#)’s (T96) magnetosphere magnetic field model. The solar wind dynamic pressure values were fairly typical, i.e., for all our events they belonged to the interval $1 < P_{dyn} < 2.5$ nPa, thus the dayside magnetopause was not under significant compression.

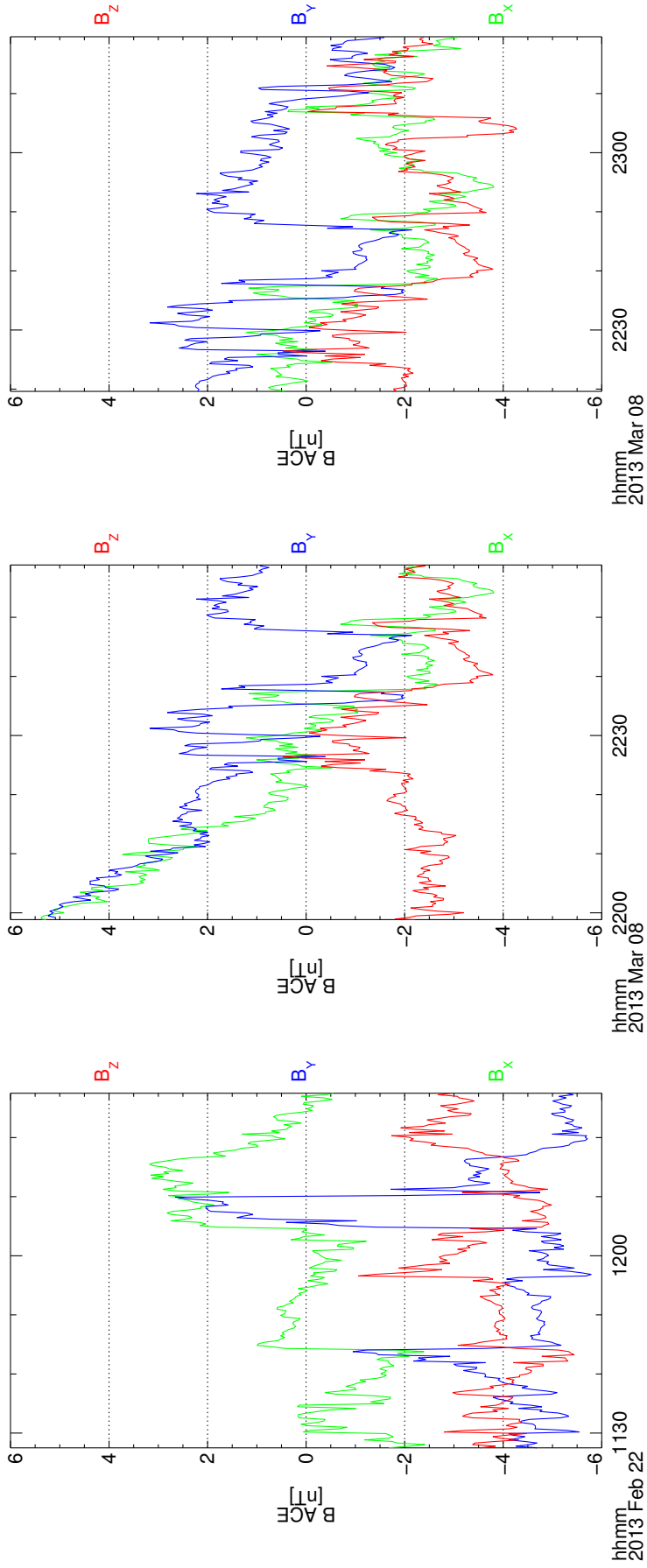


Figure 7.3 - 16 seconds resolution magnetic field data from ACE spacecraft in GSM coordinates for an one hour interval preceding the magnetopause crossing of **(left panel)** THEMIS D on 2013-02-22 at around 12:27:26 UT, **(center panel)** THEMIS D on 2013-03-08 at around 22:58:21 UT, and **(right panel)** THEMIS E spacecraft on 2013-03-08 at around 23:19:37 UT.

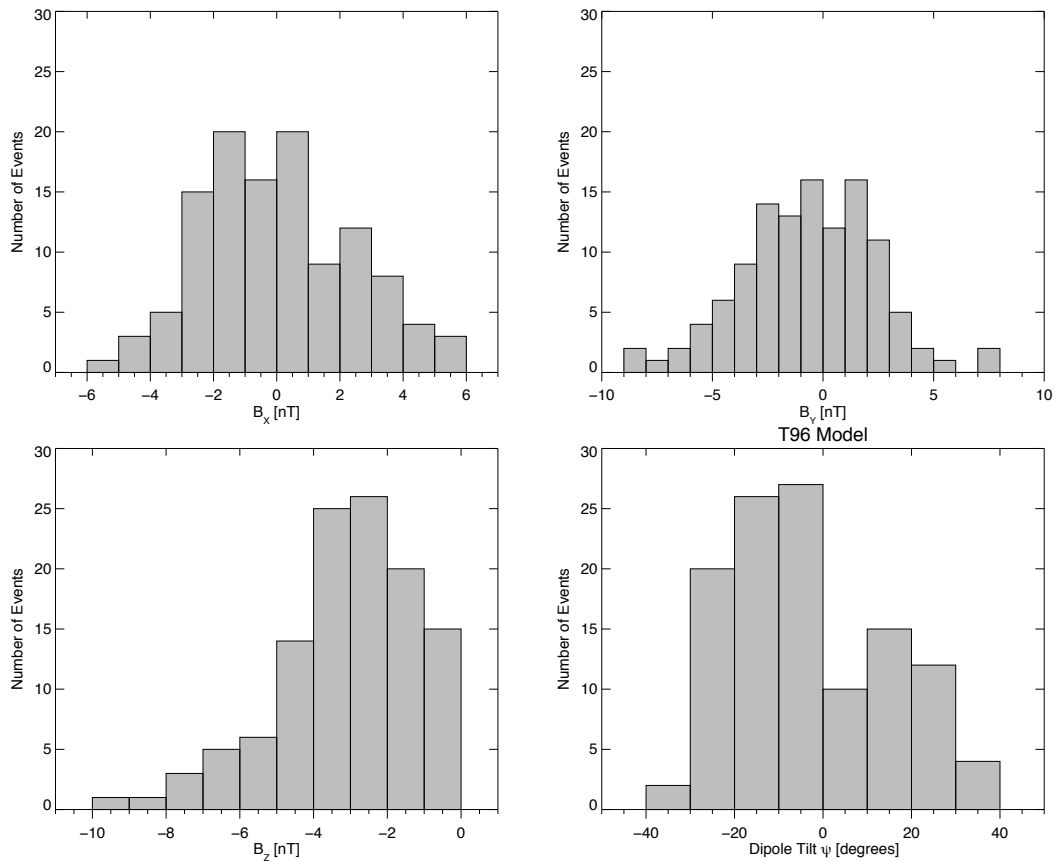


Figure 7.4 - Histograms of IMF components B_x (top left), B_y (top right), and B_z [nT] (bottom left), and at the bottom left panel the Earth's dipole tilt angle as obtained by [Tsyganenko and Stern \(1996\)](#)'s (T96) magnetosphere magnetic field model, for the 116 reconnection events analyzed in this work.

7.1.3 Single spacecraft observations of magnetic reconnection events

7.1.3.1 Reconnection signatures

In this section we show an example of a single spacecraft magnetopause crossing event, and the criteria used to categorize it as a reconnection event.

A typical reconnecting magnetopause layer found in our survey is shown in Figure 7.5 which shows, from top to bottom, a ten-minute period data of magnetic field and ion velocity components in boundary normal coordinates LMN, velocity magnitude, ion density, and ion omni-directional energy flux provided by the THEMIS E spacecraft on 2008-10-22. THEMIS E was in an outbound trajectory, i.e., it was going from the magnetosphere into the magnetosheath. Between $\sim 15:42:20$ and $\sim 15:43$ UT THEMIS E first traverses the low-latitude boundary layer (LLBL), a region with ion density values in between the typical magnetosphere ($\sim 0.3 \text{ cm}^{-3}$) and magnetosheath ($\sim 10 \text{ cm}^{-3}$) values. A second traversal of the LLBL occurs between $\sim 15:48$ and $\sim 15:49:20$ UT. At this region a mixed plasma population constituted by both magnetosphere and magnetosheath particles is present, i.e., ion plasma populations with energies of $\sim 9 \text{ keV}$ and $\sim 0.35 \text{ keV}$, respectively.

THEMIS E has encountered the magnetopause a number of times before finally exiting the magnetosphere at around 16:12 UT (not shown). A magnetopause crossing is identified here where the B_L (north-south) component of the magnetic field changes sign, going in this case from magnetospheric ($B_L > 0$) to magnetosheath orientation ($B_L < 0$). In Figure 7.5 two magnetopause crossings are identified according to this criterion, with the first one occurring at around 15:45:10 UT and the second one at $\sim 15:48$ UT. We focus on the magnetic field and plasma observations around the first of these magnetopause crossings.

The most noticeable characteristic of Earth's dayside magnetopause reconnection as observed during a magnetopause crossing by a spacecraft is the reconnection plasma jet. Plasma jet is due to a local enhancement of the plasma speed usually at the earthward side of the magnetopause, caused by the relaxation of newly, sharply-bent reconnected field lines resulting in energy transfer from the magnetic form to plasma kinetic energy form. Such a plasma speed enhancement is exemplified in the third panel of Figure 7.5 at around 15:44 UT, when the ion plasma speed reaches $\sim 230 \text{ km/s}$ corresponding to an increase of $\sim 90 \text{ km/s}$ relative to magnetosheath values of around 140 km/s . This local acceleration occurred on the earthward side of the magnetopause where the local magnetic field orientation was

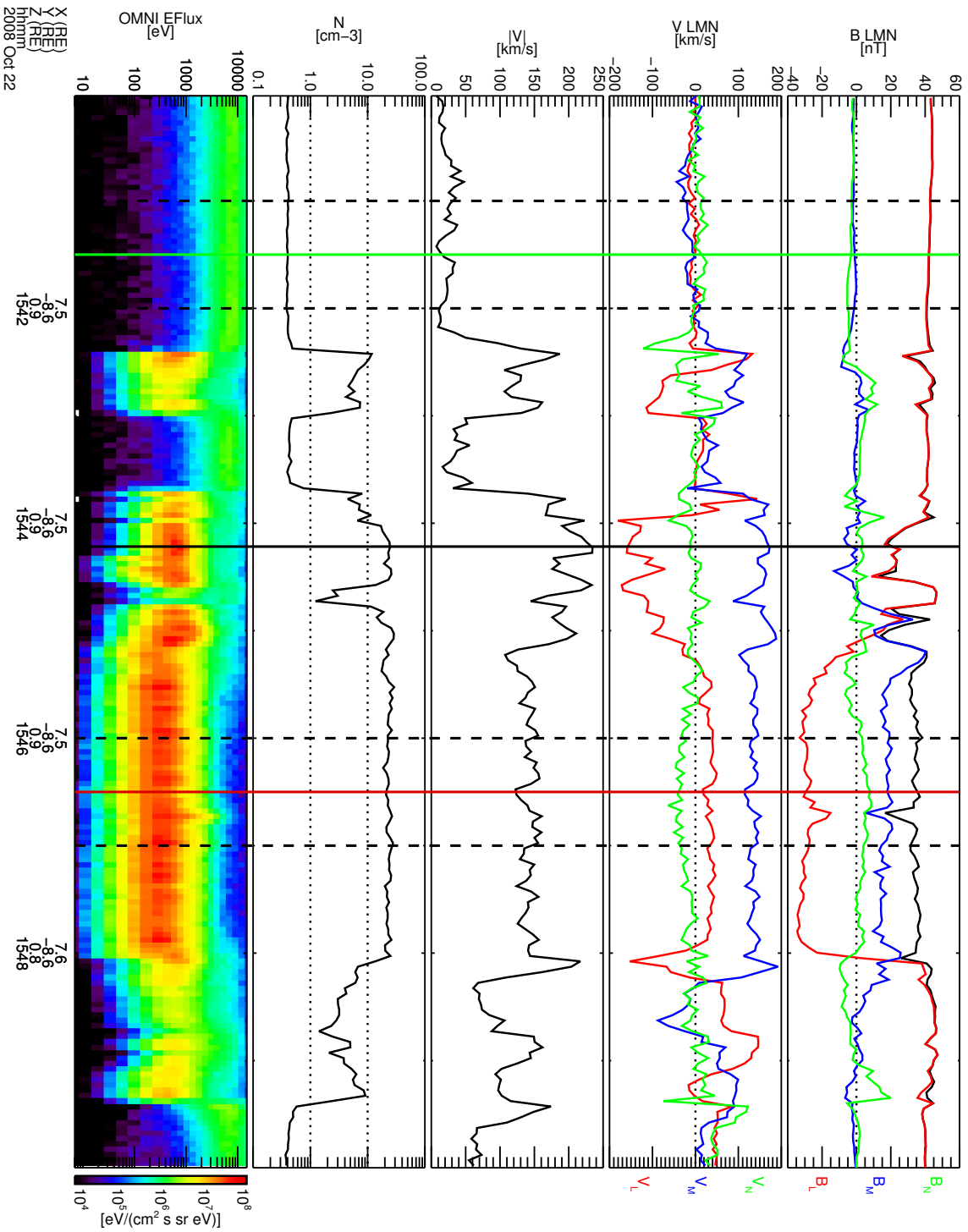


Figure 7.5 - THEMIS E outbound magnetopause crossing event on 2008-10-22. From top to bottom are shown the magnetic field and ion velocity components both in boundary normal coordinates LMN, the ion velocity magnitude, the ion density, and the ion omni-directional energy flux spectra. The two pairs of vertical dashed lines demarcate the one-minute time intervals from which the magnetosheath (rightmost pair) and magnetosphere (leftmost pair) parameters are averaged out for this event. The three vertical solid lines mark instants of time when the ion omni-directional energy flux data (bottommost panel) is going to be analyzed into more details in Figure 7.6.

mainly northward ($B_L > 0$). Another characteristic that favors the reconnection interpretation in this magnetopause crossing event is that the adjacent magnetosheath magnetic field was mainly southward ($B_L < 0$) with a magnetic shear angle $\theta_{shear} = \cos^{-1}[\mathbf{B}_{sh} \cdot \mathbf{B}_{sp}/(|\mathbf{B}_{sh}||\mathbf{B}_{sp}|)]$ of $\sim 148^\circ$, indicating magnetic fields with a major antiparallel component, which in turn favors reconnection on the dayside magnetopause (DUNGEY, 1961). \mathbf{B}_{sh} and \mathbf{B}_{sp} are the magnetosheath and magnetosphere magnetic fields, respectively, averaged over the one-minute period demarcated by the 2 pairs of dashed vertical lines.

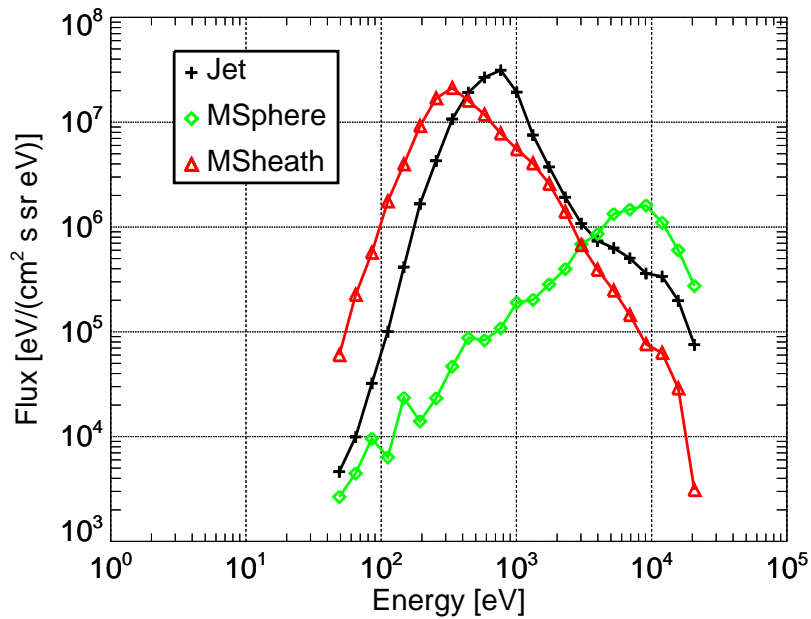


Figure 7.6 - Plot of ion energy flux versus ion energy extracted from the ion omnidirectional energy flux data at three instants of time (thick vertical lines in the bottom panel of Figure 7.5) for the THEMIS E magnetopause crossing event on 2008-10-22 shown in Figure 7.5. The green, black and red curves correspond to the magnetosphere (at 15:41:30 UT), the plasma jet (at 15:44:13 UT) and magnetosheath (at 15:46:30 UT) regions, respectively.

An important evidence that favors the reconnection interpretation for the observed flow acceleration seen in the example shown here and in a large portion (94%) of all other events analyzed in this work, can be viewed in Figure 7.6. There, three curves of the ion energy flux versus the ion energy are presented as *representatives* of three different regions shown in Figure 7.5: the magnetosphere (green vertical line), the plasma jet (black vertical line) taken at the observed maximum flow speed, and the magnetosheath proper (red vertical line). The curves in Figure 7.6 are obtained from the ion omnidirectional energy flux data shown in the bottommost panel of

Figure 7.5. The green curve of Figure 7.6, for example, shows the ion energy flux as a function of ion energy for the time instant 15:41:30 UT (green vertical line in Figure 7.5). Analogously, the black and red curves were taken at 15:44:13 UT and 15:46:30 UT, respectively. We would like to emphasize in Figure 7.6 the value of ion energy (~ 800 eV) for which the flux is the highest in the plasma jet region (black curve), as compared to that in the magnetosheath (red curve, ~ 350 eV). Also notice that the maximum flux for the black curve is comparable to that in the red curve, and both are roughly one order of magnitude higher than the highest flux in the magnetosphere (green curve). These behaviors suggest that magnetosheath particles are crossing the dayside magnetopause and being detected within the magnetosphere, which has been opened by the reconnection process, and in the meantime they are being accelerated. Within the reconnection scenario, such observed plasma acceleration is due to magnetic tension forces acting on the local plasma which accelerate it as the reconnected and highly tensioned field lines relax toward a state of minimum energy.

In order to confirm the hypothesis raised above, one needs to verify whether the observed plasma flow is Alfvénic or not. Thus, the Walén test, as presented in Section 3.5, is used. The magnetosheath and magnetosphere magnetic fields as well as plasma parameters are one-minute averaged prior to be used as input in the Walén test. In the example shown in Figure 7.5, the magnetic field and plasma parameters lying in between the leftmost (rightmost) pair of vertical dashed lines will be averaged out to in order to represent the relevant magnetospheric (magnetosheath) parameters that are considered to participate in the reconnection process. The criteria used to choose both intervals are the following:

a) Magnetospheric interval

- density values below 1 cm^{-3} ;
- major northward ($B_L > 0$) magnetic field component;
- presence of positively charged particles with energies higher than ~ 8 keV as shown by the ion omni-directional energy flux spectra (when available);
- one-minute interval as close (in time) as possible from the magnetopause satisfying all the requirements above.

b) Magnetosheath interval

- density values usually higher than or equal to 10 cm^{-3} ;

- presence of positively charged particles with energies within the energy range 200 – 350 eV as shown by the ion omni-directional energy flux spectra (when available);
- one-minute interval as close (in time) as possible from the magnetopause satisfying all the requirements above, and taken right after the magnetic field has completed its rotation through the magnetopause boundary.

Once the highest observed plasma jet speed earthward of the magnetopause boundary is identified, both plasma jet magnitude and direction which are going to be used in the Walén test must be subtracted the magnetosheath flow component in order to leave only the part which is supposedly due to the reconnection process.

For the example shown here, the observed to predicted reconnection outflow ratio was $r_{op} = 0.62$, and the direction of the observed jet was $\theta_{op} = 17^\circ$ from the field-aligned direction Walén, which gives $\Delta V_A^* = 0.59$. Although the observed jet magnitude have reached 62% of the predicted outflow speed, the jet direction showed a reasonable agreement with theory. Thus, we attribute the local plasma acceleration at $\sim 15:44$ UT for the THEMIS E magnetopause crossing event shown in Figure 7.5 as being a result from the magnetic reconnection process between the magnetosheath and magnetosphere magnetic fields along the dayside magnetopause. We emphasize that the successful Walén test result ($\Delta V_A^* > 0.5$) was not the only criteria used to deem the analyzed event as a reconnection event. In fact, a series of reconnection-related signatures discussed above were identified for this event, and the Walén test was the ultimate confirmation. When available, either ion or electron pitch angle distributions like those shown in Section 6.1.1 was also used when looking for evidence of open field lines which are an indicative that reconnection has been (or is) operating somewhere around the observation spot (FUSELIER et al., 1995).

Figures 7.7 a) and 7.7 b) show histograms of ΔV_A^* and θ_{op} values, respectively, for all 116 reconnection events analyzed in this work. The same procedure described above was applied for all cases. For the 7 DOUBLE STAR TC1 cases, however, there was no ion omni-directional energy flux spectra available, so the Walén relation was the only quantitative test that could be made. Thus, for these 7 cases the event was deemed as a reconnection event only if $\Delta V_A^* > 0.7$ and $\theta_{op} < 30^\circ$.

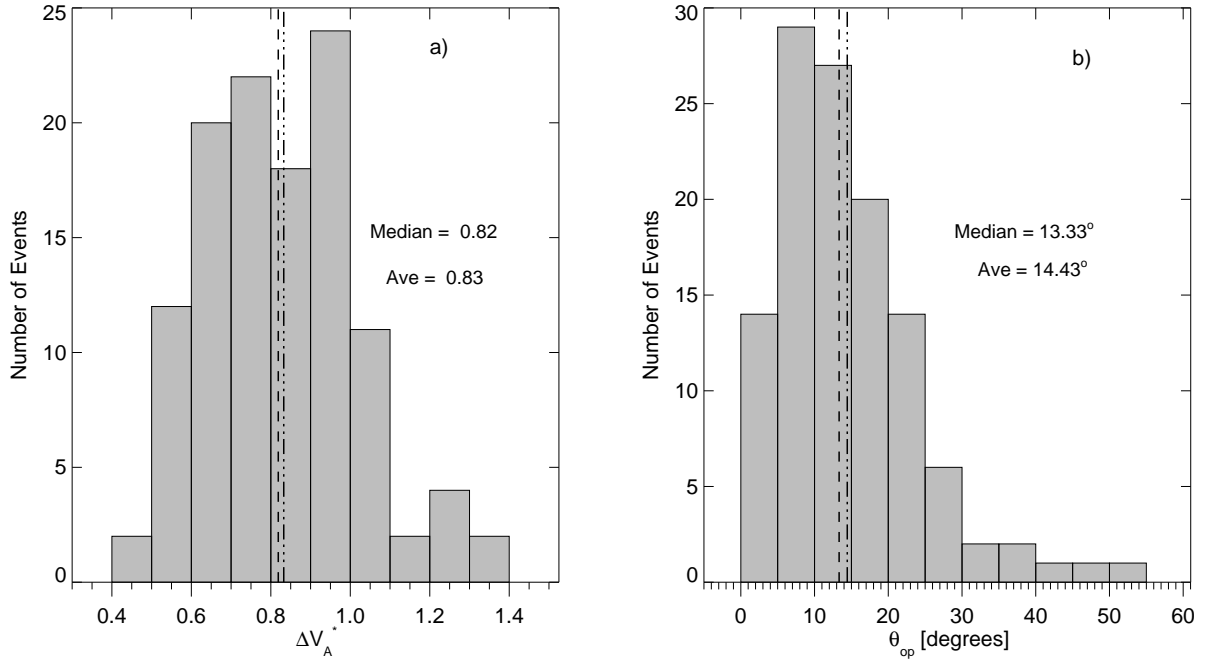


Figure 7.7 - Histogram plots of (a) the quality measure, ΔV_A^* , of the agreement between observed and predicted flow acceleration, and (b) the angular displacement, θ_{op} , of the observed jet direction from the field-aligned direction. Both average and median values of the distribution are indicated on each panel.

7.1.3.2 Large scale picture

Now we put THEMIS E observation into the context of large scale reconnection, looking into more details to the observed jet *direction* in Figure 7.5. The major tangential jet component was southward ($V_L < 0$), indicating that THEMIS E was somewhere southward of an active X-line. Notice also that during the time THEMIS E crossed the reconnection exhaust⁶ between $\sim 15:44$ and $15:45$ UT, there was a small dawnward ($V_M > 0$ or $V_y^{GSM} < 0$) enhancement in the jet direction, relative to the already high dawnward flow of the adjacent magnetosheath, meaning that besides the southward component the jet direction have also a dawnward component. In the component reconnection scenario (GONZALEZ; MOZER, 1974; SONNERUP, 1974), a southward-dawnward reconnection jet detected on the dawn sector ($y_{GSM} < 0$) of the magnetopause would be consistent with a tilted, subsolar X-line extending from the southern-dusk into the northern-dawn quadrants of the magnetopause. The IMF

⁶Region either northward or southward of an X-line where the accelerated plasma flows are detected by the spacecraft.

required for such an X-line orientation would have to have both southward ($B_z^{GSM} < 0$) and dawnward ($B_y^{GSM} < 0$) components, and that is indeed what is seen in the magnetosheath magnetic field orientation in Figure 7.5, i.e., a southward ($B_L < 0$ or $B_z^{GSM} < 0$) and dawnward ($B_M > 0$ or $B_y^{GSM} < 0$) orientation. Therefore, by using the reconnection jet direction one can infer the X-line location relative to the spacecraft, and models which predict the X-line location and orientation can be tested in this manner, as it was done throughout Section 6.1.2.

In the next section, we show how the whole dataset of single magnetopause reconnection events was divided in order to analyze the influence of both IMF and dipole tilt inclination on the X-line model predictions, and how well they fit plasma jet observations.

7.1.4 Dataset separation

The whole dataset was divided according to IMF orientation and the Earth's dipole tilt inclination. In terms of IMF, we have first divided the dataset into two subsets of events for which the observed IMF B_x component was either positive (48%) or negative (52%). For each subset, we have further separated the events into seven dipole tilt inclination bins with 10° width each. The central bin values were $\psi = 0^\circ, \pm 10^\circ, \pm 20^\circ, \pm 30^\circ$. Finally, for each dipole tilt bin, the events were divided into eight clock angle ($\theta_{CA} = \tan^{-1}(B_y/B_z)$ ⁷) bins, with four of them for positive IMF B_y : $90^\circ \leq \theta_{CA} < 105^\circ, 105^\circ \leq \theta_{CA} < 135^\circ, 135^\circ \leq \theta_{CA} < 165^\circ, 165^\circ \leq \theta_{CA} < 180^\circ$, and the remaining four for negative IMF B_y : $180^\circ \leq \theta_{CA} < 195^\circ, 195^\circ \leq \theta_{CA} < 225^\circ, 225^\circ \leq \theta_{CA} < 255^\circ, 255^\circ \leq \theta_{CA} < 270^\circ$. The central bin values were $\theta_{CA} = 97.5^\circ, 120^\circ, 150^\circ, 172.5^\circ, 187.5^\circ, 210^\circ, 240^\circ, 262.5^\circ$. Below, we present two tables showing the number of reconnection events for each combination of IMF and dipole tilt angles. The Table 7.1 shows the number of events for negative values of dipole tilt center bins, i.e., $\psi = -30^\circ, -20^\circ$, and -10° , while Table 7.2 shows the number of events for both zero and positive dipole tilt center bins, i.e., $\psi = 0^\circ, 10^\circ, 20^\circ$ and 30° .

The reason we have divided the dataset into 8 bins of clock angle θ_{CA} is that all three X-line model predictions used in this work are sensitive to the IMF B_y/B_z ratio, and therefore the regimes where B_y is bigger than B_z or vice-versa will influence

⁷The IMF clock angle provide us the IMF orientation on the yz_{GSM} plane. A zero degree clock angle means a purely northward ($z > 0$) IMF orientation on the yz plane whereas a 180° a purely southward IMF orientation. A $90^\circ(270^\circ)$ clock angle means a purely duskward (dawnward) IMF orientation.

both the X-line location and orientation. If we had divided θ_{CA} into only two bins for which the IMF B_y is either positive or negative, thereby increasing the number of events per bin, we would, however, most likely lose the opportunity for testing the influence of the relative strength of the IMF B_y and B_z components on the jet direction prediction of each X-line model.

7.1.5 Input conditions for generating the model X-lines

Now, it is specified which values of IMF and dipole tilt angles were used as input for the X-line models so we can compare the observed plasma jet directions pertaining to a given IMF and dipole tilt angle bin to the X-line prediction obtained as a representative for that specific bin.

If we consider every combination of IMF and dipole tilt angle as presented in Tables 7.1 and 7.2, a total of 112 possible X-lines, per X-line model, would have to be generated. Actually, what we have done was to generate the X-line locations, for each model, for all IMF and dipole tilt angle combinations presented in Table 7.2, i.e., 64 X-lines per model, and then invoke symmetry arguments to determine the remaining 48 X-line locations of Table 7.1. The IMF and dipole tilt angle values used to generate the 64 X-lines in Table 7.2 were IMF $B_x = \pm 5$ nT, $\psi = 0^\circ, 10^\circ, 20^\circ, 30^\circ$, IMF $B_y = 5$ nT and $B_z = 0$ nT ($\theta_{CA} = 90^\circ$), IMF $B_y = 5$ nT and $B_z = -2.886$ nT ($\theta_{CA} = 120^\circ$), IMF $B_y = 2.886$ nT and $B_z = -5$ nT ($\theta_{CA} = 150^\circ$), and finally IMF $B_y = 0$ nT and $B_z = -5$ nT ($\theta_{CA} = 180^\circ$). Notice that for each IMF B_x and a given dipole tilt angle, say $\psi = 10^\circ$, we can have as much as eight X-lines. Since we have four possible values of ψ , we will have 32 X-lines, only for positive IMF B_x , and two times this value, i.e., 64, for both positive and negative IMF B_x . We also notice that both Gonzalez and Mozer (1974) and Trattner et al. (2007) X-line models require as input the solar wind density (n_{sw} [cm^{-3}]) and speed (V_{sw} [km/s]), as well as the level of the Earth's magnetic field disturbance as measured on the ground by the D_{st} index. For all cases, we have set $D_{st} = 0$ nT, $n = 5.0$ cm^{-3} , and $V_{sw} = 400$ km/s, whose combination⁸ is well inside the range of solar wind dynamic pressure values for all events, i.e., $1.0 \leq P_{dyn} \leq 2.5$ nPa. For the Swisdak and Drake (2007) model wherein the BATS-R-US code is used as a mean for obtaining the X-line, we also need to specify the solar wind temperature as an input parameter. For all our BATS-R-US runs, the latter was set to 2×10^4 Kelvin.

We now discuss how the remaining 48 X-lines, which are related with IMF and dipole

⁸The solar wind's density and speed can be combined to obtain the solar wind dynamic pressure P_{dyn} as $P_{dyn} = m_{ion} n_{sw} V_{sw}^2$, where m_{ion} is the ionized hydrogen mass.

Table 7.1 - Number of single magnetopause crossing events during reconnection periods distributed according to IMF orientation and three Earth's dipole tilt inclination intervals, whose center bins are $\psi = -30^\circ$, -20° , and -10° .

| | | | | IMF $B_x > 0$ | | | | IMF $B_x < 0$ | | | | | | | | |
|---------------|-----------------------------|--------------------------|--------------------------|-----------------------------|-----------------------------|--------------------------|--------------------------|-----------------------------------|-----------------------------|--------------------------|--------------------------|-----------------------------|-----------------------------|--------------------------|--------------------------|-----------------------------|
| | | | | | | | | $-35^\circ \leq \psi < -25^\circ$ | | | | | | | | |
| | | | | IMF $B_y > 0$ | | | | IMF $B_y > 0$ | | | | IMF $B_y < 0$ | | | | |
| θ_{CA} | $97.5^\circ \pm 7.5^\circ$ | $120^\circ \pm 15^\circ$ | $150^\circ \pm 15^\circ$ | $172.5^\circ \pm 7.5^\circ$ | $97.5^\circ \pm 7.5^\circ$ | $120^\circ \pm 15^\circ$ | $150^\circ \pm 15^\circ$ | $172.5^\circ \pm 7.5^\circ$ | $187.5^\circ \pm 7.5^\circ$ | $210^\circ \pm 15^\circ$ | $240^\circ \pm 15^\circ$ | $262.5^\circ \pm 7.5^\circ$ | $187.5^\circ \pm 7.5^\circ$ | $210^\circ \pm 15^\circ$ | $240^\circ \pm 15^\circ$ | $262.5^\circ \pm 7.5^\circ$ |
| | 0 | 2 | 2 | 0 | 0 | 0 | 0 | 0 | 0 | 0 | 1 | 0 | 0 | 0 | 1 | 0 |
| | IMF $B_y < 0$ | | | | IMF $B_y < 0$ | | | | IMF $B_y < 0$ | | | | IMF $B_y < 0$ | | | |
| θ_{CA} | $187.5^\circ \pm 7.5^\circ$ | $210^\circ \pm 15^\circ$ | $240^\circ \pm 15^\circ$ | $262.5^\circ \pm 7.5^\circ$ | $187.5^\circ \pm 7.5^\circ$ | $210^\circ \pm 15^\circ$ | $240^\circ \pm 15^\circ$ | $262.5^\circ \pm 7.5^\circ$ | 0 | 1 | 0 | 0 | 1 | 2 | 0 | 0 |
| | | | | | | | | $-25^\circ \leq \psi < -15^\circ$ | | | | | | | | |
| | | | | IMF $B_y > 0$ | | | | IMF $B_y > 0$ | | | | IMF $B_y < 0$ | | | | |
| | 1 | 0 | 0 | 1 | 3 | 2 | 3 | 1 | 3 | 2 | 3 | 1 | 3 | 2 | 3 | 1 |
| | IMF $B_y < 0$ | | | | IMF $B_y < 0$ | | | | IMF $B_y < 0$ | | | | IMF $B_y < 0$ | | | |
| | 3 | 4 | 1 | 0 | 2 | 2 | 1 | 0 | 2 | 2 | 1 | 0 | 2 | 2 | 1 | 0 |
| | | | | | | | | $-15^\circ \leq \psi < -5^\circ$ | | | | | | | | |
| | | | | IMF $B_y > 0$ | | | | IMF $B_y > 0$ | | | | IMF $B_y < 0$ | | | | |
| | 0 | 0 | 1 | 0 | 0 | 0 | 6 | 1 | 0 | 0 | 6 | 1 | 0 | 0 | 6 | 1 |
| | IMF $B_y < 0$ | | | | IMF $B_y < 0$ | | | | IMF $B_y < 0$ | | | | IMF $B_y < 0$ | | | |
| | 0 | 4 | 7 | 0 | 3 | 4 | 1 | 0 | 3 | 4 | 1 | 0 | 3 | 4 | 1 | 0 |

Table 7.2 - (Continuation of Table 7.1) Number of single magnetopause crossing events during reconnection periods distributed according to IMF orientation and four Earth's dipole tilt inclination intervals whose center bins are $\psi = 0^\circ, 10^\circ, 20^\circ$ and 30° .

| IMF $B_x > 0$ | | | | IMF $B_x < 0$ | | | |
|---|--------------------------|--------------------------|-----------------------------|-----------------------------|--------------------------|--------------------------|-----------------------------|
| $-5^\circ \leq \psi < 5^\circ$ | | | | | | | |
| IMF $B_y > 0$ | | | | IMF $B_y > 0$ | | | |
| $\theta_{CA} = 97.5^\circ \pm 7.5^\circ$ | $120^\circ \pm 15^\circ$ | $150^\circ \pm 15^\circ$ | $172.5^\circ \pm 7.5^\circ$ | $97.5^\circ \pm 7.5^\circ$ | $120^\circ \pm 15^\circ$ | $150^\circ \pm 15^\circ$ | $172.5^\circ \pm 7.5^\circ$ |
| 0 | 0 | 2 | 0 | 0 | 2 | 1 | 1 |
| IMF $B_y < 0$ | | | | IMF $B_y < 0$ | | | |
| $\theta_{CA} = 187.5^\circ \pm 7.5^\circ$ | $210^\circ \pm 15^\circ$ | $240^\circ \pm 15^\circ$ | $262.5^\circ \pm 7.5^\circ$ | $187.5^\circ \pm 7.5^\circ$ | $210^\circ \pm 15^\circ$ | $240^\circ \pm 15^\circ$ | $262.5^\circ \pm 7.5^\circ$ |
| 3 | 3 | 2 | 1 | 1 | 1 | 0 | 0 |
| $5^\circ \leq \psi < 15^\circ$ | | | | | | | |
| IMF $B_y > 0$ | | | | IMF $B_y > 0$ | | | |
| 1 | 1 | 0 | 1 | 0 | 3 | 1 | 1 |
| IMF $B_y < 0$ | | | | IMF $B_y < 0$ | | | |
| 0 | 4 | 1 | 2 | 1 | 2 | 0 | 1 |
| $15^\circ \leq \psi < 25^\circ$ | | | | | | | |
| IMF $B_y > 0$ | | | | IMF $B_y > 0$ | | | |
| 0 | 0 | 0 | 0 | 1 | 1 | 3 | 0 |
| IMF $B_y < 0$ | | | | IMF $B_y < 0$ | | | |
| 0 | 2 | 2 | 0 | 0 | 1 | 1 | 0 |
| $25^\circ \leq \psi < 35^\circ$ | | | | | | | |
| IMF $B_y > 0$ | | | | IMF $B_y > 0$ | | | |
| 0 | 0 | 0 | 0 | 1 | 0 | 2 | 0 |
| IMF $B_y < 0$ | | | | IMF $B_y < 0$ | | | |
| 2 | 1 | 1 | 0 | 1 | 1 | 0 | 0 |

tilt combinations in Table 7.1, were obtained via symmetry arguments. When we refer to “obtaining” or “generating” the X-line, we mean determining both its y_{xline} and z_{xline} GSM coordinates over the modeled magnetopause surface as described in Chapter 4. Thus, when applying a symmetry argument we will play with the *signs* of either y_{xline} or z_{xline} GSM coordinates of the X-line. For instance, consider an IMF and dipole tilt configuration wherein IMF $B_x = 5$ nT, $\psi = 0^\circ$, and $\theta_{CA} = 90^\circ$ (IMF $B_y = 5$ nT and $B_z = 0$ nT). If we keep B_x and ψ unchanged, we can argue that the new X-line coordinates y_{new} and z_{new} that we would obtain if we had a negative, instead of a positive, B_y , i.e., $\theta_{CA} = 270^\circ$, would be such that $y_{new} \rightarrow -y_{xline}$ and $z_{new} \rightarrow z_{xline}$. That means that the z_{GSM} axis can be considered as a symmetry axis for this case. In fact we can also apply the same symmetry argument for the cases $\theta_{CA} = 120^\circ$ and 150° which will result in the X-lines for the $\theta_{CA} = 240^\circ$ and 210° cases, respectively. Another kind of symmetry can also be used, i.e., the one where the y_{GSM} axis is the symmetry axis, thus the relation between the new and old X-line coordinates is $y_{new} \rightarrow y_{xline}$, $z_{new} \rightarrow -z_{xline}$. We use this kind of symmetry when, but not only, $\theta_{CA} = 180^\circ$, since under these IMF conditions the X-line is localized mostly parallel to the equator ($z_{GSM} = 0$). We then summarize below all the IMF and dipole tilt combinations for which we have invoked symmetry arguments (left-hand side - LHS) in order to obtain a new set of X-line coordinates for another combination of IMF and dipole tilt angle (right-hand side - RHS). The IMF B_z was southward ($B_z < 0$) for all cases.

a) Replace z_{xline} by $-z_{xline}$ while keeping y_{xline} unchanged on the LHS to generate X-line coordinates consistent with conditions on the RHS:

- 1) $B_x > 0, B_y > 0, \psi \geq 0 \rightarrow B_x < 0, B_y < 0, \psi < 0$;
- 2) $B_x < 0, B_y > 0, \psi \geq 0 \rightarrow B_x > 0, B_y < 0, \psi < 0$;
- 3) $B_x < 0, B_y = 0, \psi \geq 0 \rightarrow B_x > 0, B_y = 0, \psi < 0$;
- 4) $B_x > 0, B_y = 0, \psi \geq 0 \rightarrow B_x < 0, B_y = 0, \psi < 0$.

b) Replace y_{xline} by $-y_{xline}$ while keeping z_{xline} unchanged on the LHS to generate X-line coordinates consistent with conditions on the RHS:

- 5) $B_x > 0, B_y > 0, \psi \geq 0 \rightarrow B_x > 0, B_y < 0, \psi \geq 0$;
- 6) $B_x < 0, B_y > 0, \psi \geq 0 \rightarrow B_x < 0, B_y < 0, \psi \geq 0$;
- 7) $B_x > 0, B_y > 0, \psi < 0 \rightarrow B_x > 0, B_y < 0, \psi < 0$;
- 8) $B_x < 0, B_y > 0, \psi < 0 \rightarrow B_x < 0, B_y < 0, \psi < 0$.

7.1.6 X-line models test against *in situ* magnetic reconnection plasma jet observations

Analogously to what we have done in Section 6.1.2, we test the chosen X-line models, i.e., Maximum Shear Angle (TRATTNER et al., 2007), Chapman-Ferraro current (GONZALEZ; MOZER, 1974), and Maximum Reconnection Outflow Speed (SWISDAK; DRAKE, 2007) against *in situ* observations of reconnection plasma jets obtained by a collection of single magnetopause crossing events. This time, we present in a single plot all three X-line outputs and make direct comparisons between the observed and predicted (according to the X-line location) plasma jet direction. We will present the data according to IMF orientation and dipole tilt angle bins as shown in Section 7.1.4. For instance, consider an example plot that is going to be shown below where in its top part one sees the following information: IMF $B_x = 5$ nT, $\theta_{CA} = 120^\circ$, and $\psi = -30^\circ$. Such parameters refer to those which were used as input to generate the X-line models being depicted in the plot. The plasma jet observations, however, will have, for the example at hand, correspondent IMF and dipole tilt conditions which satisfy the criteria: IMF $B_x > 0$ nT, $\theta_{CA} = 120^\circ \pm 15^\circ$, and $\psi = -30^\circ \pm 5^\circ$.

Next, we show the plots for which there was at least one plasma jet observation (cf. Tables 7.1 and 7.2). We organize the plots shown in the following manner: a set of six (6) figures is shown, with each pair of figures corresponding to a specific dipole tilt ψ bin. The first pair of figures will correspond to the $-35^\circ \leq \psi < -25^\circ$ bin, while the second and third pairs to the $-25^\circ \leq \psi < -15^\circ$ and $-15^\circ \leq \psi < -5^\circ$ bins, respectively, following the order shown, from top to bottom, in Table 7.1. The eight plots concerning the data shown in Table 7.2 wherein the plasma jet data is separated according to positive values of dipole tilt angle will be presented in the Appendix B, since we believe that the discussion of the data related to Table 7.1 will be sufficient to exemplify the arguments whether or not the X-line models correctly predicted the observed jet directions.

Now we discuss the content of each figure within the figure pair. The first (second) figure of the pair will have data corresponding to positive (negative) IMF B_x , and each figure will have a number of plots that will depend on whether there were or there were not plasma jet observations for a given clock angle θ_{CA} bin. We will give an example. Consider the top left corner of Table 7.1. The first figure that will be shown below refers to that part of the table, meaning that it will have a total of three (3) plots, with each one corresponding to the following θ_{CA} bins: $105^\circ \leq \theta_{CA} < 135^\circ$, $135^\circ \leq \theta_{CA} < 165^\circ$, and $195^\circ \leq \theta_{CA} < 225^\circ$. Notice that these θ_{CA} bins are the only

ones which have plasma jet observations in that part of Table 7.1. Likewise, the second figure of the first pair that is going to be shown refers to data corresponding to negative IMF B_x , yet the same dipole tilt bin of the first figure. The number of plots in the second figure will also be three, because for only three θ_{CA} bins, namely $135^\circ \leq \theta_{CA} < 165^\circ$, $180^\circ \leq \theta_{CA} < 195^\circ$, and $195^\circ \leq \theta_{CA} < 225^\circ$ there were plasma jet observations. Within each plot, the X-lines from all three models are shown (Max J_{CF} (GONZALEZ; MOZER, 1974), Max θ_{Shear} (TRATTNER et al., 2007), and Max V_{out} (SWISDAK; DRAKE, 2007)) along with arrows specifying the observed jet directions. Solid arrows means that the jet has a northward ($V_z^{jet} > 0$) component, while dashed arrows a southward ($V_z^{jet} < 0$) component.

The X-line length in both Gonzalez and Mozer (1974) and Swisdak and Drake (2007) models were determined by plotting the (y_{xline}, z_{xline}) points for which the local Chapman-Ferraro current density magnitude (J_{CF}) and the local reconnection outflow speed V_{out} were greater than 70%⁹ of the their maximum values, respectively, over the whole modeled dayside magnetopause. The same criterion could not be applied for the Trattner et al. (2007) model, because otherwise it would not allow some X-line points pertaining to the subsolar branch to be plotted, so the X-line would not be continuous in the subsolar region. Thus, no criterion was established to restrict the plot of X-line coordinates for the Trattner et al. (2007) model.

Figure 7.8 is the first of the fourteen¹⁰ figures showing the X-line models' test against *in situ* observations of reconnection plasma jets. The X-lines are plotted against the yz_{GSM} plane, and the spacecraft positions are marked by the filled black circles. All the plots show the results for the same IMF $B_x = 5$ nT and $\psi = -30^\circ$ conditions. For the sake of clarity, we hereafter define that the $y_{GSM} > 0$ (< 0) direction points eastward (westward) at the dayside magnetopause.

The top row plots show two cases where the IMF B_y was positive, but in the first one (leftmost panel), B_y was higher than B_z , i.e., $\theta_{CA} < 135^\circ$, while in the second one (rightmost panel) the opposite situation occurred, i.e., $\theta_{CA} > 135^\circ$. In the bottom panel, a negative B_y case is shown where B_y was higher than B_z . At all plots, the spacecraft detected southward reconnection jets (dashed arrows) which occurred above the equator ($z_{GSM} > 0$), suggesting an X-line northward of each spacecraft position. We note that all reconnection jets shown in this entire work had their magnetosheath flow component subtracted, so the remaining velocity should be due

⁹Same criterion used in Section 6.1.2.2

¹⁰From these fourteen figures, the first 6 will be discussed in this section while the remainder eight are shown in the Appendix B.

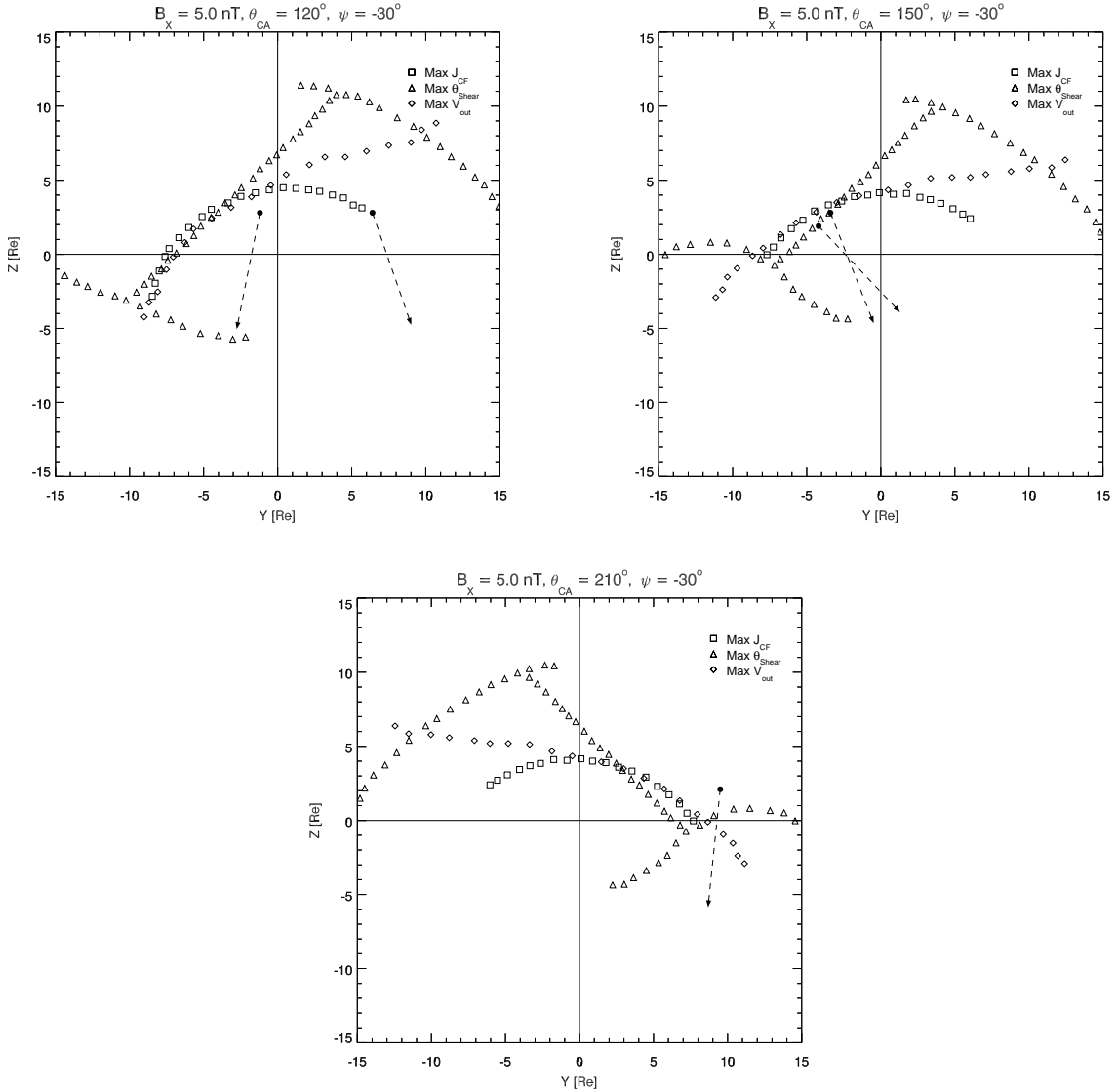


Figure 7.8 - X-line models test against *in situ* observations of reconnection plasma jets. The X-lines which are presented onto the yz_{GSM} plane are derived from the models of maximum Chapman-Ferraro current density magnitude, $\text{Max } J_{CF}$, by Gonzalez and Mozer (1974), the maximum shear angle model, $\text{Max } \theta_{Shear}$, by Trattner et al. (2007), and the maximum reconnection outflow speed, $\text{Max } V_{out}$, by Swisdak and Drake (2007). The IMF ($B_x = 5$ nT, B_z either -2.886 or -5 nT and $\theta_{CA} = \tan^{-1}(B_y/B_z)$) and Earth's dipole tilt (ψ) conditions used as input to generate the X-lines shown are presented on the top of each panel. The observed plasma jet directions are represented as solid (dashed) arrows if they have a northward (southward) V_z^{jet} component, and they were detected under IMF and dipole tilt conditions similar to those shown on the top of the respective panel (see text for details). The location of the spacecraft when it detected the plasma jet at the dayside magnetopause crossing is marked by the black filled circle.

to the reconnection component.

Now, we discuss whether the X-line models correctly or not predicted the north-south and/or east-west senses of the observed jet directions based on the simple assumption that the reconnection outflows are perpendicular to the local X-line segment, as we have assumed throughout Chapter 6.

Looking at the leftmost panel of Figure 7.8, we can see that all X-line models correctly predicted the north-south sense of the jet observed at $y_{GSM} \sim -2 R_E$, while the same did not occur for its east-west sense. The expectation was an eastward (duskward) sense, as opposed to the observed westward (dawnward) sense. As for the second plasma jet observed at $y_{GSM} \sim 7 R_E$, both north-south and east-west senses were correctly predicted by both Trattner et al. (2007) and Swisdak and Drake (2007) models. If we plot other points for the Gonzalez and Mozer (1974) X-line, thereby infringing the 70% threshold established above, we would see that the X-line would coincide with the observed jet location, and therefore no prediction would be possible to do for this X-line model.

Moving to the rightmost panel of Figure 7.8, all three X-line models make a correct prediction of the reconnection jet direction observed at $y_{GSM} \sim -4 R_E$, while at the second jet, observed duskward of the first one ($y_{GSM} \sim 3 R_E$), only the Trattner et al. (2007) model is not able to offer any prediction since the X-line location is collocated with the observed jet location. The other two models correctly predicted the whole jet direction, i.e., both its north-south and east-west senses. A feature worthwhile to mention is the lesser duskward component and more southward component of the plasma jet located at $y_{GSM} \sim -3 R_E$, suggesting that at that location the X-line should tilt toward the equator in order to generate a more pronounced southward jet component as compared to locations of further negative y_{GSM} where the X-line bend would favor reconnection jets (southward of the X-line) with higher duskward components. Both Gonzalez and Mozer (1974) and Swisdak and Drake (2007) X-lines present such a tendency for the IMF ($B_x > 0, B_y > 0, B_z < 0$) and dipole tilt ($\psi = -30^\circ$) configurations shown.

Regarding the X-lines shown on the bottom panel of Figure 7.8, it is worthwhile to mention that all X-lines from this panel were obtained by applying one of the symmetry arguments presented in the previous section, in particular the argument number 7), to the X-lines at the rightmost panel of Figure 7.8 where we had negative dipole tilt angle, and both positive IMF B_x and B_y ($\theta_{CA} = 150^\circ$), and obtained the X-lines for the same IMF B_x and dipole tilt conditions, but for a negative IMF B_y

($\theta_{CA} = 210^\circ$) with the same angular separation (30°) from 180° . Considering now the X-line's jet direction predictions at the bottom panel of Figure 7.8 none of the X-line models could correctly predict the southward sense of the observed jet direction. Two models (Gonzalez and Mozer (1974) and Swisdak and Drake (2007)) could not correctly predict the westward (dawnward) sense of the observed jet. Maybe the Trattner et al. (2007) model would correctly predict the jets east-west sense if we consider the following argument as being plausible: since the jet location is nearer from the antiparallel than the subsolar X-line branch, and since at the antiparallel branch the reconnection efficiency should be higher as compared to the subsolar branch (CROOKER, 1979), and as a consequence the outflow speed there should also be higher (BIRN et al., 2008), the outflow direction at the observed jet location would be expected to have both northward and westward components. The predicted westward component would agree with the respective observed jet component. Presently, we can not prove the validity of such argument, but considering its plausibility we will consider that the jet's east-west sense prediction by the Trattner et al. (2007)'s model is uncertain for this case, i.e., it may be correct or not.

We discuss the results shown in Figure 7.9, for which the dipole tilt condition is the same as that in Figure 7.8 ($\psi = -30^\circ$), but the IMF B_x is now negative. In this case, only three plots are shown corresponding to the three θ_{CA} bins for which there were plasma jet observations available, i.e., $\theta_{CA} = 150^\circ \pm 15^\circ$, $187.5^\circ \pm 7.5^\circ$, and $210^\circ \pm 15^\circ$.

We begin the discussion with the leftmost plot. According to the component-type reconnection X-line scenario (SONNERUP, 1974), the duskward ($0^\circ < \theta_{CA} < 180^\circ$) IMF orientation suggests a tilted, subsolar reconnection X-line which would give rise to southward-eastward (northward-westward) jets at locations below (above) the X-line. One can see that only the Trattner et al. (2007) (Max θ_{Shear}) model was able to correctly predict the jet's both north-south and east-west senses. For the Swisdak and Drake (2007) model, the predicted jet direction would be precisely opposite to what is shown, i.e., a northward-westward direction. Judging by the local Max J_{CF} 's orientation near the jet location ($y_{GSM} \sim 2 R_E$), one can argue that the predicted jet direction would have a small, yet positive y_{GSM} component, i.e., an eastward component, which agrees with the east-west sense of the observed plasma jet. Thus, we claim that only the east-west sense of the observed jet was correctly predicted by the Gonzalez and Mozer (1974) model.

Moving to the rightmost panel in Figure 7.9 where the IMF clock angle used as input

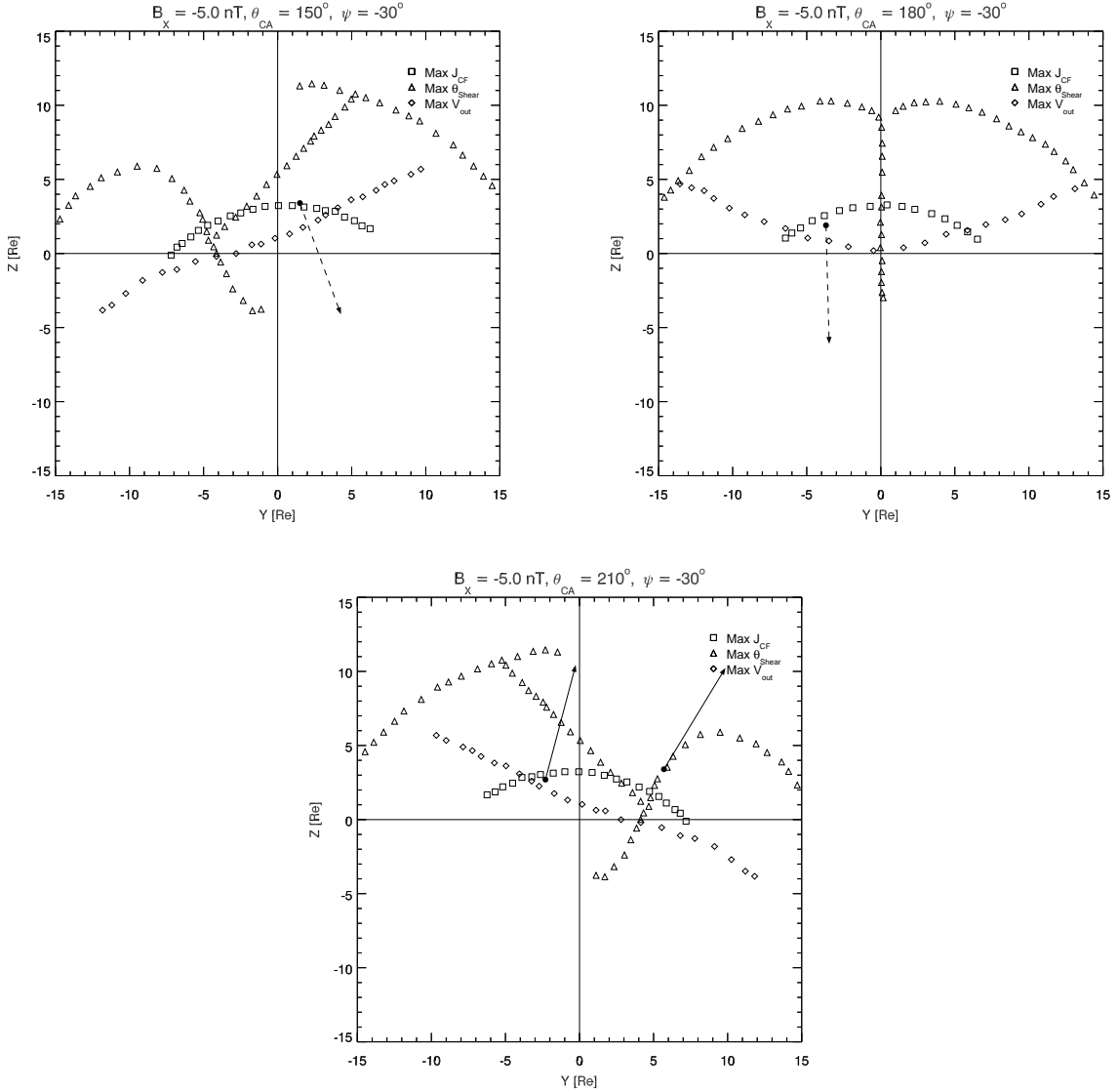


Figure 7.9 - X-line models test against *in situ* observations of reconnection plasma jets. The X-lines which are presented onto the yz_{GSM} plane are derived from the models of maximum Chapman-Ferraro current density magnitude, $\text{Max } J_{CF}$, by Gonzalez and Mozer (1974), the maximum shear angle model, $\text{Max } \theta_{Shear}$, by Trattner et al. (2007), and the maximum reconnection outflow speed, $\text{Max } V_{out}$, by Swisdak and Drake (2007). The IMF ($B_x = -5$ nT, B_z either -2.886 or -5 nT, and $\theta_{CA} = \tan^{-1}(B_y/B_z)$) and Earth's dipole tilt (ψ) conditions used as input to generate the X-lines shown are presented on the top of each panel. The observed plasma jet directions are represented as solid (dashed) arrows if they have a northward (southward) V_z^{jet} component, and they were detected under IMF and dipole tilt conditions similar to those shown on the top of the respective panel (see text for details). The location of the spacecraft when it detected the plasma jet at the dayside magnetopause crossing is marked by the black filled circle.

for the X-line models was 180° , we can see that the [Gonzalez and Mozer \(1974\)](#)'s X-line location would be consistent with the observed (southward) jet direction, although some eastward component would be expected given the X-line curvature near the location where the jet was detected ($y_{GSM} \sim -4 R_E$). Looking closely at the jet direction, though, one will see a very small displacement of the arrow toward the east (duskside magnetopause), indicating that there could be an X-line, northward and dawnward of the observation site, whose orientation away from the noon-midnight meridian plane ($y_{GSM} = 0$) would tilt slightly toward the equator on the dawnside magnetopause ($y_{GSM} < 0$), akin to what happens with the [Gonzalez and Mozer \(1974\)](#)'s X-line. Thus, we consider that the jet's both north-south and east-west senses were correctly predicted by the Max J_{CF} 's X-line. On the other hand, the [Swisdak and Drake \(2007\)](#) model could correctly predict only the east-west sense of the observed jet direction. Based on the simple assumption of locally perpendicular (to the X-line) reconnection outflows, the prediction for the [Trattner et al. \(2007\)](#) model would not be straightforward. When the IMF clock angle is 180° , as it is the case shown in the rightmost panel of [Figure 7.9](#), the maximum shear X-line does not have a subsolar X-line branch that resembles a component-type X-line, i.e., a subsolar X-line with a tilt relative to the equator proportional to the IMF B_y/B_z ratio. Instead, the X-line will only follow the location over the dayside magnetopause where the local shear angle (θ_{Shear}) is near 180° . For a purely southward IMF B_z with no dipole tilt inclination, such an X-line would be located exactly over the equator ($z_{GSM} = 0$). On the other hand, with a large IMF B_x component compared to the total IMF magnitude and also the presence of a dipole tilt inclination in such a way that the product $B_x\psi$ is larger than zero, as happen with the analyzed case, the X-line will split into two antiparallel branches, with each one mapping to one of the two magnetospheric cusp regions. These two branches can be visualized in the rightmost panel of [Figure 7.9](#). The noon-meridian branch ($y_{GSM} \sim 0$) reaches to the southern cusp (located at $z_{GSM} \sim -4 R_E$), while the dawn-to-dusk ($y_{GSM} > 0$) branch maps to the northern magnetospheric cusp (at $z_{GSM} \sim 9 R_E$), similar to [Figure 4 panel a\)](#) of [Trattner et al. \(2007\)](#). Thus, we would have to assume that at the jet observation site ($y_{GSM} \sim -4 R_E$) the predicted jet direction by the maximum shear angle model would be a composition of a strong westward component due to the proximity from the dawnside antiparallel branch of the X-line at low latitudes ($z_{GSM} \sim 2 R_E$) plus a weaker southward component emerging from the high latitude dawnside branch of the X-line. Therefore, we claim that the [Trattner et al. \(2007\)](#) X-line correctly predicted only the due southward component of the observed jet direction.

Akin to what happen with the X-lines shown in the bottom panel of Figure 7.8, the X-lines shown in the bottom panel of Figure 7.9 were also obtained via symmetry arguments, by doing $y_{new} = -y_{xline}$ while keeping z_{xline} unchanged. The (y_{xline}, z_{xline}) coordinates were extracted from the X-lines shown at the leftmost panel of Figure 7.9. Considering then the bottom panel of Figure 7.9 where the input IMF clock angle had a negative B_y component, i.e., $180^\circ < \theta_{CA} \leq 360^\circ$, only the Swisdak and Drake (2007) X-line model was able to provide the correct northward-duskward direction of both observed plasma jets. As for the Gonzalez and Mozer (1974) X-line model only one of the jets ($y_{GSM} \sim 6 R_E$) had its entire direction correctly predicted, while for the second plasma jet ($y_{GSM} \sim -2 R_E$), only the east-west (eastward) sense was correctly predicted, since according to the local Max J_{CF} 's X-line orientation at the observed jet site a southward-eastward jet direction would be expected. Once again, the jet direction prediction is not so clear for the maximum shear angle model for the east-west component of the duskside ($y_{GSM} \sim 6 R_E$) jet. At that location the X-line orientation suggests a strong westward jet component, but an eastward component emerging from the tilted subsolar X-line branch is also expected. It may happen, as argued above, that the reconnection outflow speed near the antiparallel branch, and hence near the analyzed plasma jet observation site, is higher than that near the subsolar X-line branch location, since the reconnection efficiency on the former is expected to be higher than on the latter due to higher local shear angles, thus a net westward reconnection flow component could arise from that configuration. Such an east-west sense would not be consistent, though, with the observed east-west sense, then the maximum shear angle model would not correctly predict it, but only its northward sense. Nevertheless, since we can not prove the argument raised above, we will establish the east-west (duskside) jet prediction by the Max θ_{shear} X-line as uncertain. At the dawnside jet location the Trattner et al. (2007) model fails to predict both north-south and east-west senses of the observed jet.

The next two figures, Figures 7.10 and 7.11, refer to observed plasma jet data shown in the middle part of Table 7.1, where the dipole tilt angle bin is $-25^\circ \leq \psi < -15^\circ$. We start out discussing the plots in Figure 7.10 wherein the IMF B_x component is positive. The top left corner plot of Figure 7.10 show the three X-line models for an IMF with no B_z component, and with a duskward ($B_y > 0$) component ($\theta_{CA} = 90^\circ$). We claim that only the Trattner et al. (2007) X-line model could correctly predict the jet's southward-eastward direction.

Moving to the center panel on the top row of Figure 7.10, all X-line modes failed to predict the observed southward sense of the plasma jet, however all of them

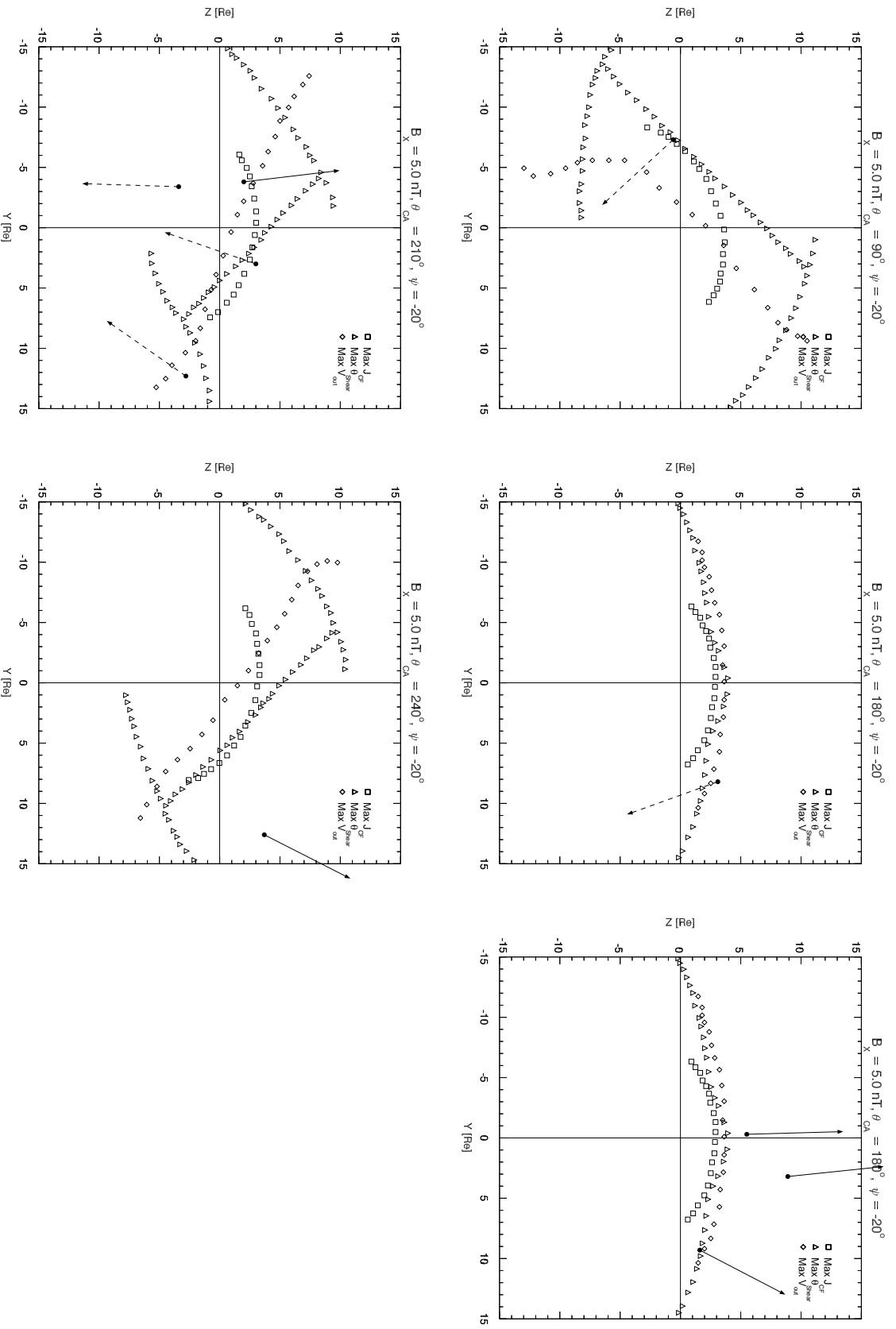


Figure 7.10 - X-line models test against *in situ* observations of reconnection plasma jets. The X-lines which are presented onto the yz_{GSM} plane are derived from the models of maximum Chapman-Ferraro current density plasma jets, Max J_{CF} , by Gonzalez and Mozer (1974), the maximum shear angle model, Max θ_{Shear} , by Trattner et al. (2007), and the maximum reconnection outflow speed, Max V_{CF} , by Swisdak and Drake (2007). The IMF ($B_x = 5$ nT, $B_z = 0, -2.886$ or -5 nT and $\theta_{CA} = \tan^{-1}(B_y/B_z)$) and Earth's dipole tilt (ψ) conditions used as input to generate the X-lines shown are presented on the top of each panel. The observed plasma jet directions are represented as solid (dashed) arrows if they have a northward (southward) V_z^{jet} component, and they were detected under IMF and dipole tilt conditions similar to those shown on the top of the respective panel (see text for details). The location of the spacecraft when it detected the plasma jet at the dayside magnetopause crossing is marked by the black filled circle.

correctly predict its eastward sense. We note that the actual IMF conditions under which the plasma jet being presented was collected belong to the IMF clock angle bin of $165^\circ \leq \theta_{CA} < 180^\circ$, so a non-negligible IMF $B_y > 0$ component could be present, and thus resulting on the observed small eastward jet component.

In the rightmost panel on the top row of Figure 7.10, the actual IMF conditions under which the plasma jets being presented were collected belong to the IMF clock angle bin of $180^\circ \leq \theta_{CA} < 195^\circ$, so a non-negligible IMF $B_y < 0$ component could be present and be responsible for the noticeable eastward component of the jet located at $y_{GSM} \sim 9 R_E$. In fact for this jet the IMF B_y component value corresponded to as much as 25% of the respective B_z component value. The mainly northward component of the other two jets suggest that the IMF B_y component for these two cases was negligibly small compared to the IMF B_z component, and they indeed corresponded to only $\sim 10\%$ of the respective B_z components. Looking at the $y_{GSM} \sim 9 R_E$ jet, we can see that only the [Gonzalez and Mozer \(1974\)](#) X-line model would be able to predict the northward-eastward direction of the observed jet, since the X-line lies southward and dawnward of the observation site. The [Swisdak and Drake \(2007\)](#) model fails to predict the full jet direction since the local X-line segment would be able to predict at the observed jet location a precisely opposite direction, i.e., a southward-westward direction. The prediction for the [Trattner et al. \(2007\)](#) model is not clear since the observation site is collocated with the local X-line trace. As for the other two jets, all three X-line models could correctly predict the mainly northward component of both jets. Given the curvature of all X-line models an increasingly westward (eastward) jet component also seems to be expected as one goes away from the noon-midnight meridian plane towards the dawnside (duskside) flank, besides the expected northward jet component at regions above the X-line location. Such a westward jet component consistent with all X-line curvatures is detected at $y_{GSM} \sim -1 R_E$. The westward jet component is indeed very small compared to the northward component, but still discernible. As for the jet detected at $y_{GSM} \sim 3 R_E$, any X-line model could correctly predict its westward sense, which in turn is not consistent with the presence, although small, of a negative IMF B_y component. Perhaps some local effect which we do not know is generating this plasma flow component. Therefore, we conclude that the east-west sense prediction of the $y_{GSM} \sim 3 R_E$ jet by all X-lines is uncertain, and as a result it may or may not be right.

We now discuss the leftmost panel on the bottom row of Figure 7.10. None of the X-line models correctly predicted the northward sense of the plasma jet located at $([y_{GSM}, z_{GSM}] \sim [-3, 2] R_E)$, since all of the X-lines were located above (northward

of) the plasma jet observation site. We note that such a plasma jet possess a slight westward component. It turns out that for locations above the reconnection X-line, as the northward jet component suggests, and with the presence of a noticeable negative IMF B_y component an eastward, rather than westward, jet component is expected. Thus, we conclude that we can not evaluate the X-line model east-west predictions for this jet since the jet component itself does not show the expected behavior. As argued above, although the local plasma jet being analyzed showed clear characteristics of a reconnection-generated jet, some other local mechanism must be acting on the plasma in order to create such a small westward jet component. As for the other three jets shown, all of them possess a westward flow component consistent with the spacecraft location being below of a tilted, subsolar X-line. At one of these jet locations ($[y_{GSM}, z_{GSM}] \sim [3, 3] R_E$), no X-line model predicted the correct observed jet direction. In particular, for that location all X-line models would predict a northward-eastward jet direction. For the jet at $y_{GSM} \sim 12 R_E$, only the duskside antiparallel branch of the maximum shear angle (TRATTNER et al., 2007) X-line would correctly predict the southward sense of the observed jet direction. On the other hand, judging by the local Max θ_{Shear} X-line orientation, the east-west sense of the jet would not be correctly predicted. Instead of westward, an eastward sense would result from the local Max θ_{Shear} X-line configuration. For the remaining due southward plasma jet located at $y_{GSM} \sim -3 R_E$, all X-line models correctly predicted the full jet direction.

In the last plot of Figure 7.10, i.e., the rightmost panel on the bottom row, it is shown that all X-line models correctly predicted the jet's full direction, i.e., its both north-south and east-west components. The observed jet direction is consistent with being above of a tilted, subsolar X-line which extends from the northern-dawn up to the southern-dusk regions of the dayside magnetopause.

We now move to Figure 7.11 wherein the IMF B_x component is negative, while the dipole tilt angle bin remains the same as that in Figure 7.10. We start out the analysis with the top row from left to right, then going to the bottom row also from left to right. In the top row's leftmost panel the two observed reconnection plasma jets closest in the $(y, z)_{GSM}$ location had their full (northward-westward) direction correctly predicted by all three X-line models, while the jet located closer to the noon-midnight meridian ($y_{GSM} = 0$) had its full (northward-westward) direction correctly predicted by two X-line models, namely the Trattner et al. (2007) and Swisdak and Drake (2007) models. The Gonzalez and Mozer (1974) X-line model failed to predict both jet's north-south and east-west senses.

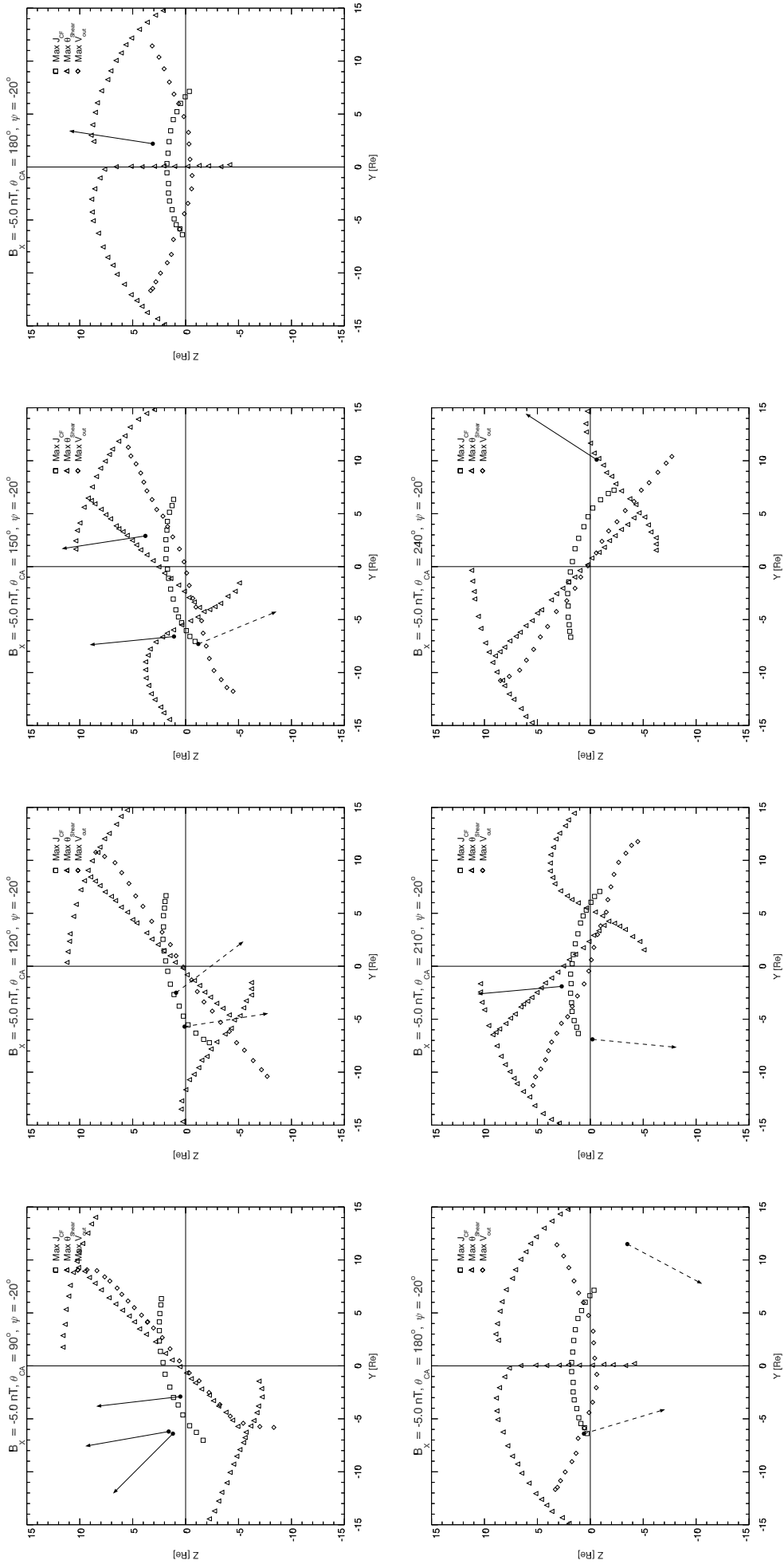


Figure 7.11 - X-line models test against *in situ* observations of reconnection plasma jets. The X-lines which are presented onto the yz_{GSM} plane are derived from the models of maximum Chapman-Ferraro current density magnitude, $\text{Max } J_{CF}$, by Gonzalez and Mozer (1974), the maximum shear angle model, $\text{Max } \theta_{shear}$, by Trattner et al. (2007), and the maximum reconnection outflow speed, $\text{Max } V_{out}$, by Swisdak and Drake (2007). The IMF ($B_x = -5$ nT, $B_z = 0$, -2.886 or -5 nT and $\theta_{CA} = \tan^{-1}(B_y/B_z)$) and Earth's dipole tilt (ψ) conditions used as input to generate the X-lines shown are presented on the top of each panel. The observed plasma jet directions are represented as solid (dashed) arrows if they have a northward (southward) V_z^{jet} component, and they were detected under IMF and dipole tilt conditions similar to those shown on the top of the respective panel (see text for details). The location of the spacecraft when it detected the plasma jet at the dayside magnetopause crossing is marked by the black filled circle.

Moving to the second panel from left to right on the top row of Figure 7.11, the jet located closer to the noon-midnight meridian plane had its full (southward-eastward) direction correctly predicted only by the [Gonzalez and Mozer \(1974\)](#) model, while the second jet ($y_{GSM} \sim -6 R_E$) did not have its north-south sense correctly predicted by all X-line models. Regarding the observed jet's east-west sense, neither the [Gonzalez and Mozer \(1974\)](#) nor the [Swisdak and Drake \(2007\)](#) models were able to do a correct prediction. As for the [Trattner et al. \(2007\)](#) model the prediction is not so clear, since the observed jet location is approximately equidistant from both subsolar and antiparallel X-line branches, thus we would have to assume, as we have done before, that the reconnection outflow speed would be expected to be higher near the antiparallel X-line than in the subsolar branch due to (the expected) higher reconnection efficiency at the former location. Since they are approximately equidistant from the observation site a net *eastward* flow component consistent with the observation would arise at the analyzed jet location. Although the argument seems plausible, we will deem this east-west prediction as uncertain, as previously done.

Analyzing the third panel from left to right on the top row of Figure 7.11, in particular the southward plasma jet (dashed arrow), one is able to see that the jet location is collocated with the [Gonzalez and Mozer \(1974\)](#) X-line, so no prediction from this model can be made for this plasma jet. Still considering the same southward plasma jet, the [Swisdak and Drake \(2007\)](#) model did not correctly predict neither its north-south nor east-west senses. As for the [Trattner et al. \(2007\)](#) model only the east-west sense of this plasma jet was not correctly predicted, since a major westward component would be expected as opposed to the observed eastward component. Looking at the due northward plasma jet at $y_{GSM} \sim -7 R_E$, both [Gonzalez and Mozer \(1974\)](#) and [Swisdak and Drake \(2007\)](#) models correctly predicted both north-south and east-west components of the jet. The maximum shear angle, $\text{Max } \theta_{Shear}$, X-line correctly predicts only the east-west sense of this plasma jet. For the second due northward plasma jet at the duskside magnetopause only the [Swisdak and Drake \(2007\)](#) model correctly predicted the northward-westward plasma jet direction, while the [Gonzalez and Mozer \(1974\)](#) model prediction agreed only with the jet's north-south sense. The [Trattner et al. \(2007\)](#) failed to predict any sense of the jet direction.

Continuing the analysis in the rightmost panel on the top row of Figure 7.11, the plasma jet shown was collected during an IMF clock angle pertaining to the bin $165^\circ \leq \theta_{CA} < 180^\circ$, and the observed northward-eastward jet direction suggests a

subsolar X-line southward of the observation site. Both [Gonzalez and Mozer \(1974\)](#) and [Swisdak and Drake \(2007\)](#) X-line models satisfy this criterion for the IMF conditions at hand, but only the [Gonzalez and Mozer \(1974\)](#) X-line seems to have the appropriate curvature that would give rise to the observed eastward jet component. Since the observed eastward jet component does not agree with the expected westward jet component which in turn would be due to the presence of a positive IMF B_y component, we consider that the east-west jet prediction by the X-line models can not be evaluated, thus we deem such predictions as uncertain. The [Trattner et al. \(2007\)](#) model failed to correctly predict the north-south sense of the plasma jet.

Moving to the bottom row of Figure 7.11, we discuss the results shown on the leftmost panel. Both plasma jets shown were collected during an IMF clock angle pertaining to the bin $180^\circ \leq \theta_{CA} < 195^\circ$. Looking at the dawnside jet ($y_{GSM} \sim -6 R_E$), both the [Swisdak and Drake \(2007\)](#) and [Trattner et al. \(2007\)](#) models could correctly predict only the southward jet component. The observed eastward component, however, did not agree with the expected westward jet component (with the spacecraft being located below the X-line) which in turn would be due to the presence of a negative IMF B_y component. Thus, the east-west sense prediction of this jet could not be evaluated by any X-line model, thus we deem it as uncertain, analogous to what happen with the analysis presented in the paragraph above. The [Gonzalez and Mozer \(1974\)](#) model would predict a jet direction precisely opposite to what was observed. If we extend the number of points of the Max J_{CF} X-line to below the threshold established in the beginning of this section (70% of J_{CF}^{max}) we would find that the Max J_{CF} X-line would be located below the observation site of the second due southward jet ($y_{GSM} \sim 12 R_E$), thus being unable to correctly predict the observed jet direction. Both [Swisdak and Drake \(2007\)](#) and [Trattner et al. \(2007\)](#) models can unambiguously predict only the southward jet component, while the east-west jet component as predicted by the latter model is not so clear since there may be a competition between due westward and due eastward reconnection jets emanating from the both antiparallel X-line branches on low and high latitudes, respectively, so the east-west jet prediction is not unambiguous.

Let's analyze the middle panel on the bottom row of Figure 7.11. Looking at the southward jet, both [Swisdak and Drake \(2007\)](#) and [Trattner et al. \(2007\)](#) models could correctly predict both the jet's north-south and east-west senses, while the [Gonzalez and Mozer \(1974\)](#) model would make a correct prediction of only the north-south sense, since the curvature of the X-line suggests an eastward jet sense opposite to what was observed. As for the due northward jet, both [Swisdak and](#)

Drake (2007) and Gonzalez and Mozer (1974) X-line models correctly predicted only the jet’s north-south sense, while the Trattner et al. (2007) model failed to predict the due northward sense. The observed jet’s east-west (westward) sense, although small when compared to the northward component, was correctly predicted only by the Trattner et al. (2007) model.

At the rightmost panel on the bottom row of Figure 7.11, both Swisdak and Drake (2007) and Gonzalez and Mozer (1974) models correctly predicted both the observed jet’s north-south and east-west senses. The local maximum shear angle X-line, however, could correctly predict only the jet’s north-south sense, since the local X-line orientation suggests a strongly westward jet component, instead of the observed eastward jet component.

We now discuss the data related with the bottom and last part of Table 7.1 wherein the dipole tilt angle bin is $-15^\circ \leq \psi < -5^\circ$. In Figure 7.12 where the IMF B_x is always positive, we start out the discussion with the leftmost panel on the top row. We can argue that all three X-line models correctly predicted the jet’s north-south sense. The slight eastward jet component suggests an X-line whose curvature is akin to the dawnside antiparallel X-line branch of the Trattner et al. (2007) model, thus only this model was able to also correctly predict the jet’s east-west sense.

In the rightmost panel on the top row of Figure 7.12 only the Gonzalez and Mozer (1974) model could correctly predict the due northward (solid arrows) sense of all three plasma jets located above the equator ($z_{GSM} = 0$), while the local Max J_{CF} X-line curvature suggests westward jet components which do not agree with the observed eastward components. The extended version of the Max J_{CF} X-line, i.e., if we added more points to the Gonzalez and Mozer (1974) increasing its length, one would infer that the due southward (dashed arrow) jet would have its full direction correctly predicted by the Max J_{CF} X-line model. The Swisdak and Drake (2007) model could only predict the full jet direction, i.e., both north-south and east-west senses, of the jet located closest to the noon-midnight meridian plane ($y_{GSM} = 0$). Regarding the due southward jet, the Max V_{out} X-line model correctly predicted only the jet’s north-south sense. For this same jet, we argue that the Trattner et al. (2007) model could predict only the southward jet component, while the east-west prediction is ambiguous since we presently can not say for sure which X-line branch will have a larger influence on the jet direction. As for the three jets above the equator, the maximum shear angle, Max θ_{Shear} , X-line correctly predicted only the east-west sense of the two jets farther away from the noon-midnight meridian

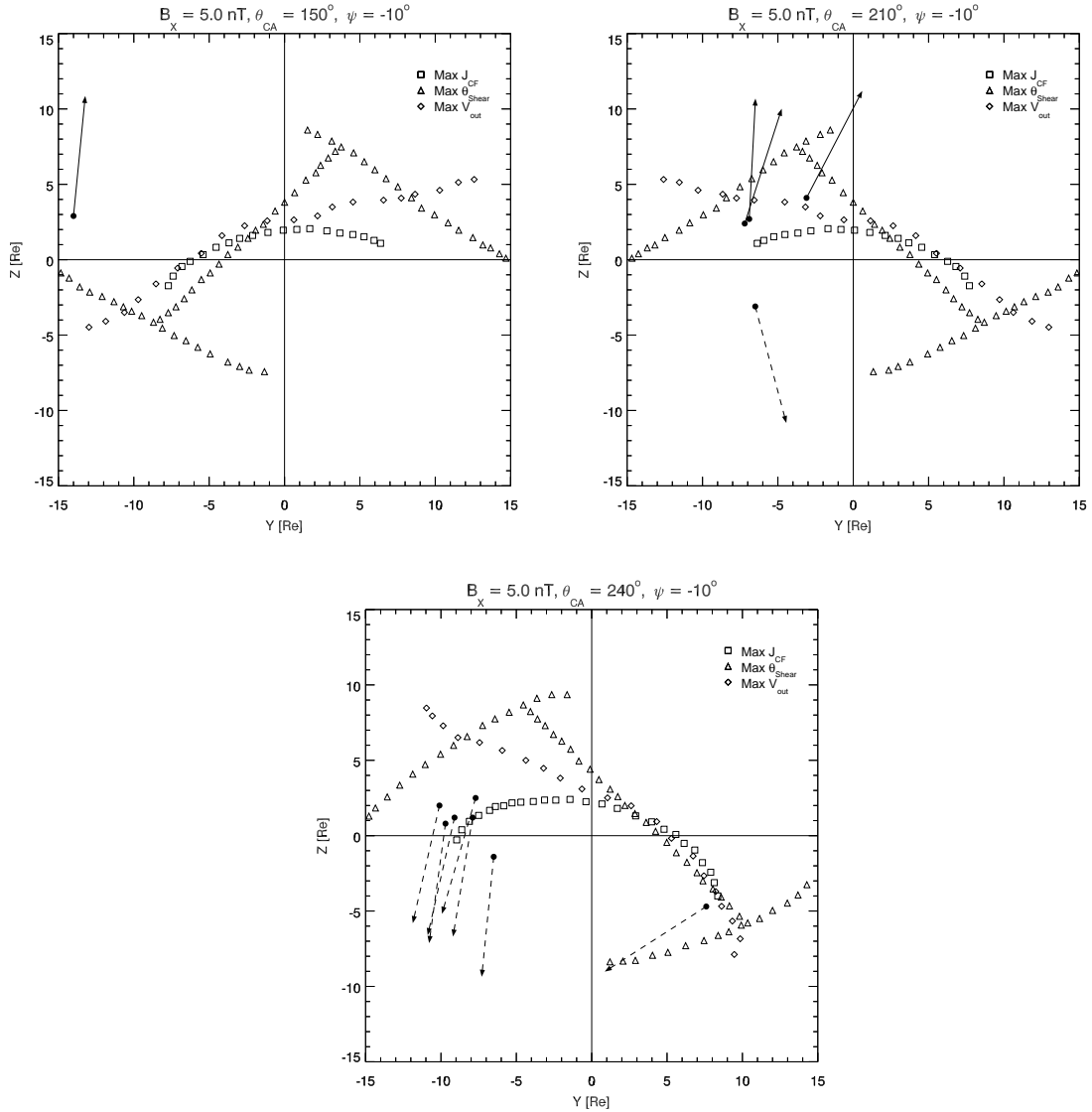


Figure 7.12 - X-line models test against *in situ* observations of reconnection plasma jets. The X-lines which are presented onto the yz_{GSM} plane are derived from the models of maximum Chapman-Ferraro current density magnitude, $\text{Max } J_{CF}$, by Gonzalez and Mozer (1974), the maximum shear angle model, $\text{Max } \theta_{Shear}$, by Trattner et al. (2007), and the maximum reconnection outflow speed, $\text{Max } V_{out}$, by Swisdak and Drake (2007). The IMF ($B_x = 5$ nT, $B_z = -2.886$ or -5 nT and $\theta_{CA} = \tan^{-1}(B_y/B_z)$) and Earth's dipole tilt (ψ) conditions used as input to generate the X-lines shown are presented on the top of each panel. The observed plasma jet directions are represented as solid (dashed) arrows if they have a northward (southward) V_z^{jet} component, and they were detected under IMF and dipole tilt conditions similar to those shown on the top of the respective panel (see text for details). The location of the spacecraft when it detected the plasma jet at the dayside magnetopause crossing is marked by the black filled circle.

plane, whereas the model failed to correctly predict their north-south senses. The Max θ_{Shear} X-line model also failed to correctly predict the full direction of the jet closest to the noon-midnight meridian plane.

Moving to the bottom panel of Figure 7.12, all three X-line models could correctly predict the southward-westward direction of the jet located at the duskside ($y_{GSM} > 0$) magnetopause region. For the six southward-westward reconnection plasma jets located on the dawnside ($y_{GSM} < 0$) magnetopause region, the Swisdak and Drake (2007) model correctly predicted both north-south and east-west senses of all of them. As for the Trattner et al. (2007) model, we claim that only the north-south jet directions were correctly predicted due to the proximity of the jet's observation sites from the dawnside antiparallel X-line branch which would give as a prediction southward-eastward jet directions, as opposed to the observed southward-westward jet directions. The Gonzalez and Mozer (1974) model could correctly predict the full direction of only one of the six dawnside jets. One out of the remaining five had no clear prediction since its position was collocated with the Max J_{CF} X-line.

We now move to the last set of observational data related with Table 7.1. Figure 7.13 shows the cases wherein the IMF B_x component was negative, and the dipole tilt bin remained the same of Figure 7.12, i.e., $-15^\circ \leq \psi < -5^\circ$.

Let's start with the leftmost panel on the top row of Figure 7.13. For the five reconnection jets located at the dawnside magnetopause region, both Gonzalez and Mozer (1974) and Swisdak and Drake (2007) X-line models correctly predicted the due northward direction of all of them. The Trattner et al. (2007) model achieved an agreement with the observed (dawnside) jet's north-south sense in four out of five cases. The non-agreement case occurred for the jet at $y_{GSM} \sim -10 R_E$. Contrary to expectations, four (4) of these jets did not present a westward flow component despite the presence of a positive IMF B_y for the clock angle bin being shown, i.e., $135^\circ \leq \theta_{CA} < 165^\circ$. Thus, any X-line model correctly predicted four of the dawnside jets east-west sense. The only dawnside jet which presented a quite small, but still noticeable, westward component was located at $[y_{GSM}, z_{GSM}] \sim [-5, 5] R_E$, and thus both Gonzalez and Mozer (1974) and Swisdak and Drake (2007) models correctly predicted its east-west sense. The same behavior did not occurred for the duskside ($y_{GSM} > 0$) jet, where both Gonzalez and Mozer (1974) and Swisdak and Drake (2007) X-line models correctly predicted the due eastward jet component, but failed to correctly predict its due northward component. The Max θ_{Shear} model could not correctly predict the duskside jet's northward component, while its east-

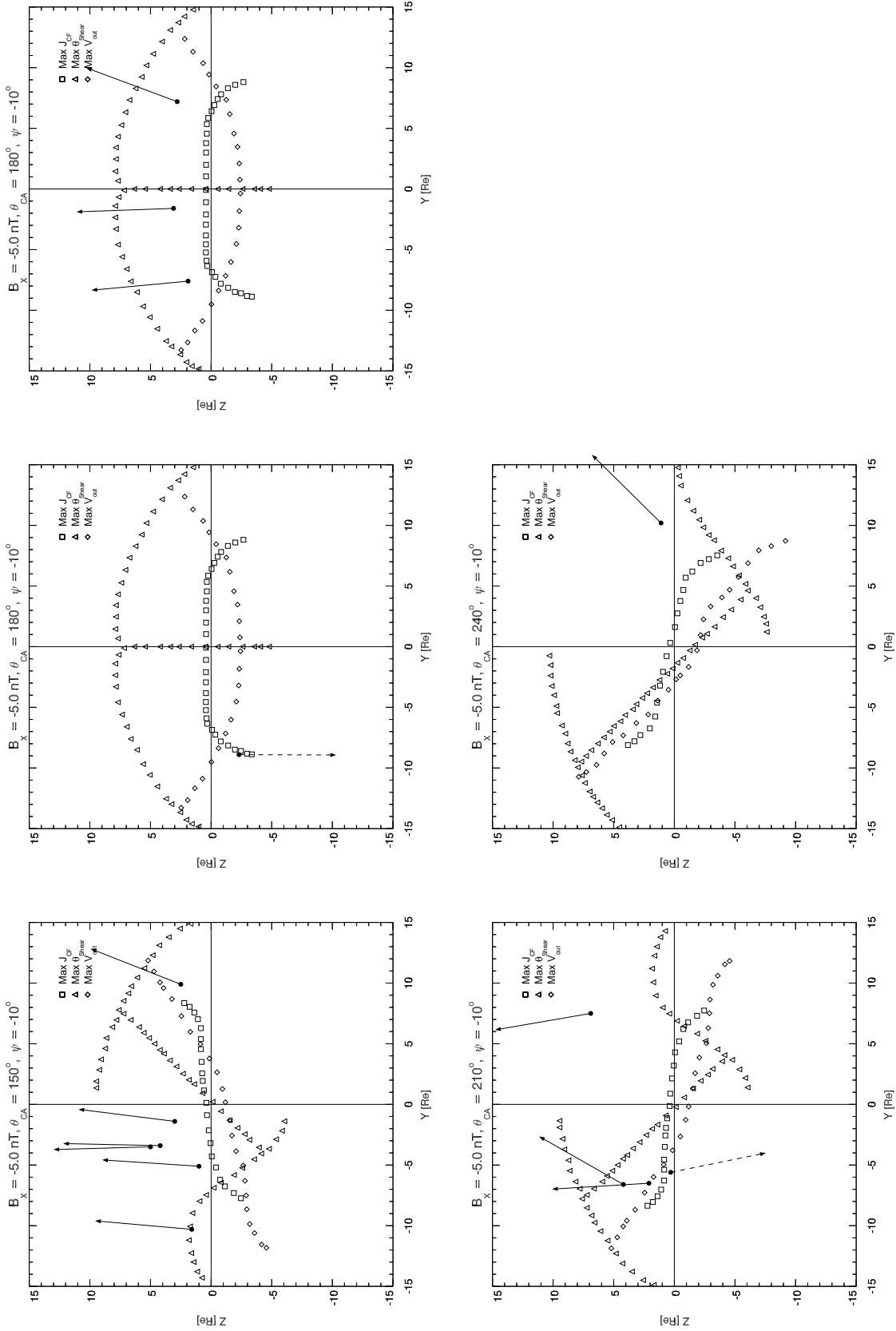


Figure 7.13 - X-line models test against *in situ* observations of reconnection plasma jets. The X-lines which are presented onto the yz_{GSM} plane are derived from the models of maximum Chapman-Ferraro current density magnitude, Max J_{CF} , by Gonzalez and Mozer (1974), the maximum shear angle model, Max θ_{Shear} , by Trattner et al. (2007), and the maximum reconnection outflow speed, Max V_{out} , by Swisdak and Drake (2007). The IMF ($B_x = -5$ nT, $B_z = -2.886$ or -5 nT and $\theta_{CA} = \tan^{-1}(B_y/B_z)$) and Earth's dipole tilt (ψ) conditions used as input to generate the X-lines shown are presented on the top of each panel. The observed plasma jet directions are represented as solid (dashed) arrows if they have a northward (southward) V_z^{jet} component, and they were detected under IMF and dipole tilt conditions similar to those shown on the top of the respective panel (see text for details). The location of the spacecraft when it detected the plasma jet at the dayside magnetopause crossing is marked by the black filled circle.

west component prediction was not clear, since at the duskside jet location both due eastward and due westward reconnection flows emerging from the subsolar and antiparallel X-line branches, respectively, can be present at the jet location, and it is not straightforward to conclude which of these two sources will prevail.

In the middle panel on the top row of Figure 7.13, where the clock angle bin being shown is $165^\circ \leq \theta_{CA} < 180^\circ$, only the [Trattner et al. \(2007\)](#) and [Swisdak and Drake \(2007\)](#) models correctly predicted the due southward component of the observed jet. Due to the almost purely southward jet direction, no X-line model correctly predict the jet's east-west sense, since the observed jet direction suggests a local X-line segment northward of the observation site and parallel to the equator.

Moving to the rightmost panel on the top row of Figure 7.13, where the clock angle bin being shown is $180^\circ \leq \theta_{CA} < 195^\circ$, the [Gonzalez and Mozer \(1974\)](#) X-line model was the only one to correctly predict all jets' full direction, i.e., both north-south and east-west senses. The [Swisdak and Drake \(2007\)](#) model correctly predicted the observed almost purely northward direction of the jet closest to the noon-midnight meridian plane. For the other two jets, only the north-south sense predictions agreed with observations. The maximum shear angle X-line failed to correctly predict any sense of any plasma jet direction shown.

Analyzing the leftmost panel on the bottom row of Figure 7.13, the [Gonzalez and Mozer \(1974\)](#) model could correctly predict the north-south sense of all four reconnection plasma jets shown. The [Swisdak and Drake \(2007\)](#) model prediction was in agreement with both north-south and east-west senses of the observed northward-eastward jet ($[y_{GSM}, z_{GSM}] \sim [-7, 4] R_E$) on the dawnside magnetopause region. For the due northward reconnection jet in the same region, however, the model prediction was not clear since the jet observation site was collocated with the Max V_{out} X-line location. For the due northward jet on the duskside magnetopause region the Max V_{out} X-line prediction agreed only with the jet's north-south sense. The southward (dashed arrow) reconnection jet located near the equator had only its north-south sense correctly predicted by all three X-line models. The maximum shear X-line model failed to correctly predict both north-south and east-west senses of both northward jets on the dawnside magnetopause region. As for the other northward jet on the duskside magnetopause region, however, the nearest portion from the jet observation site of the [Trattner et al. \(2007\)](#) X-line seems to have the appropriate curvature in order to give rise to a northward-westward reconnection jet, as observed. Thus, we claim that the maximum shear X-line correctly predicted the

full jet direction on the duskside magnetopause region.

For the rightmost panel on the bottom row of Figure 7.13, both Swisdak and Drake (2007) and Gonzalez and Mozer (1974) models correctly predicted the jet’s both north-south and east-west senses. As for the Trattner et al. (2007) model, only the due northward jet component was correctly predicted. The local curvature of the duskside ($y_{GSM} > 0$) antiparallel branch of the maximum shear angle X-line ($\text{Max } \theta_{Shear}$), which is located closest from the jet observation site, seems to suggest a westward, rather than eastward, jet component. Therefore, we argue that the Trattner et al. (2007) X-line failed to correctly predict the east-west sense of the reconnection jet shown.

7.1.6.1 Summary of X-line models test against *in situ* magnetic reconnection plasma jet observations

In a way similar to what we have done in Section 6.1.2.4, we count the number of times the model X-line location was such that it would correctly predict the north-south (N-S) and/or east-west (E-W) senses of the observed jet direction at a given spacecraft location. In what follows, a total of six (6) tables are shown. Each pair of tables refers to the assessment of a given X-line model. Tables 7.3 and 7.4 evaluate the Trattner et al. (2007) model for the cases where the Earth’s dipole tilt center bin, ψ , was negative ($\psi < 0$) and greater than or equal to zero ($\psi \geq 0$), respectively. The same pattern follows for Tables 7.5 and 7.6 where the Gonzalez and Mozer (1974) model is evaluated, and also for Tables 7.7 and 7.8 where the Swisdak and Drake (2007) model is evaluated.

Each pair of tables has the same format of Tables 7.1 and 7.2, i.e., the reader will see the number of times the given X-line model correctly predicted the observed jet directions for different combinations of IMF and Earth’s dipole tilt angle.

We now proceed to describe the contents of the tables which are going to be presented below. The number of reconnection events available for each IMF clock angle ($\theta_{CA} = \tan^{-1}(B_y/B_z)$) interval is presented by a bold number within parenthesis alongside each clock angle bin. When there were no events for a given clock angle bin, and therefore no X-line model prediction could be performed, an “N/A” (not applicable) sign was shown below the respective θ_{CA} bin. When there were reconnection observations for a given clock angle bin, an information is shown indicating the number of times the given X-line correctly predicted the north-south (N-S) and/or the east-west (E-W) senses of the observed jet directions. Whenever a question mark

“?” is present, it means that either N-S or E-W, or even both, predictions were not clear due to 1) the X-line geometry was such that it did not allow an unambiguous prediction or 2) the X-line trace was collocated with the spacecraft location.

Earth’s dipole tilt center bin less than zero $\psi < 0$

Let’s first analyze the X-line models agreement with observed reconnection plasma jets for the cases where the Earth’s dipole tilt was negative, i.e., the results shown in Tables 7.3, 7.5 and 7.7. There were 60 reconnection events for which the Earth’s dipole tilt values were around central negative ψ values, namely $\psi = -10^\circ, -20^\circ$ and -30° . If we collect the total number of times, within these 60 events, the maximum shear angle (TRATTNER et al., 2007) model correctly predicted the north-south sense of the observed jets, we will find that such a number, i.e., 37, corresponds to 62% of the cases, while the Gonzalez and Mozer (1974) and Swisdak and Drake (2007) models made correct north-south predictions in 65% (39 out of 60) and 73% (44 out of 60) of the cases, respectively. The Trattner et al. (2007) and Gonzalez and Mozer (1974) models have fairly equal amounts of correct jet’s north-south predictions, while the Swisdak and Drake (2007) model seems to perform better than the other two, although the difference among them is not too large. Looking at the east-west predictions, the percentage of agreement for the three models are 33% (TRATTNER et al., 2007), 43% (GONZALEZ; MOZER, 1974) and 48% (SWISDAK; DRAKE, 2007). In this analysis the Swisdak and Drake (2007) model performs slightly better in the number of correct east-west predictions than Trattner et al. (2007)’s, which in turn achieves a higher percentage of agreement than the Gonzalez and Mozer (1974) model, although, again, the difference in numbers is not too large.

Earth’s dipole tilt center bin greater than or equal to zero $\psi \geq 0$

Moving to the cases where the Earth’s dipole tilt was positive, i.e., the 56 reconnection events shown in each one of Tables 7.4, 7.6 and 7.8, we find that the percentage of agreement with observations of the jet’s north-south component for the three models are 71% (40/56, Trattner et al. (2007)), 55% (31/56, Gonzalez and Mozer (1974)) and 71% (40/56, Swisdak and Drake (2007)). In this case, both Trattner et al. (2007) and Swisdak and Drake (2007) models perform equally well, followed by the Gonzalez and Mozer (1974) model. If we look at the percentage of correct jet’s east-west sense prediction for the three models we obtain: 41% (23/56, Trattner et al. (2007) and Gonzalez and Mozer (1974)), and 61% (34/56, Swisdak and Drake (2007)). Once again, the Swisdak and Drake (2007) model had a somewhat better performance than the other two if we take into account both jet’s north-south and

east-west predictions.

Overall agreement

Considering the total number of events, i.e., $60 + 56 = 116$ for all dipole tilt ψ , we can find the percentages for which the three X-line models correctly predicted the reconnection plasma jet's north-south (N-S) and east-west (E-W) senses as being

| | | |
|----------------------------|------------------|------------------|
| Trattner et al. (2007): | 66% (77/116) N-S | 37% (43/116) E-W |
| Gonzalez and Mozer (1974): | 60% (70/116) N-S | 42% (49/116) E-W |
| Swisdak and Drake (2007): | 72% (84/116) N-S | 54% (63/116) E-W |

The results shown above seem to confirm the tendency shown in Section 6.1.2.4 that the Swisdak and Drake (2007) X-line model appears to be more suited to describe the large scale reconnection process at Earth's dayside magnetopause since it correctly predicts the observed jet directions for a higher number of cases as compared to the other two models. We note, however, that the differences in the numbers of correct jet direction predictions among the X-line models were not too large, i.e., less than 20% difference.

We note that the number of correct east-west predictions was always lesser than the north-south, when they were expected to be roughly the same. The main cause for such a discrepancy is that even with the magnetosheath flow component subtracted off the observed accelerated flow, the resultant jet directions, in some cases, are not always in the expected east-west sense which in turn is derived by the knowledge of the observed sign of the IMF B_y component¹¹. As a result, the representative X-line trace could not provide a correct prediction of the jet's east-west component, except in cases where the X-line geometry possessed some curvature in such a way that it would correctly predict the jet's east-west sense.

We emphasize that any of the X-line models used in this work provides a prediction of the resultant reconnection outflow direction. The Swisdak and Drake (2007) model, for instance, addresses only the reconnection outflow magnitude. The jet direction predictions were based on the simple assumption that the reconnection flows leave the X-line in a direction perpendicular to the local X-line segment, as predicted by standard reconnection theories (VASYLIUNAS, 1975). Such a prediction, however, is valid for observed jet locations near the X-line. On the other hand, reconnection outflow direction predictions further away from the X-line may have their original

¹¹For instance, for a positive IMF B_y with the spacecraft detecting a plasma jet above (below) the reconnection X-line, a westward (eastward) jet component would be expected.

directions changed possibly by the curvature of the magnetopause boundary and therefore its direction on the yz_{GSM} plane is not determined in a straightforward manner. This limitation was not addressed in this work. Thus, the results obtained here have some degree of uncertainty and must be interpreted with care, which is why we argue that all X-line models presented roughly the same performance, despite the modest differences in the number of correct jet direction predictions, but with a slight tendency toward the [Swisdak and Drake \(2007\)](#) model to better fit the observational dataset in an overall sense.

Influence of the IMF B_y component

Separating the number of observed reconnection plasma jets data into eight clock angle (θ_{CA}) bins as shown, for instance, in [Table 7.4](#), regardless of both IMF B_x and dipole tilt ψ signs, we obtain:

$$\begin{array}{cccc}
 \theta_{CA} = 97.5^\circ \pm 7.5^\circ & 120^\circ \pm 15^\circ & 150^\circ \pm 15^\circ & 172.5^\circ \pm 7.5^\circ, \\
 7 & 11 & 22 & 6, \\
 \theta_{CA} = 187.5^\circ \pm 7.5^\circ & 210^\circ \pm 15^\circ & 150^\circ \pm 240^\circ & 262.5^\circ \pm 7.5^\circ, \\
 17 & 32 & 17 & 4.
 \end{array}$$

If we sum the number of times the X-line models correctly predicted the north-south and east-west senses of the observed jets for each clock angle bin shown above, we find the following result: at least one X-line model, at each clock angle bin, correctly predicted as much as 52% of the number of north-south jet components for that specific bin, and also as much as 44% of the number of east-west jet components for the same bin. In spite of the intrinsic limitations of each analytical X-line model which in turn elected a small amount of parameters to describe the possibly complex large scale behavior of Earth's dayside magnetopause reconnection, we argue that part (more than 40%) of the results are consistent with a component-type reconnection scenario ([GONZALEZ; MOZER, 1974](#); [SONNERUP, 1974](#)), in the sense that tilted, subsolar X-lines are able to explain the observed jet directions.

External versus local boundary conditions

Undoubtedly, the interplanetary magnetic field (IMF) has a primordial importance on orienting and determining the dayside magnetopause reconnection X-line location ([DALY et al., 1984](#); [PHAN et al., 2006](#); [SIBECK; LIN, 2011](#); [DUNLOP et al., 2011](#)). The results shown here also seem to suggest that local plasma and magnetic field

parameters, as given by the Swisdak and Drake (2007) X-line model, may play an important role since this model has been shown to fit a higher percentage of the observed reconnection jets data, probably because it takes into account the realistic asymmetric magnetic field and plasma conditions across the dayside magnetopause boundary. We note, however, that both the magnetosheath magnetic field and density, as being part of the parameters involved in controlling the Swisdak and Drake (2007) X-line orientation, are in turn ultimately governed by solar wind conditions. Thus, we claim that both the internal and external boundary conditions are coupled in such a way that presently we can not say for sure which one is more important for the occurrence of the magnetic reconnection process.

It is worthwhile to mention that both Gonzalez and Mozer (1974) and Trattner et al. (2007) X-line models have been separately tested against *in situ* observations of accelerated plasma flows before (TRENCHI et al., 2008; TRATTNER et al., 2012), and the results were indicative that the observational reconnection signatures would be consistent with the presence of the X-line model being tested. As far as we know, the Swisdak and Drake (2007) X-line model orientation has been successfully tested only in Hall-MHD numerical simulations (SCHREIER et al., 2010). We therefore argue that it is not just one parameter, e.g., magnetic field or plasma density, that will dictate the way the large-scale dayside reconnection X-line will orient itself, but possibly a combination of them. It has been observationally shown, for instance, that in both solar wind (PHAN et al., 2010) and Earth’s magnetopause (PHAN et al., 2013) current sheets, the plasma β parameter, i.e., the ratio of thermal to magnetic plasma pressures, is an important controlling factor for the onset of magnetic reconnection, meaning that for high plasma β regimes reconnection should occur only for high shear angles (θ_{shear}) in order to overcome the X-line’s diamagnetic drift¹² which tends to suppress the reconnection process, while for low plasma β regimes reconnection can occur for a large range of shear angles without being torn apart by the diamagnetic drift.

We have performed a test to verify whether the local plasma and magnetic field parameters in our statistical survey would, in theory, allow magnetic reconnection to occur or not by looking at the relation between the local magnetic shear angle θ_{shear} and the difference between the plasma beta (β) values from the magnetosheath (β_{sh}) and magnetosphere (β_{sp}), i.e., the so-called $\Delta\beta$ condition (SWISDAK et al., 2003). In

¹²In the presence of a thermal pressure gradient across the reconnection layer, the X-line experiences a diamagnetic drift in a direction parallel to the reconnection outflow which may suppress the reconnection process if the drift speed reaches the reconnection outflow speed. The reader is referred to the work of Swisdak et al. (2003) for more details on this phenomena.

this scenario, reconnection is suppressed if the condition below is satisfied

$$\Delta\beta > 2 \left(\frac{L}{\lambda_i} \right) \tan(\theta_{shear}/2), \quad (7.5)$$

where L/λ_i is the width of the plasma pressure gradient layer in units of the ion inertial length λ_i . Notice that if L is lower (greater) than λ_i , the relation 7.5 becomes easier (harder) to be satisfied, since the product $2(L/\lambda_i) \tan(\theta_{shear}/2)$ tends to diminish (increase) toward (away from) zero for a given θ_{shear} value. Thus, when relation 7.5 is used, three values for the ratio L/λ_i are taken: 0.5, 1 and 2.

What we have done was to apply relation 7.5 for all THEMIS magnetopause crossing events in order to check whether the local plasma and magnetic field parameters were in the regime wherein magnetic reconnection should be suppressed or not. The reason why only THEMIS data was used is that when determining $\Delta\beta$ one needs the total beta value, i.e., the contribution from both ions and electrons, and electron moments were always available in THEMIS data, as opposed to DOUBLE STAR TC1 and CLUSTER spacecraft. The $\Delta\beta$ condition provides a further confirmation whether reconnection may or may not occur, and also give us a clue on what are some of the key parameters controlling the reconnection process.

In order to apply the $\Delta\beta$ condition on the dayside magnetopause context we need to determine the plasma β values on both sides of the magnetopause, i.e., on the magnetosheath side (β_{sh}) and on the magnetospheric side (β_{sp}). The plasma β parameter is defined as the ratio between thermal and magnetic pressures

$$\beta = \frac{2\mu_0 k_B (n_i T_i + n_e T_e)}{B^2}, \quad (7.6)$$

where k_B is the Boltzmann constant, and $n_{i,e}$ [cm^{-3}], $T_{i,e}$ [K] and B [nT] are either the ion or electron densities and temperatures and the magnetic field magnitude taken either on the magnetosheath side or on the magnetospheric side of the magnetopause boundary. Looking at Figure 7.5 the plasma and magnetic field values on both sides of the magnetopause boundary are obtained as one-minute period averages demarcated by the 2 pairs of vertical dashed lines. For the example at hand, we find that the $\Delta\beta$ value for this crossing was $\Delta\beta = 1.04 \pm 0.20$, while the shear angle was $\theta_{shear} = 148.13 \pm 4.78$. If we insert these values in relation 7.5 we see that it is not satisfied for any of the three chosen values of the L/λ_i ratio, i.e.,

$L/\lambda_i = 0.5, 1, 2$, since $2(L/\lambda_i) \tan(\theta_{shear}/2)$ lies between 3.07 and 16.99, and the smallest of these values, 3.07, is larger than $\Delta\beta$ even if we include the 0.20 uncertainty in $\Delta\beta$ determination. That means that given these magnetic field and plasma conditions, reconnection would not be suppressed by the X line drift.

Figure 7.14 shows the plot of the magnetic shear angle θ_{shear} versus $\Delta\beta$ values for all 90 THEMIS reconnection events. We note that β_{sh} is usually much higher than β_{sp} , thus $\Delta\beta \approx \beta_{sh}$ most of the time. The majority of the events are concentrated in the region where reconnection should not be suppressed as predicted by theory, meaning that the local shear angle and $\Delta\beta$ values for these events were likely to be representative of conditions at the X line, probably because the X line was near from each spacecraft location (PHAN et al., 2013). On the other hand, for those events whose magnetic fields and plasma signatures were consistent with reconnection and even so fell out of the regime where reconnection should not be suppressed were likely far from the X line, and the local magnetic field and plasma parameters were possibly not representative of the conditions at the X line. The trend shown in Figure 7.14 is in line with earlier claims based on *in situ* observations that dayside magnetopause reconnection is prone to occur for low magnetosheath β_{sh} values (see e.g., Phan et al. (2013) and references therein), and that the X line's drift as caused by plasma pressure gradients across the reconnection layer may be a controlling factor for reconnection to occur on that region.

Thus, we see that a combination of plasma parameters, or alternatively a competition of different forces on the plasma may act to favor or not the magnetic reconnection process.

Table 7.3 - Number of times the Trattner et al. (2007)'s X-line model correctly predicted the north-south (N-S) and/or east-west (E-W) senses of the observed plasma jet directions. The single magnetopause crossing (reconnection) events from which the observed plasma jets were obtained have been distributed according to IMF orientation and three Earth's dipole tilt inclination intervals, whose center bins are $\psi = -30^\circ$, -20° , and -10° . The bold number within parenthesis (when present) alongside each clock angle (θ_{CA}) bin means the number of reconnection events for that specific bin. N/A (not applicable) means that there were no reconnection events for a specific clock angle bin, thus no X-line model prediction was applicable. Question marks represent either not clear or ambiguous predictions.

| | | Maximum Shear Angle Model: Trattner et al. (2007) | |
|---|-----------------|---|---------------|
| | | IMF $B_x > 0$ | IMF $B_x < 0$ |
| | | $-35^\circ \leq \psi < -25^\circ$ | |
| $\theta_{CA} = 97.5^\circ \pm 7.5^\circ$ | N/A | 2 N-S / 1 E-W | N/A |
| | N/A | 1,? N-S / 1,? E-W | N/A |
| $\theta_{CA} = 187.5^\circ \pm 7.5^\circ$ | N/A | 0 N-S / ? E-W | N/A |
| | N/A | 0 N-S / ? E-W | N/A |
| $-25^\circ \leq \psi < -15^\circ$ | | | |
| $\theta_{CA} = 97.5^\circ \pm 7.5^\circ$ (1) | 1 N-S / 1 E-W | N/A | N/A |
| | 1 N-S / 1 E-W | N/A | N/A |
| $\theta_{CA} = 187.5^\circ \pm 7.5^\circ$ (3) | 2 N-S / 1,? E-W | 2 N-S / 1 E-W | N/A |
| | 2 N-S / 1,? E-W | 2 N-S / 1 E-W | N/A |
| $-15^\circ \leq \psi < -5^\circ$ | | | |
| $\theta_{CA} = 97.5^\circ \pm 7.5^\circ$ | N/A | N/A | N/A |
| | N/A | 1 N-S / 1 E-W | N/A |
| $\theta_{CA} = 187.5^\circ \pm 7.5^\circ$ (4) | 1 N-S / 2,? E-W | 7 N-S / 1 E-W | N/A |
| | N/A | 1 N-S / 1 E-W | N/A |

Table 7.4 - Number of times the [Trattner et al. \(2007\)](#)'s X-line model correctly predicted the north-south (N-S) and/or east-west (E-W) senses of the observed plasma jet directions. The single magnetopause crossing (reconnection) events from which the observed plasma jets were obtained have been distributed according to IMF orientation and four Earth's dipole tilt inclination intervals, whose center bins are $\psi = 0^\circ, 10^\circ, 20^\circ$, and 30° . The bold number within parenthesis (when present) alongside each clock angle (θ_{CA}) bin means the number of reconnection events found for that specific bin. N/A (not applicable) means that there were no reconnection events for a specific clock angle bin, thus no X-line model prediction was applicable. Question marks represent either not clear or ambiguous predictions.

| Maximum Shear Angle Model: Trattner et al. (2007) | | | | | | | | | | | |
|---|-------------------------------------|--|-------------------------------------|---|--|-------------------------------------|-------------------------------------|-------------------------------------|--|--|--|
| $-5^\circ \leq \psi < 5^\circ$ | | | | | | $5^\circ \leq \psi < 15^\circ$ | | | | | |
| IMF $B_x > 0$ | | | IMF $B_x < 0$ | | | IMF $B_x > 0$ | | | IMF $B_x < 0$ | | |
| IMF $B_y > 0$ | | | | | | IMF $B_y > 0$ | | | | | |
| IMF $B_y < 0$ | | | | | | IMF $B_y < 0$ | | | | | |
| $\theta_{CA} = 97.5^\circ \pm 7.5^\circ$ | $120^\circ \pm 15^\circ$ | 2 | $150^\circ \pm 15^\circ$ | 2 | $172.5^\circ \pm 7.5^\circ$ | $97.5^\circ \pm 7.5^\circ$ | $120^\circ \pm 15^\circ$ | (2) | $150^\circ \pm 15^\circ$ | (1) | $172.5^\circ \pm 7.5^\circ$ |
| N/A | N/A | 1 N-S / 1,? E-W | N/A | N/A | N/A | N/A | 2 N-S / 1,? E-W | 1 N-S / ? E-W | 1 N-S / ? E-W | 0 N-S / ? E-W | 0 N-S / ? E-W |
| IMF $B_y < 0$ | | | | | | IMF $B_y < 0$ | | | | | |
| $\theta_{CA} = 187.5^\circ \pm 7.5^\circ$ (3) | $210^\circ \pm 15^\circ$ (3) | 240^\circ \pm 15^\circ (2) | $240^\circ \pm 15^\circ$ (1) | 262.5^\circ \pm 7.5^\circ (1) | $187.5^\circ \pm 7.5^\circ$ (1) | $210^\circ \pm 15^\circ$ (1) | $210^\circ \pm 15^\circ$ (1) | $240^\circ \pm 15^\circ$ (1) | $240^\circ \pm 15^\circ$ | $262.5^\circ \pm 7.5^\circ$ | $262.5^\circ \pm 7.5^\circ$ |
| 2 N-S / 0 E-W | 1 N-S / 2 E-W | 2 N-S / 0,? E-W | 1 N-S / 1 E-W | 1 N-S / 1 E-W | 1 N-S / 0 E-W | 1 N-S / 0 E-W | 1 N-S / 0 E-W | N/A | N/A | N/A | N/A |
| IMF $B_y > 0$ | | | | | | IMF $B_y > 0$ | | | | | |
| $\theta_{CA} = 97.5^\circ \pm 7.5^\circ$ (1) | $120^\circ \pm 15^\circ$ (1) | $150^\circ \pm 15^\circ$ | $150^\circ \pm 15^\circ$ | $172.5^\circ \pm 7.5^\circ$ (1) | $97.5^\circ \pm 7.5^\circ$ | $120^\circ \pm 15^\circ$ (3) | $150^\circ \pm 15^\circ$ (1) | $150^\circ \pm 15^\circ$ (1) | $172.5^\circ \pm 7.5^\circ$ (1) | $172.5^\circ \pm 7.5^\circ$ (1) | $172.5^\circ \pm 7.5^\circ$ (1) |
| 0 N-S / 0 E-W | 0 N-S / 0 E-W | N/A | N/A | 1 N-S / ? E-W | N/A | 3 N-S / 2 E-W | 1 N-S / 0 E-W | 1 N-S / 0 E-W | 0 N-S / 0 E-W | 0 N-S / 0 E-W | 0 N-S / 0 E-W |
| IMF $B_y < 0$ | | | | | | IMF $B_y < 0$ | | | | | |
| $\theta_{CA} = 187.5^\circ \pm 7.5^\circ$ | $210^\circ \pm 15^\circ$ (4) | $240^\circ \pm 15^\circ$ (1) | $240^\circ \pm 15^\circ$ (1) | 262.5^\circ \pm 7.5^\circ (2) | $187.5^\circ \pm 7.5^\circ$ (1) | $210^\circ \pm 15^\circ$ (2) | $240^\circ \pm 15^\circ$ (2) | $240^\circ \pm 15^\circ$ | $262.5^\circ \pm 7.5^\circ$ (1) | $262.5^\circ \pm 7.5^\circ$ (1) | $262.5^\circ \pm 7.5^\circ$ (1) |
| N/A | 3 N-S / 3,? E-W | 1 N-S / 0 E-W | 1 N-S / 0 E-W | 2 N-S / 2 E-W | 1 N-S / ? E-W | 1,? N-S / 1,? E-W | N/A | N/A | 0 N-S / 0 E-W | 0 N-S / 0 E-W | 0 N-S / 0 E-W |
| IMF $B_y > 0$ | | | | | | IMF $B_y > 0$ | | | | | |
| $\theta_{CA} = 97.5^\circ \pm 7.5^\circ$ | $120^\circ \pm 15^\circ$ | $150^\circ \pm 15^\circ$ | $150^\circ \pm 15^\circ$ | $172.5^\circ \pm 7.5^\circ$ | $97.5^\circ \pm 7.5^\circ$ (1) | $120^\circ \pm 15^\circ$ (1) | $150^\circ \pm 15^\circ$ (3) | $150^\circ \pm 15^\circ$ (3) | $172.5^\circ \pm 7.5^\circ$ | $172.5^\circ \pm 7.5^\circ$ | $172.5^\circ \pm 7.5^\circ$ |
| N/A | N/A | N/A | N/A | N/A | 0 N-S / 0 E-W | 1 N-S / 1 E-W | 1 N-S / 0 E-W | 1 N-S / 0 E-W | N/A | N/A | N/A |
| IMF $B_y < 0$ | | | | | | IMF $B_y < 0$ | | | | | |
| $\theta_{CA} = 187.5^\circ \pm 7.5^\circ$ | $210^\circ \pm 15^\circ$ (2) | $240^\circ \pm 15^\circ$ (2) | $240^\circ \pm 15^\circ$ (2) | 262.5^\circ \pm 7.5^\circ | $187.5^\circ \pm 7.5^\circ$ | $210^\circ \pm 15^\circ$ (1) | $240^\circ \pm 15^\circ$ (1) | $240^\circ \pm 15^\circ$ (1) | 262.5^\circ \pm 7.5^\circ | 262.5^\circ \pm 7.5^\circ | 262.5^\circ \pm 7.5^\circ |
| N/A | 2 N-S / 1 E-W | 2 N-S / 1 E-W | 2 N-S / 1 E-W | N/A | N/A | 1 N-S / 1 E-W | 1 N-S / 1 E-W | 1 N-S / 1 E-W | N/A | N/A | N/A |
| IMF $B_y > 0$ | | | | | | IMF $B_y > 0$ | | | | | |
| $\theta_{CA} = 97.5^\circ \pm 7.5^\circ$ | $120^\circ \pm 15^\circ$ | $150^\circ \pm 15^\circ$ | $150^\circ \pm 15^\circ$ | $172.5^\circ \pm 7.5^\circ$ | $97.5^\circ \pm 7.5^\circ$ (1) | $120^\circ \pm 15^\circ$ | $150^\circ \pm 15^\circ$ (2) | $150^\circ \pm 15^\circ$ (2) | $172.5^\circ \pm 7.5^\circ$ | $172.5^\circ \pm 7.5^\circ$ | $172.5^\circ \pm 7.5^\circ$ |
| N/A | N/A | N/A | N/A | N/A | 0 N-S / 1 E-W | N/A | 1 N-S / 1 E-W | 1 N-S / 1 E-W | N/A | N/A | N/A |
| IMF $B_y < 0$ | | | | | | IMF $B_y < 0$ | | | | | |
| $\theta_{CA} = 187.5^\circ \pm 7.5^\circ$ (2) | $210^\circ \pm 15^\circ$ (1) | $240^\circ \pm 15^\circ$ (1) | $240^\circ \pm 15^\circ$ (1) | 262.5^\circ \pm 7.5^\circ | $187.5^\circ \pm 7.5^\circ$ (1) | $210^\circ \pm 15^\circ$ (1) | $240^\circ \pm 15^\circ$ (1) | $240^\circ \pm 15^\circ$ | 262.5^\circ \pm 7.5^\circ | 262.5^\circ \pm 7.5^\circ | 262.5^\circ \pm 7.5^\circ |
| 2 N-S / 2 E-W | 1 N-S / ? E-W | 1 N-S / ? E-W | 1 N-S / ? E-W | N/A | 1 N-S / 1 E-W | 1 N-S / ? E-W | N/A | N/A | N/A | N/A | N/A |

Table 7.5 - Number of times the Gonzalez and Mozer (1974)'s X-line model correctly predicted the north-south (N-S) and/or east-west (E-W) senses of the observed plasma jet directions. The single magnetopause crossing (reconnection) events from which the observed plasma jets were obtained have been distributed according to IMF orientation and three Earth's dipole tilt inclination intervals, whose center bins are $\psi = -30^\circ, -20^\circ$, and -10° . The bold number within parenthesis (when present) alongside each clock angle (θ_{CA}) bin means the number of reconnection events for that specific bin. N/A (not applicable) means that there were no reconnection events for a specific clock angle bin, thus no X-line model prediction was applicable. Question marks represent either not clear or ambiguous predictions.

| Maximum Chapman-Ferraro Current Density Model: Gonzalez and Mozer (1974) | | | |
|--|-------------------------------------|-------------------------------------|-------------------------------------|
| IMF $B_x > 0$ | | IMF $B_x < 0$ | |
| $-35^\circ \leq \psi < -25^\circ$ | | | |
| IMF $B_y > 0$ | | IMF $B_y > 0$ | |
| $\theta_{CA} = 97.5^\circ \pm 7.5^\circ$ | $120^\circ \pm 15^\circ$ (2) | $120^\circ \pm 15^\circ$ | $150^\circ \pm 15^\circ$ (1) |
| N/A | 1,? N-S / 0,? E-W | N/A | 0 N-S / 1 E-W |
| IMF $B_y < 0$ | | IMF $B_y < 0$ | |
| $\theta_{CA} = 187.5^\circ \pm 7.5^\circ$ | $210^\circ \pm 15^\circ$ (1) | $210^\circ \pm 15^\circ$ (1) | $240^\circ \pm 15^\circ$ |
| N/A | 0 N-S / 0 E-W | N/A | 1 N-S / 2 E-W |
| $-25^\circ \leq \psi < -15^\circ$ | | | |
| IMF $B_y > 0$ | | IMF $B_y > 0$ | |
| $\theta_{CA} = 97.5^\circ \pm 7.5^\circ$ (1) | $120^\circ \pm 15^\circ$ | $120^\circ \pm 15^\circ$ (3) | $150^\circ \pm 15^\circ$ (3) |
| 0 N-S / 0 E-W | N/A | 2 N-S / 2 E-W | 2,? N-S / 1,? E-W |
| IMF $B_y < 0$ | | IMF $B_y < 0$ | |
| $\theta_{CA} = 187.5^\circ \pm 7.5^\circ$ (3) | $210^\circ \pm 15^\circ$ (4) | $210^\circ \pm 15^\circ$ (2) | $240^\circ \pm 15^\circ$ (1) |
| 3 N-S / 2,? E-W | 1 N-S / 1,? E-W | 0 N-S / 1 E-W | 1 N-S / 1 E-W |
| $-15^\circ \leq \psi < -5^\circ$ | | | |
| IMF $B_y > 0$ | | IMF $B_y > 0$ | |
| $\theta_{CA} = 97.5^\circ \pm 7.5^\circ$ | $120^\circ \pm 15^\circ$ | $120^\circ \pm 15^\circ$ | $150^\circ \pm 15^\circ$ (6) |
| N/A | N/A | N/A | 5 N-S / 2 E-W |
| IMF $B_y < 0$ | | IMF $B_y < 0$ | |
| $\theta_{CA} = 187.5^\circ \pm 7.5^\circ$ (4) | $210^\circ \pm 15^\circ$ (4) | $210^\circ \pm 15^\circ$ (3) | $240^\circ \pm 15^\circ$ (4) |
| N/A | 4 N-S / 1 E-W | 3 N-S / 3 E-W | 1 N-S / 1 E-W |

Table 7.6 - Number of times the Gonzalez and Mozer (1974)'s X-line model correctly predicted the north-south (N-S) and/or east-west (E-W) senses of the observed plasma jet directions. The single magnetopause crossing (reconnection) events from which the observed plasma jets were obtained have been distributed according to IMF orientation and four Earth's dipole tilt inclination intervals, whose center bins are $\psi = 0^\circ, 10^\circ, 20^\circ$, and 30° . The bold number within parenthesis (when present) alongside each clock angle (θ_{CA}) bin means the number of reconnection events found for that specific bin. N/A (not applicable) means that there were no reconnection events for a specific clock angle bin, thus no X-line model prediction was applicable. Question marks represent either not clear or ambiguous predictions.

| Maximum Chapman-Ferraro Current Density Model: Gonzalez and Mozer (1974) | | | | | | | | | | | |
|--|----------------|----------------|-------------------|--|--|--------------------------------|----------------|----------------|-------------------|--|--|
| $-5^\circ \leq \psi < 5^\circ$ | | | | | | $-5^\circ \leq \psi < 5^\circ$ | | | | | |
| IMF $B_y > 0$ | | | | | | IMF $B_y < 0$ | | | | | |
| IMF $B_y > 0$ | | | | | | IMF $B_y > 0$ | | | | | |
| $\theta_{CA} = 97.5^\circ \pm 7.5^\circ$ | 120° ± 15° | 150° ± 15° (2) | 172.5° ± 7.5° | | | 97.5° ± 7.5° | 120° ± 15° (2) | 150° ± 15° (1) | 172.5° ± 7.5° (1) | | |
| N/A | N/A | 1 N-S / 1 E-W | N/A | | | N/A | 2 N-S / 2 E-W | 1 N-S / 1 E-W | 1 N-S / 1 E-W | | |
| IMF $B_y < 0$ | | | | | | IMF $B_y < 0$ | | | | | |
| $\theta_{CA} = 187.5^\circ \pm 7.5^\circ$ (3) | 210° ± 15° (3) | 240° ± 15° (2) | 262.5° ± 7.5° (1) | | | 187.5° ± 7.5° (1) | 210° ± 15° (1) | 240° ± 15° | 262.5° ± 7.5° | | |
| 1,? N-S / 2,? E-W | 2 N-S / 2 E-W | 2 N-S / 1 E-W | 1 N-S / 1 E-W | | | 1 N-S / 1 E-W | 1 N-S / 0 E-W | N/A | N/A | | |
| IMF $B_y > 0$ | | | | | | IMF $B_y > 0$ | | | | | |
| $\theta_{CA} = 97.5^\circ \pm 7.5^\circ$ (1) | 120° ± 15° (1) | 150° ± 15° | 172.5° ± 7.5° (1) | | | 97.5° ± 7.5° | 120° ± 15° (3) | 150° ± 15° (1) | 172.5° ± 7.5° (1) | | |
| 0 N-S / 0 E-W | 0 N-S / 0 E-W | N/A | 0 N-S / 0 E-W | | | N/A | 3 N-S / 0 E-W | ? N-S / ? E-W | 1 N-S / 1 E-W | | |
| IMF $B_y < 0$ | | | | | | IMF $B_y < 0$ | | | | | |
| $\theta_{CA} = 187.5^\circ \pm 7.5^\circ$ | 210° ± 15° (4) | 240° ± 15° (1) | 262.5° ± 7.5° (2) | | | 187.5° ± 7.5° (1) | 210° ± 15° (2) | 240° ± 15° | 262.5° ± 7.5° (1) | | |
| N/A | 4 N-S / 2 E-W | 1 N-S / 1 E-W | 2 N-S / 2 E-W | | | ? N-S / ? E-W | 0 N-S / 1 E-W | N/A | ? N-S / ? E-W | | |
| IMF $B_y > 0$ | | | | | | IMF $B_y > 0$ | | | | | |
| $\theta_{CA} = 97.5^\circ \pm 7.5^\circ$ | 120° ± 15° | 150° ± 15° | 172.5° ± 7.5° | | | 97.5° ± 7.5° (1) | 120° ± 15° (1) | 150° ± 15° (3) | 172.5° ± 7.5° | | |
| N/A | N/A | N/A | N/A | | | 0 N-S / 0 E-W | 1 N-S / 1 E-W | ? N-S / ? E-W | N/A | | |
| IMF $B_y < 0$ | | | | | | IMF $B_y < 0$ | | | | | |
| $\theta_{CA} = 187.5^\circ \pm 7.5^\circ$ | 210° ± 15° (2) | 240° ± 15° (2) | 262.5° ± 7.5° | | | 187.5° ± 7.5° | 210° ± 15° (1) | 240° ± 15° (1) | 262.5° ± 7.5° | | |
| N/A | 2 N-S / 1 E-W | 1 N-S / 1 E-W | N/A | | | N/A | ? N-S / ? E-W | 1 N-S / 0 E-W | N/A | | |
| IMF $B_y > 0$ | | | | | | IMF $B_y > 0$ | | | | | |
| $\theta_{CA} = 97.5^\circ \pm 7.5^\circ$ | 120° ± 15° | 150° ± 15° | 172.5° ± 7.5° | | | 97.5° ± 7.5° (1) | 120° ± 15° | 150° ± 15° (2) | 172.5° ± 7.5° | | |
| N/A | N/A | N/A | N/A | | | 0 N-S / 0 E-W | N/A | 0 N-S / 0 E-W | N/A | | |
| IMF $B_y < 0$ | | | | | | IMF $B_y < 0$ | | | | | |
| $\theta_{CA} = 187.5^\circ \pm 7.5^\circ$ (2) | 210° ± 15° (1) | 240° ± 15° (1) | 262.5° ± 7.5° | | | 187.5° ± 7.5° (1) | 210° ± 15° (1) | 240° ± 15° | 262.5° ± 7.5° | | |
| 0 N-S / 0 E-W | ? N-S / ? E-W | 1 N-S / 1 E-W | N/A | | | 0 N-S / 0 E-W | 1 N-S / 0 E-W | N/A | N/A | | |
| IMF $B_y > 0$ | | | | | | IMF $B_y > 0$ | | | | | |
| $\theta_{CA} = 97.5^\circ \pm 7.5^\circ$ | 120° ± 15° | 150° ± 15° | 172.5° ± 7.5° | | | 97.5° ± 7.5° (1) | 120° ± 15° | 150° ± 15° (2) | 172.5° ± 7.5° | | |
| N/A | N/A | N/A | N/A | | | 0 N-S / 0 E-W | N/A | 0 N-S / 0 E-W | N/A | | |
| IMF $B_y < 0$ | | | | | | IMF $B_y < 0$ | | | | | |
| $\theta_{CA} = 187.5^\circ \pm 7.5^\circ$ (2) | 210° ± 15° (1) | 240° ± 15° (1) | 262.5° ± 7.5° | | | 187.5° ± 7.5° (1) | 210° ± 15° (1) | 240° ± 15° | 262.5° ± 7.5° | | |
| 0 N-S / 0 E-W | ? N-S / ? E-W | 1 N-S / 1 E-W | N/A | | | 0 N-S / 0 E-W | 1 N-S / 0 E-W | N/A | N/A | | |

Table 7.7 - Number of times the Swisdak and Drake (2007)'s X-line model correctly predicted the north-south (N-S) and/or east-west (E-W) senses of the observed plasma jet directions. The single magnetopause crossing (reconnection) events from which the observed plasma jets were obtained have been distributed according to IMF orientation and three Earth's dipole tilt inclination intervals, whose center bins are $\psi = -30^\circ, -20^\circ$, and -10° . The bold number within parenthesis (when present) alongside each clock angle (θ_{CA}) bin means the number of reconnection events for that specific bin. N/A (not applicable) means that there were no reconnection events for a specific clock angle bin, thus no X-line model prediction was applicable. Question marks represent either not clear or ambiguous predictions.

| Maximum Reconnection Outflow Speed Model: Swisdak and Drake (2007) | | | |
|--|-----------------------------------|----------------|-------------------|
| | IMF $B_x > 0$ | IMF $B_x < 0$ | |
| | $-35^\circ \leq \psi < -25^\circ$ | | |
| | IMF $B_y > 0$ | | IMF $B_y > 0$ |
| $\theta_{CA} = 97.5^\circ \pm 7.5^\circ$ | 120° ± 15° (2) | 150° ± 15° (2) | 172.5° ± 7.5° |
| N/A | 2 N-S / 1 E-W | 2 N-S / 2 E-W | N/A |
| | IMF $B_y < 0$ | | IMF $B_y < 0$ |
| $\theta_{CA} = 187.5^\circ \pm 7.5^\circ$ | 210° ± 15° (1) | 240° ± 15° | 262.5° ± 7.5° |
| N/A | 0 N-S / 0 E-W | N/A | N/A |
| | $-25^\circ \leq \psi < -15^\circ$ | | |
| | IMF $B_y > 0$ | | IMF $B_y > 0$ |
| $\theta_{CA} = 97.5^\circ \pm 7.5^\circ$ (1) | 120° ± 15° | 150° ± 15° | 172.5° ± 7.5° (1) |
| 0 N-S / 0 E-W | N/A | N/A | 0 N-S / 1 E-W |
| | IMF $B_y < 0$ | | IMF $B_y < 0$ |
| $\theta_{CA} = 187.5^\circ \pm 7.5^\circ$ (3) | 210° ± 15° (4) | 240° ± 15° (1) | 262.5° ± 7.5° |
| 2 N-S / 1,? E-W | 1 N-S / 1,? E-W | 1 N-S / 1 E-W | N/A |
| | $-15^\circ \leq \psi < -5^\circ$ | | |
| | IMF $B_y > 0$ | | IMF $B_y > 0$ |
| $\theta_{CA} = 97.5^\circ \pm 7.5^\circ$ | 120° ± 15° | 150° ± 15° (1) | 172.5° ± 7.5° |
| N/A | N/A | 1 N-S / 0 E-W | N/A |
| | IMF $B_y < 0$ | | IMF $B_y < 0$ |
| $\theta_{CA} = 187.5^\circ \pm 7.5^\circ$ | 210° ± 15° (4) | 240° ± 15° (7) | 262.5° ± 7.5° |
| N/A | 2 N-S / 1 E-W | 7 N-S / 7 E-W | N/A |

Table 7.8 - Number of times the Swisdak and Drake (2007)'s X-line model correctly predicted the north-south (N-S) and/or east-west (E-W) senses of the observed plasma jet directions. The single magnetopause crossing (reconnection) events from which the observed plasma jets were obtained have been distributed according to IMF orientation and four Earth's dipole tilt inclination intervals, whose center bins are $\psi = 0^\circ, 10^\circ, 20^\circ$, and 30° . The bold number within parenthesis (when present) alongside each clock angle (θ_{CA}) bin means the number of reconnection events found for that specific bin. N/A (not applicable) means that there were no reconnection events for a specific clock angle bin, thus no X-line model prediction was applicable. Question marks represent either not clear or ambiguous predictions.

| Maximum Reconnection Outflow Speed Model: Swisdak and Drake (2007) | | | | | | | | | | | |
|--|----------------|----------------|-------------------|--|--|--------------------------------|----------------|----------------|-------------------|--|--|
| $-5^\circ \leq \psi < 5^\circ$ | | | | | | $5^\circ \leq \psi < 15^\circ$ | | | | | |
| IMF $B_y > 0$ | | | | | | IMF $B_y < 0$ | | | | | |
| IMF $B_y > 0$ | | | | | | IMF $B_y > 0$ | | | | | |
| $\theta_{CA} = 97.5^\circ \pm 7.5^\circ$ | 120° ± 15° | 150° ± 15° (2) | 172.5° ± 7.5° | | | 97.5° ± 7.5° | 120° ± 15° (2) | 150° ± 15° (1) | 172.5° ± 7.5° (1) | | |
| N/A | N/A | 2 N-S / 2 E-W | N/A | | | N/A | 2 N-S / 2 E-W | 1 N-S / 1 E-W | 1 N-S / 1 E-W | | |
| IMF $B_y < 0$ | | | | | | IMF $B_y < 0$ | | | | | |
| $\theta_{CA} = 187.5^\circ \pm 7.5^\circ$ (3) | 210° ± 15° (3) | 240° ± 15° (2) | 262.5° ± 7.5° (1) | | | 187.5° ± 7.5° (1) | 210° ± 15° (1) | 240° ± 15° | 262.5° ± 7.5° | | |
| 1 N-S / 1 E-W | 2 N-S / 2 E-W | 2 N-S / 2 E-W | 1 N-S / 1 E-W | | | 1 N-S / 1 E-W | 1 N-S / 0 E-W | N/A | N/A | | |
| IMF $B_y > 0$ | | | | | | IMF $B_y > 0$ | | | | | |
| $\theta_{CA} = 97.5^\circ \pm 7.5^\circ$ (1) | 120° ± 15° (1) | 150° ± 15° | 172.5° ± 7.5° (1) | | | 97.5° ± 7.5° | 120° ± 15° (3) | 150° ± 15° (1) | 172.5° ± 7.5° (1) | | |
| 0 N-S / 0 E-W | 0 N-S / 0 E-W | N/A | 0 N-S / 1 E-W | | | N/A | 3 N-S / 3 E-W | 1 N-S / 0 E-W | 1 N-S / 1 E-W | | |
| IMF $B_y < 0$ | | | | | | IMF $B_y < 0$ | | | | | |
| $\theta_{CA} = 187.5^\circ \pm 7.5^\circ$ | 210° ± 15° (4) | 240° ± 15° (1) | 262.5° ± 7.5° (2) | | | 187.5° ± 7.5° (1) | 210° ± 15° (2) | 240° ± 15° | 262.5° ± 7.5° (1) | | |
| N/A | 4 N-S / 2 E-W | 1 N-S / 1 E-W | 2 N-S / 2 E-W | | | 0 N-S / 1 E-W | 1 N-S / 2 E-W | N/A | 0 N-S / 0 E-W | | |
| IMF $B_y > 0$ | | | | | | IMF $B_y > 0$ | | | | | |
| $\theta_{CA} = 97.5^\circ \pm 7.5^\circ$ | 120° ± 15° | 150° ± 15° | 172.5° ± 7.5° | | | 97.5° ± 7.5° (1) | 120° ± 15° (1) | 150° ± 15° (3) | 172.5° ± 7.5° | | |
| N/A | N/A | N/A | N/A | | | 0 N-S / 0 E-W | 1 N-S / 1 E-W | 1 N-S / 0 E-W | N/A | | |
| IMF $B_y < 0$ | | | | | | IMF $B_y < 0$ | | | | | |
| $\theta_{CA} = 187.5^\circ \pm 7.5^\circ$ | 210° ± 15° (2) | 240° ± 15° (2) | 262.5° ± 7.5° | | | 187.5° ± 7.5° | 210° ± 15° (1) | 240° ± 15° (1) | 262.5° ± 7.5° | | |
| N/A | 2 N-S / 1 E-W | 1 N-S / 1 E-W | N/A | | | N/A | 0 N-S / 0 E-W | 1 N-S / 1 E-W | N/A | | |
| IMF $B_y > 0$ | | | | | | IMF $B_y > 0$ | | | | | |
| $\theta_{CA} = 97.5^\circ \pm 7.5^\circ$ | 120° ± 15° | 150° ± 15° | 172.5° ± 7.5° | | | 97.5° ± 7.5° (1) | 120° ± 15° | 150° ± 15° (2) | 172.5° ± 7.5° | | |
| N/A | N/A | N/A | N/A | | | 0 N-S / 1 E-W | N/A | 1 N-S / 1 E-W | N/A | | |
| IMF $B_y < 0$ | | | | | | IMF $B_y < 0$ | | | | | |
| $\theta_{CA} = 187.5^\circ \pm 7.5^\circ$ (2) | 210° ± 15° (1) | 240° ± 15° (1) | 262.5° ± 7.5° | | | 187.5° ± 7.5° (1) | 210° ± 15° (1) | 240° ± 15° | 262.5° ± 7.5° | | |
| 2 N-S / 0 E-W | 1 N-S / ? E-W | 1 N-S / 1 E-W | N/A | | | 1 N-S / 1 E-W | 1 N-S / 0 E-W | N/A | N/A | | |

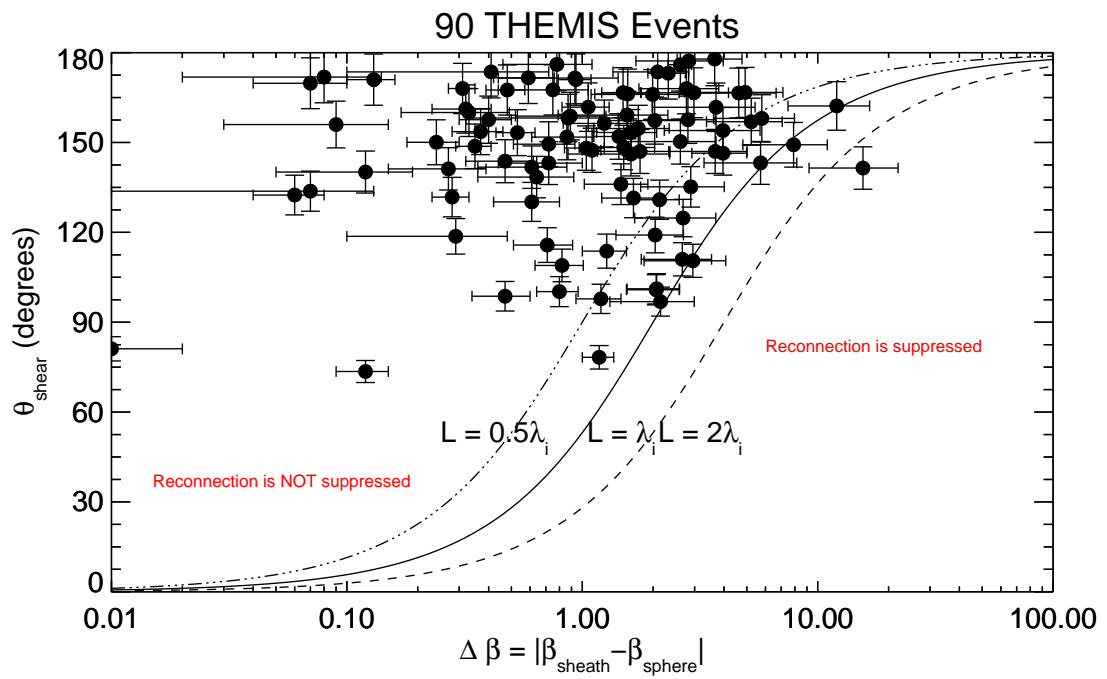


Figure 7.14 - Plot of the magnetic shear angle θ_{shear} versus $\Delta\beta$ values for all 90 THEMIS reconnection events analyzed in this study.

8 CONCLUSIONS

In this work, we have dealt with the large scale feature of magnetic reconnection, i.e., the X-line extent, at Earth's dayside magnetopause via *in situ* observations of accelerated plasma flows, also known as reconnection jets. Three analytical models which predict both location and orientation of the X-line, namely the maximum shear angle model (TRATTNER et al., 2007), the maximum Chapman-Ferraro current density magnitude model (GONZALEZ; MOZER, 1974), and the maximum asymmetric reconnection outflow speed model (SWISDAK; DRAKE, 2007) have been used. To the best of our knowledge this is the first comparison between different X-line model predictions.

The present study was divided into two parts in order to investigate the possible large scale operation of magnetic reconnection at Earth's dayside magnetopause, and also to assess which plasma parameters may play a role in determining the reconnection X-line location and orientation. The first of them was to analyze a set of four fortuitous, quasi-simultaneous magnetopause crossing events. For each event, two widely separated ($> 5 R_E$) satellites detected reconnection signatures, in particular accelerated (and Alfvénic) plasma flows which are known to be the most standard and readily discernible reconnection signatures at Earth's dayside magnetopause. Then, we have used three distinct analytical models which predict the large scale reconnection X-line location and orientation in order to check whether or not the reconnection signatures shown would be consistent with the existence of an extended X-line. Such a test was done in the following way: we plotted both the spacecraft location and the respective jets' directions over the yz_{GSM} plane, and overplotted the X-line location as given by each of the three X-line models used in this work. By taking into account standard reconnection theory considerations that the resultant outflows should leave the X-line in a direction perpendicular to the local X-line segment, we could infer whether the given X-line's jet direction prediction was correct or not. We checked if the given X-line model would correctly predict both north-south and east-west senses of the observed plasma jet directions. We found that the Swisdak and Drake (2007) model had a slightly better performance in correctly predicting both the jet's north-south and east-west senses, as compared to the other two models. The most important finding was that an extended reconnection X-line connecting the two widely separated observation points may in fact exist, since we could find at least one event (2007-03-05) for which an X-line model could correctly predict the jet's full direction at the two spacecraft locations. In another event (2009-07-07) one X-line model correctly predicted the north-south sense

of both jets and the east-west sense of one of them, showing that also in this case an extended X-line may be present at the Earth’s dayside magnetopause connecting points far away from each other, as proposed by [Phan et al. \(2006\)](#) and [Dunlop et al. \(2011\)](#).

The second part was to perform a statistical analysis for the agreement between observed reconnection plasma jet directions and the location of the respective X-line from the model predictions. Since we could not find a large number of quasi-simultaneous reconnection events, we turned to single spacecraft magnetopause crossings which occur roughly twice a day, thus increasing the chances of finding periods when dayside magnetic reconnection was active. We have collected 116 reconnection events where alfvénic plasma jets were clearly present. We note that for all the reconnection events analyzed in this work the Earth’s magnetosphere was under nominal solar wind conditions, with a dynamic pressure, P_{dyn} , value within the range $1.0 < P_{dyn} < 2.5$ nPa. From the total number of events, 90 of them have been provided by the spacecraft constellation THEMIS, 19 by the spacecraft constellation CLUSTER, and 7 by the DOUBLE STAR TC1 spacecraft. The same methodology applied for the quasi-simultaneous events mentioned above was used in this case. We have found that, once again, the [Swisdak and Drake \(2007\)](#) X-line model had a slightly better performance in predicting both jet components: north-south (72% of the cases) and east-west (54% of the cases), as compared to the [Trattner et al. \(2007\)](#) model (66% north-south, 37% east-west), and [Gonzalez and Mozer \(1974\)](#) model (60% north-south, 42% east-west). The [Swisdak and Drake \(2007\)](#) X-line model takes into account the realistic asymmetrical magnetic fields and plasma density conditions across the magnetopause boundary layer, thus the above result suggests that local, in addition to external, conditions may also play an important role in determining the large scale X-line location. In particular, magnetosheath magnetic field and densities have been shown to play an important role, via the plasma β parameter, in controlling the magnetic reconnection onset at Earth’s dayside magnetopause ([PHAN et al., 2013](#)). In this regard, we have used all THEMIS observations (90 events) in our statistical survey to assess whether the plasma β would play a role in our reconnection events. The conclusion is that for the majority (90/116 - 78%) of the reconnection events analyzed in this work both median (1.24) and average (1.90) delta beta ($\Delta\beta = \beta_{sheath} - \beta_{sphere} \approx \beta_{sheath}$) values indicate that thermal plasma pressure, and therefore plasma density and temperature, had as much influence as the magnetic field on determining whether reconnection would occur or not. Therefore, a possible explanation for a somewhat better performance of the [Swisdak and Drake \(2007\)](#) model is that differently from both [Gonzalez and](#)

Mozer (1974) and Trattner et al. (2007) X-line models which use only the magnetic field information for deriving the X-line location and orientation, the Swisdak and Drake (2007) model also takes into account the effect of plasma densities which have been shown to play an important role on determining whether reconnection should occur or not at the Earth's dayside magnetopause.

The statistical analysis results also showed that in more than 40% of the cases, at least one X-line model could correctly predict the east-west sense of the observed plasma jets, indicating that a component-type, i.e., tilted and subsolar, reconnection X-line can be a common feature at the dayside magnetopause in times when the IMF have both negative and non-zero B_z and B_y components, respectively.

Despite the relatively small differences in the numbers of correctly predicted jet directions among the analyzed X-line models, and also given the uncertainties involved in the assumption adopted here regarding the way the reconnection outflow should leave the X-line, we believe that all models have their validity domains and the conclusions drawn here are not meant to disfavor any model. On the contrary, as mentioned above, there were no major differences among the jet direction predictions in spite of the intrinsic limitations of each model, which in turn elect a small amount of parameters, or even only one parameter, to describe the possibly complex behavior of the large scale magnetopause reconnection X-line.

As a future work, one can make use of conjunctions between the three THEMIS satellites and the forthcoming NASA's Magnetospheric Multiscale Mission (MMS) to acquire multi-point observations, for instance THEMIS on the dayside and MMS on the nightside magnetosphere, in order to better understand the global effects of the reconnection process which are ultimately triggered by (possibly) large scale reconnection on the dayside magnetopause.

Also as a future work, one can extend the number of X-line models to be tested against *in situ* observations of dayside magnetopause reconnection. Among them would be the those which are determined entirely by numerical (MHD) models, such as the four-field line model (LAITINEN et al., 2007), which has shown to present a component reconnection-like behavior.

REFERENCES

ALEXEEV, I. I.; BELENKAYA, E. S.; BOBROVNIKOV, S. Y.; KALEGAEV, V. V. Modelling of the electromagnetic field in the interplanetary space and in the earth's magnetosphere. In: CHIAN, A.-L.; CAIRNS, I.; GABRIEL, S.; GOEDBLOED, J.; HADA, T.; LEUBNER, M.; NOCERA, L.; STENING, R.; TOFFOLETTO, F.; UBEROI, C.; VALDIVIA, J.; VILLANTE, U.; WU, C.-C.; YAN, Y. (Ed.). **Advances in space environment research**. Springer Netherlands, 2003. p. 7–26. xv, 29, 31, 88, 89, 92

ALEXEEV, I. I.; SIBECK, D. G.; BOBROVNIKOV, S. Y. Concerning the location of magnetopause merging as a function of the magnetopause current strength. **Journal of Geophysical Research: Space Physics**, v. 103, n. A4, p. 6675–6684, 1998. ISSN 2156-2202. Available from: <<http://dx.doi.org/10.1029/97JA02863>>. 37

ANGELOPOULOS, V. The themis mission. **Space Science Reviews**, v. 141, n. 1–4, p. 5–34, 2008. 59

AUSTER, H.; GLASSMEIER, K.; MAGNES, W.; AYDOGAR, O.; BAUMJOHANN, W.; CONSTANTINESCU, D.; FISCHER, D.; FORNACON, K.; GEORGESCU, E.; HARVEY, P.; HILLENMAIER, O.; KROTH, R.; LUDLAM, M.; NARITA, Y.; NAKAMURA, R.; OKRAFKA, K.; PLASCHKE, F.; RICHTER, I.; SCHWARZL, H.; STOLL, B.; VALAVANOGLOU, A.; WIEDEMANN, M. The themis fluxgate magnetometer. **Space Science Reviews**, v. 141, n. 1–4, p. 235–264, 2008. 59

BALOGH, A.; CARR, C. M.; NA, M. H. A.; DUNLOP, M. W.; BEEK, T. J.; BROWN, P.; FORNACON, K.-H.; GEORGESCU, E.; GLASSMEIER, K.-H.; HARRIS, J.; MUSMANN, G.; ODDY, T.; SCHWINGENSCHUH, K. The cluster magnetic field investigation: overview of in-flight performance and initial results. **Annales Geophysicae**, v. 19, n. 10/12, p. 1207–1217, 2001. 60

BAUMJOHANN, W.; TREUMANN, R. A. **Basic space plasma physics**. Imperial College Press, London, 1996. 6, 7, 8, 9, 14, 20

BIRN, J.; BOROVSKY, J. E.; HESSE, M. Properties of asymmetric magnetic reconnection. **Physics of Plasmas (1994-present)**, v. 15, n. 3, p. –, 2008. Available from: <[http:](http://)

[//scitation.aip.org/content/aip/journal/pop/15/3/10.1063/1.2888491](http://scitation.aip.org/content/aip/journal/pop/15/3/10.1063/1.2888491)>. 124

BITTENCOURT, J. A. **Fundamentals of plasma physics**. Springer, 2004. 11, 12

CARR, C.; BROWN, P.; ZHANG, T. L.; GLOAG, J.; HORBURY, T.; LUCEK, E.; MAGNES, W.; O'BRIEN, H.; ODDY, T.; AUSTER, U.; AUSTIN, P.; AYDOGAR, O.; BALOGH, A.; BAUMJOHANN, W.; BEEK, T.; EICHELBERGER, H.; FORNACON, K.-H.; GEORGESCU, E.; GLASSMEIER, K.-H.; LUDLAM, M.; NAKAMURA, R.; RICHTER, I. The double star magnetic field investigation: instrument design, performance and highlights of the first year's observations. **Annales Geophysicae**, v. 23, n. 8, p. 2713–2732, 2005. 61

CASSAK, P. A.; SHAY, M. A. Scaling of asymmetric magnetic reconnection: General theory and collisional simulations. **Physics of Plasmas (1994-present)**, v. 14, n. 10, p. –, 2007. Available from: <<http://scitation.aip.org/content/aip/journal/pop/14/10/10.1063/1.2795630>>. 13, 42

COOLING, B. M. A.; OWEN, C. J.; SCHWARTZ, S. J. Role of the magnetosheath flow in determining the motion of open flux tubes. **Journal of Geophysical Research**, v. 106, p. 18763–18776, sep. 2001. xv, 27, 28, 30, 89, 92

CROOKER, N. U. Dayside merging and cusp geometry. **Journal of Geophysical Research: Space Physics**, v. 84, n. A3, p. 951–959, 1979. ISSN 2156-2202. Available from: <<http://dx.doi.org/10.1029/JA084iA03p00951>>. xv, 1, 25, 26, 124

DALY, P. W.; SAUNDERS, M. A.; RIJNBEEK, R. P.; SCKOPKE, N.; RUSSELL, C. T. The distribution of reconnection geometry in flux transfer events using energetic ion, plasma and magnetic data. **Journal of Geophysical Research: Space Physics**, v. 89, n. A6, p. 3843–3854, 1984. ISSN 2156-2202. Available from: <<http://dx.doi.org/10.1029/JA089iA06p03843>>. 143

DAUGHTON, W.; ROYTERSHTEYN, V.; KARIMABADI, H.; YIN, L.; ALBRIGHT, B. J.; BERGEN, B.; BOWERS, K. J. Role of electron physics in the development of turbulent magnetic reconnection in collisionless plasmas. **Nat Phys**, Nature Publishing Group, v. 7, n. 7, p. 539–542, 07 2011. Available from: <<http://dx.doi.org/10.1038/nphys1965>>. 13

DUNGEY, J. W. Interplanetary magnetic field and the auroral zones. **Phys. Rev. Lett.**, American Physical Society, v. 6, p. 47–48, Jan 1961. Available from: <<http://link.aps.org/doi/10.1103/PhysRevLett.6.47>>. 19, 111

DUNLOP, M. W.; ZHANG, Q.-H.; BOGDANOVA, Y. V.; LOCKWOOD, M.; PU, Z.; HASEGAWA, H.; WANG, J.; TAYLOR, M. G. G. T.; BERCHEM, J.; LAVRAUD, B.; EASTWOOD, J.; VOLWERK, M.; SHEN, C.; SHI, J.-K.; CONSTANTINESCU, D.; FREY, H.; FAZAKERLEY, A. N.; SIBECK, D.; ESCOUBET, P.; WILD, J. A.; LIU, Z.-X. Extended magnetic reconnection across the dayside magnetopause. **Physical Review Letters**, v. 107, n. 2, p. 025004, jul. 2011. 65, 74, 76, 77, 78, 93, 143, 156

ESCOUBET, C. P.; FEHRINGER, M.; GOLDSTEIN, M. The cluster mission. **Annales Geophysicae**, v. 19, n. 10/12, p. 1197–1200, 2001. 60

FARRIS, M. H.; RUSSELL, C. T. Determining the standoff distance of the bow shock: Mach number dependence and use of models. **Journal of Geophysical Research: Space Physics**, v. 99, n. A9, p. 17681–17689, 1994. ISSN 2156-2202. Available from: <<http://dx.doi.org/10.1029/94JA01020>>. 5, 67, 101

FAZAKERLEY, A. N.; CARTER, P. J.; WATSON, G.; SPENCER, A.; SUN, Y. Q.; COKER, J.; COKER, P.; KATARIA, D. O.; FONTAINE, D.; LIU, Z. X.; GILBERT, L.; HE, L.; LAHIFF, A. D.; MIHALJCIC, B.; SZITA, S.; TAYLOR, M. G. G. T.; WILSON, R. J.; DEDIEU, M.; SCHWARTZ, S. J. The double star plasma electron and current experiment. **Annales Geophysicae**, v. 23, n. 8, p. 2733–2756, 2005. 61

FEAR, R. C. **Cluster multi-spacecraft observations of flux transfer events**. PhD Thesis (PhD) — University College London (University of London), 2006. 60

FUSELIER, S. A. Kinetic aspects of reconnection at the magnetopause. In: _____. **Physics of the magnetopause**. American Geophysical Union, 1995. p. 181–187. 19

FUSELIER, S. A.; ANDERSON, B. J.; ONSAGER, T. G. Particle signatures of magnetic topology at the magnetopause: Ampte/cce observations. **Journal of Geophysical Research: Space Physics**, v. 100, n. A7, p. 11805–11821, 1995. ISSN 2156-2202. Available from: <<http://dx.doi.org/10.1029/94JA02811>>. 113

FUSELIER, S. A.; FRAHM, R.; LEWIS, W. S.; MASTERS, A.; MUKHERJEE, J.; PETRINEC, S. M.; SILLANPAA, I. J. The location of magnetic reconnection

at saturn's magnetopause: A comparison with earth. **Journal of Geophysical Research: Space Physics**, v. 119, n. 4, p. 2563–2578, 2014. ISSN 2169-9402. Available from: <<http://dx.doi.org/10.1002/2013JA019684>>. 1, 2

GIOVANELLI, R. G. A Theory of Chromospheric Flares. **Nature**, v. 158, p. 81–82, jul. 1946. 13

GONZALEZ, W. D.; JOSELYN, J. A.; KAMIDE, Y.; KROEHL, H. W.; ROSTOKER, G.; TSURUTANI, B. T.; VASYLIUNAS, V. M. What is a geomagnetic storm? **Journal of Geophysical Research**, v. 99, n. A4, p. 5771–5792, 1994. 13

GONZALEZ, W. D.; MOZER, F. S. A Quantitative Model for the Potential Resulting from Reconnection with an Arbitrary Interplanetary Magnetic Field. **Journal of Geophysical Research**, v. 79(28), p. 4186–4194, 1974. xi, xiii, xvi, xix, xxiii, xxiv, 1, 2, 3, 36, 37, 39, 86, 88, 91, 92, 94, 96, 97, 98, 114, 116, 120, 121, 122, 123, 124, 125, 126, 127, 128, 129, 130, 131, 132, 133, 134, 135, 136, 137, 138, 139, 140, 142, 143, 144, 149, 150, 155, 156, 157, 180, 181, 182, 183, 184, 185, 186, 187

GOSLING, J. T.; Skoug, R. M.; McComas, D. J.; Smith, C. W. Direct evidence for magnetic reconnection in the solar wind near 1 AU. **Journal of Geophysical Research**, v. 110, p. 1107, jan. 2005. 1

GOSLING, J. T.; THOMSEN, M. F.; BAME, S. J.; RUSSELL, C. T. Accelerated plasma flows at the near-tail magnetopause. **Journal of Geophysical Research: Space Physics**, v. 91, n. A3, p. 3029–3041, 1986. ISSN 2156-2202. Available from: <<http://dx.doi.org/10.1029/JA091iA03p03029>>. 19

HARALICK, R. M. Ridges and valleys on digital images. **Computer Vision, Graphics, and Image Processing**, v. 22, n. 1, p. 28–38, April 1983. 175

HOILIJOKI, S.; SOUZA, V. M.; WALSH, B. M.; JANHUNEN, P.; PALMROTH, M. Magnetopause reconnection and energy conversion as influenced by the dipole tilt and the imf bx. **Journal of Geophysical Research: Space Physics**, v. 119, n. 6, p. 4484–4494, 2014. ISSN 2169-9402. Available from: <<http://dx.doi.org/10.1002/2013JA019693>>. 74

HUDSON, P. D. Discontinuities in an anisotropic plasma and their identification in the solar wind. **Planetary and Space Science**, v. 18, p. 1611–1622, nov. 1970. 20

JAUER, P. R. **Earth's magnetopause magnetic reconnection study through a 3D MHD BATS-R-US simulation (in portuguese)**. PhD Thesis (PhD) — Instituto Nacional de Pesquisas Espaciais (INPE), April 2014. Available from: <<http://urlib.net/sid.inpe.br/mtc-m21b/2014/04.17.16.08>>. 48

JOHNSTONE, A.; ALSOP, C.; BURGE, S.; CARTER, P.; COATES, A.; COKER, A.; FAZAKERLEY, A.; GRANDE, M.; GOWEN, R.; GURGIOLO, C.; HANCOCK, B.; NARHEIM, B.; PREECE, A.; SHEATHER, P.; WINNINGHAM, J.; WOODLIFFE, R. Peace: A plasma electron and current experiment. **Space Science Reviews**, v. 79, n. 1–2, p. 351–398, 1997. 60

KESSEL, R. L.; CHEN, S.-H.; GREEN, J. L.; FUNG, S. F.; BOARDSEN, S. A.; TAN, L. C.; EASTMAN, T. E.; CRAVEN, J. D.; FRANK, L. A. Evidence of high-latitude reconnecting during northward imf: Hawkeye observations. **Geophysical Research Letters**, v. 23, n. 5, p. 583–586, 1996. ISSN 1944-8007. Available from: <<http://dx.doi.org/10.1029/95GL03083>>. 19

KOBEL, E.; FLÜCKIGER, E. O. A model of the steady state magnetic field in the magnetosheath. **Journal of Geophysical Research: Space Physics**, v. 99, n. A12, p. 23617–23622, 1994. ISSN 2156-2202. Available from: <<http://dx.doi.org/10.1029/94JA01778>>. 27, 28

KOMAR, C. M.; CASSAK, P. A.; DORELLI, J. C.; GLOCER, A.; KUZNETSOVA, M. M. Tracing magnetic separators and their dependence on imf clock angle in global magnetospheric simulations. **Journal of Geophysical Research: Space Physics**, v. 118, n. 8, p. 4998–5007, 2013. ISSN 2169-9402. Available from: <<http://dx.doi.org/10.1002/jgra.50479>>. 3, 46

KULSRUD, R. M. Magnetic reconnection: Sweet–parker versus petschek. **Earth, Planets and Space**, v. 53, n. 6, p. 417–422, 2001. 17

LAITINEN, T. V.; PALMROTH, M.; PULKKINEN, T. I.; JANHUNEN, P.; KOSKINEN, H. E. J. Continuous reconnection line and pressure-dependent energy conversion on the magnetopause in a global mhd model. **Journal of Geophysical Research: Space Physics**, v. 112, n. A11, p. n/a–n/a, 2007. ISSN 2156-2202. Available from: <<http://dx.doi.org/10.1029/2007JA012352>>. 74, 157

LEPPING, R.; ACÚÑA, M.; BURLAGA, L.; FARRELL, W.; SLAVIN, J.; SCHATTE, K.; MARIANI, F.; NESS, N.; NEUBAUER, F.; WHANG, Y.; BYRNES, J.; KENNON, R.; PANETTA, P.; SCHEIFELE, J.; WORLEY, E. The

wind magnetic field investigation. **Space Science Reviews**, v. 71, n. 1-4, p. 207–229, 1995. 67

LINDEBERG, T. Discrete derivative approximations with scale-space properties: A basis for low-level feature extraction. **Journal of Mathematical Imaging and Vision**, v. 3, n. 4, p. 349–376, November 1993. xvii, 173, 177

_____. Edge Detection and Ridge Detection with Automatic Scale Selection. **International Journal of Computer Vision**, v. 30, n. 2, p. 117–156, November 1998. 32, 33, 36, 39, 40, 57, 58, 173, 175, 177, 178

LUHMANN, J. G.; WALKER, R. J.; RUSSELL, C. T.; CROOKER, N. U.; SPREITER, J. R.; STAHERA, S. S. Patterns of potential magnetic field merging sites on the dayside magnetopause. **Journal of Geophysical Research: Space Physics**, v. 89, n. A3, p. 1739–1742, 1984. ISSN 2156-2202. Available from: <<http://dx.doi.org/10.1029/JA089iA03p01739>>. 1, 25

MCFADDEN, J.; CARLSON, C.; LARSON, D.; LUDLAM, M.; ABIAD, R.; ELLIOTT, B.; TURIN, P.; MARCKWORDT, M.; ANGELOPOULOS, V. The themis esa plasma instrument and in-flight calibration. **Space Science Reviews**, v. 141, n. 1–4, p. 277–302, 2008. 59

MOZER, F. S.; BALE, S. D.; PHAN, T. D. Evidence of diffusion regions at a subsolar magnetopause crossing. **Phys. Rev. Lett.**, American Physical Society, v. 89, p. 015002, Jun 2002. Available from: <<http://link.aps.org/doi/10.1103/PhysRevLett.89.015002>>. 13

ENDO, K., **Artist rendition of the solar wind**. S.L.: NOAA, Available at: <http://www.ngdc.noaa.gov/geomag/icons/solarexp.jpg>. Accessed on April 2015. 5

PARKER, E. N. Sweet's mechanism for merging magnetic fields in conducting fluids. **Journal of Geophysical Research**, v. 62, n. 4, p. 509–520, 1957. ISSN 2156-2202. Available from: <<http://dx.doi.org/10.1029/JZ062i004p00509>>. 15

PASCHMANN, G.; BAUMJOHANN, W.; SCKOPKE, N.; PAPAMASTORAKIS, I.; CARLSON, C. W. The magnetopause for large magnetic shear - ampte/irm observations. **Journal of Geophysical Research**, v. 91, p. 11099–11115, oct. 1986. 20, 21

PASCHMANN, G.; ØIEROSET, M.; PHAN, T. D. In-situ observations of reconnection in space. **Space Science Reviews**, v. 178, n. 2-4, p. 385–417, 2013. Available from: <<http://dx.doi.org/10.1007/s11214-012-9957-2>>. 1, 80

PASCHMANN, G.; SONNERUP, B. U. O.; PAPAMASTORAKIS, I.; SCKOPKE, N.; HAERENDEL, G.; BAME, S. J.; ASBRIDGE, J. R.; GOSLING, J. T.; RUSSELL, C. T.; ELPHIC, R. C. Plasma acceleration at the earth's magnetopause - evidence for reconnection. **Nature**, v. 282, p. 243–246, nov. 1979. 19, 70, 84

PETSCHEK, H. E. Magnetic field annihilation. In: AAS-NASA SYMPOSIUM ON THE PHYSICS OF SOLAR FLARES, 1964, Greenbelt, MD, USA. **Proceedings...** Washington, DC: AAS-NASA, 1964. p. 425–439. Note: NASA Spec. Publ. SP-50. 17

PHAN, T.; FREEMAN, M.; KISTLER, L.; KLECKER, B.; HAERENDEL, G.; PASCHMANN, G.; SONNERUP, B.; BAUMJOHANN, W.; BAVASSANO-CATTANEO, M.; CARLSON, C.; DILELLIS, A.; FORNACON, K.-H.; FRANK, L.; FUJIMOTO, M.; GEORGESCU, E.; KOKUBUN, S.; MOEBIUS, E.; MUKAI, T.; PATERSON, W.; REME, H. Evidence for an extended reconnection line at the dayside magnetopause. **Earth, Planets and Space**, v. 53, n. 6, p. 619–625, 2001. 66

PHAN, T.; FREY, H. U.; FREY, S.; PETICOLAS, L.; FUSELIER, S.; CARLSON, C.; RÈME, H.; BOSQUED, J.-M.; BALOGH, A.; DUNLOP, M.; KISTLER, L.; MOUIKIS, C.; DANDOURAS, I.; SAUVAUD, J.-A.; MENDE, S.; MCFADDEN, J.; PARKS, G.; MOEBIUS, E.; KLECKER, B.; PASCHMANN, G.; FUJIMOTO, M.; PETRINEC, S.; MARCUCCI, M. F.; KORTH, A.; LUNDIN, R. Simultaneous cluster and image observations of cusp reconnection and auroral proton spot for northward imf. **Geophysical Research Letters**, v. 30, n. 10, p. n/a–n/a, 2003. ISSN 1944-8007. Available from: <<http://dx.doi.org/10.1029/2003GL016885>>. 19

PHAN, T. D.; DRAKE, J. F.; SHAY, M. A.; MOZER, F. S.; EASTWOOD, J. P. Evidence for an elongated (> 60 ion skin depths) electron diffusion region during fast magnetic reconnection. **Phys. Rev. Lett.**, American Physical Society, v. 99, p. 255002, Dec 2007. Available from: <<http://link.aps.org/doi/10.1103/PhysRevLett.99.255002>>. 13

PHAN, T. D.; DUNLOP, M. W.; PASCHMANN, G.; KLECKER, B.; BOSQUED, J. M.; RÈME, H.; BALOGH, A.; TWITTY, C.; MOZER, F. S.; CARLSON,

C. W.; MOUIKIS, C.; KISTLER, L. M. Cluster observations of continuous reconnection at the magnetopause under steady interplanetary magnetic field conditions. **Annales Geophysicae**, v. 22, n. 7, p. 2355–2367, 2004. Available from: <<http://www.ann-geophys.net/22/2355/2004>>. 19, 66

PHAN, T. D.; GOSLING, J. T.; PASCHMANN, G.; PASMA, C.; DRAKE, J. F.; ØIEROSET, M.; LARSON, D.; LIN, R. P.; DAVIS, M. S. The dependence of magnetic reconnection on plasma beta and magnetic shear: Evidence from solar wind observations. **The Astrophysical Journal Letters**, v. 719, n. 2, p. L199, 2010. Available from: <<http://stacks.iop.org/2041-8205/719/i=2/a=L199>>. 144

PHAN, T. D.; HASEGAWA, H.; FUJIMOTO, M.; OIEROSET, M.; MUKAI, T.; LIN, R. P.; PATERSON, W. Simultaneous geotail and wind observations of reconnection at the subsolar and tail flank magnetopause. **Geophysical Research Letters**, v. 33, n. 9, p. n/a–n/a, 2006. ISSN 1944-8007. Available from: <<http://dx.doi.org/10.1029/2006GL025756>>. 19, 65, 143, 156

PHAN, T. D.; KISTLER, L. M.; KLECKER, B.; HAERENDEL, G.; PASCHMANN, G.; SONNERUP, B. U. O.; BAUMJOHANN, W.; BAVASSANO-CATTANEO, M. B.; CARLSON, C. W.; DILELLIS, A. M.; FORNACON, K. H.; FRANK, L. A.; FUJIMOTO, M.; GEORGESCU, E.; KOKUBUN, S.; MOEBIUS, E.; MUKAI, T.; OIEROSET, M.; PATERSON, W. R.; REME, H. Extended magnetic reconnection at the earth's magnetopause from detection of bi-directional jets. **Nature**, v. 404, n. 6780, p. 848–850, 04 2000. Available from: <<http://dx.doi.org/10.1038/35009050>>. 19, 66

PHAN, T. D.; LOVE, T. E.; GOSLING, J. T.; PASCHMANN, G.; EASTWOOD, J. P.; OIEROSET, M.; ANGELOPOULOS, V.; MCFADDEN, J. P.; LARSON, D.; AUSTER, U. Triggering of magnetic reconnection in a magnetosheath current sheet due to compression against the magnetopause. **Geophysical Research Letters**, v. 38, n. 17, p. n/a–n/a, 2011. ISSN 1944-8007. Available from: <<http://dx.doi.org/10.1029/2011GL048586>>. 100

PHAN, T. D.; PASCHMANN, G.; GOSLING, J. T.; OIEROSET, M.; FUJIMOTO, M.; DRAKE, J. F.; ANGELOPOULOS, V. The dependence of magnetic reconnection on plasma beta and magnetic shear: Evidence from magnetopause observations. **Geophysical Research Letters**, v. 40, n. 1, p. 11–16, 2013. ISSN 1944-8007. Available from: <<http://dx.doi.org/10.1029/2012GL054528>>. xi, xiii, 3, 23, 80, 144, 146, 156

PINNOCK, M.; CHISHAM, G.; COLEMAN, I. J.; FREEMAN, M. P.; HAIRSTON, M.; VILLAIN, J.-P. The location and rate of dayside reconnection during an interval of southward interplanetary magnetic field. **Annales Geophysicae**, v. 21, n. 7, p. 1467–1482, 2003. 66, 67

PU, Z. Y.; XIAO, C. J.; ZHANG, X. G.; HUANG, Z. Y.; FU, S. Y.; LIU, Z. X.; DUNLOP, M. W.; ZONG, Q. G.; CARR, C. M.; RÉME, H.; DANDOURAS, I.; FAZAKERLEY, A.; PHAN, T.; ZHANG, T. L.; ZHANG, H.; WANG, X. G. Double star tc-1 observations of component reconnection at the dayside magnetopause: a preliminary study. **Annales Geophysicae**, v. 23, n. 8, p. 2889–2895, 2005. 2, 19

PUHL-QUINN, P. A.; SCUDDER, J. D. Systematics of ion walén analysis of rotational discontinuities using e/z measurements. **Journal of Geophysical Research: Space Physics**, v. 105, n. A4, p. 7617–7627, 2000. ISSN 2156-2202. Available from: <<http://dx.doi.org/10.1029/1999JA000314>>. 80

RÉME, H.; AOUSTIN, C.; BOSQUED, J. M.; DANDOURAS, I.; LAVRAUD, B.; SAUVAUD, J. A.; BARTHE, A.; BOUYSSOU, J.; CAMUS, T.; COEUR-JOLY, O.; CROS, A.; CUVILO, J.; DUCAY, F.; GARBAROWITZ, Y.; MEDALE, J. L.; PENOU, E.; PERRIER, H.; ROMEFORT, D.; ROUZAUD, J.; VALLAT, C.; ALCAYDÉ, D.; JACQUEY, C.; MAZELLE, C.; D'USTON, C.; MÖBIUS, E.; KISTLER, L. M.; CROCKER, K.; GRANOFF, M.; MOUIKIS, C.; POPECKI, M.; VOSBURY, M.; KLECKER, B.; HOVESTADT, D.; KUCHARAK, H.; KUENNETH, E.; PASCHMANN, G.; SCHOLER, M.; SCKOPKE, N.; SEIDENSCHWANG, E.; CARLSON, C. W.; CURTIS, D. W.; INGRAHAM, C.; LIN, R. P.; MCFADDEN, J. P.; PARKS, G. K.; PHAN, T.; FORMISANO, V.; AMATA, E.; BAVASSANO-CATTANEO, M. B.; BALDETTI, P.; BRUNO, R.; CHIONCHIO, G.; LELLIS, A. D.; MARCUCCI, M. F.; PALLOCCHIA, G.; KORTH, A.; DALY, P. W.; GRAEVE, B.; ROSENBAUER, H.; VASYLIUNAS, V.; MCCARTHY, M.; WILBER, M.; ELIASSON, L.; LUNDIN, R.; OLSEN, S.; SHELLEY, E. G.; FUSELIER, S.; GHIEMMETTI, A. G.; LENNARTSSON, W.; ESCOUBET, C. P.; BALSIGER, H.; FRIEDEL, R.; CAO, J.-B.; KOVRAZHNIKIN, R. A.; PAPAMASTORAKIS, I.; PELLAT, R.; SCUDDER, J.; SONNERUP, B. First multispacecraft ion measurements in and near the earth's magnetosphere with the identical cluster ion spectrometry (cis) experiment. **Annales Geophysicae**, v. 19, n. 10/12, p. 1203–1354, 2001. 60

- RUSSELL, C. T.; ELPHIC, R. C. Initial ISEE magnetometer results - Magnetopause observations. **Space Science Reviews**, v. 22, p. 681–715, dec. 1978. 62, 84
- SCHOPPER, R.; LESCH, H.; BIRK, G. T. Magnetic reconnection and particle acceleration in active galactic nuclei. **Astronomy and Astrophysics**, v. 335, n. 1, p. 26–32, July 1998. 13
- SCHREIER, R.; SWISDAK, M.; DRAKE, J. F.; CASSAK, P. A. Three-dimensional simulations of the orientation and structure of reconnection x-lines. **Physics of Plasmas (1994-present)**, v. 17, n. 11, p. –, 2010. Available from: <<http://scitation.aip.org/content/aip/journal/pop/17/11/10.1063/1.3494218>>. 2, 144
- SEMENOV, V. S.; PUDOVKIN, M. I. Localization and features of the development of reconnection processes at the magnetopause. **Geomagnetism and Aeronomy**, v. 25, p. 592–597, August 1985. 37
- SHUE, J.-H.; SONG, P.; RUSSELL, C. T.; STEINBERG, J. T.; Chao, J. K.; ZASTENKER, G.; VAISBERG, O. L.; KOKUBUN, S.; SINGER, H. J.; DETMAN, T. R.; KAWANO, H. Magnetopause location under extreme solar wind conditions. **Journal of Geophysical Research**, v. 103, p. 17691–17700, aug. 1998. xv, xvi, 28, 29, 61, 62, 68, 69, 70, 75, 78
- SIBECK, D.; PASCHMANN, G.; TREUMANN, R.; FUSELIER, S.; LENNARTSSON, W.; LOCKWOOD, M.; LUNDIN, R.; OGILVIE, K.; ONSAGER, T.; PHAN, T.-D.; ROTH, M.; SCHOLER, M.; SCKOPKE, N.; STASIEWICZ, K.; YAMAUCHI, M. Plasma transfer processes at the magnetopause. **Space Science Reviews**, v. 88, n. 1–2, p. 207–283, 1999. 6, 7, 19
- SIBECK, D. G.; LIN, R.-Q. Concerning the motion and orientation of flux transfer events produced by component and antiparallel reconnection. **Journal of Geophysical Research: Space Physics**, v. 116, n. A7, p. n/a–n/a, 2011. ISSN 2156-2202. Available from: <<http://dx.doi.org/10.1029/2011JA016560>>. 2, 37, 143
- SIBECK, D. G.; LOPEZ, R. E.; ROELOF, E. C. Solar wind control of the magnetopause shape, location, and motion. **Journal of Geophysical Research: Space Physics**, v. 96, n. A4, p. 5489–5495, 1991. ISSN 2156-2202. Available from: <<http://dx.doi.org/10.1029/90JA02464>>. 7

SONNERUP, B. U. Ö. Magnetopause reconnection rate. **Journal of Geophysical Research**, v. 79, n. 10, p. 1546–1549, 1974. ISSN 2156-2202. Available from: <<http://dx.doi.org/10.1029/JA079i010p01546>>. 1, 36, 37, 86, 94, 96, 114, 124, 143

SONNERUP, B. U. Ö.; CAHILL, J. L. J. Magnetopause Structure and Attitude from Explorer 12 Observations. **Journal of Geophysical Research**, v. 72, p. 171, jan. 1967. 68

SONNERUP, B. U. Ö.; PASCHMANN, G.; PAPAMASTORAKIS, I.; SCKOPKE, N.; HAERENDEL, G.; BAME, S. J.; ASBRIDGE, J. R.; GOSLING, J. T.; RUSSELL, C. T. Evidence for magnetic field reconnection at the earth's magnetopause. **Journal of Geophysical Research: Space Physics**, v. 86, n. A12, p. 10049–10067, 1981. ISSN 2156-2202. Available from: <<http://dx.doi.org/10.1029/JA086iA12p10049>>. 13, 19

SONNERUP, B. U. Ö.; PASCHMANN, G.; PHAN, T.-D. Fluid aspects of reconnection at the magnetopause: In situ observations. In: _____. **Physics of the magnetopause**. American Geophysical Union, 1995. p. 167–180. Available from: <<http://dx.doi.org/10.1029/GM090p0167>>. 19, 20

SONNERUP, B. U. Ö.; SCHEIBLE, M. Minimum and maximum variance analysis. **ISSI Scientific Reports Series**, v. 1, p. 185–220, 1998. 68, 70

STERN, D. P. The motion of magnetic field lines. **Space Science Reviews**, v. 6, n. 2, p. 147–173, 1966. 12

STONE, E.; FRANSEN, A.; MEWALDT, R.; CHRISTIAN, E.; MARGOLIES, D.; ORMES, J.; SNOW, F. The advanced composition explorer. **Space Science Reviews**, v. 86, n. 1-4, p. 1–22, 1998. 67, 103

SU, Y.; VERONIG, A. M.; HOLMAN, G. D.; DENNIS, B. R.; WANG, T.; TEMMER, M.; GAN, W. Imaging coronal magnetic-field reconnection in a solar flare. **Nat Phys**, Nature Publishing Group, v. 9, n. 8, p. 489–493, 08 2013. Available from: <<http://dx.doi.org/10.1038/nphys2675>>. 1, 13

SWEET, P. A. The neutral point theory of solar flares. In: LEHNERT, B. (Ed.). **Electromagnetic phenomena in cosmic physics**. London: Cambridge University Press, 1958. p. 123–134. 15

SWISDAK, M.; DRAKE, J. F. Orientation of the reconnection X-line. **Geophysical Research Letters**, v. 34, p. 11106, jun. 2007. xi, xiii, xv, xvi, xix,

xxiii, xxiv, 2, 3, 39, 42, 43, 44, 46, 55, 57, 58, 86, 88, 94, 95, 96, 97, 98, 116, 120, 121, 122, 123, 124, 125, 126, 127, 128, 129, 130, 131, 132, 133, 134, 135, 136, 137, 138, 139, 140, 142, 143, 144, 151, 152, 155, 156, 157, 180, 181, 182, 183, 184, 185, 186, 187

SWISDAK, M.; ROGERS, B. N.; DRAKE, J. F.; SHAY, M. A. Diamagnetic suppression of component magnetic reconnection at the magnetopause. **Journal of Geophysical Research: Space Physics**, v. 108, n. A5, p. n/a–n/a, 2003. ISSN 2156-2202. Available from: <<http://dx.doi.org/10.1029/2002JA009726>>. 13, 144

TÓTH, G.; HOLST, B. van der; SOKOLOV, I. V.; ZEEUW, D. L. D.; GOMBOSI, T. I.; FANG, F.; MANCHESTER, W. B.; MENG, X.; NAJIB, D.; POWELL, K. G.; STOUT, Q. F.; GLOCER, A.; MA, Y.-J.; OPPER, M. Adaptive numerical algorithms in space weather modeling. **Journal of Computational Physics**, v. 231, n. 3, p. 870 – 903, 2011. 48

TÓTH, G.; SOKOLOV, I. V.; GOMBOSI, T. I.; CHESNEY, D. R.; CLAUER, C. R.; ZEEUW, D. L. D.; HANSEN, K. C.; KANE, K. J.; MANCHESTER, W. B.; OEHMKE, R. C.; POWELL, K. G.; RIDLEY, A. J.; ROUSSEV, I. I.; STOUT, Q. F.; VOLBERG, O.; WOLF, R. A.; SAZYKIN, S.; CHAN, A.; YU, B.; KÓTA, J. Space weather modeling framework: A new tool for the space science community. **Journal of Geophysical Research: Space Physics**, v. 110, n. A12, p. n/a–n/a, 2005. ISSN 2156-2202. Available from: <<http://dx.doi.org/10.1029/2005JA011126>>. 46

TRATTNER, K. J.; MULCOCK, J. S.; PETRINEC, S. M.; FUSELIER, S. A. Probing the boundary between antiparallel and component reconnection during southward interplanetary magnetic field conditions. **Journal of Geophysical Research: Space Physics**, v. 112, n. A8, p. n/a–n/a, 2007. ISSN 2156-2202. Available from: <<http://dx.doi.org/10.1029/2007JA012270>>. xi, xiii, xv, xvi, xix, xxiii, xxiv, 2, 3, 25, 26, 27, 32, 33, 34, 36, 86, 88, 89, 90, 97, 98, 116, 120, 121, 122, 123, 124, 125, 126, 127, 128, 129, 130, 131, 132, 133, 134, 135, 136, 137, 138, 139, 140, 142, 144, 147, 148, 155, 156, 157, 180, 181, 182, 183, 184, 185, 186, 187

TRATTNER, K. J.; PETRINEC, S. M.; FUSELIER, S. A.; PHAN, T. D. The location of reconnection at the magnetopause: Testing the maximum magnetic shear model with themis observations. **Journal of Geophysical Research: Space Physics**, v. 117, n. A1, p. n/a–n/a, 2012. ISSN 2156-2202. Available from: <<http://dx.doi.org/10.1029/2011JA016959>>. 144

TRENCHI, L.; MARCUCCI, M. F.; PALLOCCHIA, G.; CONSOLINI, G.; CATTANEO, M. B. B.; LELLIS, A. M. D.; RÈME, H.; KISTLER, L.; CARR, C. M.; CAO, J. B. Occurrence of reconnection jets at the dayside magnetopause: Double star observations. **Journal of Geophysical Research: Space Physics**, v. 113, n. A7, p. n/a–n/a, 2008. ISSN 2156-2202. Available from: <<http://dx.doi.org/10.1029/2007JA012774>>. 2, 19, 144

TSYGANENKO, N. A.; STERN, D. P. Modeling the global magnetic field of the large-scale Birkeland current systems. **Journal of Geophysical Research**, v. 101, p. 27187–27198, dec. 1996. 87, 106, 108

TUFTS University, Medford/Somerville, Massachusetts, USA. A noon-midnight meridian cut of the Earth's magnetosphere.

http://ase.tufts.edu/cosmos/print_images.asp?id=29. Accessed on November 2014 8

VASYLIUNAS, V. M. Theoretical models of magnetic field line merging. **Reviews of Geophysics**, v. 13, n. 1, p. 303–336, 1975. ISSN 1944-9208. Available from: <<http://dx.doi.org/10.1029/RG013i001p00303>>. 1, 13, 14, 142

WALSH, B. M.; PHAN, T. D.; SIBECK, D. G.; SOUZA, V. M. The plasmaspheric plume and magnetopause reconnection. **Geophysical Research Letters**, v. 41, n. 2, p. 223–228, 2014. ISSN 1944-8007. Available from: <<http://dx.doi.org/10.1002/2013GL058802>>. 13, 19, 66

ZWEIBEL, E. G.; YAMADA, M. Magnetic reconnection in astrophysical and laboratory plasmas. **Annual Review of Astronomy and Astrophysics**, v. 47, n. 1, p. 291–332, 2009. Available from: <<http://www.annualreviews.org/doi/abs/10.1146/annurev-astro-082708-101726>>. 1, 13, 16, 18

APPENDIX A - Ridge Detection Method

Here, it is summarized the method depicted in Lindeberg (1998) and references therein to detect ridges in 2-D images. As we go through it, it is briefly shown the conceptual basis on which the method is based.

A.1 Scale-Space Representation

When using mathematical language for describing features within an image, such as edges and ridges, it is important to bear in mind that these features “exist as meaningful entities only over certain finite ranges of scale”, as pointed out by Lindeberg (1993, p. 349). Thus, the so-called *multiscale representation* is required to properly address the image structure.

As described in Lindeberg (1993), the scale-space representation $\mathcal{L} : \mathbb{Z}^2 \times \mathbb{R}_+ \rightarrow \mathbb{R}$ of a discrete image $f : \mathbb{Z}^2 \rightarrow \mathbb{R}$ is achieved by means of a convolution of this image with a discrete analogue of a gaussian kernel $T : \mathbb{Z}^2 \times \mathbb{R}_+ \rightarrow \mathbb{R}$:

$$\mathcal{L}(x, y; s) = \sum_{m=-\infty}^{+\infty} \sum_{n=-\infty}^{+\infty} T(n; s)T(m; s) \times f(x - m, y - n), \quad (\text{A.1})$$

where

$$T(n; s) = \exp^{-t} I_n(s). \quad (\text{A.2})$$

In Equation A.2, I_n are the modified Bessel functions of integer order, and s is the scale parameter. Here, s corresponds to σ^2 , where σ is the standard deviation of the gaussian kernel. The scale-space representation, \mathcal{L} , is the smoothed version of the original image $f(x, y)$ on a scale s . As the scale parameter increases, the higher is the degree of smoothing. Figure A.1 illustrates this idea.

It can also be shown (cf. Lindeberg (1993)) that the $(i + j)$ -th order derivative of the scale-space representation of the image is calculated by applying the i -th order derivative of the (one-dimensional) discrete analogue of the gaussian kernel along the x-direction T_{x^i} and the j -th order derivative of the discrete analogue of the gaussian kernel along the y-direction T_{y^j} :

$$\frac{\partial^{i+j} \mathcal{L}}{\partial x^i \partial y^j} \equiv \mathcal{L}_{x^i y^j} = (T_{x^i}) * (T_{y^j}) * f \quad (\text{A.3})$$

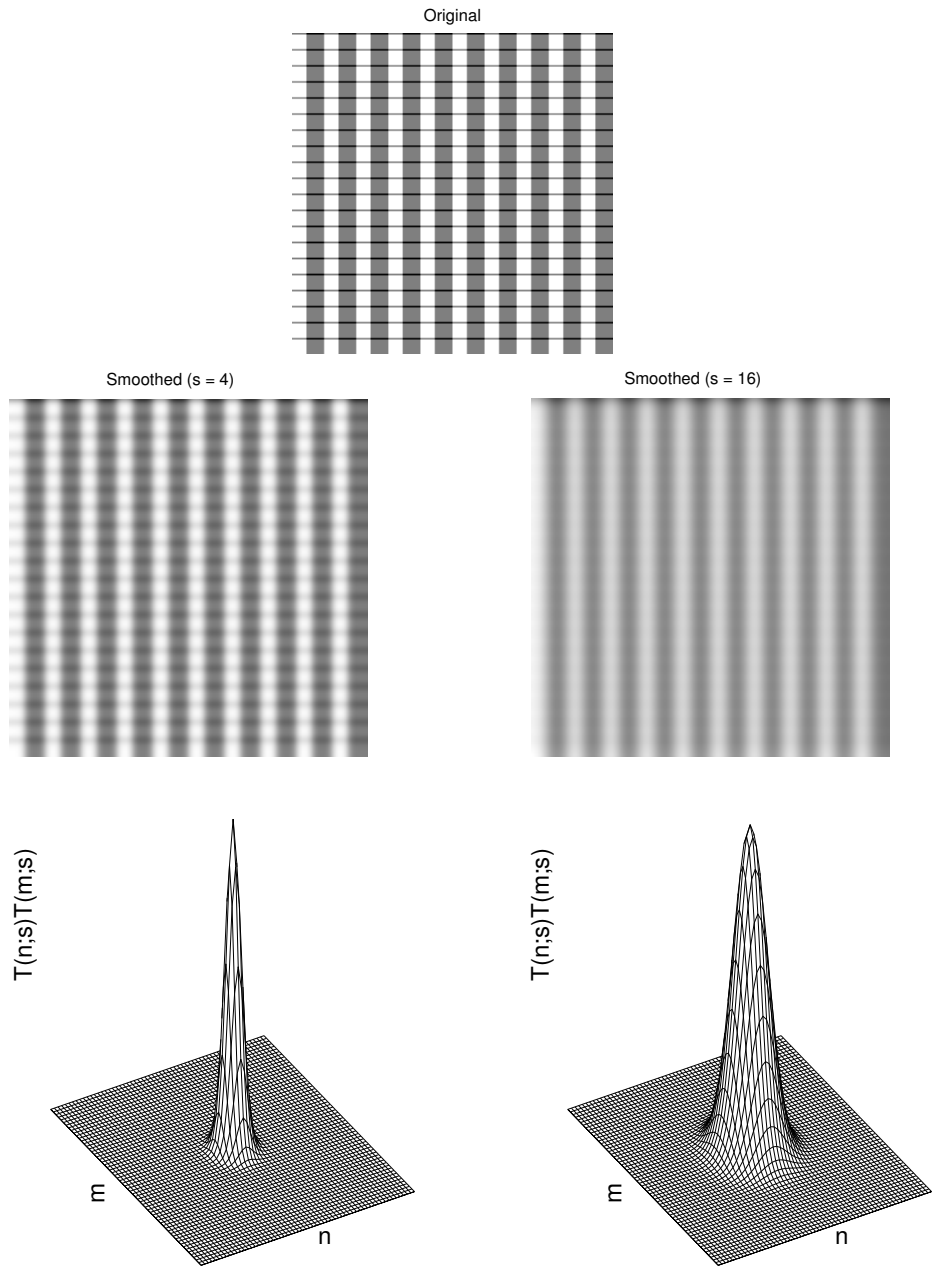


Figure A.1 - Scale-space representation (middle row) of a synthetic image (top row) by convolution with the separable discrete kernel $T(n; s)T(m; s)$ (bottom row) for two scales (left) $s = 4$ and (right) $s = 16$.

The (one-dimensional) derivatives of T are approximated by centered finite differences. As an example, it is presented the even order derivatives of T at a point x_o (y_o), as given by Equation A.4 (A.5) below, when the spacing between adjacent points in the x (Δx) and y (Δy)-directions are uniform and equal to one:

$$T_{x^{(2n)}}^{x_o} = \sum_{l=0}^{2n} (-1)^l \binom{2n}{l} T_x^{x_o-(n-l)}, \quad n, l \in \mathbb{Z}_+, \quad (\text{A.4})$$

$$T_{y^{(2n)}}^{y_o} = \sum_{l=0}^{2n} (-1)^l \binom{2n}{l} T_y^{y_o-(n-l)}, \quad n, l \in \mathbb{Z}_+. \quad (\text{A.5})$$

A.2 Ridge Definition at a Fixed Scale

According to [Haralick \(1983\)](#), a standard definition of a bright (dark) ridge is that it consists of a collection of points for which the eigenvalue of the Hessian matrix assumes a local maximum (minimum) in the main eigendirection of the Hessian matrix. The Hessian matrix provides information regarding the local curvature of the function (image) $f(x, y)$: its eigendirection gives the direction where the curvature is a local extremum, while the sign of the eigenvalue says whether the extremum curvature value is a maximum (positive sign) or a minimum (negative sign). Within the framework developed in this thesis it is of interest to determine the loci in the image where its grey-level intensities are the highest, thus the bright ridge definition is used. Such definitions can be applied either directly to the original image or, more preferably, to its smoothed version \mathcal{L} (at a given scale s), since the derivatives calculated for the Hessian matrix using the points of \mathcal{L} are prone to be more well-defined.

For any smoothed version \mathcal{L} (or alternatively at any given scale s) of the original image it is possible, at any given point (x, y) in \mathcal{L} , to rotate by an angle β_o the local Hessian matrix to a (p, q) -system where its off-diagonal terms (mixed second order derivatives, i.e. \mathcal{L}_{pq} and \mathcal{L}_{qp}) vanish. The remainder terms in the diagonal of the Hessian matrix ($\frac{\partial^2 \mathcal{L}}{\partial p^2} \equiv \mathcal{L}_{pp}$ and \mathcal{L}_{qq}) turns out to be the eigenvalues associated with the eigendirections ([Lindeberg \(1998\)](#)).

The unit vectors along the p - and q -directions are defined as $\mathbf{e}_p = (\sin \beta_o, -\cos \beta_o)$ and $\mathbf{e}_q = (\cos \beta_o, \sin \beta_o)$, where the rotation angle β_o is locally defined as:

$$\cos \beta_o|_{(x,y)} = \sqrt{\frac{1}{2} \left(1 + \frac{\mathcal{L}_{xx} - \mathcal{L}_{yy}}{\sqrt{(\mathcal{L}_{xx} - \mathcal{L}_{yy})^2 + 4\mathcal{L}_{xy}^2}} \right)} \Big|_{(x,y)}, \quad (\text{A.6})$$

$$\sin \beta_o|_{(x,y)} = (\text{sign } \mathcal{L}_{xy}) \sqrt{\frac{1}{2} \left(1 - \frac{\mathcal{L}_{xx} - \mathcal{L}_{yy}}{\sqrt{(\mathcal{L}_{xx} - \mathcal{L}_{yy})^2 + 4\mathcal{L}_{xy}^2}} \right)} \Big|_{(x,y)}. \quad (\text{A.7})$$

The rotated Hessian matrix H is then written as follows:

$$H|_{(x,y)} = \begin{vmatrix} \mathcal{L}_{pp} & 0 \\ 0 & \mathcal{L}_{qq} \end{vmatrix}, \quad (\text{A.8})$$

where the second-order derivatives with respect to p (\mathcal{L}_{pp}) and q (\mathcal{L}_{qq}) are calculated by using Equation A.9 below for the case when $i = 2$ and $j = 0$, and $i = 0$ and $j = 2$, respectively:

$$\mathcal{L}_{p^{(i)}q^{(j)}} = \sum_{r=0}^i \sum_{u=0}^j (-1)^r \binom{i}{r} \binom{j}{u} (\sin \beta_o)^{(i-r+u)} (\cos \beta_o)^{(j+r-u)} \mathcal{L}_{x^{(i+j-(r+u))}y^{(r+u)}}. \quad (\text{A.9})$$

In this formulation, a bright ridge point, hereafter called only ridge point, will be such that it satisfies

$$\mathcal{L}_p = 0, \quad \mathcal{L}_q = 0, \quad (\text{A.10})$$

$$\mathcal{L}_{pp} < 0, \quad \text{or} \quad \mathcal{L}_{qq} < 0, \quad (\text{A.11})$$

$$|\mathcal{L}_{pp}| \geq |\mathcal{L}_{qq}|, \quad |\mathcal{L}_{qq}| \geq |\mathcal{L}_{pp}|, \quad (\text{A.12})$$

depending on whether the p - or the q -direction corresponds to the maximum absolute eigenvalue of the Hessian matrix.

A.3 Determining the ridge-like points in an 2-D image

We notice that the condition expressed in equation A.10 is seldom exactly satisfied in real-life images, i.e., \mathcal{L}_p or \mathcal{L}_q will not be strictly zero at a given pixel of the image.

However, one may find that at one (x, y) pixel, with $x, y \in \mathbb{Z}$, \mathcal{L}_p (in the case of the p -direction being associated with the largest eigenvalue of the Hessian matrix), is positive and at some neighbouring pixel, say $(x, y + 1)$, the \mathcal{L}_p sign is negative. That means that somewhere in between the (x, y) and $(x, y + 1)$ direction \mathcal{L}_p has reached zero, and in that “sub-pixel” equation A.10 will be considered to be satisfied. This sub-pixel is estimated as the linear interpolation between the neighbouring pixels, which in this case would be $(x, y + 1/2)$. By using this and other criteria, Lindeberg (1993) has developed an algorithm whereby edges within images could be detected. The same idea can be applied to determine ridge points (LINDBERG, 1998). Below, the sub-pixel ridge detection method used in this thesis work to determine ridge-like points, which in turn satisfy equations A.10 through A.12, is described. For in depth analysis of such a method, the reader is referred to the work of Lindeberg (1993) and Lindeberg (1998).

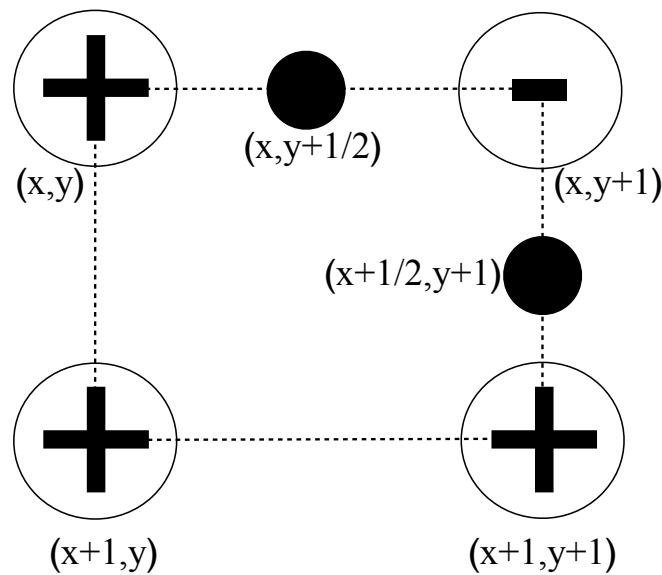


Figure A.2 - Sub-pixel ridge detection method as presented in Lindeberg (1993), and applied at a cell of four adjacent pixels, $\{(x, y), (x + 1, y), (x, y + 1), (x + 1, y + 1)\}$, for the simple situation where the \mathcal{L}_p (or \mathcal{L}_q) sign is negative at one pixel location and positive at all others, and \mathcal{L}_{pp} is negative at one pixel. The ridge point (filled black circle) is placed along an edge of the cell where in its corners the \mathcal{L}_p (or \mathcal{L}_q) signs are opposite. The ridge point location is determined by linear interpolation (see text for details).

Consider a cell of four-adjacent points in an 2-D image, $\{(x, y), (x + 1, y), (x, y + 1), (x + 1, y + 1)\}$, as shown in Figure A.2. In order to find the ridge-like points, it is required that in at least one of the four pixels within this cell equation A.11 be sat-

ified, i.e., that the extremum grey-level value of the analyzed image is a maximum. After that, we evaluate \mathcal{L}_p ¹ at each pixel and store their respective signs. Then, we look at the corners of each edge of this four pixels cell and check if \mathcal{L}_p at these corners have opposite signs. If that happens, the sub-pixel (ridge point) is determined as a linear interpolation between the neighbouring pixels forming the analyzed edge of the cell. Figure A.2 shows a simple situation where at one pixel, $(x, y + 1)$, the \mathcal{L}_p sign is negative and at all others \mathcal{L}_p is positive, whereas \mathcal{L}_{pp} is negative at one pixel². The adjacent pixel pairs that have opposite \mathcal{L}_p signs are $[(x, y), (x, y + 1)]$ and $[(x, y + 1), (x + 1, y + 1)]$. The respective sub-pixels (or ridge points) will be located as filled black circles in Figure A.2, with their locations determined by the linear interpolation described above. At the current implementation, as occurred with Lindeberg (1998)'s, the maximum number of sub-pixels (ridge points) within a given cell is two. That means that some combinations of \mathcal{L}_p signs over the four pixel locations are not taken into account. For instance, if one looks at Figure A.2, one of such configurations would be achieved if instead of a '+' sign at the pixel $(x + 1, y)$ there was a 'minus' sign. In that case, there would be four ridge points. On Lindeberg (1998)'s implementation, the restriction of only two sub-pixels per analyzed cell had taken place because he was concerned with a post-processing step related with linking the sub-pixels found, and including more than two sub-pixels per cell would introduce an ambiguity in such a procedure. In our implementation, on the other hand, we are not worried with linking sub-pixels, but only with determining their location. Even so, we have decided to maintain Lindeberg (1998)'s original implementation. The same procedure described above is done for all the other four-pixel cells in the image and the ridge points determined accordingly.

¹It will be either \mathcal{L}_p or \mathcal{L}_q , again depending on whether the p - or q -direction corresponds to the maximum absolute eigenvalue of the Hessian matrix

²Looking at the method's implementation description in Lindeberg (1998, p. 148), it is not clear whether it is important or not to keep track of the pixel(s) where the \mathcal{L}_{pp} sign is (are) negative as long as in *at least one* of the four adjacent pixels being analyzed the condition $\mathcal{L}_{pp} < 0$ be satisfied.

APPENDIX B - X-line model test against *in situ* reconnection jet observations - Part II

Here we present the results relative to the reconnection plasma jet data presented in Table 7.2 of Chapter 7. The discussion of similar plots was done in Section 7.1.6, and here the plots are only shown. The first two of the 8 figures that will be presented below refer to plasma jet data whose dipole tilt bin is $-5^\circ \leq \psi < 5^\circ$ and for which the IMF B_x is either positive (Figure B.1) or negative (Figure B.2). The second pair of figures refer to plasma jet data whose dipole tilt bin is $5^\circ \leq \psi < 15^\circ$ and also for which the IMF B_x is either positive (Figure B.3) or negative (Figure B.4). The same applies for the remainder set of 4 figures being the first two of these four related with reconnection plasma jet data whose dipole tilt bin is $15^\circ \leq \psi < 25^\circ$, and the other two with the dipole tilt bin $25^\circ \leq \psi < 35^\circ$.

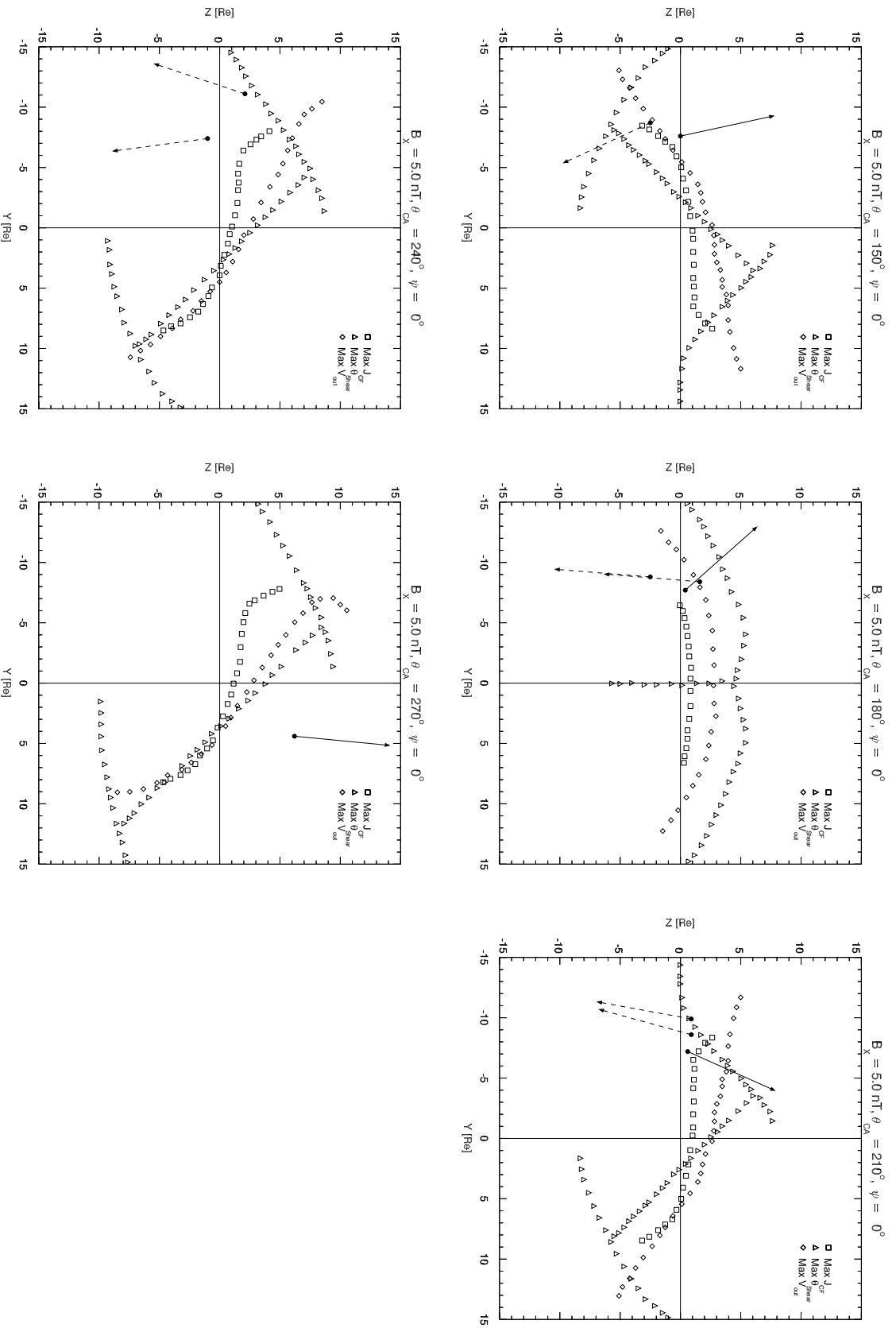


Figure B.1 - X line models test against *in situ* observations of reconnection plasma jets. The X lines which are presented onto the yz_{GSM} plane are derived from the models of maximum Chapman-Ferraro current density magnitude, Max J_{CF} , by Gonzalez and Mozer (1974), the maximum shear angle model, Max θ_{Shear} , by Trattner et al. (2007), and the maximum reconnection outflow speed, Max V_{out} , by Swisdak and Drake (2007). The IMF ($B_x = 5$ nT, $B_z = 0, -2.886$ or -5 nT and $\theta_{CA} = \tan^{-1}(B_y/B_z)$) and Earth's dipole tilt (ψ) conditions used as input to generate the X lines shown are presented on the top of each panel. The observed plasma jet directions are represented as solid (dashed) arrows if they have a northward (southward) V_z^{jet} component, and they were detected under IMF and dipole tilt conditions similar to those shown on the top of the respective panel (see text for details). The location of the spacecraft when it detected the plasma jet at the dayside magnetopause crossing is marked by the black filled circle.

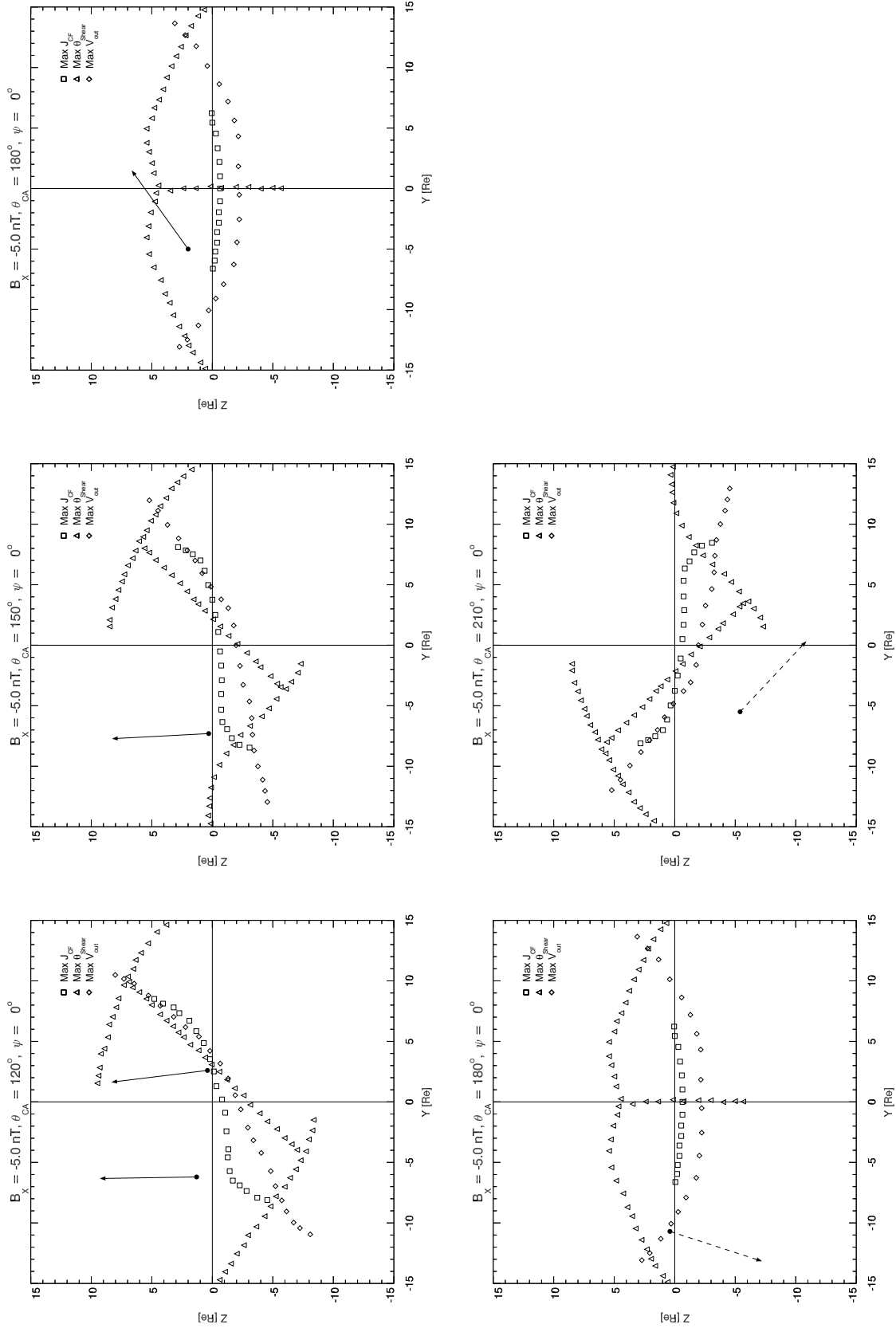


Figure B.2 - X line models test against *in situ* observations of reconnection plasma jets. The X lines which are presented onto the yz_{GSM} plane are derived from the models of maximum Chapman-Ferraro current density magnitude, Max J_{CF} , by Gonzalez and Mozer (1974), the maximum shear angle model, Max θ_{Shear} , by Trattner et al. (2007), and the maximum reconnection outflow speed, Max V_{out} , by Swisdak and Drake (2007). The IMF ($B_x = -5$ nT, $B_z = 0$, -2.886 or -5 nT and $\theta_{CA} = \tan^{-1}(B_y/B_z)$) and Earth's dipole tilt (ψ) conditions used as input to generate the X lines shown are presented on the top of each panel. The observed plasma jet directions are represented as solid (dashed) arrows if they have a northward (southward) V_z^{jet} component, and they were detected under IMF and dipole tilt conditions similar to those shown on the top of the respective panel (see text for details). The location of the spacecraft when it detected the plasma jet at the dayside magnetopause crossing is marked by the black filled circle.

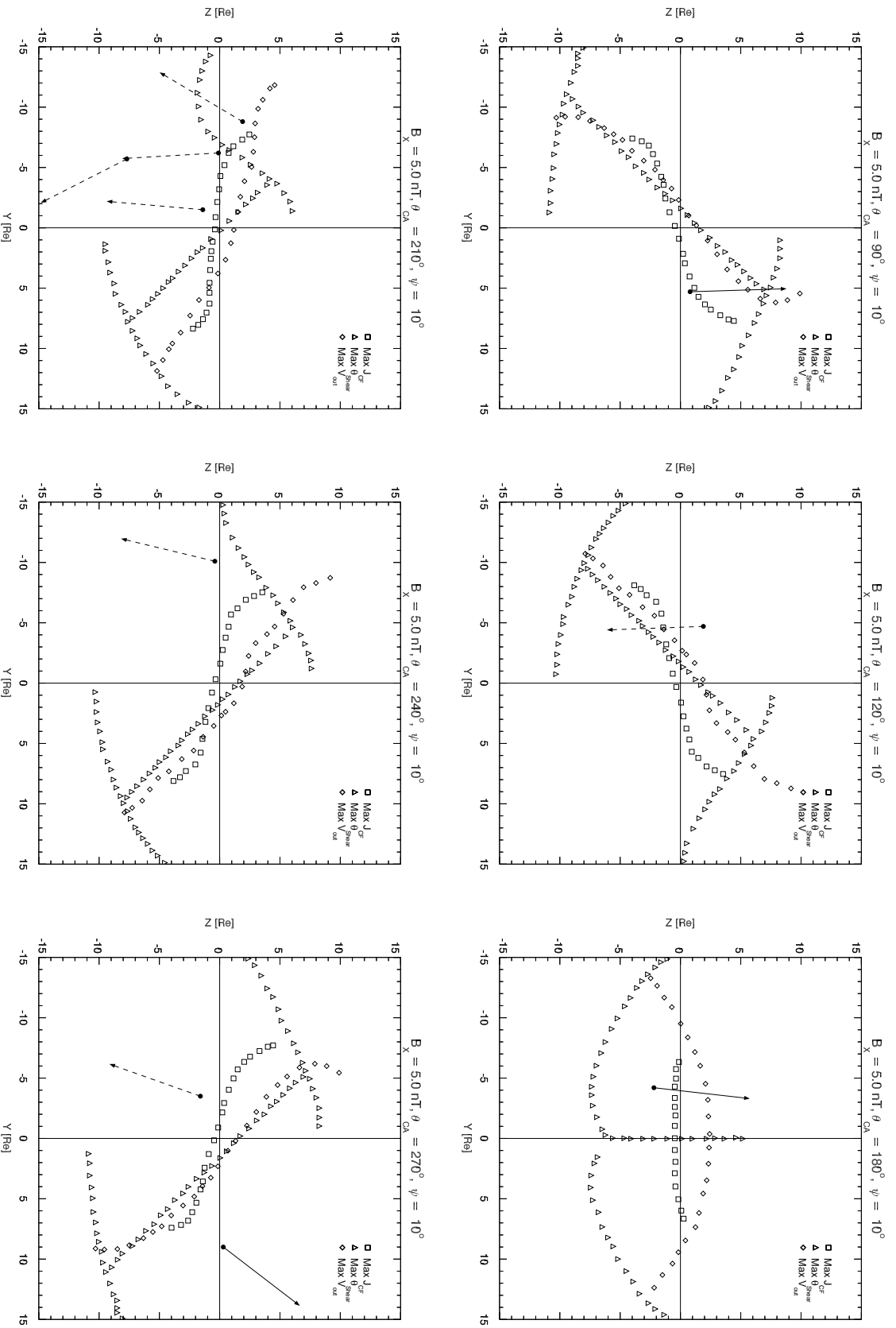


Figure B.3 - X line models test against *in situ* observations of reconnection plasma jets. The X lines which are presented onto the $yzGSM$ plane are derived from the models of maximum Chapman-Ferraro current density magnitude, Max J_{CF} , by Gonzalez and Mozer (1974), the maximum shear angle model, Max θ_{Shear} , by Trattner et al. (2007), and the maximum reconnection outflow speed, Max V_{out} , by Swisdak and Drake (2007). The IMF ($B_x = 5$ nT, $B_z = 0, -2.886$ or -5 nT and $\theta_{CA} = \tan^{-1}(B_y/B_z)$) and Earth's dipole tilt (ψ) conditions used as input to generate the X lines shown are presented on the top of each panel. The observed plasma jet directions are represented as solid (dashed) arrows if they have a northward (southward) V_z^{jet} component, and they were detected under IMF and dipole tilt conditions similar to those shown on the top of the respective panel (see text for details). The location of the spacecraft when it detected the plasma jet at the dayside magnetopause crossing is marked by the black filled circle.

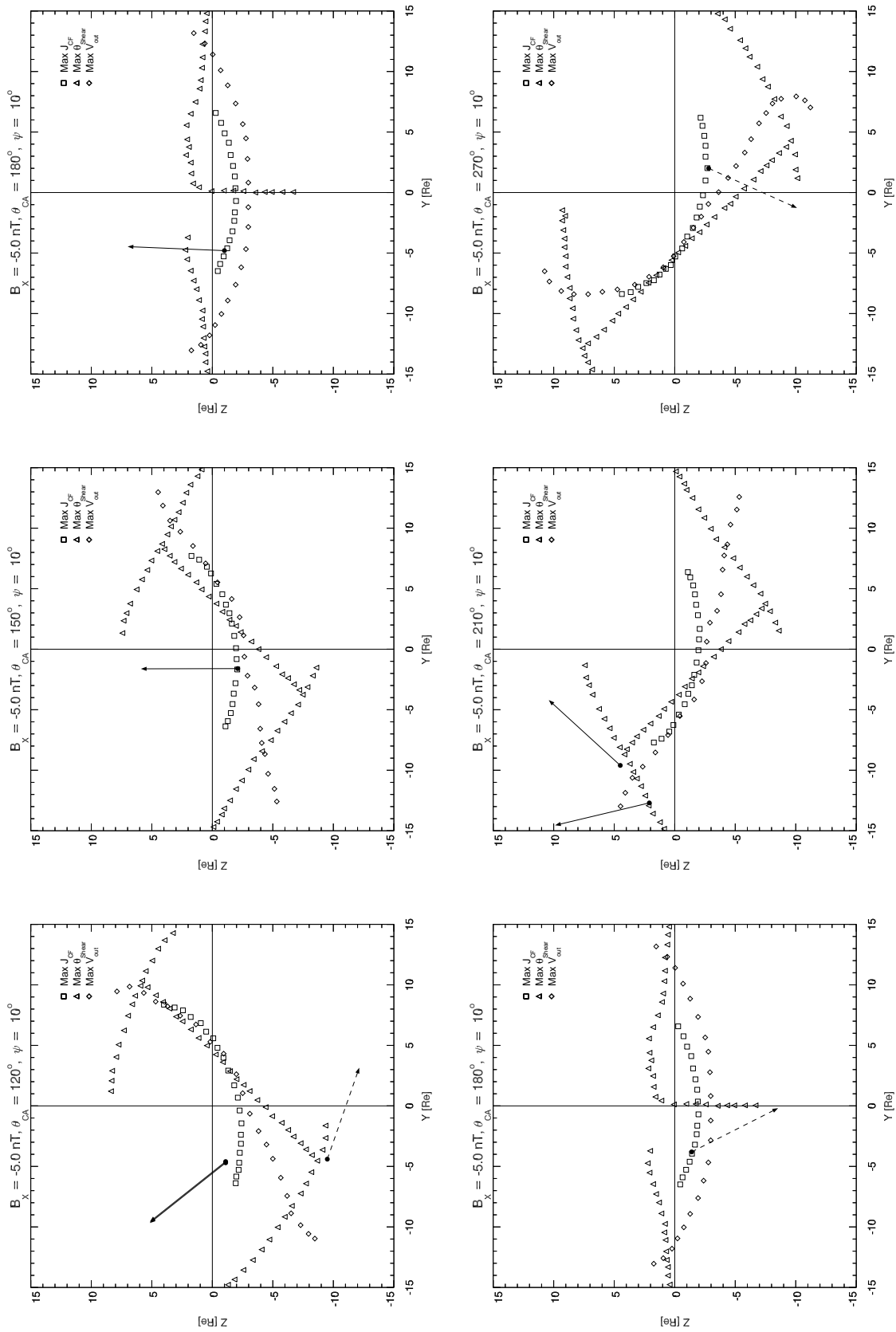


Figure B.4 - X line models test against *in situ* observations of reconnection plasma jets. The X lines which are presented onto the yz_{GSM} plane are derived from the models of maximum Chapman-Ferraro current density magnitude, $\text{Max } J_{CF}$, by Gonzalez and Mozer (1974), the maximum shear angle model, $\text{Max } \theta_{S_{near}}$, by Trattner et al. (2007), and the maximum reconnection outflow speed, $\text{Max } V_{out}$, by Swisdak and Drake (2007). The IMF ($B_x = -5$ nT, $B_z = 0$, -2.886 or -5 nT, $B_y/B_z = \tan^{-1}(B_y/B_z)$) and Earth's dipole tilt (ψ) conditions used as input to generate the X lines shown are presented on the top of each panel. The observed plasma jet directions are represented as solid (dashed) arrows if they have a northward (southward) V_z^{jet} component, and they were detected under IMF and dipole tilt conditions similar to those shown on the top of the respective panel (see text for details). The location of the spacecraft when it detected the plasma jet at the dayside magnetopause crossing is marked by the black filled circle.

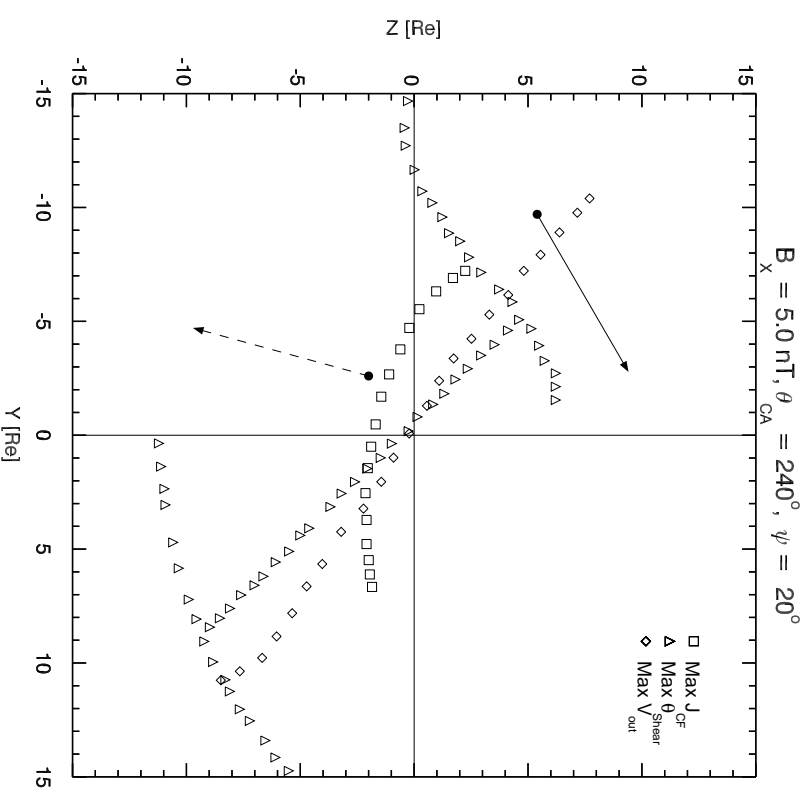
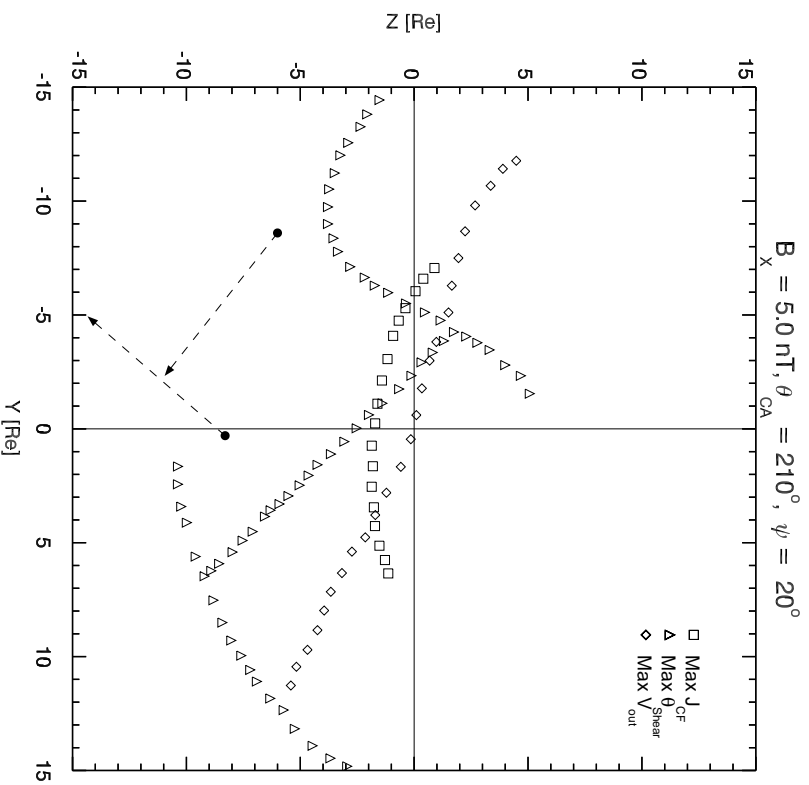


Figure B.5 - X line models test against *in situ* observations of reconnection plasma jets. The X lines which are presented onto the yz_{GSM} plane are derived from the models of maximum Chapman-Ferraro current density magnitude, $\text{Max } J_{CF}$, by Gonzalez and Mozer (1974), the maximum shear angle model, $\text{Max } \theta_{Shear}$, by Trattner et al. (2007), and the maximum reconnection outflow speed, $\text{Max } V_{out}$, by Swisdak and Drake (2007). The IMF ($B_x = 5 \text{ nT}$, $B_z = -2.886$ or -5 nT and $\theta_{CA} = \tan^{-1}(B_y/B_z)$) and Earth's dipole tilt (ψ) conditions used as input to generate the X lines shown are presented on the top of each panel. The observed plasma jet directions are represented as solid (dashed) arrows if they have a northward (southward) V_{jet}^z component, and they were detected under IMF and dipole tilt conditions similar to those shown on the top of the respective panel (see text for details). The location of the spacecraft when it detected the plasma jet at the dayside magnetopause crossing is marked by the black filled circle.

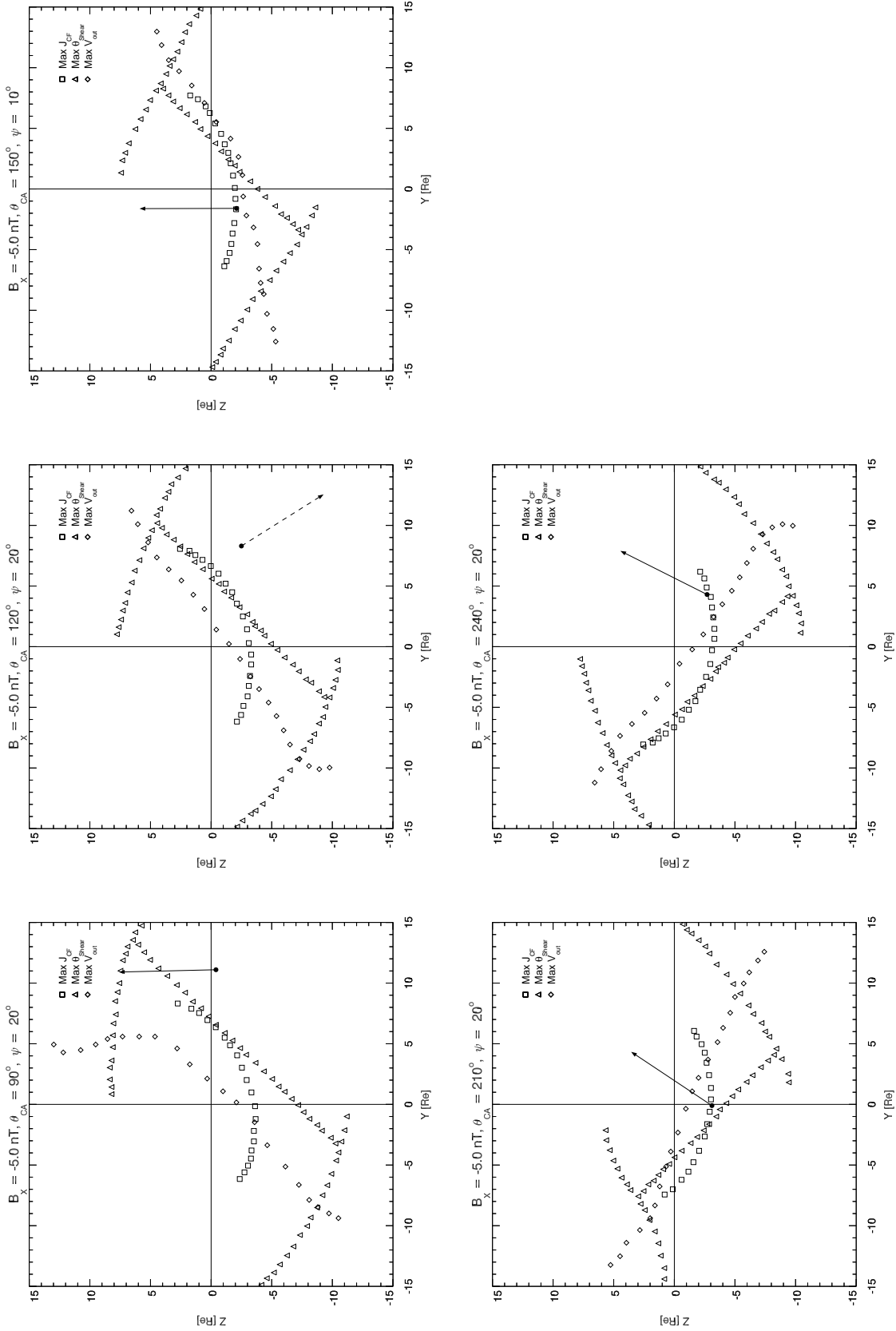


Figure B.6 - X line models test against *in situ* observations of reconnection plasma jets. The X lines which are presented onto the yz_{GSM} plane are derived from the models of maximum Chapman-Ferraro current density magnitude, Max J_{CF} , by Gonzalez and Mozer (1974), the maximum shear angle model, Max θ_{Shear} , by Trattner et al. (2007), and the maximum reconnection outflow speed, Max V_{out} , by Swisdak and Drake (2007). The IMF ($B_x = -5$ nT, $B_z = 0$, -2.886 or -5 nT and $\theta_{CA} = \tan^{-1}(B_y/B_z)$) and Earth's dipole tilt (ψ) conditions used as input to generate the X lines shown are presented on the top of each panel. The observed plasma jet directions are represented as solid (dashed) arrows if they have a northward (southward) V_z^{jet} component, and they were detected under IMF and dipole tilt conditions similar to those shown on the top of the respective panel (see text for details). The location of the magnetopause crossing is marked by the black filled circle.

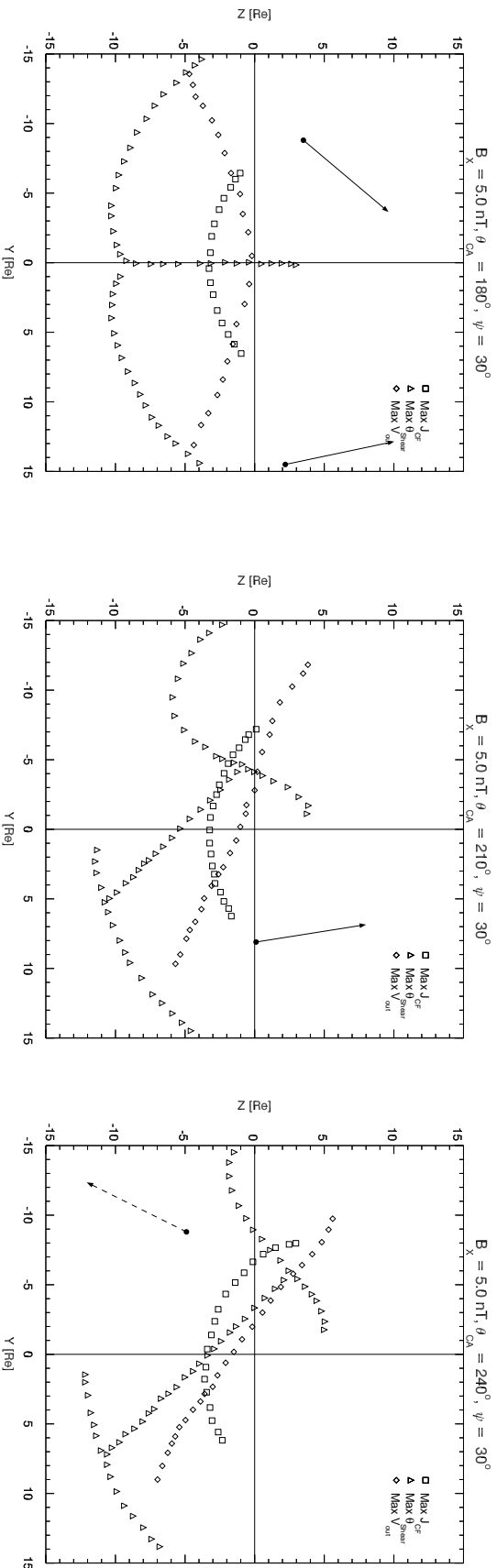


Figure B.7 - X line models test against *in situ* observations of reconnection plasma jets. The X lines which are presented onto the yz_{GSM} plane are derived from the models of maximum Chapman-Ferraro current density magnitude, Max J_{CF} , by Gonzalez and Mozer (1974), the maximum shear angle model, Max θ_{Shear} , by Trattner et al. (2007), and the maximum reconnection outflow speed, Max V_{out} , by Swisdak and Drake (2007). The IMF ($B_x = 5$ nT, B_z either -2.886 or -5 nT and $\theta_{CFA} = \tan^{-1}(B_y/B_z)$) and Earth's dipole tilt (ψ) conditions used as input to generate the X lines shown are presented on the top of each panel. The observed plasma jet directions are represented as solid (dashed) arrows if they have a northward (southward) V_z^{jet} component, and they were detected under IMF and dipole tilt conditions similar to those shown on the top of the respective panel (see text for details). The location of the spacecraft when it detected the plasma jet at the dayside magnetopause crossing is marked by the black filled circle.

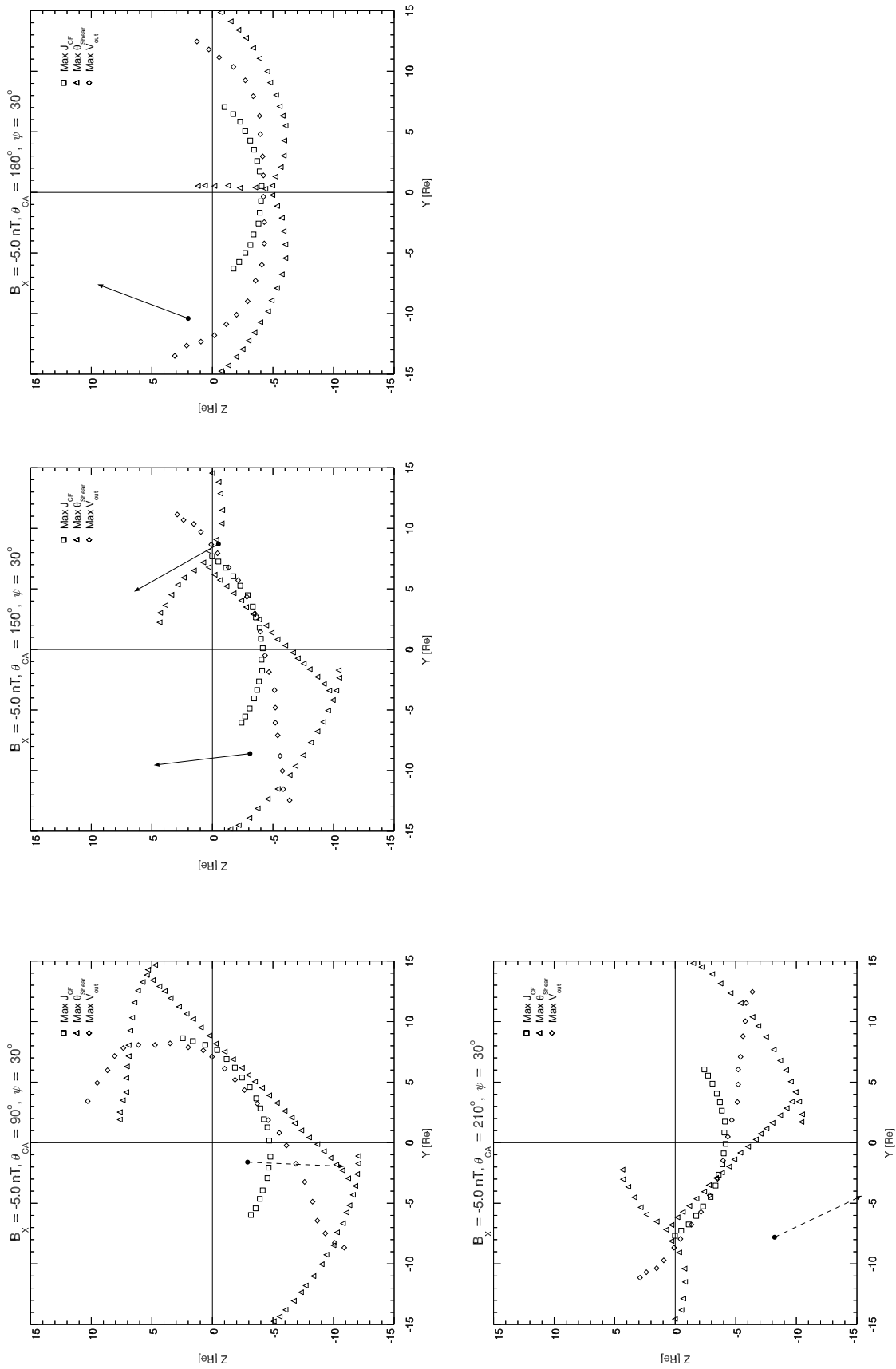


Figure B.8 - X line models test against *in situ* observations of reconnection plasma jets. The X lines which are presented onto the yz_{GSM} plane are derived from the models of maximum Chapman-Ferraro current density magnitude, Max J_{CF} , by Gonzalez and Mozer (1974), the maximum shear angle model, Max θ_{Shear} , by Trattner et al. (2007), and the maximum reconnection outflow speed, Max V_{out} , by Swisdak and Drake (2007). The IMF ($B_x = -5$ nT, $B_z = 0$, -2.886 or -5 nT and $\theta_{CA} = \tan^{-1}(B_y/B_z)$) and Earth's dipole tilt (ψ) conditions used as input to generate the X lines shown are presented on the top of each panel. The observed plasma jet directions are represented as solid (dashed) arrows if they have a northward (southward) V_z^{jet} component, and they were detected under IMF and dipole tilt conditions similar to those shown on the top of the respective panel (see text for details). The location of the spacecraft when it detected the plasma jet at the dayside magnetopause crossing is marked by the black filled circle.

PUBLICAÇÕES TÉCNICO-CIENTÍFICAS EDITADAS PELO INPE

Teses e Dissertações (TDI)

Teses e Dissertações apresentadas nos Cursos de Pós-Graduação do INPE.

Manuais Técnicos (MAN)

São publicações de caráter técnico que incluem normas, procedimentos, instruções e orientações.

Notas Técnico-Científicas (NTC)

Incluem resultados preliminares de pesquisa, descrição de equipamentos, descrição e ou documentação de programas de computador, descrição de sistemas e experimentos, apresentação de testes, dados, atlas, e documentação de projetos de engenharia.

Relatórios de Pesquisa (RPQ)

Reportam resultados ou progressos de pesquisas tanto de natureza técnica quanto científica, cujo nível seja compatível com o de uma publicação em periódico nacional ou internacional.

Propostas e Relatórios de Projetos (PRP)

São propostas de projetos técnico-científicos e relatórios de acompanhamento de projetos, atividades e convênios.

Publicações Didáticas (PUD)

Incluem apostilas, notas de aula e manuais didáticos.

Publicações Seriadas

São os seriados técnico-científicos: boletins, periódicos, anuários e anais de eventos (simpósios e congressos). Constam destas publicações o Internacional Standard Serial Number (ISSN), que é um código único e definitivo para identificação de títulos de seriados.

Programas de Computador (PDC)

São a seqüência de instruções ou códigos, expressos em uma linguagem de programação compilada ou interpretada, a ser executada por um computador para alcançar um determinado objetivo. Aceitam-se tanto programas fonte quanto os executáveis.

Pré-publicações (PRE)

Todos os artigos publicados em periódicos, anais e como capítulos de livros.